HARVESTING ENERGY FROM ACOUSTIC PRESSURE FLUCTUATIONS WITHIN HYDRAULIC SYSTEMS VIA EXCITATION OF PIEZOELECTRIC STACKS

A Dissertation
Presented to
The Academic Faculty

by

Ellen A. Skow

In Partial Fulfillment
of the Requirements for the Degree
Doctor of Philosophy in the
George W. Woodruff School of Mechanical Engineering

Georgia Institute of Technology
August 2017

HARVESTING ENERGY FROM ACOUSTIC PRESSURE FLUCTUATIONS WITHIN HYDRAULIC SYSTEMS VIA EXCITATION OF PIEZOELECTRIC STACKS

Approved by:

Dr. Kenneth A. Cunefare, Committee Chair, Advisor
School of Mechanical Engineering
Georgia Institute of Technology

Dr. Alper Erturk, Co-Advisor
School of Mechanical Engineering
Georgia Institute of Technology

Dr. F. Levent Degertekin
School of Mechanical Engineering
Georgia Institute of Technology

Dr. Aldo A. Ferri
School of Mechanical Engineering
Georgia Institute of Technology

Dr. Christopher S. Lynch
Mechanical and Aerospace Engineering Department
University of California, Los Angeles

Date Approved: May 8, 2017

To all my parents.

ACKNOWLEDGEMENTS

First and foremost, I would like to thank my advisor Dr. Ken Cunefare for his encouragement and guidance, with regards to technical problems, professional development, and dealing with stress that accompanies the PhD process; for his enthusiasm when teaching new concepts or discussing new ideas; for his understanding when accidents happened; and his early reassurance and counsel when presenting my work at technical conferences and in journals. I would second like to thank my co-advisor Dr. Alper Erturk, who motivated me to pursue publications and conferences early on, provided technical guidance both with experiments and models, and was overall an excellent mentor. I would also like to thank the other members of my reading committee: Dr. Degertekin, Dr. Ferri, and Dr. Lynch. In addition, thank you to Dr. Lynch's lab for providing some of the test specimens used in this project.

Elliott Gruber and I went through the graduate school process together in the same lab from the very beginning, and I am immensely grateful I had him as someone that truly understood. EIJ kept my spirits up, even when things were at their worst. The amount of help he provided as a labmate and a friend (excluding a few gold bars) cannot be overstated. Shima Shahab was another golden labmate that provided encouragement, kindness, and an ally, especially when equipment decided to take a vacation. A special thanks also goes to Stephen Leadenham, who provided both a wide range of technical knowledge and true enthusiasm for science. Thank you to Dr. Ben Beck and Dr. Nick Earnhart for their initial friendship, training, and tips on surviving the rules of graduate school. And thank you to all my lab mates in IAL and SSDSL (both foreign and

domestic), who I consider both friends and colleagues; it was a joy bouncing ideas off of you all.

During the course of this project, much of the prototype design work (hermetic sealing, stress analysis, CAD, etc.) and some of the testing in this project were performed by undergraduate research students working with me. They helped advance this project and helped me become a better instructor; I am very grateful to all their hard work and ideas. These students (in chronological order) are Nalin Verma, Jeremy Savor, Daniel Kim, Aaron Kranc, Zachary Koontz, Brian Hults, Karthika P. V., Chong Woo (John) Han, Tanya Johnson, Tri Nguyen, David Cavanaugh, Bradley Argauer, Zach Hussin, Mark Cops, Forest Schwartz, Charles Xiao, and Jamie Burdell. This leads me to thank Steven Sheffield and others at the machine shop for all their help with manufacturing these prototypes and test structures. Also, a big thank you to J.D. Huggins, who was extremely helpful for both working with hydraulic equipment and in the machine shop.

I am also extremely grateful for my friends outside of lab that made Atlanta feel like home and provided so many fun memories, especially to Arto Kivila, Wayne Maxwell, Jr., Anne Mallow, Stephen Leadenham, Hannes Daepp, Martin Cacan, Theresa Wilks, and Kavin Manickaraj. You all made my day brighter and motivated me to keep on going.

I further would like to express my gratitude to Arto Kivila and my family. My family not only put up with me telling them I was working on the same project for years, but also continued to show me support and stabilizing advice to keep me grounded through this process. Arto has been not only been my go to person if I need a smile or to calm down, but also provided lots of encouragement to push beyond my comfort zone.

Finally, I must thank the Center for Compact and Efficient Fluid Power, a National Science Foundation Engineering Research Center, for their financial support and the networking this group provided to me.

TABLE OF CONTENTS

LIST OF TABLES

LIST OF FIGURES

LIST OF SYMBOLS AND ABBREVIATIONS

A Cross sectional area of piezoelectric

A_{eff} Effective area of interface between fluid and piezoelectric element in hydraulic pressure area harvester

$A_{interface}$ Area of interface between fluid and piezoelectric element (e.g. spacer or membrane)

A_{neck} Cross sectional area of HR neck

A_{stack} Area on piezoelectric element interfacing with fluid

a Neck radius of HR

b_0 Initial air volume fraction at reference temperature and atmospheric pressure

b Air volume fraction within HR

C Capacitance, Compliance

C_{air} Compliance of entrained air within HR cavity

C_{eff} Effective compliance in HR cavity

C_{fl} Compliance of oil within HR cavity

C_N Compliance of N, where N is either air, hydraulic oil, or foam

C_p^i Capacitance of a single piezoelectric layer

C_p Piezoelectric capacitance

c Speed of sound

$\mathbf{D}, D$ Electric displacement

d_{klm}^i Piezoelectric strain constant for stress in σ_{kl} direction and on layer i

d_{33}^{eff} Effective piezoelectric strain constant for entire piezoelectric stack in 33-direction

d_{cav} HR cavity diameter

d_{neck} HR neck diameter

d_v Viscous boundary layer, $\sqrt{2\nu_f/\omega}$

E Electric field

E_p^E, E_p^s Elastic modulus of short circuited (superscript *E*) and shunted (superscript *s*) piezoelectric element

FEO – Ferroelectric orthorhombic crystalline phase

FER – Ferroelectric rhombohedral crystalline phase

F_0 Force amplitude

F_{bvpre} Preload force on Belleville spring

F_{rms} Root-mean-square force

F_{SCpre} Preload force on single crystal specimen

f Frequency in Hertz; function (reference Eq. 3.5)

f_{res} Natural resonant frequency of HR

G Power gain from Helmholtz resonator (dB)

g Pressure ratio, or P_{HPEH} / P_{pipe}

H Heaviside function

h Thickness of single piezoelectric layer

HBM – Harmonic balance method

HPEH – Hydraulic pressure energy harvester

HR – Helmholtz Resonator

I_{ac} Acoustic intensity

I_s Reverse, or saturation, current of diode

$\Im$ Imaginary function (imaginary portion of complex term)

i Current (function of time)

i_D Current of diode

i_L Current across inductive load

J_{ij} Jacobian matrix

j Imaginary number

$K_{0,T}$ Isothermal secant bulk modulus at atmospheric temperature (in GPa)

$K_{P,T}$ Isothermal secant bulk modulus for a given pressure (in GPa)

K_f Isothermal tangent bulk modulus of hydraulic oil for a given system pressure

K_N Bulk modulus of *N*, where *N* is a given substance, e.g. oil or foam

k_{33} Electromechanical coupling coefficient

k_b Boltzmann constant, $\approx 1.380 \times 10^{-23}$ J/K

k_{bv} Stiffness of Belleville springs

k_{pz} Stiffness of piezoelectric element (stack or single crystal)

k_f wavenumber of hydraulic oil

L Inductive load

l_{cav} Length of HR cavity

l_{neck} Length of HR neck

$l_{n,eff}$ Effective length of HR neck

M_a Acoustic mass

m Mass of fluid in HR neck

N Number of piezoelectric layers in piezoelectric element or number of

n Vector of surface normal of the electrodes

n Quality (or ideality) factor, ranges in value from 1 to 2

PIN-PMN-PT – Lead indium niobate - lead magnesium niobate - lead titanate

PMN-PT – Lead magnesium niobate - lead titanate

PT – Lead titanate

PZT – Lead zirconate titanate (piezoelectric material used in most HPEH)

P_0 Pressure amplitude of dynamic pressure

P_{atm} Atmospheric pressure, 0.1 MPa

P_{dyn} Peak to peak dynamic pressure

P_{HPEH} Pressure amplitude within HPEH HR cavity

P_{op} Operating static pressure level

P_{pipe} Pressure amplitude within pipe (system flow)

P_s, P_{static} Static pressure (mean pressure of hydraulic system)

q Magnitude of electrical charge on an electron, $\approx 1.602 \times 10^{-19}$ C

R – Circuit with resistive load only

R-L – Circuit with resistive load in parallel with inductive load

R_a Acoustic resistance

R_{air} Specific gas constant for air, 287.058 J/(kg K)

R_{in} Internal resistance of inductive load

R_l Resistive load

R_r Sound radiation resistance

R_w Resistance due to viscous effects within HR neck

R_x Reaction force on spacer when force shunt is enacted

$\Re$ Real function (real part of complex term)

S.G. Specific gravity

SSHI – Synchronized switch harvesting on inductor

T, T_C Temperature in degrees Celsius

T_c Characteristic time (Chapter 5, Eq. (5.6))

T_K Temperature in Kelvin

T_{ref} Reference temperature

t time

U Potential energy

u Nondimensional state vector (used for voltage multiplier)

VM – Voltage multiplier, also known as cascade circuit in literature

V_0 Voltage amplitude

V_c Characteristic voltage (Chapter 5, Eq. (5.6))

V_{cav} Volume of HR cavity

V_N Volume of *N*, where *N* is either air, hydraulic oil, or foam.

V_{stack} Volume of piezoelectric element

V_T Thermal voltage, about 26 mV at room temperature (300 K)

v Voltage (function of time)

v_p Voltage of piezoelectric

v_D Voltage of *p-n* junction on diode

W Weighted pressure-frequency gain

$W_{R_{opt}}$ Weighted pressure-frequency gain for resistive only circuits

x_{spacer} Spacer displacement

Y_s Shunted admittance

Z Impedance

Z_c Impedance of HR cavity

Z_e Total electrical impedance of circuit

Z_m Impedance of acoustic mass in HR

Z_p Impedance of HR neck

Z_s Impedance of electrical shunt load

α Frequency response function between voltage and force (Chapter 2); volumetric expansion coefficient (Chapter 3)

α_w Loss factor of complex wavenumber

ε Permittivity (subscript 0 indicates permittivity of free space $\approx 8.8542 \times 10^{12}$ F/m)

γ Area ratio, or $A_{interface} / A_{stack}$

γ_s Ratio of specific heats

γ_{air} Ratio of specific heats for air, 1.402

η_s Electrical shunt efficiency

κ Force shunt ratio

μ_f Absolute (dynamic) viscosity

ν_f Kinematic viscosity of fluid

Π Power

π (reserved for ratio of circle's circumference over diameter)

ρ Density

σ Stress

τ Nondimensional time

υ Poisson's ratio

ω Angular (radial) frequency

ω_0 Angular frequency of interest, e.g. dominant frequency in dynamic pressure

ω_d Damped natural frequency of HR

ω_{res} Natural resonant frequency of HR

ξ Complex coefficient for viscous effects

ξ^*	Term related to viscous effects complex coefficient, $\sqrt{\nu_f / (j\omega a^2)}$	ζ	HR neck correction ratio, d_{neck}/d_N, where N is either pipe or cavity diameter

SUMMARY

Hydraulic systems provide a unique opportunity to convert acoustic energy into electric energy due to the high intensity pressure ripple in the system. Hydraulic pressure energy harvesters (HPEHs) aim to provide a power source for powering or recharging wireless sensor networks on hydraulic systems through using an inherent byproduct of the pumps and actuators – the pressure ripple. HPEHs are able to connect to hydraulic systems via ports typically used for other sensors, such as for static pressure or temperature monitoring. HPEHs convert the pressure ripple into electricity by coupling the fluid fluctuations to a piezoelectric element, such as a stack or single crystal. The pressure ripple dominant frequencies are typically contained within the first or second harmonic of the pump operating frequency, which is usually in the 100s of Hz range, meaning the piezoelectric element is excited well below its resonance frequency. The combination of low-frequency excitation and high piezoelectric stack capacitance allow implementing an inductive load and resistive load in parallel with the piezoelectric stack to provide a passive resonant circuit. Using a soft PZT stack within a HPEH device and a parallel resistive load, a HPEH is able to provide 12.8 mW of AC power for a 202 kPa dynamic pressure amplitude, which corresponded to 0.31 $\mu W/(kPa)^2$ of power per squared dynamic pressure amplitude, which is sufficient to power sensors. Power needed for a wireless sensor transmitting data once every second is estimated to be 3.7 mW. This work introduces the HPEH devices, provides an electromechanical model, and investigates multiple methods to increase the power conversion efficiency and regulate the power output.

There are three main parts of HPEH devices: (1) the mechanical coupling between the hydraulic fluid & piezoelectric element; (2) the piezoelectric material; and (3) an

electrical circuit connected to the piezoelectric element. In regards to the mechanical coupling element, a Helmholtz resonator design is introduced and modeled for the coupling between a HPEH and the hydraulic system to provide pressure – and thus force – amplification to the piezoelectric element, resulting in a doubling of the normalized power response. For the piezoelectric material selection, a [011] cut lead indium niobate – lead magnesium niobate – lead titanate (PIN-PMN-PT) single crystal that goes through a phase transformation between ferroelectric rhombohedral and ferroelectric orthorhombic is presented as a higher power efficiency per cycle solution for HPEH devices, resulting in power output levels 100 times greater than soft PZT stacks tested. And finally for the electrical circuitry, this work provides a solution and model for power conditioning of low-voltage, low-frequency piezoelectric stack energy harvesting through the use of an inductive load in parallel with a voltage multiplier (VM), or cascade circuit. The inductive-VM circuit raised the AC voltage level from 0.59 Vrms to 2.4 VDC. A harmonic balance method model of the inductive-VM circuit is presented and provides an average error of 25%, with minimum error of less than 1%, and performed over 600 times faster than SPICE-based time domain transient analysis.

CHAPTER 1

INTRODUCTION

Energy scavenging or energy harvesting is a research area that aims to turn unused ambient energy, such as heat, vibrations, light, and noise, into usable electricity to power wireless sensor networks. Key conditions to make energy harvesting feasible are (1) there must be adequate ambient energy available to harvest and (2) the energy harvester must be able to convert a sufficient amount of the ambient energy for the dependent system. First, the fluid-borne noise within pumped fluid systems, such as hydraulic equipment and pipelines, has milliwatt per square centimeter to 10s of Watts per square centimeter intensity levels that is typically unwanted and wasted; it therefore exceeds the first condition as a feasible energy harvesting source. Second, converting sufficient amounts of the fluid-borne noise into electricity would enable self-powered wireless sensor networks, allow sensors in remote or wire-inaccessible locations, and reduce maintenance contact for replacing batteries or wire connections to sensors. Piezoelectric materials are commonly used for vibration and noise transduction into electricity for both sensing devices, such as pressure measurements [1], and for energy harvesting [2-4]. Sensor technology within hydraulics is well established, and wireless sensors powered by batteries are beginning to emerge in the market [5-7]. Energy conversion within pipes using vibrations or induced turbulence within the fluid flow has been researched [8-10], however converting the pressure ripple, or fluid borne acoustic noise, into usable electrical power in MPa-level pressure fluidic systems is a new research topic [11, 12]. This work aims to expand research in energy harvesting from an acoustic energy source and within a high stress environment. This includes using piezoelectric elements excited off-resonance to transduce acoustic

energy into electrical energy; increasing power through resonance amplification of narrow-port fluid based Helmholtz resonators; inducing piezoelectric single crystals through a crystal phase transition at a hundreds of Hertz frequency level; and introducing power conditioning of low voltage level, high capacitive energy harvesters.

Portions of this chapter have been reviewed and published in Smart Materials and Structures [11] and at the International Congress on Acoustics, 2013 [13].

1.1 Overview of hydraulic systems

The process of using confined, pressurized fluid to transmit forces and motions is known as fluid power, and includes both pneumatics, which uses air, and hydraulics, which typically uses oil [14]. From construction and mining equipment to water pipelines and the Jaws of Life, hydraulic systems provide a high force density and power density method to transmit forces and motion.

Hydraulic systems use sensors for monitoring the health, pressure level, temperature, etc., and can be difficult to wire to for power and data transmission, especially if on a moving (including rotating) component, remote area or inaccessible location. Some companies are introducing battery powered wireless sensors, thus eliminating the wire dilemma, however still requiring maintenance contact for periodic battery replacements. For instance, Eaton LifeSense and Parker's SensoNODE Blue provide condition monitoring for predictive maintenance [5, 7]. The SensoNODE Blue uses a CR123A battery that has a 1.5 A-hr capacity; for a data transmission rate once every second and an assumed voltage level of 3 Vdc, the battery is expected to last for 50 days, which corresponds to 3.7 mW needed power [7]. Another example is the MEAS M5600 Wireless Pressure Transducer by TE Connectivity Sensors; this sensor uses a replaceable battery

that has a 350 mA-hr capacity with a supply voltage typically at 3 Vdc. For a 5 second transmission interval, it is reported to last for 2 years, which corresponds to a 60 μW power consumption level. This body of work aims to convert acoustic energy present on the hydraulic system into electricity that can be used to power wireless sensor nodes or recharge batteries, thus reducing maintenance contact frequency. This work aims to reach or exceed the power levels required for current wireless sensors on the market.

Hydraulic systems use hydraulic pumps to convert mechanical energy into hydraulic energy by producing liquid flow necessary for system pressure development. According to the editors of Hydraulics & Pneumatics website, the most common type is positive displacement pumps, which displaces the same volume of liquid for each rotation cycle of the pumping mechanism [15]. This creates a pulsating flow that may cause leaks and other problems in a high pressure system, and is typically reduced through noise control devices such as suppressors and accumulators. Periodic pressure disturbances, called dynamic pressure or pressure ripple, are a wasted byproduct of pumps that is a high energy density acoustic source, even with noise control devices. However, since pressure ripple is viewed as a negative aspect and research in noise attenuation solutions continues to be researched, efficient energy conversion methods and effective modeling of these methods will be necessary for an energy harvester to be a long-term viable solution. The relationship between the fluidic power intensity and dynamic pressure quantifies the ambient energy available for harvesting.

The periodic pressure disturbances have a high power intensity, meaning there is sufficient mechanical power per unit area available to convert for powering the targeted electrical subsystems described earlier (sensor nodes and rechargeable batteries). For many

hydraulic systems, most of the energy within the system is contained in a narrow frequency band, such as a harmonic of the pump operating frequency. Additionally, the dynamic pressure typically increases with the static, or mean, pressure of the system, which can reach up to 35 MPa in industrial hydraulic systems. For example, Figure 1.1a shows the frequency spectrum measured from a hydraulic system that uses a 9 piston positive displacement pump operating at 1500 rpm, which corresponds to an operating frequency of 225 Hz. Most of the energy in this system is within the first or second harmonic of the

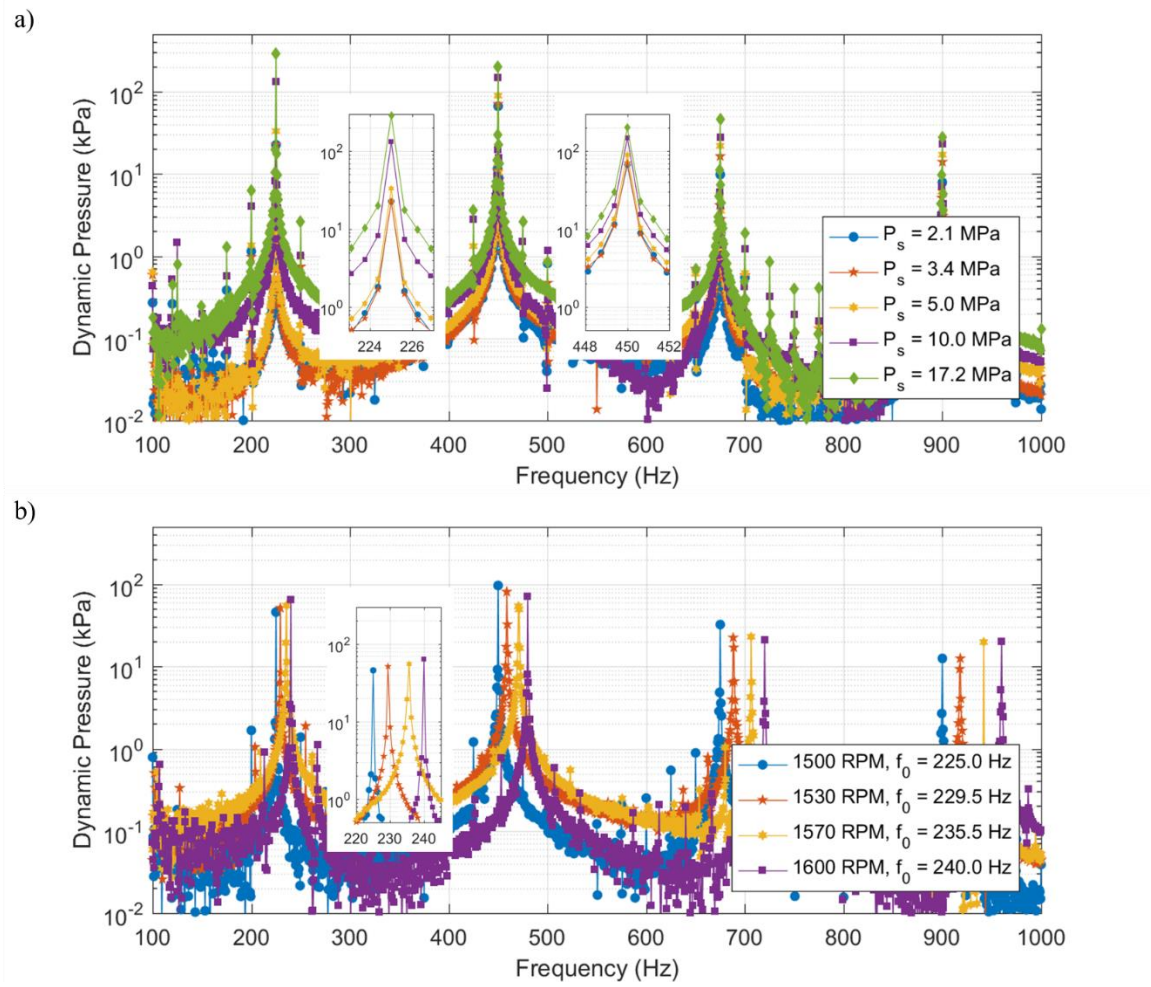

Figure 1.1: Frequency spectrum of pressure ripple in a hydraulic system due to a 9-piston pump (measured results): a) operating at 1500 rpm and various static pressure levels; b) operating at various speeds.

pump operating frequency, and the dynamic pressure increases with the static pressure. This is shown in Figure 1.1, where Figure 1.1a are measured results at various static pressure levels and Figure 1.1b are measured results at various operating speeds. In each case, most of the energy is within the first or second harmonic of the operating frequency.

To provide a sense of the acoustic pressure levels within the fluid of the hydraulic system, it is useful to provide a comparison to familiar airborne acoustic pressure levels. Typical airborne acoustic pressure root-mean-square amplitudes for a conversational level (60 dB *re* 20 μPa), a motorcycle (100 dB), a loud rock concert (114 dB), and the threshold of pain (140 dB) are about 0.02 Pa, 2 Pa, 10 Pa, and 200 Pa, respectively. The peak dynamic pressure amplitudes within hydraulic systems, as seen in Figure 1.1, can regularly be well above 10 kPa, with levels typically reaching up to 10 percent of the static pressure level; furthermore, digital hydraulics have started developing even higher pressure ripples.

In a hydraulic system with plane wave pressure fluctuations, such as in pipes with relatively rigid walls, the acoustic intensity I_{ac} is described by

$$I_{ac} = P_0^2 \big/ 2\rho c \ , \tag{1.1}$$

where the speed of sound c in the hydraulic fluid (ISO VG 46) is approximately 1400 m/s, the density ρ of hydraulic fluid is 881 kg/m^3, and P_0 is the amplitude of the dynamic pressure in Pa. Measurement of the pressure ripple then allows for the intensity to be calculated, which is shown in Figure 1.2 for possible dynamic pressure amplitudes exhibited in a hydraulic system. Pressure ripple in the hydraulics community represents the peak-to-peak amplitude of the dynamic pressure. Figure 1.2 displays the intensity in units of mW/cm^2 because the power harvested is expected to be on the order of milliwatts, as

referenced earlier, and the cross sectional area of a pipe is on the order of square centimeters.

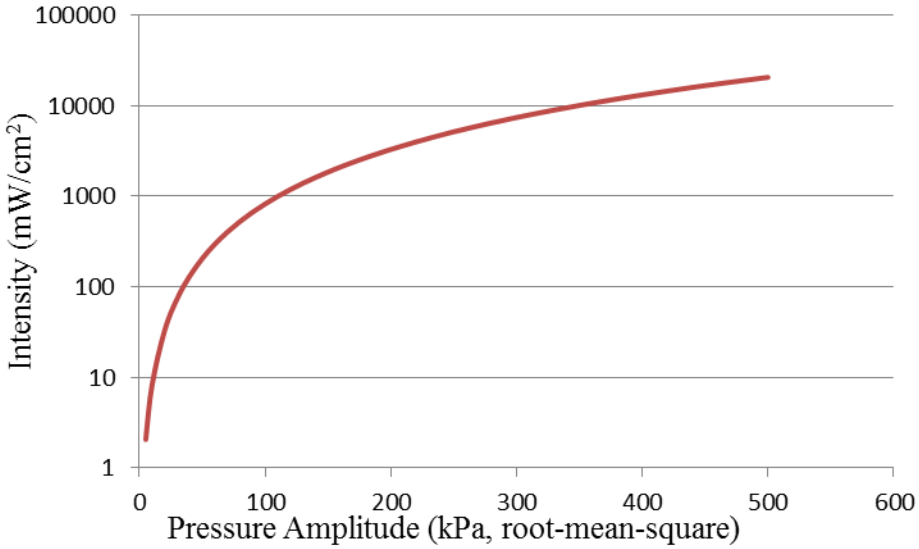

Figure 1.2: Dynamic pressure intensity in oil based hydraulic systems

In comparison with typical intensity levels of acoustic noise in air, the intensity level within hydraulic systems is high. For example, a plane wave with a sound pressure level of 114 dB *re* 20 μPa has an intensity of 0.024 mW/cm^2, whereas the intensity of a 10 kPa pressure amplitude within a hydraulic system is about 8 mW/cm^2, which is sufficient to power small sensor nodes if converted into electricity.

While pumped fluids have significant intensities within high pressure hydraulic systems, such as mobile excavators, the intensities are reduced within cross-country pipelines or water distribution networks. The available power for various pipe sizes is shown in Figure 1.3 for water-based pipes to demonstrate this; while there is still sufficient power for wireless sensor nodes, it does require high transduction efficiency because wireless sensors have similar power requirements to the available power levels.

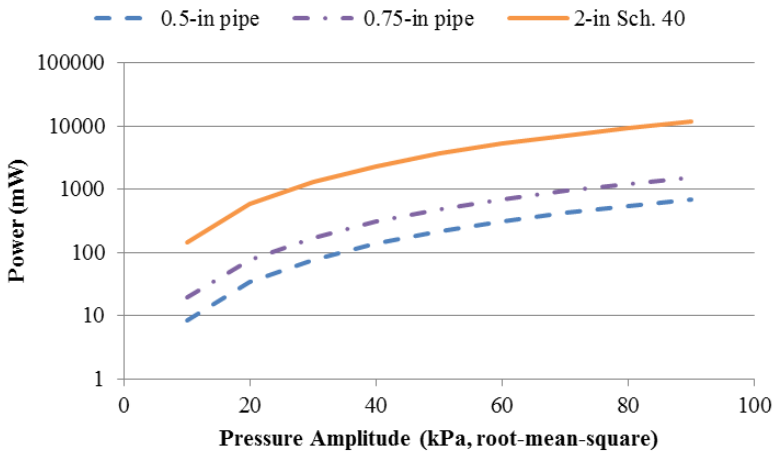

Figure 1.3: Available power from acoustic pressure within pipes containing water at 20°C; previously published by author in [16].

The pressure ripple can be converted to electricity via the direct piezoelectric effect. The direct piezoelectric effect, first discovered by Jacques and Pierre Currie in 1880 [17], is where stress applied to non-centrosymmetric materials results in a net polarization, where polarization is charge per unit area. If the pressure disturbances in hydraulic systems produce stress changes in a piezoelectric element, then the mechanical energy is converted to electrical energy and can be "harvested" for powering an electrical subsystem. In other words, a piezoelectric element mechanically coupled to the pressure ripple in a hydraulic system and electrically coupled to an electrical subsystem can be termed an energy harvester. The energy harvester presented by this work and detailed in Chapter 2 usually employs piezoelectric stacks, formed by multiple piezoelectric layers.

Through the comparison presented and the increase of the power intensity when increasing the mean pressure, it is evident that pressure ripple represents a significantly high-energy-intensity source as compared to other sources. With a large power intensity available in a hydraulic system, it is possible to convert hydraulic pressure fluctuation energy into electrical power without negatively affecting the hydraulic system.

Additionally, the high energy density allows for a piezoelectric stack coupled to the system to perform off-resonance of the piezoelectric element, which is uncommon for energy harvesting systems, while still transforming milliwatt level power. Accordingly, a review of energy harvesting methods in fluidic and acoustic systems is appropriate.

1.2 Energy harvesting literature review

The main goal in energy harvesting is to enable self-powered wireless electronic systems, and thus reduce the maintenance requirements for battery replacement as well as the chemical waste of conventional batteries. Most of the existing research on energy harvesting has focused on the direct conversion of vibrations into electricity [18]. Flow-excited power generators covered in the existing literature are mainly focused on (1) converting flow-induced aeroelastic or hydroelastic vibrations into electricity or (2) implementing Helmholtz resonators and sonic crystals for indirect use of flow pressure (mostly air flow), by creating vibrations of the energy harvesting (EH) system. The EH system is typically a piezoelectric beam or membrane, an electroactive polymer, or an inductive coil and magnet arrangement.

1.2.1 Energy harvesting from fluidic systems

Other than the efforts toward miniaturizing the classical wind turbine design [19-22] in conjunction with fan rotors and DC motors, researchers have become interested in exploiting aeroelastic/hydroelastic and acoustic phenomena for flow energy harvesting by means of electromechanical transducers. The first use of a piezoelectric interface in flow energy harvesting appears to be the bluff body – a PVDF (polyvinylidene fluoride) membrane configuration known as the “energy harvesting eel” – tested under water by Allen and Smits [9]. The von Kármán vortex street formed behind the bluff body excites

the piezoelectric PVDF to extract electricity from flow-induced vibrations through the piezoelectric effect. Unlike piezoelectric ceramics, PVDF films are very weakly coupled (in terms of their piezoelectric constants) to generate usable electricity, but they are very compliant, such that they may undergo large deformations at low frequencies. Vortex-induced oscillations of piezoelectric cantilevers (PZT-based ceramic and/or PVDF) located behind bluff bodies (variants and extensions of the configuration introduced by Allen and Smits [9]) were also investigated by Pobering and Schwesinger [23] and Akaydin et al. [8] through experiments and numerical simulations.

For the piezoaeroelastic problem of energy harvesting from airflow excitation of a cantilevered plate with embedded piezoceramics, De Marqui et al. [24, 25] presented finite-element models based on the vortex-lattice method [24] and the doublet-lattice method [25] of aeroelasticity. Time-domain simulations [24] were given for a cantilevered plate with embedded piezoceramics for various airflow speeds below the linear flutter speed and at the flutter boundary. Frequency-domain simulations [25] considering resistive and resistive-inductive circuits were also presented focusing on the linear response at the flutter boundary. Bryant et al. [26, 27] studied the aeroelastic energy harvesting problem for a typical section by using a finite state theory. Erturk et al. [28] presented an experimentally validated lumped-parameter model for an airfoil with piezoceramics attached to plunge stiffness members using Theodorsen's unsteady aerodynamic model. Piezoelectric power generation at the flutter boundary and the minor shift in the linear flutter speed were also discussed. More recently, the nonlinear version of the same setup with a free play in the pitch degree of freedom has been investigated for reducing the cut-in speed of limit-cycle oscillations (LCO) [29]. An extensive analysis of the energy harvesting potential for a foil-

damper system was presented by Peng and Zhu [30] using a Navier-Stokes model without focusing on a specific transduction mechanism.

As an alternative to airfoil-based and cantilevered wing-based configurations, St. Clair et al. [31] presented a "harmonica-inspired" design that uses a piezoelectric beam embedded within a cavity under airflow from a pressurized chamber. Elvin and Elvin [32] theoretically investigated the flutter response of a cantilevered pipe with piezoceramic patches for power generation from liquid flow and its effect on the flutter instability. Tang et al. [33] presented a rigorous analysis of the energy transfer from the fluid to the structure for self-excited vibrations due to axial flow over a cantilever. Piezoelectric energy harvesting from LCO under axial flow over a cantilever beam has also been discussed by Dunnmon et al. [34] recently. Kwon [35] considered a T-shaped cantilever beam that causes vortex street formation over the cantilever in response to axial flow (with the cut-in speed of 4 m/s). Giacomello and Porfiri [36] investigated underwater flapping of an ionic polymer-metal composite (IPMC) flag. Recent efforts have also employed electromagnetic induction for converting aeroelastic vibrations into electricity through flutter [37], wake galloping [38], and bluff body-based oscillations [39].

As mentioned previously, the energy harvester studied in this work employs a piezoelectric stack or a piezoelectric single crystal for transducing the acoustic energy within hydraulic systems into electricity. The high static pressure within hydraulic system argues against using unbacked piezoelectric diaphragms, wafers, or films that are employed in other energy harvesting applications because the high pressure may puncture the material and impede oscillating motions require for transduction [12, 40]. This work describes methods to increase the power converted by a pressure energy harvester while

also accommodating for the high stress environment caused by the static pressure within hydraulic systems. The resonance frequency of piezoelectric stacks is typically much higher than the dominant pressure frequency within hydraulic systems, and is therefore unlike resonant energy harvesting systems described above. Excitation of a piezoelectric stack well below its resonance frequency indicates that the stress field is not affected by changing electrical load; this has been studied in a controlled shaker environment by Zhao, et al. [41]. Furthermore, this work is targeting the acoustic pressure inherent in hydraulic systems; energy harvesting from acoustic pressure is reviewed in the next sub-section.

1.2.2 Energy harvesting from acoustic systems

A fundamental challenge of harvesting energy from acoustic noise is the very low energy density that is typically available. In air, a 60 dB plane wave has an intensity of approximately 1 $\mu W/m^2$, a 100 dB plane wave intensity is 10 mW/m^2, and the intensity of a 140 dB plane wave is approximately 100 W/m^2. These sound fields correspond to a conversational level, an uncomfortable loud level which would cause hearing damage from continuous exposure (and a temporary shift in hearing threshold for shorter exposures) and a level beyond the threshold of pain. If one seeks to harvest energy from a typical low level acoustic signal in the environment, either one must have a large device (or efficient focusing), or have a need for only very low power levels.

Taylor et al. [42] developed an electromechanical acoustic energy harvester based on a Helmholtz Resonator as a means for increasing the pressure amplitude from an acoustic field. This development, as well as those of Liu et al. [43] and Phipps et al. [44] considered an electromechanical Helmholtz Resonator energy harvester for use as an element within a self-powered active control method for noise within the nacelle of a jet

aircraft engine. One wall of the Helmholtz Resonator was a circular piezoceramic plate, such that the pressure response of the resonator would drive the piezoceramic and thereby permit electrical energy extraction, as shown in Figure 1.4. Phipps asserted that the sound field within engine nacelles could approach 160 dB, an intense airborne field. In a related development of the concept, Horowitz et al. [37] considered a MEMS acoustic energy harvester that produced 0.34 μW cm^{-2} over the 6.45 cm^2 cross sectional area of the plane wave tube used for excitation at an acoustic pressure of 149 dB ref. 20 μPa. A more recent Helmholtz-resonator-based energy harvester targeting aircraft noise developed by Matsuda et al. [45] uses a similar approach (with PZT), however implements a cone-shaped design to increase the power converted and bandwidth of the energy harvester. Also, a multilayer PVDF cantilever within a Helmholtz resonator with the purpose to target in-air sound pressure levels of 118 dB or higher was investigated by Lee and Choi [46]. A key point to make about this approach, though, is that the power output of a Helmholtz Resonator-based energy harvester is still limited by the incident intensity of the acoustic wave field; a Helmholtz Resonator acts as a concentrator and effectively increases the "size" of the device, but it cannot extract more energy than is present.

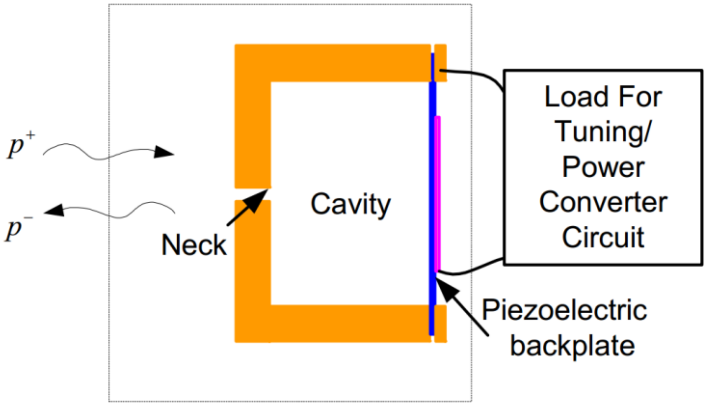

Figure 1.4: Helmholtz resonator energy harvester used for self powered noise control system within jet engine nacelle; from Taylor et al. [42].

Addressing the low intensity of typical airborne acoustic wavefields, Wu et al. [47-49] used a periodic array of rods to create a "sonic crystal" to focus incident sound into a cavity within the sonic crystal. They placed a PVDF membrane inside the cavity and were able to generate a peak output of approximately 35 nano-watts from a 7 Pa pressure difference across the membrane.

Lallart et al. [50] considered a means to increase the energy harvesting efficiency from an acoustic source through a nonlinear harvesting circuit. The device used a circular PZT disk on a baffled flexible metallic membrane exposed to an incident wave field. The device generated up to 55 µW for excitation at resonance with an imposed 100 dB sound pressure level. The surface area of the membrane was 78.54 cm^2, such that the surface power density of the device was 0.7 $\mu W/cm^2$.

A related class of work uses an acoustic response as an intermediate energy conversion process. For example, Kim et al. [51] developed on energy harvester using a Helmholtz resonator excited by a mean flow with electromagnetic transduction. Stevens [52] implanted a thermoacoustic engine driven by the temperature difference between

ambient air and ground; electrical conversion was handled using the thermoelectric effect. Another group, Nouh et al. [53] and Smoker et al. [54], developed a (in-air) thermo-acoustic-piezoelectric resonator, which creates acoustic pressure fluctuations within the resonator when at a particular temperature gradient threshold; a piezoelectric diaphragm is placed at the back end of the resonator and converts the acoustic pressure into electricity. Hernandez et al. [55] used flow instability to excite a tonal response of a pipe; a piezoelectric element was used for electrical energy production. A development by Monthéard et al. [56] uses air passing over a cavity with a piezoelectric membrane within the cavity to produce an aeroacoustic energy harvester. Power produced by this device is dependent on the Mach number and can reach up to 2 mW of RMS power. Khan and Khattak [57] recently provided a review of airborne acoustic energy harvesting devices, and reported the highest power output is the electromechanical Helmholtz Resonator device presented by Liu et al. [43], at 30 mW from 161 dB re 20 µPa sound pressure level.

Within liquids, flow-induced vibration energy harvesting (as discussed earlier) are far more common than direct or intermediate acoustic energy harvesting. A shear-mode piezoelectric energy harvester operated under pressurized water flow was presented by Wang and Liu [40] by combining a pressure chamber with a flexible diaphragm and piezoelectric film configuration. The reported 0.45 nW instantaneous output power from a 45 Hz and 20.8 kPa pressure amplitude excitation from pumped water flowing from a tube to pressure chamber to an open-air tank. Deterre et al. [12] provided a model and preliminary tests for fluidic pressure energy harvesting through the deflection of a piezoelectric diaphragm for use in low mean pressure environments (appears to be 1 kPa in paper), meant for implantable medical devices exposed to pressure from blood; the test

setup used for that experiment was pressurized air. Both Wang et al. and Deterre et al. utilize a flexible piezoelectric diaphragm (with a thickness of less than 300μm) in combination with a pressure chamber to induce bending vibrations in the piezoelectric to generate power. Given the system mean pressure present within hydraulic systems, a flexible piezoelectric diaphragm would either burst or require backing by a stiffer material, such as a hose or pipe, if used in systems targeted by this research.

1.3 Dissertation outline

This dissertation contains four main topics. Chapter 2 describes the energy harvester that is used to convert acoustic energy within hydraulic systems into electrical energy via piezoelectric elements, along with an electromechanical model, simulations, and experimental validations for resistive and resistive-inductive electrical loading. The next three chapters describe methods to improve this conversion and include the main topics of research contribution. In the order of the energy flow, these are: Chapter 3, which investigates a method of amplifying the acoustic energy via a traditional acoustic impedance matching means – a Helmholtz resonator; Chapter 4, which investigates using a single crystal that undergoes a crystal phase transformation when under high stress oscillations (around -30 to -15 MPa); and Chapter 5, which introduces a modified power conditioning method to both rectify the current and raise the voltage output from the energy harvester. The final chapter summarizes the research contributions and discusses future research opportunities.

CHAPTER 2

HYDRAULIC PRESSURE ENERGY HARVESTING

Piezoelectric elements, such as stacks and single crystals, are employed for converting the acoustic pressure, or pressure ripple, within hydraulic systems into low-power level electricity. A number of prototypes, termed hydraulic pressure energy harvesters (HPEHs), were built for studying this concept. This chapter will introduce HPEHs, provide an electromechanical model for HPEHs employing piezoelectric stacks excited below the stack's resonance frequency, discuss testing methods and results, and present mechanical design advancements to accommodate various hydraulic systems.

Portions of this chapter have been reviewed and published in Smart Materials and Structures [11, 58].

2.1 Hydraulic pressure energy harvester (HPEH) design

A HPEH is defined by a piezoelectric stack(s) (or single crystal, which is presented in Chapter 4) being mechanically coupled to the dynamic pressure of a hydraulic system. As depicted in Figure 2.1a, the piezoelectric stack is contained within a sealed housing and protected from the hydraulic fluid by a thin metal diaphragm interface. The static pressure of the system provides a pre-compressive stress on the piezoelectric stack, while the dynamic pressure excites the stack, providing the acoustic power to be converted into electric power. The force applied to the piezoelectric stack can be amplified through an increase of the effective area between the stack and fluid. The piezoelectric stack is connected to a generic shunt impedance that can be modified to amplify the power response for a given pressure input. During testing, as shown in Figure 2.1b, a HPEH device is

connected to a mounting block that is in-line with the fluid flow and upstream of a needle valve used for controlling the static pressure. A pressure transducer measures the pressure for the same cross-sectional area as the input pressure to a HPEH. The piezoelectric stack is connected to an impedance load (such as a resistive load), and then connected to a data acquisition (DAQ) setup for measuring the voltage produced. The testing details and HPEH design aspects are discussed in detail in Section 2.3. Key design considerations of a HPEH include the hydraulic fluid impedance, the fluid-stack interface, the piezoelectric stack, and the harvesting circuit; the importance of these considerations is further clarified by an electromechanical model of a HPEH device presented in the next section.

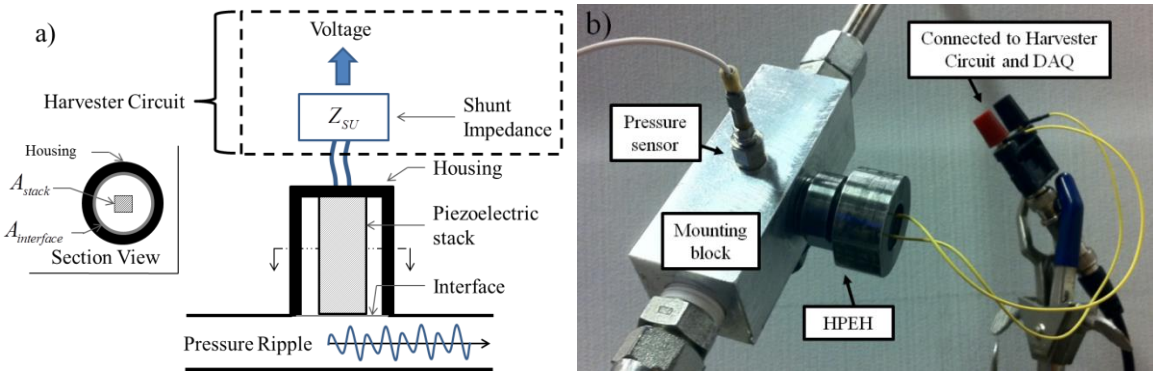

Figure 2.1: Hydraulic pressure energy harvester (HPEH) (a) schematic and (b) test set up

2.2 Electromechanical model of HPEH employing piezoelectric stacks

HPEH devices utilize piezoelectric stacks excited by the pressure ripple in hydraulic systems and, as discussed in Section 1.1, the dominant excitation frequencies are typically either the first or second harmonic of the pump operating frequency (ranging in the 100s of Hertz). Thus, the excitation frequency is much lower than a typical stack resonance frequency (typically much greater than 1000 Hertz). Due to this, the

piezoelectric stress field is assumed to be insensitive to the electrical load, and therefore HPEH devices can be modeled as a first-order mechanical system. Electromechanical modeling details of deterministic and stochastic energy harvesting from piezoelectric stack under direct force excitation and resistive shunt loading have also been investigated by Zhao et al. [41].

An electromechanical model has been developed to model the alternating current (AC) power output of HPEH devices. For a piezoelectric stack with N thickness-poled layers connected in parallel to an external shunt impedance Z_s, the governing circuit equations is obtained from the time derivative of Gauss's law,

$$\sum_{i=1}^{N} \frac{d}{dt}\left(\int_{A_i} \mathbf{D} \cdot \mathbf{n} dA_i \right) = \frac{v(t)}{Z_s} \tag{2.1}$$

where $v(t)$ is the voltage response across the shunt (i.e. across the terminals of the stack), **D** is the vector of electric displacements, **n** is the vector of surface normal of the electrodes, and the integration of their inner product is performed over the electrode area A_i of the i-th layer. The nonzero contribution from the electric displacement is from

$$D_3 = d_{33}^i \sigma_3 + \varepsilon_{33}^\sigma E_3 \tag{2.2}$$

where σ_3 and E_3 are the stress and electric field components, respectively, d_{33} is the piezoelectric strain constant for each layer, and ε_{33}^σ is the permittivity constant for each layer at constant stress [59]. The stress component σ_3 can be related to a harmonic response of the hydraulic pressure ripple by $\sigma_3(t) = P_0 e^{j\omega t}$, with P_0 being the pressure amplitude, j

is the imaginary number, and ω is the excitation frequency, such as the dominant hydraulic pressure ripple frequency. The electric field E_3 is related to the stack voltage through $E_3(t) = -v(t)/h$, where h is the thickness of a single piezoelectric layer and the steady state voltage output can be represented by $v(t) = V_0 e^{j\omega t}$.

Substitution of Eq. (2.2) into Eq. (2.1), in addition to the defined electric field and stress terms, results in

$$\frac{NA_{stack}\varepsilon_{33}^{\sigma}}{h}\dot{v}(t) + \frac{1}{Z_s}v(t) = \dot{P}(t)A\left(Nd_{33}^{i}\right), \tag{2.3}$$

which is the governing equation for hydraulic pressure energy harvesting devices. This can be further simplified by defining effective terms for the entire piezoelectric stack in use rather than a single layer of piezoelectric material. The piezoelectric layers are connected electrically in parallel, which results in the effective capacitance represented as

$$C_p = NC_p^i = \frac{NA\varepsilon_{33}^{\sigma}}{h} \tag{2.4}$$

and the effective piezoelectric strain represented as

$$d_{33}^{eff} = Nd_{33}^{i}. \tag{2.5}$$

The voltage output for the steady state condition can therefore be represented as

$$v(t) = V_0 e^{j\omega t} = j\omega Z_e d_{33}^{eff} A P_0 e^{j\omega t}, \tag{2.6}$$

where the total electrical impedance (Z_e) is

$$Z_e = \left(j\omega C_p + \frac{1}{Z_s} \right)^{-1}, \tag{2.7}$$

which contains both the stack capacitance and a generic shunt impedance. This also leads to a voltage output-to-force input frequency response function (FRF) for an arbitrary shunt impedance, defined as

$$\alpha = \frac{v(t)}{AP_0 e^{j\omega t}} = j\omega Z_e d_{33}^{eff} \ . \tag{2.8}$$

A circuit diagram of this electromechanical model is visually depicted in Figure 2.2.

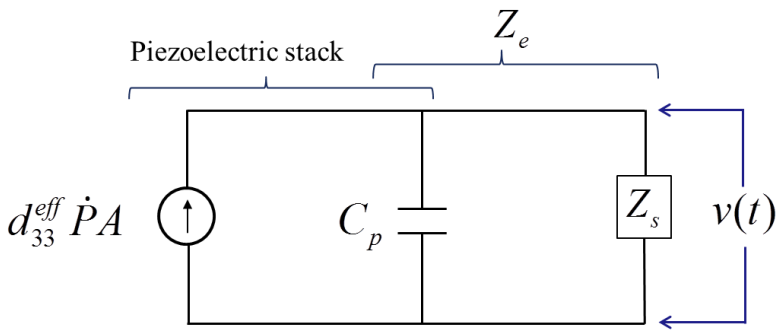

Figure 2.2: HPEH circuit diagram for generic shunt impedance

The average power dissipated in a shunt is

$$\Pi_{avg} = \frac{|Z_e|^2 (\omega d_{33}^{eff} A P_0)^2}{2|Z_s|^2} \Re(Z_s), \tag{2.9}$$

where $\Re$ indicates the real function and the average power dissipated in a resistive electrical load (R_l) is given by

$$\Pi_{avg,l} = \frac{v_{rms}^2}{R_l} = \frac{|Z_e|^2 \left(\omega d_{33}^{eff} A P_0\right)^2}{2R_l} \tag{2.10}$$

where v_{rms} is the root-mean-square voltage. If any area amplification is included within a HPEH, such as the interface being larger than the cross-sectional area of the stack shown in Figure 2.1a, then $A = A_{stack}\gamma$, where the area amplification ratio is $\gamma = A_{interface} / A_{stack}$. The average power dissipated in a resistive electrical load is used for analysis. The total average power response is found from Eq. (2.10) by summing the corresponding power components in the frequency domain

$$\Pi_{avg,l}^{total} = \sum_{n=1}^{N} \frac{\left|Z_e\right|^2 \left(\omega_n d_{33}^{eff} A P_{0,n}\right)^2}{2R_l} \text{ for n} \in \omega . \tag{2.11}$$

The total average power presented in Eq. (2.11) is used for comparing tests to the electromechanical model.

It is useful to note that the combination of low frequency excitation and high piezoelectric capacitance (relative to the capacitance of one or two piezoelectric layers as in typical benders) allow for the use of a shunted piezoelectric containing a load resistance in parallel with a load inductance. A decade before the research explosion in energy harvesting field, Hagood and von Flotow [60] proposed using this shunt to take advantage of the electrical resonant effects with the end application providing for passive structural damping. While synthetic impedances have been introduced [61], the system parameters of HPEH devices do not require synthetic inductance or impedance. With regard to power generation with a mechanically and electrically resonant (second-order) system, Renno et al. [62] analyzed the parallel resonant circuit and piezoelectric parameters and found that it is possible to maximize the power output for all excitation frequencies when using an optimal resistive and optimal inductive load. The capacitance of typical mechanically second-order piezoelectric energy harvesters, such as linear or nonlinear cantilevers [63-

66], is typically low (on the order of nF), making the inductance requirement very high at ambient vibration frequencies. This is part of the reason linear (and passive) resistive-inductive circuits have not been effectively used to date in the energy harvesting literature since the theoretical work by Renno et al. [62]. However, piezoelectric stacks used in HPEH devices have larger capacitance values (order of μF) than typical bimorphs or unimorphs (order of nF), making linear and passive resistive-inductive loading a viable solution.

For this reason, two shunt impedances are presented: (1) a resistive electrical load (R_l) where $Z_s = R_l$ and (2) a resistive-inductive loading in parallel (R-L circuit). The second case can ideally be represented as

$$Z_s^{ideal} = \left(\frac{1}{R_l} + \frac{1}{j\omega L} \right)^{-1}, \tag{2.12}$$

however for the model to accurately reflect the test results, the internal resistance (R_{in}) of the inductive load (L) must be included, which changes the shunt impedance to

$$Z_s = \left(\frac{1}{R_l} + \frac{1}{R_{in} + j\omega L} \right)^{-1}. \tag{2.13}$$

Once again, the combination of low frequency excitation and high piezoelectric capacitance of a stack (relative to one or two piezoelectric layers) allow for the use of a resistive-inductive loading in parallel without needing synthetic impedances.

The shunt impedance loads can be used in Eq. (2.10) to solve for the predicted power response of the HPEH device. Finding the optimal shunt impedance to maximize

the power response for a given pressure input is important for understanding the capability of a HPEH device. When solving for the optimal power for the first case, where the shunt impedance is simply the load resistance, the optimal loading case is found as $R_l^{opt} = 1/(\omega C_p)$ and the maximum power response is

$$\Pi_{avg,l}\Big|_{R_l = R_l^{opt}} = \frac{\omega\left(d_{33}^{eff} A P_0\right)^2}{2C_p} = \frac{\omega\left(NhA_{stack}\right)\left(\gamma P_0 d_{33}^i\right)^2}{2\varepsilon_{33}^\sigma} = \frac{\omega V_{stack}\left(\gamma P_0 d_{33}^i\right)^2}{2\varepsilon_{33}^\sigma} \qquad (2.14)$$

where V_{stack} is the volume of the piezoelectric stack. Therefore for the resistive load shunt, when the resistive load is at its optimal loading, the power is proportional to the volume of the piezoelectric stack. In addition, when choosing a piezoelectric material, a higher ratio of the squared piezoelectric constant over the permittivity, $d_{33}^i/\varepsilon_{33}^\sigma$, indicates higher power potential for a resistive load shunt.

A similar analysis can be performed to find the optimal loading for the resistive and inductive loads to maximize the power response of an R-L circuit for a single excitation frequency. The electrical circuit equivalent of this shunt loading is shown in Figure 2.3. Similar to the resistive load case, the optimal inductor and resistive loads can be determined by setting the gradient of the power equal to zero, yielding

$$\frac{\partial \Pi_{avg,l}}{\partial L} = 0 \rightarrow L_{opt} = \frac{\left(R_l + 2R_{in}\right) + \sqrt{\left(R_l + 2R_{in}\right)^2 + 4\omega^2 R_{in}^2 R_l^2 C_p{}^2}}{2\omega^2 C_p R_l} \qquad (2.15)$$

and

$$\frac{\partial \Pi_{avg,l}}{\partial R_l} = 0 \rightarrow R_l^{opt,RL} = \frac{\sqrt{\left(-2\omega^2 C_p L + 1 + \omega^4 C_p^2 L^2 + \omega^2 C_p^2 R_{in}^2\right)\left(\omega^2 L^2 + R_{in}^2\right)}}{-2\omega^2 C_p L + 1 + \omega^4 C_p^2 L^2 + \omega^2 C_p^2 R_{in}^2} \; . \qquad (2.16)$$

In practical testing, the internal resistance of an optimal inductance-resistance combination may be difficult to determine prior to solving, or may cause the assumed solution to change. Depending on the design of the inductor (winding, wire material, magnetic core, wire gage, etc.), the internal resistance varies. Thus, the internal resistance of an inductive load is determined by measuring the inductor(s) intended for testing, rather than by calculation. However, as seen in Eq. (2.15), the optimal inductive load is dependent on the internal resistance, so an iterative process for a number of inductors and corresponding internal resistive loads may be required. Therefore, determining an initial inductive load for the iterative solution can be useful for determining optimal loads for a test setting.

If the inductive load was ideal (with no internal resistance), then the power-optimized inductive load is much simpler, however causes a physically unrealizable power prediction:

$$L_{opt} = \frac{1}{\omega^2 C_p} \rightarrow \Pi_{avg,l}\Big|_{L=L_{opt}} = R_l (\omega d_{33}^{eff} A P_0)^2 \ . \tag{2.17}$$

This simplified optimal inductive load unrealistically indicates that as the resistive load approaches infinity, so does the power. While this can be used to estimate starting values for optimal inductance, a more useful simplification of Eq. (2.15) is the limit when the resistive load is infinitely large,

$$L_{opt} = \frac{1}{\omega^2 C_p}\left(\frac{1+\sqrt{1+4\omega^2 R_{in}^2 C_p^2}}{2}\right) \tag{2.18}$$

as it provides a more realistic representation of how the inductive parasitic resistance affects the power response and optimal loading case.

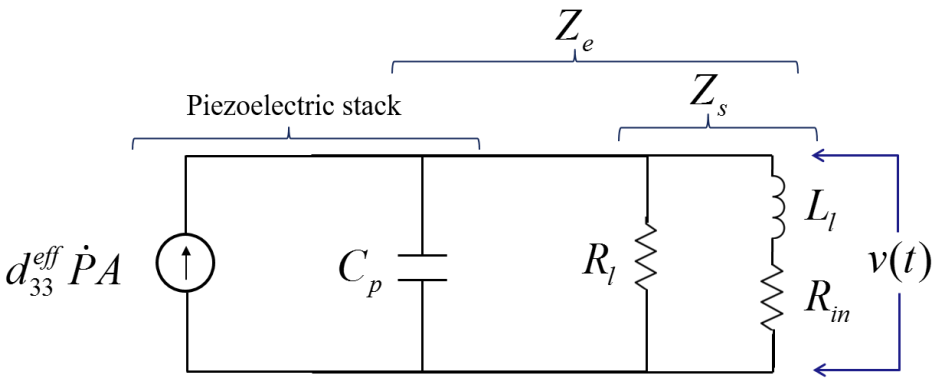

Figure 2.3: HPEH circuit diagram for R-L shunt impedance with reference to generic loading case.

For energy harvesting devices, it is of interest to determine the best broadband shunt impedance loading, which in turn requires the shunt efficiency, η_s, to be analyzed. As discussed earlier, Renno et al. [62] found that it is possible to maximize the power output for all excitation frequencies when using an optimal resistive and optimal inductive load. An analysis of the shunt efficiency can help determine the best broadband scenario for a HPEH device when using an R-L circuit. The shunt efficiency is defined using the average power dissipated in the total electrical shunt, Eq. (2.9), and the average power dissipated across a resistive load, Eq. (2.10). The shunt efficiency relation for an R-L circuit is

$$\eta_s = \frac{\Pi_{avg,l}}{\Pi_{avg}} = \frac{R_{in}^2 + \omega_0^2 L^2}{R_{in}^2 + R_l R_{in} + \omega_0^2 L^2} \ . \tag{2.19}$$

A higher shunt efficiency indicates more broadband behavior for frequencies above the frequency of interest, indicated by the radial frequency ω_0 in Eq. (2.19). However, higher shunt efficiency does not always indicate higher overall power output. To demonstrate this concept, simulated normalized power responses for a piezoelectric stack used in tests is shown in Figure 2.4. A target frequency was chosen along with a theoretical parasitic resistive load; using these values, the optimal inductive and resistive loads for a single

frequency were determined (using Eqs. (2.15) and (2.16)). The average power response (Eq. (2.10)) normalized by the piezoelectric stack volume and squared input force is calculated for a wide range of frequencies, normalized to the first harmonic of the pump operating frequency used in testing, 225 Hz.

As can be seen in Figure 2.4, the circuit parameters with higher shunt efficiency have a consistent peak normalized power for frequencies above the target frequency, however a very poor response for frequencies below the target frequency. This is an important point in hydraulic systems because most of the energy is contained within a narrow band, typically the first or second harmonic of the pump operating frequency. Choosing a circuit with high shunt efficiency for a low target frequency provides a lower power response than for a higher target frequency; however, if the circuit is chosen for a frequency above the frequencies containing the most energy, then the overall performance is worse. In addition, circuits containing low parasitic resistance with respect to the resistive load have lower shunt efficiency, but higher normalized power response at the target frequency. If there is little energy contained outside of the target frequency band, then it may be beneficial to have lower shunt efficiency in favor of higher normalized power response at the target frequency.

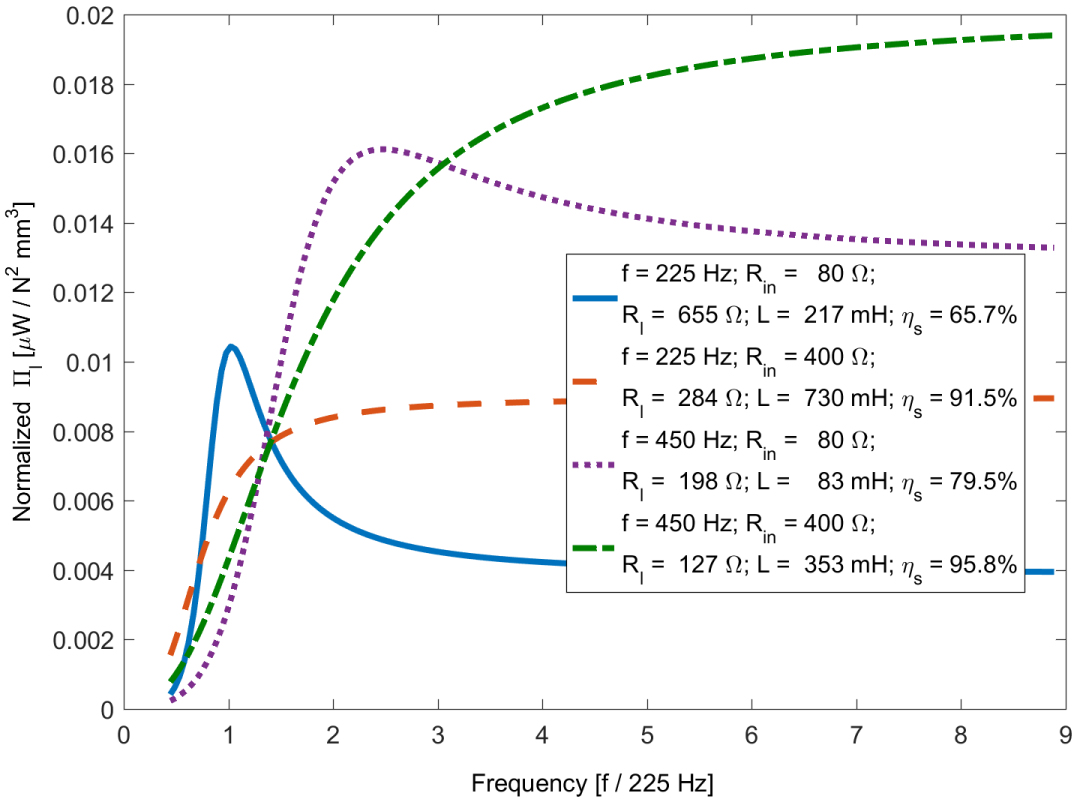

Figure 2.4: Power normalized by squared force and stack volume to demonstrate broadband response for higher shunt efficiencies in combination with calculated $R_{l,opt}$ and L_{opt} values using predefined frequency (f) and internal resistance (R_{in}); d_{33}^{eff} = 182.9 nC/N, C_p = 3.08 µF, x-axis frequency normalized by 225 Hz excitation. Simulation originally presented by author in [58].

2.3 Testing procedures

Multiple HPEH prototypes were developed to provide proof-of-concept, demonstrate feasibility, and compare the electromechanical model of converting hydraulic pressure ripple into electricity through the use of piezoelectric stacks and single crystals. The different prototypes are introduced in Section 2.4. A hydraulic pump system was used to test the HPEH prototypes. Testing involved: (1) a dynamic test using a shaker and (2) a dynamic test on a hydraulic rig. First, the piezoelectric stack is tested using a shaker with a known excitation force in order to determine the effective piezoelectric strain constant,

d_{33}^{eff}. Second, the HPEH prototype is attached to a hydraulic system to assess the performance of the device and compare the results to the electromechanical model presented in Section 2.2.

2.3.1 Phase 1: Determine effective piezoelectric strain constant of piezoelectric stack

In order to determine an effective piezoelectric strain constant of a stack, a manipulation of the resistive load only power equation is used, which can be determined using Eq. (2.10) as

$$d_{33}^{eff} = \frac{\sqrt{\Pi_{avg,l}\left(1+\left(\omega R_l C_p\right)^2 R_l^{-1}\right)}}{\left|F_{rms}\omega\right|} \quad . \tag{2.20}$$

The force, F_{rms}, is measured using an impedance head, the average power can be calculated from the measured voltage across the resistive load, and the stack capacitance can be measured using a capacitance meter. A frequency sweep and resistive sweep is performed and the effective piezoelectric strain constant can be determined from the average of the test results. A picture of the experimental test setup is shown in Figure 2.5.

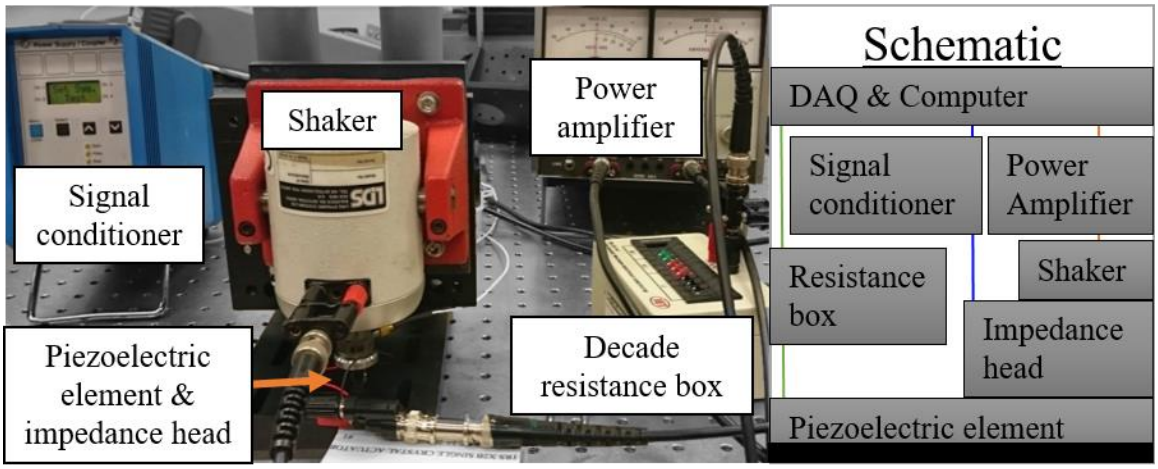

Figure 2.5: Shaker test setup for determining stack piezoelectric strain constant, d_{33}^{eff}.

Multiple piezoelectric stacks were tested within HPEH prototypes to compare model applicability and design iterations, with most being composed of a soft PZT material for its relatively high piezoelectric strain properties. Descriptions of the piezoelectric stacks used in HPEH prototypes (except for the single crystal presented in Chapter 4) and calculated effective piezoelectric strain constants are in Table 1. The resultant effective piezoelectric strain constant (d_{33}^{eff}) is calculated from the average d_{33}^{eff} value for each sweep; the average value and standard deviation for piezoelectric stacks tested is shown in Table 1. The number of layers is either calculated using a provided piezoelectric constant value for one layer and Eq. (2.5), provided by the manufacturer, or directly counted.

Table 1: Piezoelectric stacks and single crystals used in HPEH prototypes (*indicates number of layers provided; † indicates single layer material data provided; ‡ indicates layers counted).

Stack Manufacturer (Part No.) <HPEH>	**Electrode area, mm²**	**Height mm**	**Capacitance µF**	d_{33}^{eff} **nC/N**	d_{33}^{i} **pC/N**	**N layers**
EPCOS (LN 03 / 8516; Nd-doped PZT) <1>	46.24	30	2.7	182.93 +/- 0.56	750 †	243
EPCOS (LN 03 / 8516; Nd-doped PZT)	46.24	30	2.9	150.59 +/- 0.87	750 †	200
Piezo Systems (TS18-H5-104, [67]) <3>	25	18	1.9	105.090 +/- 0.002	1480	71 ‡
PI (PAH-009 .13.255; PIC 255, [68]) <2>	126.9	6.75	.23	10.98 +/- 0.09	400 †	27
PI (PAH-009 .13.255; PIC 255, [68])	126.9	6.75	.23	9.66 +/- 0.05	400 †	24
Piezomechanik (PCh 50/5x5/2, [69]) <4>	25	2	1.3	9.386 +/- 0.005	unknown	unknown
Single Crystal stack (TRS X2B, PMN-PT) <6>	25	11.75	.038	37.208 +/- 0.133	1860	20 *
Parker (C03618-001; NEC TOKIN N10, [70]) <5> **A5**	25	20	1.89	141.92 +/- 0.04	635 †	223
Parker (C03618-001; NEC TOKIN N10, [70]) <5> **A6**	25	20	1.88	143.68 +/- 0.03	635 †	226
Parker A5A6 series	50	20	0.994	70.67 +/- 0.03	-	-
Parker A5A6 parallel	50	20	3.74	147.92 +/- 0.04	-	-
Parker (C03618-001; NEC TOKIN N10, [70]) <5> **A7**	25	20	1.85	148.45 +/- 0.03	635 †	233
Parker (C03618-001; NEC TOKIN N10, [70]) <5> **A8**	25	20	1.98	144.09 +/- 0.06	635 †	226
Parker (C03618-001; NEC TOKIN N10, [70]) <5> **A9**	25	20	1.89	141.87 +/- 0.07	635 †	223

To compare the test results from the shaker test to the accuracy of the model using a calculated piezoelectric strain constant, the frequency response function (FRF) between the piezoelectric stack and force input can be compared. Derived from Eq. (2.8), the FRF for a resistive load circuit is modeled as

$$\alpha(\omega) = j\omega d_{33}^{eff}\left(j\omega C_p + \frac{1}{R_l}\right)^{-1}. \tag{2.21}$$

As an example, the test results compared to the absolute value of the modeled FRF for one piezoelectric stack (Parker [C03618-001] A7) is provided in Figure 2.6. The model and test results match well; in addition, they correspond to results found by Zhao et al. [41].

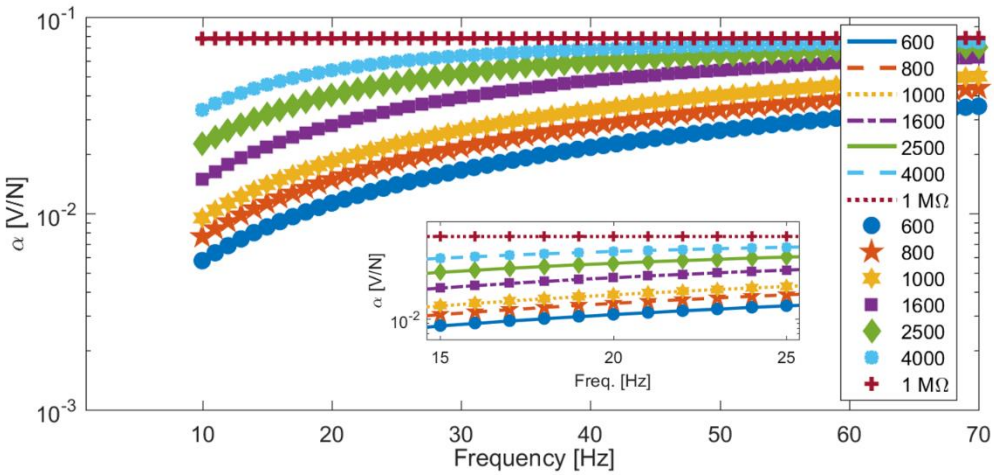

Figure 2.6: Absolute value of frequency response function comparing piezoelectric shaker test results (for Parker A7) and model using the calculated effective piezoelectric strain constant (value averaged from 14 tests); lines indicate model; points indicate test measurements.

2.3.2 Phase 2: Testing HPEH device on hydraulic rig

Once the material properties of the piezoelectric stack used within a HPEH device have been determined, the next steps are to test the design integrity of the device, determine the capacitance of the device under load, and test the piezoelectric device on a hydraulic rig. The HPEH prototype is placed under a static load using a deadweight tester to assess the pressure integrity of the device and measure the effective piezoelectric stack capacitance under load. The HPEH device is installed on a mounting block, which is incorporated in-line with a deadweight tester. This step allowed the pressure integrity of the device to be tested and allowed any change in the capacitance due to the static load to be measured. This includes ensuring that no leaking of hydraulic fluid occurs around the threads into the block or past the fluid-mechanical interface into the internals of the device. After installing the HPEH device and mounting block to the deadweight tester, weights

were added in increments that yielded static pressure changes of approximately 0.25-2.5 MPa, until the desired pressure limit was reached.

The system pressure in hydraulic systems can reach 35 MPa, or 5000 psi, and in HPEH devices, the interface between the stack and fluid amplifies this system pressure further, with the highest amplification area ratio being 14 times greater for one HPEH prototype. At high compressive stress levels, such as -35 MPa, the permittivity of piezoelectric material can change compared to the permittivity at no stress [71]. In addition, if the compressive stress level of the piezoelectric material is great enough, such as $-35\ \text{MPa} \times 14 = -490\ \text{MPa}$, the remnant polarization is decreased by mechanical depolarization with a corresponding drop in the piezoelectric strain constant [72, 73]. While soft PZT exhibits higher piezoelectric strain constants than hard PZT, one drawback is it has a smaller linear range for stress loading. According to Schäufele and Härdtl, the transition to nonlinear depolarization behavior in soft PZT can occur from compressive stress levels as low as -20 MPa, whereas hard PZT does not experience this transition until -60 MPa [72]; however, this has a strong temperature dependence and will be affected by the cyclic negative field. This issue will be further discussed in Section 2.4.3 and in Chapter 4, however for most devices, the piezoelectric stress was kept below -20 MPa unless specifically interested in this transition phase.

The capacitance of the piezoelectric stack was measured using a multimeter during the deadweight testing to provide data to permit the estimation of the optimal resistance value and for better agreement with the model for the system pressure values tested during dynamic testing. This helped further account for any potential change in material

permittivity due to the stress loading, allowing for the identification of the statically-loaded capacitance and a simpler troubleshooting process, as fewer parameters were involved.

The HPEH and block are then installed in a hydraulic pump system, as can be seen in Figure 2.7. Key components of the hydraulic pump system are a nine-piston pump operating at 1500 rpm, yielding a fundamental pressure ripple frequency of 225 Hz, and a needle valve for controlling the static pressure. To ensure the measurement of the dynamic pressure is co-located to the HPEH, the mounting block includes a connection for a dynamic pressure sensor (PCB model 101A06) directly opposite of the HPEH installation location. The static pressure in the system was measured using Hydac pressure sensor 908404 and 908428 (Model code: EDS 3478-5-6000-400 and EDS 3478-5-3000-400).

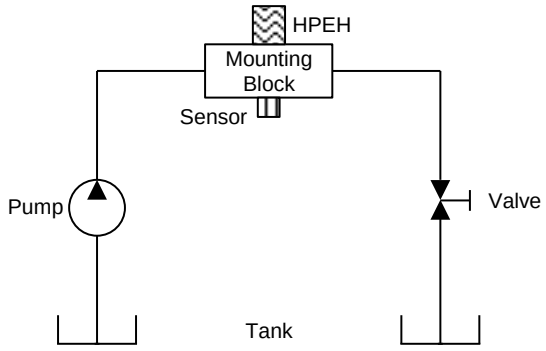

Figure 2.7. A schematic of the hydraulic pump system used for testing the HPEH in the inline mounting block.

The final phase of testing was to perform a sweep of resistance or inductance values to determine the peak power output of the system, with a schematic of the test set-up shown in Figure 2.8. A shunt impedance (either R only or R-L load) is connected in parallel to the HPEH leads. The impedance sweep values depend on the predicted optimal resistance or inductance for the stack being tested within the HPEH device. The voltage across the load resistance and the output signal from the dynamic pressure sensor are acquired via a data

acquisition system (either SigLab or an NI system). The impedance sweep was then performed for static pressure levels of interest. Time- and frequency-domain data were recorded for each test. The model can then be compared to the measured test values, as is presented in the next section.

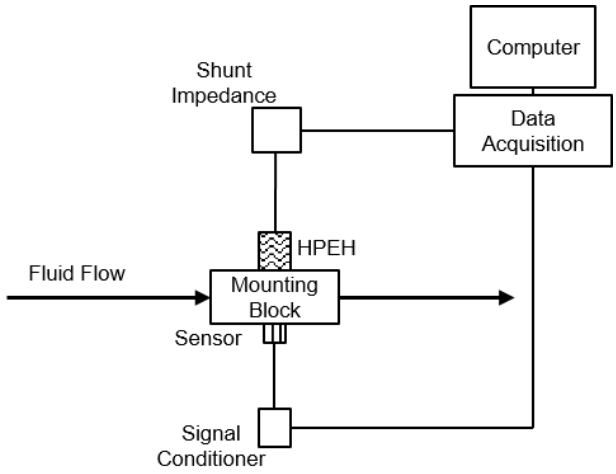

Figure 2.8. Testing configuration for dynamic testing on hydraulic system, including the pressure sensor, shunt impedance, and data acquisition system.

2.4 Model and test results for various HPEH designs

Many HPEH devices were developed to explore different design concepts and various piezoelectric materials. The performance comparison of the HPEH devices is shown in Figure 2.9, where the points represent the measured data and the lines represent modeled data using the electromechanical model presented in Section 2.2. A summary of the HPEH prototypes developed is shown in Table 2, and a picture of all the prototypes and piezoelectric stacks tested is shown in Figure 2.10. The labeling of HPEH devices is HPEHX-Y, where X represents which type of piezoelectric stack is used (see Table 1) and Y indicates design iteration.

The important design implementations are discussed in the following subsections of this chapter, and further research developments of acoustic energy transduction in hydraulic systems is discussed in Chapter 4 and Chapter 3. The following subsections discuss various methods to improve HPEH performance: RL shunt loading; area amplification; and force shunting.

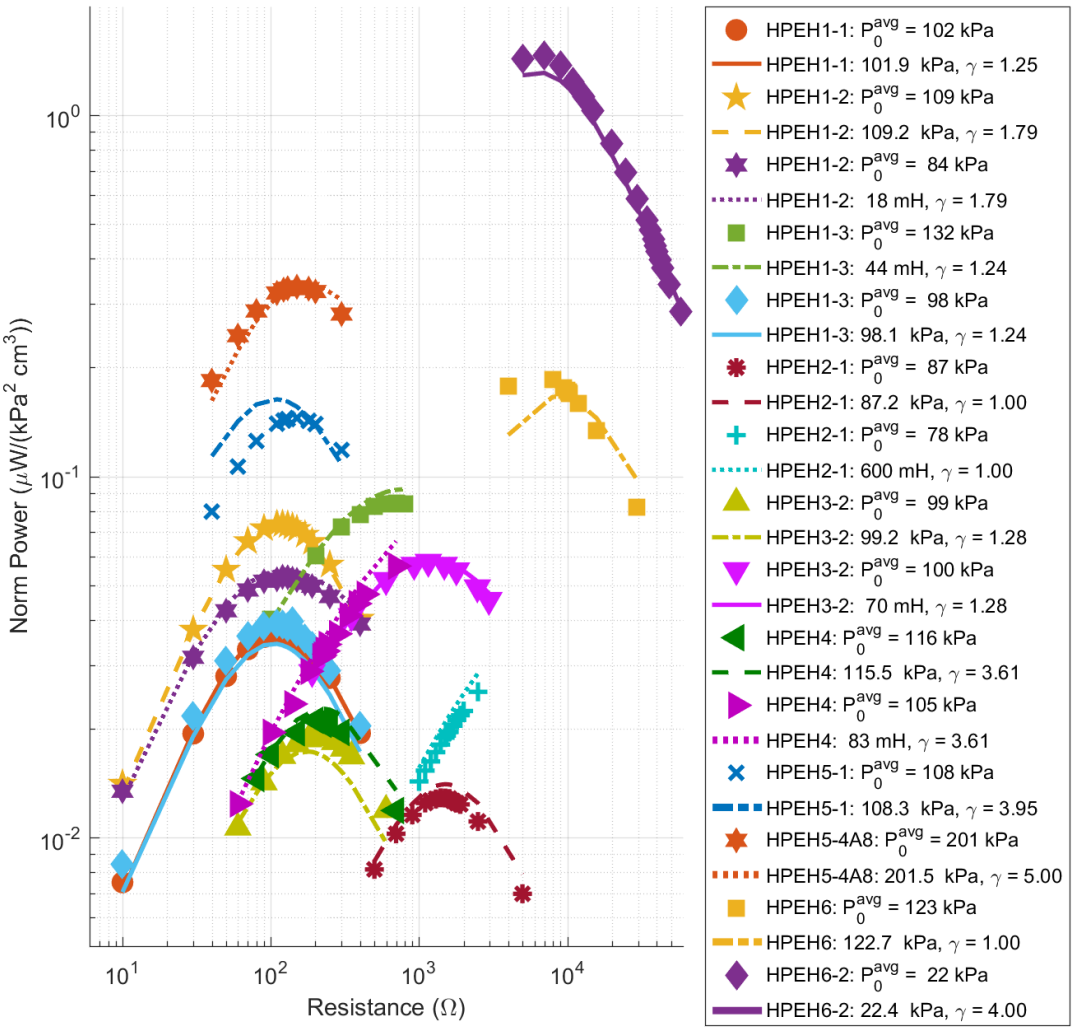

Figure 2.9: Power normalized by squared pressure and stack volume for multiple HPEH devices for resistive load sweeps, including both R circuit and R-L circuit.

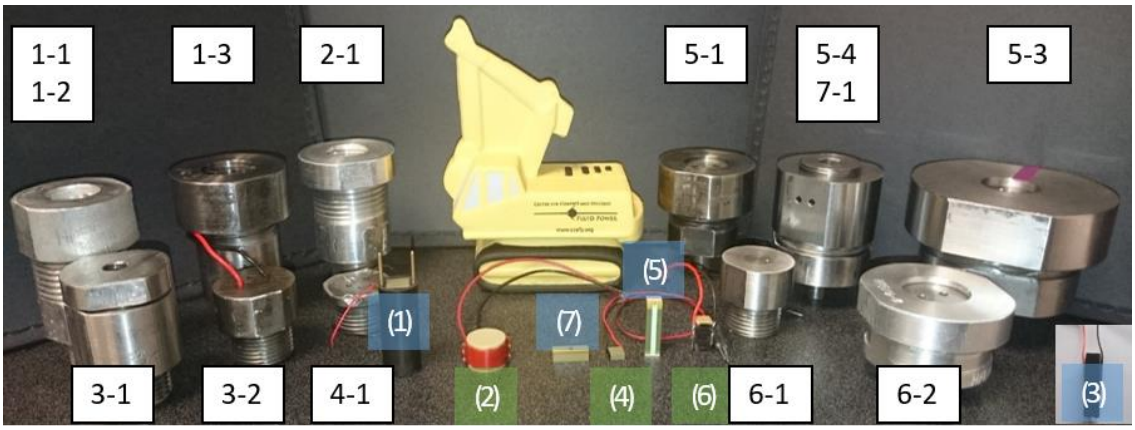

Figure 2.10: HPEH devices and corresponding piezoelectric stacks and single crystals, where X in HPEHX-Y corresponds to the piezoelectric element. Piezoelectric stacks & single crystals manufacturers corresponding to (X) (see Table 1, left to right): (1) EPCOS, (2) PI Ceramics, (7) single crystal by TRS (PIN-PMN-PT), (4) Piezomechanik, (5) Parker/ Nec Tokin, (6) TRS single crystal stack (custom made), (3) Piezo Systems.

Table 2: Summary of HPEH device performance

Device	**Power*** **µW**	**P_0** **kPa, rms**	**Vrms**	**Stack Vol.** **mm^3**	**Norm Power** **$\mu W/(Pa^2\ m^3)$**
HPEH1-1	522	101	0.24	1387	0.037
HPEH1-2^{RL}	2187	85.6	0.93	1387	0.215
HPEH1-3^{RL}	3324	205	1.29	1387	0.057
HPEH2-1^{RL}	130	77.5	0.57	856	0.025
HPEH3-2 ^{RL}	259	99.9	0.55	450	0.058
HPEH4-1^{RL}	158	397	0.33	50	0.020
HPEH5-1^{RL}	1639	115	0.57	500	0.248
HPEH5-3^{RL}	1743	350	0.48	500	0.028
HPEH5-4‡	6828	201	1.01	500	0.179
HPEH6-1**^{RL}	1349	98.9	4.14	294	0.469
HPEH6-2**	124	25.9	2.4	294	0.629
HPEH7-1†‡	13070	141.3	80.6	192	3.409
HPEH-HR‡	12820	202.3	1.13	500	0.626

* Maximum power measured from tests of a given device
** PMN-PT layered single crystal stack (20 layers)
‡ Force Shunt design
† PIN(0.24)-PMN-PT, [011] cut single crystal, results compared in Figure 4.23 and discussed in Chapter 4
^{RL} Indicates resistive-inductive parallel circuit; otherwise, resistive load only
HR Helmholtz resonator – results shown and discussed in Chapter 3

2.4.1 Resistive load vs. Resistive-inductive load

To compare the power response when normalized by the squared pressure amplitude for a given shunt impedance, a HPEH prototype was tested with the different loading conditions, with results shown in Figure 2.11. While the optimal inductive and resistive loads for the resonant shunt are not the same as for the ideal resonant circuit, the ideal resonant circuit optimal inductive load can be used as an estimate for testing. When solving for the maximum power using the shunt impedance from Eq. (2.12), the resulting inductive loading is found to be $L_{ideal}^{opt} = 1/\left(\omega^2 C_p\right)$. The HPEH tested has a capacitance of about 3 μF, which varied with static pressure by less than 5 percent; the model uses the capacitance value measured during a static pressure deadweight test at corresponding static pressures, taken prior to the dynamic test. The harmonic with the highest energy content of the 9 piston pump operating at 1500 RPM for the static pressures shown was the second harmonic, 450 Hz. This corresponds to an estimated optimal resistive load of 117 Ω for the resistive load (R circuit) shunt model and an estimated ideal optimal inductive load of 41 mH for the resistive-inductive load (R-L circuit) shunt.

Figure 2.11a shows the power normalized by the squared dynamic pressure for HPEH1-2, which is a device that uses a piezoelectric stack made by EPCOS with an effective piezoelectric strain constant of 182.9 nC/N. The piezoelectric strain constant was measured in a separate test, as explained previously. Two static pressures and three circuit configurations are shown: (1) R-L circuit using the optimal inductive load for 450 Hz of 41 mH, with a corresponding internal resistance of 13 Ω, at static pressures of 2.1 MPa and 3.4 MPa; (2) R-L circuit using an inductive load that matches to 675 Hz of 18 mH, with a corresponding internal resistance of 8.9 Ω, at a static pressure of 3.4 MPa; and (3) R circuit

at a static pressure of 3.4 MPa. The error bars on the R-L circuit tests correspond to the standard deviation between two tests, where the entire device was reassembled between tests; the error bars on the R circuit test also correspond to standard deviation, but between three tests.

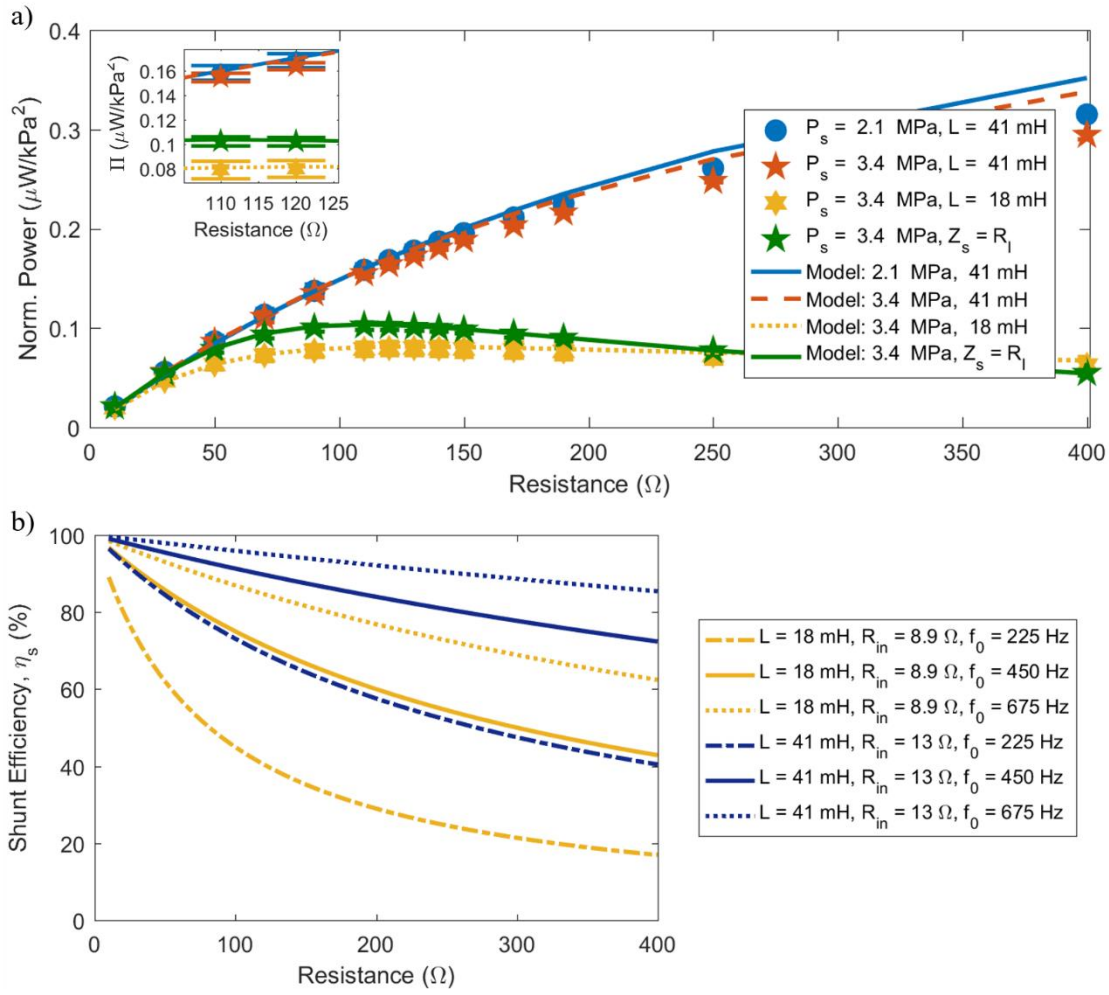

Figure 2.11: a) Comparison of power normalized by pressure for two types of shunt impedances (using HPEH1-2 device, with model using an area ratio of 1.79 and effective d_{33} = 183 nC/N), and b) corresponding shunt efficiency for R-L circuits tested. Error bars indicate standard deviation of two separate test runs for R-L circuit, standard deviation for three separate test runs for R circuit. Error bars are generally too small to see, so callout figure is included.

As can be seen Figure 2.11a, the resistive-inductive shunt has a higher power response when operating with an impedance matched to the dominant frequency compared

to the resistive shunt. However, if the shunt is matched to a frequency higher than the dominant frequency, the power response is worse. This is further demonstrated by Figure 2.11b, which shows the shunt efficiency for the R-L circuits tested for the pump operating frequency, 225 Hz, and the 2nd and 3rd harmonic. Note that dominant frequency for the tests shown was 450 Hz, or the 2nd harmonic of the pump operating frequency, which corresponds to the R-L circuit (1) of 41 mH, with a corresponding internal resistance of 13 Ω.

Recall from Figure 2.4 that the higher normalized power response is expected to come from the circuit that is matched to the higher frequency component, which in this case corresponds to R-L circuit (2) 18 mH. Also recall that the higher shunt efficiency corresponds to more broadband response after this matched frequency component, which in this case corresponds to R-L circuit (1) 41 mH. The highest power response recorded occurred at 400 Ω for R-L circuit (1), which has a shunt efficiency η_s of only 72.3% for 450 Hz. This is a lower shunt efficiency than the shunt efficiency at 110 Ω for both R-L circuit (1) of 90.5% at 450 Hz and R-L circuit (2) of 85.8% for 675 Hz, and 73.2% for 450 Hz. However, because most of the energy is at 450 Hz, the circuit efficiency for R-L circuit (2) is matched improperly to benefit from higher power response, since the broadband effects occur after the dominant frequency, as discussed previously and shown in Figure 2.4. Also, while R-L circuit (1) at 110 Ω does have a higher shunt efficiency and more broadband response, the resonant peak that occurs at the dominant frequency when using the higher resistive load of 400 Ω is more beneficial to the overall power response. The balancing of an R-L circuit for both broadband response and overall power response for a given hydraulic system is an important aspect of HPEH circuit choice.

Accompanying the R-L circuit results in Figure 2.11, the estimated optimal resistive load for the resistance only circuit is near the maximum power produced. The model matches well for all test conditions, however small deviation between the model and test results occur at high resistive loads in the matched R-L circuit model; this may be due to the piezoelectric stack capacitance measured during the deadweight test being different from the capacitance during the dynamic tests. In addition, the normalized power results for both static pressure conditions for the R-L circuit using matched inductance have nearly identical responses, indicating that the power results for this loading condition is not affected by the static pressure.

To further demonstrate the concept of shunt efficiency, an inductive sweep for the R-L circuit was tested where the resistive load was 115 Ω, which is near the estimated optimal resistive load of 117 Ω for the resistive load (R circuit) shunt model. This test was performed twice, with the average power normalized by dynamic pressure amplitude is shown in Figure 2.12a, including the standard deviation between the tests shown by the error bars. The shunt efficiency calculated for 450 Hz is shown in Figure 2.12b using the measured internal resistive loads, which is why small spikes occur. Once again, for the system tested, the dominant frequency was at 450 Hz.

The optimal inductive load for an ideal R-L circuit for 450 Hz and a piezoelectric capacitance of 3 μF is 41.7 mH. Inductive loads above this level correspond to tuning the circuit to lower frequency levels, whereas inductive loads below correspond to higher frequency levels. The ideal optimal inductive load is inversely proportional to the capacitance of the piezoelectric stack, so small changes to this value would not drastically change the ideal optimal load. As seen in Figure 2.12a, near the optimal inductive load, the

maximum normalized power occurs, however the decrease in power is not as significant at the higher optimal inductive loads compared to the lower loads. This is because the higher inductive load tests have higher shunt efficiency than the lower values (recall Eq. (2.19) and Figure 2.4). Figure 2.12b demonstrates that the shunt efficiency corresponding to 450 Hz increases, meaning the system response becomes more broadband (especially with respect to frequencies above 450 Hz), as the inductive load increases. Yet the combined effects of Figure 2.12a and b show that higher shunt efficiency does not correspond to higher power response when normalized by the pressure amplitude. The important feature for HPEH circuits is which frequency band contains the most energy.

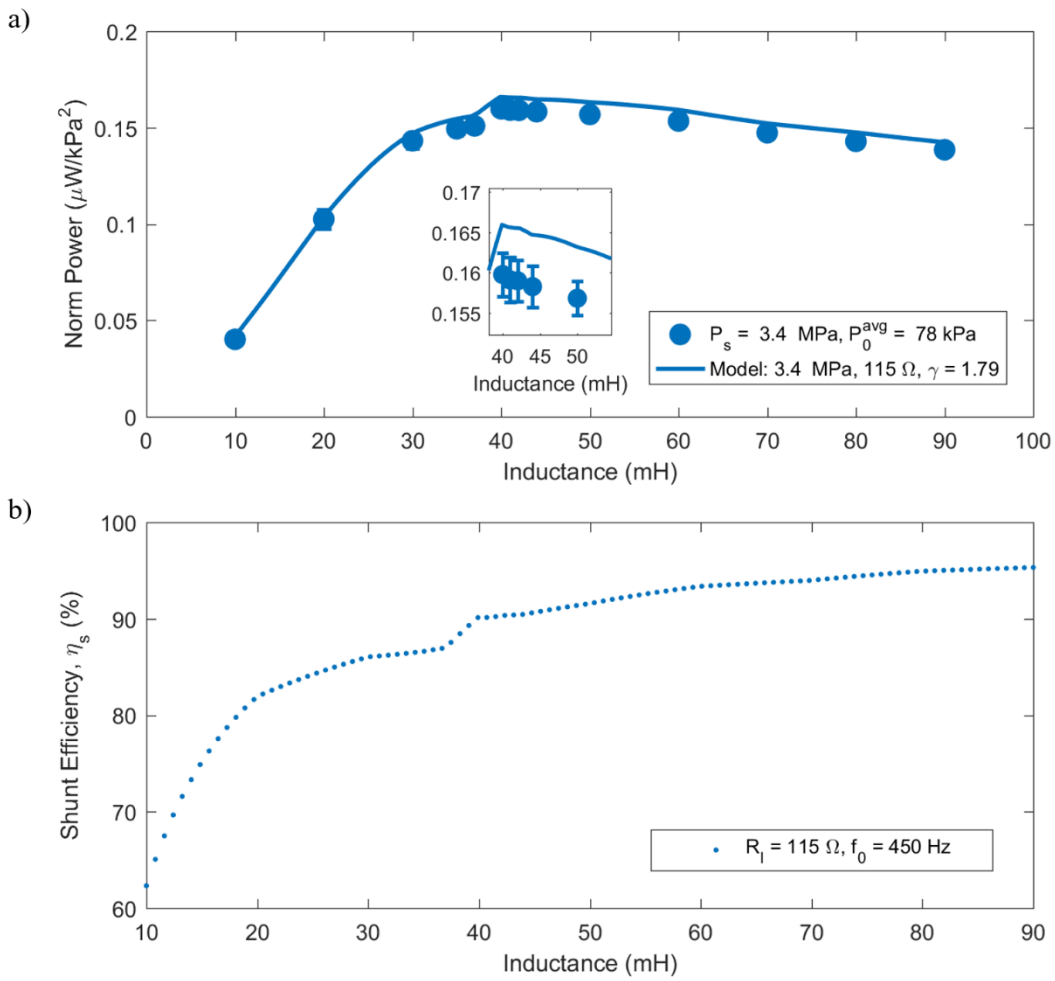

Figure 2.12: a) Power normalized by pressure for R-L shunt impedance, with inductive values being swept (using HPEH1-2 device, with model using an area ratio of 1.79 and effective d_{33} = 183 nC/N), and b) corresponding shunt efficiency calculated using 450 Hz. Error bars indicate standard deviation of two separate test runs for the R-L circuit. Error bars are generally too small to see, so callout figure is included.

2.4.2 Area Amplification

An important aspect in the HPEH design is the fluid-mechanical coupling of the piezoelectric surface area and the pressure fluctuation. The interface needs to be flexible to allow for maximum surface deflection (while still protecting the piezoelectric), but stiff enough to prevent failure of the part. Within the HPEH devices is a diaphragm interface to prevent oil (or other liquid) from leaking out of the hydraulic system. Leaks can be hazardous to a hydraulic system and to users. The HPEH interface that isolated the stack from the fluid was composed of either a 0.0762 mm (.003") thick aluminum diaphragm or

a 0.025 mm (.001”) thick steel diaphragm, which allowed the diaphragm stiffness to be much less than the stack stiffness while still preventing leaks.

In addition to providing protection from leaks, the interface can increase the effective area of a HPEH device for increased power output. The diaphragm area is larger than the area of the stack, and hence it is expected that the effective area is slightly larger than the area of the stack, as schematically shown in Figure 2.13a. Note that the effective area and the dynamic pressure will combine to form force components in the 1- and 3-direction of the piezoelectric stack, where only the 3-direction forces are considered as contributing to the overall power output. The overall effective force can be increased by using a spacer, or small metal disc, between the diaphragm and piezoelectric stack, as shown in Figure 2.13b. Additionally, the spacer reduces the amount of force transferred into the HPEH outer housing via the diaphragm and diaphragm seal, thus primarily loading the spacer and piezoelectric material.

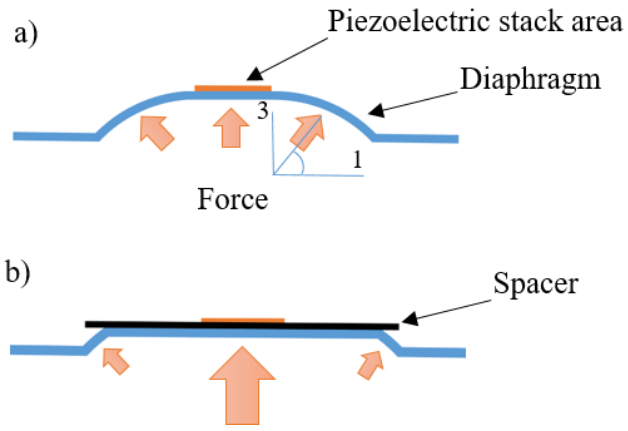

Figure 2.13: Schematic of effective area ratio for (a) diaphragm interface only and (b) diaphragm with spacer interface.

To analyze the area ratio effect, two versions of a prototype were tested with different internal configurations, denoted as HPEH1-1 and HPEH1-2. A spacer was applied to HPEH1-2 with a designed area ratio of 2.4, allowing more force to be transmitted from the dynamic pressure to the stack. Otherwise, the two devices were identical.

In order to estimate the effective area ratio, γ, the modelled average power with $\gamma = 1$ is compared to the test results, such that

$$\gamma = \sqrt{\Pi_{measured}} \Big/ \sqrt{\Pi_{\gamma=1}} \ , \tag{2.22}$$

then the resultant value is used as a constant within the power model. Note that if any changes of the piezoelectric material properties occur due to the static pressure, such as change in the effective piezoelectric strain constant [71, 74-76], this would also be lumped into the area ratio calculation. However, the same area ratio is used for all static pressure levels tested, therefore this change is assumed to be constant with respect to frequency and impedance loading. This assumption and calculation is made for every HPEH device modelled unless noted otherwise.

The comparison of HPEH1-1, where only a diaphragm is used, to HPEH1-2, where both a spacer and diaphragm is used, can be seen in Figure 2.14. It compares the power normalized by the squared pressure amplitude of the measured dynamic pressure. The effective area of HPEH1-1 used in the model is 1.25, and the effective area of HPEH1-2 used in the model is 1.79; note that small deviation between 2.1 MPa and 3.4 MPa modelled results is due to the capacitance values for the two static pressure levels changing from 3.08 µF to 3.11 µF. Only one test was performed using HPEH1-1. The errorbars shown on the HPEH1-2 data points represent the standard deviation of three separate measurements performed, where the mean result of the normalized power is indicated by the points. As

can be clearly seen, increasing the effective area of the interface in a HPEH increases the power performance of the device.

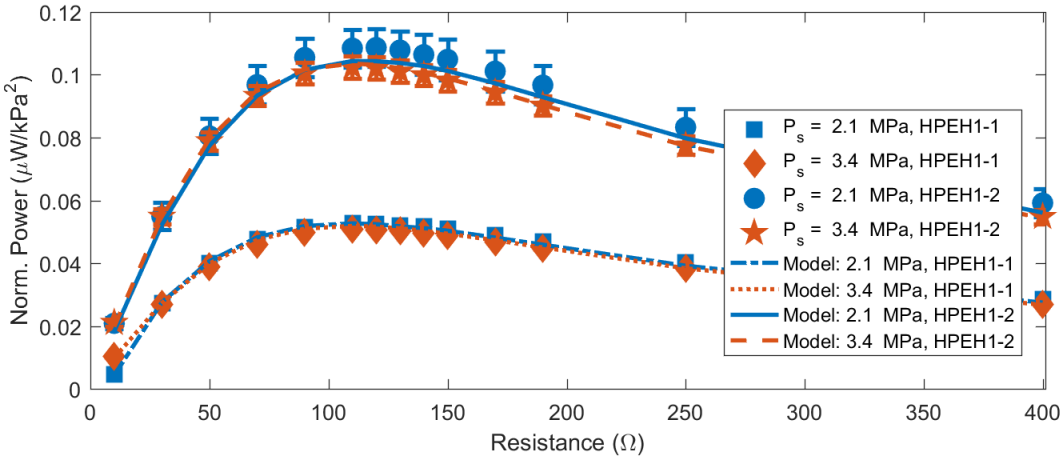

Figure 2.14: Comparison of HPEH devices with only a diaphragm (HPEH1-1, area ratio of 1.25) and with a diaphragm and spacer to amplify force input (HPEH1-2, area ratio of 1.79). Error bars on HPEH1-2 results represent standard deviation between three separate tests. Both devices use the same piezoelectric stack made by EPCOS, with d_{33}^{eff} = 183 nC/N.

2.4.3 Force Shunt

As indicated previously, one challenge of converting the acoustic energy from hydraulic systems is balancing high conversion efficiency with a high stress environment. The area amplification method presented in Section 2.4.2 provides much higher conversion efficiency by amplifying the dynamic force, however it also amplifies the static force applied to the piezoelectric element. As presented in Eq. (2.10), the power is proportional to the squared dynamic pressure, not the static pressure, and therefore the objective of area amplification is to increase the dynamic force. Recalling from the discussion of deadweight testing in Section 2.3.2, at high stress levels, the piezoelectric stack can enter a nonlinear loading behavior, and potentially partially (or fully) depolarize the piezoelectric stack (depending if the domain switching process is reversible), thus reducing the transduction efficiency [72]. In order to ensure HPEH devices can be used on hydraulic systems that

reach system pressures higher than 20 MPa, a method to relieve the static force, called force shunting, was developed.

Multiple parameters within hydraulics systems may affect the performance of piezoelectric devices: stress level, stress loading order, and oil temperature. It is therefore important to ensure that HPEH devices are robust to static pressure changes that occur during a hydraulic system work load, and robust to temperature changes in oil. The reduction in normalized power has been observed in HPEH experiments, as shown in Figure 2.15. It is assumed that the cause for this reduction is primarily due to increased compressive stress derived from the high system static pressure, however piezoelectric performance changes due to increased dynamic pressure, changes in oil temperature, or order of system loading may also be contributing factors. Therefore, prior to introducing the force shunt concept, test results are discussed that isolate the static pressure as the primary source of decreased normalized power.

Figure 2.15 shows power normalized squared pressure test results for HPEH4-1 device, which has an area amplification of 3.47. The compressive stress within the piezoelectric element is expected to have reached around -60 MPa, or -8.7 kpsi, which may have resulted in residual strain and depolarization, however not complete depolarization. If no material change had occurred, it would be expected that the normalized power results would all be equivalent, as seen with the 3.4 and 5.0 MPa test results.

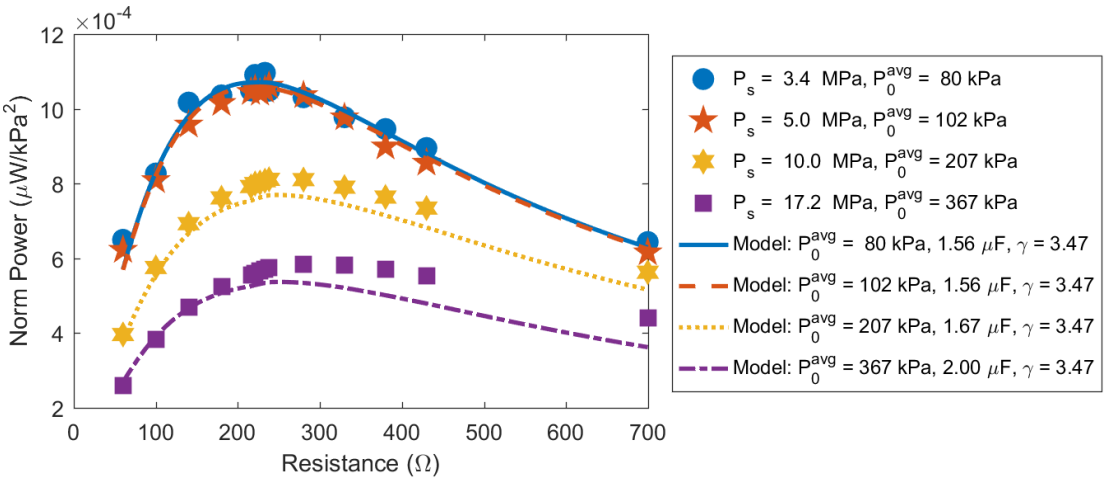

Figure 2.15: Power normalized by pressure for various dynamic and static pressure amplitudes for HPEH4-1; increasing capacitance causes normalized power to decrease.

To ensure that the power reduction is due to increasing static pressure rather than other system parameters (e.g. loading order, dynamic pressure, or oil temperature), multiple resistive sweep tests at different loading conditions were performed on HPEH1-3. In order to change the dynamic pressure levels, the charge pressure, and thus impedance, of a downstream bladder-style suppressor (typically used for noise control) was changed while keeping the static pressure the same. The HPEH1-3 device was tested two different times, with a summary of these tests shown in Figure 2.16. The first set of tests cycled from 6.9 MPa to 3.45 MPa and back to 6.9 MPa twice, with the dynamic pressure amplitudes ranging from 97.4 kPa to 105.7 kPa at the low static pressure level and from 137 kPa to 158 kPa at the high static pressure level. The second set of tests also performed a static pressure and dynamic pressure cycling, however also recorded oil temperature. This set started at a static pressure level of 3.2 MPa and raised to 6.2 MPa, and then returned to 3.2 MPa. The dynamic pressure at 3.2 MPa ranged from 72 kPa to 106 kPa; for the 6.2 MPa test, it ranged from 147 kPa to 171 kPa. The temperature of the oil raised from 22.2°C to

45.4ºC. While the normalized power did decrease at the higher static pressure levels, the standard deviation of the 18 tests performed was less than 10 percent of the average normalized power for all resistive loads except the lowest value, which had a standard deviation of 10.3 percent.

The results of the tests described are shown in Figure 2.16, however some have been omitted for clarity. Figure 2.16a shows the average results of the tests performed around 3.4 MPa, 6.2 MPa, 6.9 MPa, and all tests, including error bars to indicate the standard deviation of the results. Figure 2.16b shows multiple tests performed around 3.4 MPa to indicate the range of static pressure levels; this is also shown for the 6 to 6.9 MPa tests in Figure 2.16c. The modeled lines are for either the corresponding test or the averaged model results.

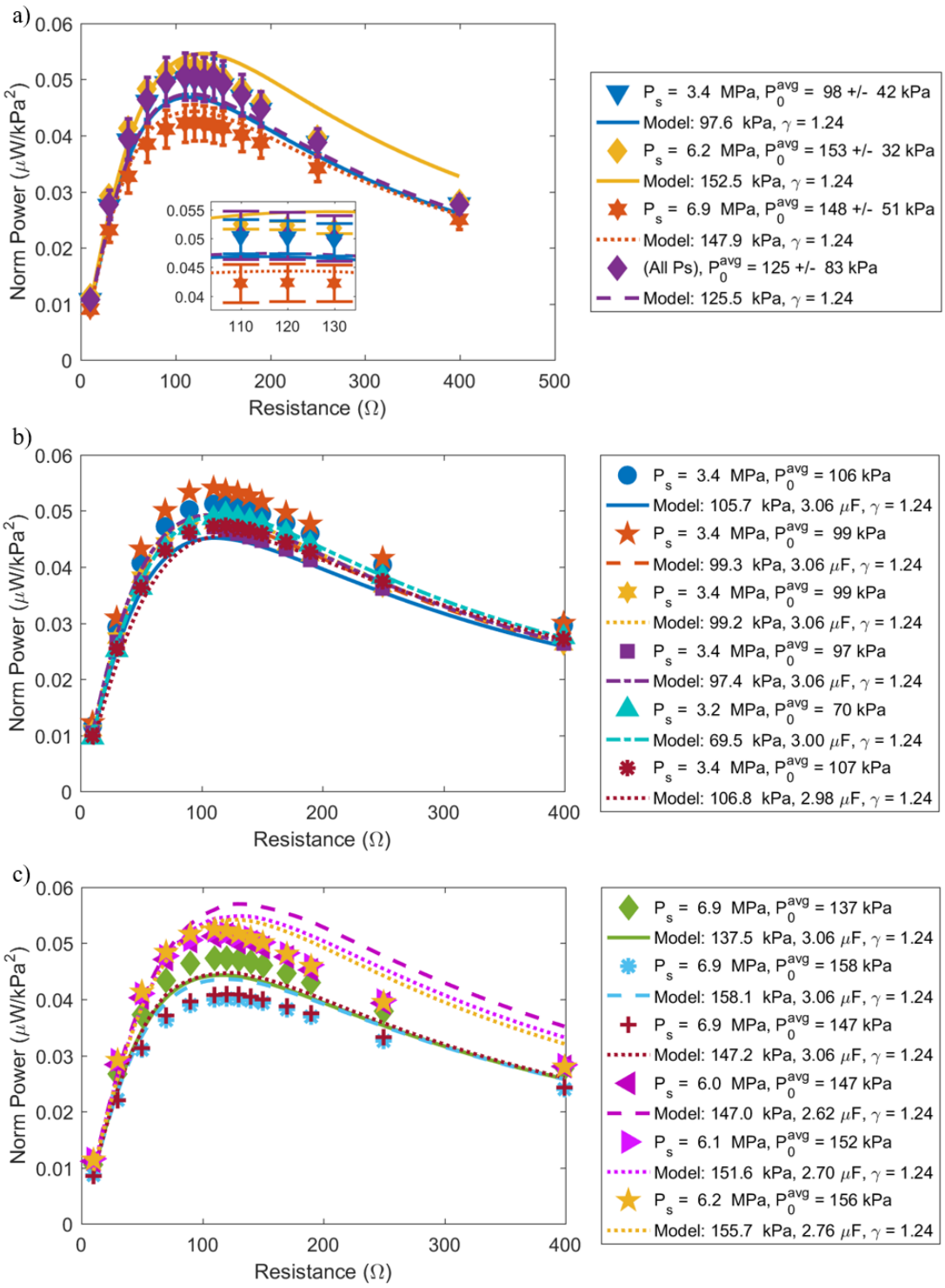

Figure 2.16: Comparing power normalized by squared dynamic pressure for multiple static pressure levels, various loading cycles, and hydraulic oil temperatures, where a) shows a summary of all tests, b) is tests performed at about 3.4 MPa, and c) are tests performed at about 6.2 MPa and 6.9 MPa. Tests were performed using HPEH1-3. Error bars are generally too small to see in a), so callout figure is included.

Now that it is established that HPEH devices have consistent power responses below a certain piezoelectric stress level, the force shunt topic can be resumed. The key to the force shunt design is relative stiffness: a spring mechanically in parallel with the piezoelectric stack can relieve the static pressure by being preloaded, thus preventing spacer motion, but must be soft relative to the piezoelectric stack to allow for minimal reduction of the dynamic force once the static pressure applied to the spacer area overcomes the preload force. Figure 2.17 shows this concept schematically, including the bottom edge of a HPEH outer housing (where the diaphragm sealing surface is located), a HPEH spacer, a soft spring with stiffness k_{bv} , the piezoelectric stack represented as a spring with stiffness k_{pz} , and the preload force on the soft spring F_{bvpre}. In addition, it shows the level of the hydraulic system static pressure P_{static} , the dynamic pressure P_{dyn} oscillating about the static pressure, and an operating pressure level P_{op} that is used in the analysis of this concept.

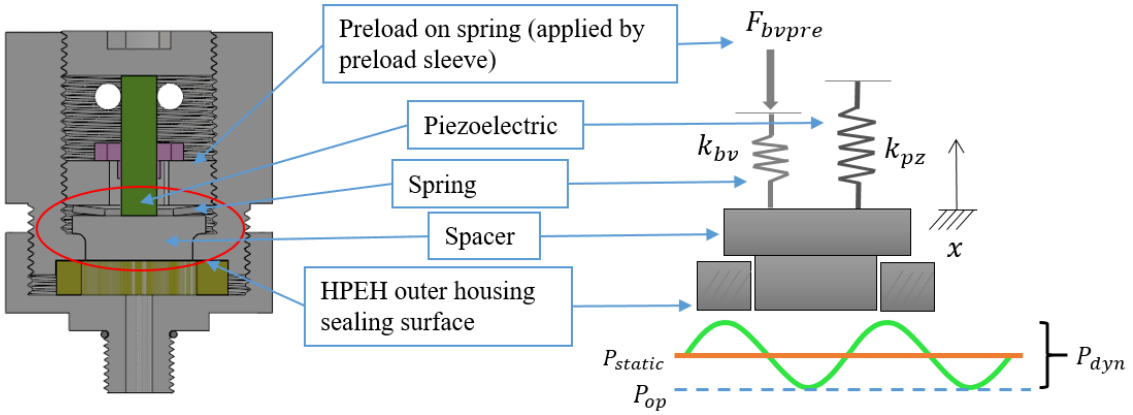

Figure 2.17: Internal design of HPEH5-4, which includes a force shunt, and schematic view of force shunt concept.

The equation of motion for this system can be represented using a modified Heaviside function, where the function is defined as

$$H(x)=\begin{cases}1 \text{ for } x>0\\0 \text{ for } x\le 0\end{cases} \tag{2.23}$$

for this analysis. It is never expected that the displacement of the spacer will be less than zero. The equation of motion is

$$\left[m_{spacer}\ddot{x}+\left(k_{bv}+k_{pz}\right)x\right]H(x)=\left(P_0+P_s\right)A^{eff}-F_{bvpre}+R_x\left[1-H(x)\right] \tag{2.24}$$

where R_x is the reaction force for when the spacer is stationary. In order to maximize the work applied to the piezoelectric stack, it is important to maximize the force shunt ratio, or ratio of potential energies, defined as

$$\kappa=\frac{U_{piezoelectric}}{U_{total}}=\frac{k_{pz}}{k_{bv}+k_{pz}}\ . \tag{2.25}$$

The HPEH power response would thus change to $\kappa^2\Pi_{avg,l}$. The equivalent stiffness of a piezoelectric stack can be determined by using the stack dimensions (where $k_{pz}\approx E_p^s A_{stack}/Nh$) and the equivalent Young's modulus for a shunted piezoelectric, as defined by Park and Palumbo [77],

$$E_p^s=\frac{E_p^E\left(j\omega C_p+Y_s\right)}{j\omega C_p\left(1-k_{33}^2\right)+Y_s} \tag{2.26}$$

where E_p^E is the Young's modulus of a short-circuited piezoelectric stack, k_{33} is the electromechanical coupling coefficient, and Y_s is the inverse of the shunted impedance defined in Section 2.2.

The preload force should be equal to the desired static pressure level minus the approximate dynamic pressure amplitude, or

$$F_{bvpre}=\left(P_s-0.5P_{dyn}\right)A_{spacer}=P_{op}A_{spacer} \tag{2.27}$$

where P_{op} is the pressure when the spacer begins to move. This is because the HPEH device will not be excited by the entire dynamic pressure until

$$\left(P_s + 0.5P_{dyn}\right)A_{spacer} - F_{bvpre} = P_{dyn}A_{spacer} \ . \tag{2.28}$$

In addition, the operating range of a force shunt HPEH is from the operating pressure up to the safe stress limit of a piezoelectric stack divided by the area ratio and force shunt ratio, in other words

$$\max\left\{P_s + P_0\right\} = P_{op} + \left|\sigma\right|/\left(\gamma\kappa\right). \tag{2.29}$$

HPEH5-4 was developed for testing this concept and utilizes a Parker piezoelectric stack made by Nec Tokin. The reported parameters for this device for calculating the Young's modulus of the piezoelectric stack are shown in Table 3. The soft springs used in the design were Belleville springs with the reported stiffness of 4115 kN/m when assuming linear stiffness, with a flat load value of 1846 N. Near the flat load limit, the linear stiffness assumption is no longer valid. For HPEH5-4, which has a spacer area of 182 mm^2, this corresponds to a maximum loading pressure of 10 MPa. Granted, the maximum loading can be increased by placing multiple springs in parallel, and the approximate stiffness can be lowered by placing springs in series.

Table 3: HPEH5-4 piezoelectric stack properties, from Nec Tokin data [70]

Shorted Young's modulus, E_p^E	55 GPa
Electromechanical coupling, k_{33}	0.68
Relative permittivity, $\varepsilon_{33}^{\sigma}/\varepsilon_0$	5440
Stack Capacitance, C_p	2 µF
Stack cross sectional area, A_{stack}	25 mm^2
Stack total height, Nh	20 mm
Piezoelectric strain constant, d_{33}^i	635 pm/V

Comparing the real part of the piezoelectric stiffness to four Belleville springs in series, the approximate force shunt ratio was 98% for HPEH5-4 tests, however this neglects any friction between the spring edges and the spacer, preloading sleeve, and other springs. As the spacer moves and the springs compress, the contact surface area changes and the angle of contact changes, which may inhibit motion. The designed area ratio was 7.3, and a device tested with no springs confirmed this area ratio to be accurate. However, the product of the area ratio and force shunt ratio for unloaded springs was 4.1, and for loaded springs was 5.0, therefore the actual force shunt ratio is expected to have been between 56-69%. Assuming a piezoelectric stack stress limit of -20 MPa, the designed area ratio provides a 2.8 MPa operating range above the operating pressure. The modeled and measured test results for the power normalized by dynamic pressure and the overall power are shown in Figure 2.18, Figure 2.19, and Figure 2.20.

The tests shown in Figure 2.18 are for when the springs have no preload, thus the operating range is at 0 MPa. The normalized power for each test are equivalent except for the lowest pressure value, which may be caused by viscous losses or Helmholtz resonator trapped air effects (see Chapter 3, specifically Section 3.4.2, for more details). As can be seen, the highest safe pressure level is less than 1 MPa.

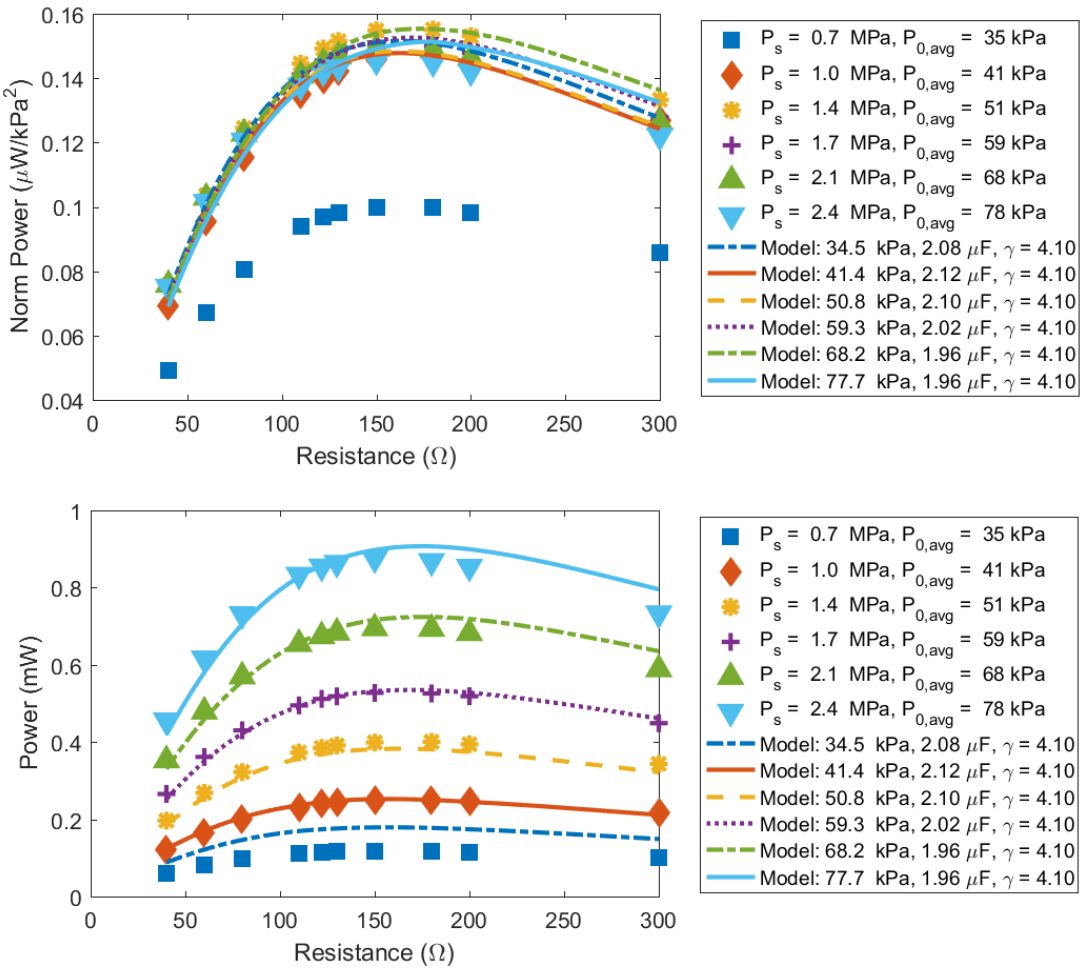

Figure 2.18: HPEH5-4, force shunt with four springs in series, no preload on springs

In Figure 2.19, the results shown for tests when a preload is applied to the Belleville springs. The modelled results do not match well to the test results because the model does not take into account HPEH performance that is excited by less than the full pressure ripple. As the static pressure increases, the test and model results begin to match because less of the dynamic pressure is clipped by the preloaded spacer. The highest static pressure value shown corresponds well with the model, and this pressure represents the target static pressure testing value, or $P_{op} + P_{dyn}$.

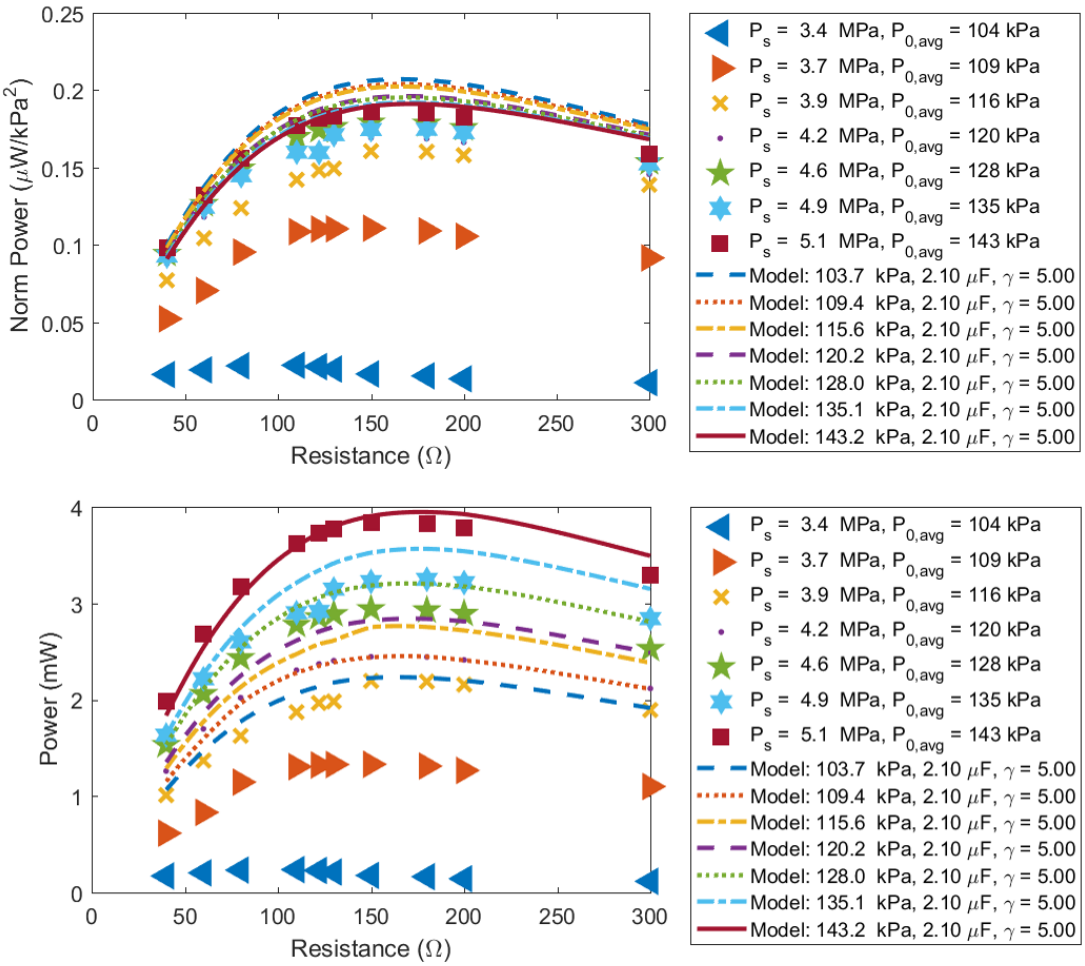

Figure 2.19: HPEH5-4, force shunt with four springs in series, P_{op} near 3.4 MPa (created with a 10 lb-in torque applied to preload sleeve).

The final test results shown in Figure 2.20 have the preload force nearing the flat load of the Belleville springs. These results have the highest power response because they benefit from the higher dynamic pressure levels, however the normalized power has decreased compared to the results shown in Figure 2.19.

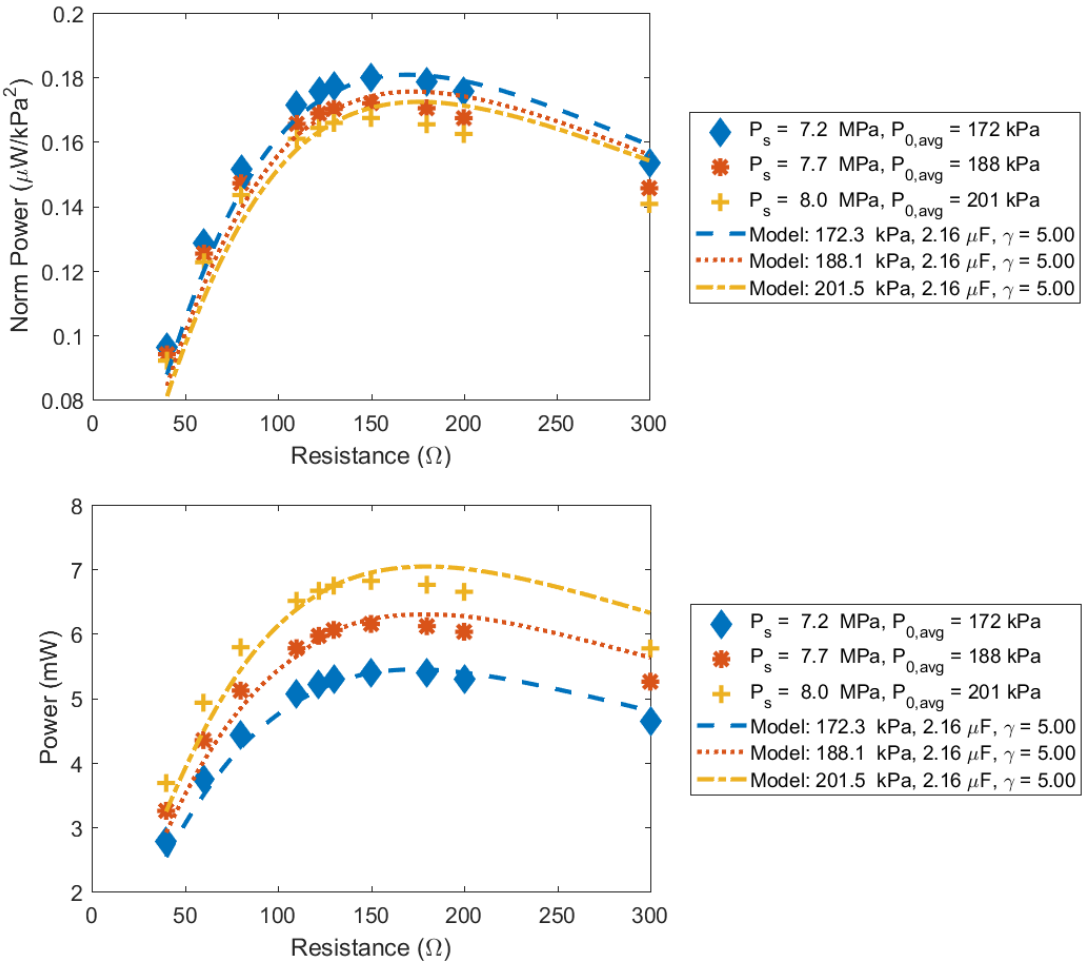

Figure 2.20: HPEH5-4, force shunt with four springs in series with 20 lb-in torque for preload

The force shunt concept allows HPEH devices to perform at high static pressure levels without reaching piezoelectric stack depolarization levels, however it causes the HPEH device to not function below the set operating pressure level. In addition to allowing piezoelectric devices to benefit from higher dynamic pressure levels, it also allows the devices to benefit from higher area ratios if the static pressure level is not expected to vary too far above the target static pressure. As mentioned, the force shunt does not protect the piezoelectric stack if the defined safe maximum pressure level is exceeded; it only relieves the target static pressure level. Future design work could investigate HPEH devices that are protected when this level is exceeded. Furthermore, if that concept was developed, then

multiple stages of force shunts could allow for a full range of static pressures in hydraulic systems. Short term future work can include doing a operating load study to determine the best preload level to provide for a given task while maximizing HPEH power performance.

2.5 Conclusions

This chapter introduced a hydraulic pressure energy harvester that utilizes piezoelectric stacks. It presented a general overview of the main components of a HPEH device, which were then further investigated for increasing the power performance. These parts include the shunt impedance, the interface coupling the piezoelectric stack to the hydraulic pressure ripple, and the piezoelectric material itself. In addition, an electromechanical model was presented, with various shunt configurations, optimal power loads, and shunt efficiencies investigated. Next, the testing procedures were presented, and the test results of multiple HPEH prototypes were compared to the electromechanical model. This included showing that R-L shunt circuits have higher power performance due to canceling the reactance of the piezoelectric material; increasing the power response by increasing the effective area; establishing that the power response increases with dynamic pressure; and presenting a method to target higher dynamic forces by using a force shunt design. The main components of a HPEH device are investigated further in the following chapters in order to increase the overall power response of HPEH devices. This includes the HPEH circuitry, the piezoelectric material selection, and increasing the dynamic pressure that is applied to a HPEH device.

CHAPTER 3

ACOUSTIC IMPEDANCE MATCHING

Hydraulic pressure energy harvester (HPEH) devices only convert a fraction of the energy within the acoustic pressure ripple, indicating that employing traditional acoustic focusing methods, such as a Helmholtz resonator, may improve the conversion efficiency without introducing energy into the system. This chapter explores the conversion improvement and practicality of employing a Helmholtz resonator in combination with a HPEH device.

3.1 Background of Helmholtz resonator models

As introduced Chapter 1, acoustic ambient energy typically has low intensity levels which require most acoustic harvester implementations to need either a large device (or system of devices), efficient focusing methods, or low power requirements. The high intensity levels found within hydraulic systems (recall Figure 1.2) allowed HPEH devices to convert microWatt level power without any focusing methods, and via area amplification and resonant circuit designs increased this to milli-Watt power levels when excited by 85 kPa rms-pressure amplitude. Conversely, if HPEH devices are used on low-level pressure ripple systems (less than 1 MPa static pressure), such as cross-country pipelines or water distribution networks, then the amount of power available decreases, indicating additional pressure amplification methods will be required. The power level available in such systems was previously demonstrated in Figure 1.3.

HPEH power output is proportional to the squared pressure amplitude and squared frequency at the interface to the material. Most of the energy from the acoustic pressure in

hydraulic systems is from a deterministic source, e.g. a pump operating frequency, and produced within a narrow band, such as centered around the pump operating frequency or harmonics, as is shown in Figure 1.1. The acoustic pressure is an unwanted byproduct of hydraulic systems that is typically reduced as much as possible. In addition, HPEH devices only convert a small fraction of the acoustic energy available within the system. It is therefore of interest to exploit the acoustic pressure available for exciting the piezoelectric stack within a HPEH device. If the pressure exciting the piezoelectric material can be amplified for the frequencies of interest, such as the pump harmonics, then the energy conversion efficiency of a HPEH can increase.

One well-established method in acoustic literature for absorbing or amplifying pressures within a particular frequency band [78-82], and previously incorporated into air-based acoustic energy harvesting devices (as discussed in Section 1.2.2 [42, 43, 45, 46, 51, 56]), is a Helmholtz resonator (HR). As an analogy, it is the acoustic equivalent of a spring-mass-damper mechanical system or a resistor-inductor-capacitor electrical circuit. It consists of a narrow port entrance (or neck), which contains fluid acting as the mass/inductor, opening into a larger volume or cavity, which has compressible fluid acting as a spring/capacitor element; acoustic radiation when the fluid exits the neck and fluid viscous effects within the neck account for the damper/resistor element. HRs are typically used to remove or reduce the acoustic energy from the frequency band at which the device resonates. This also means the pressure within the cavity for that resonant frequency is amplified; thus, when part of the cavity couples with a piezoelectric material, then the energy converted for that frequency increases. Given that only a fraction of the acoustic

energy within hydraulic systems is converted by HPEH devices, incorporating a Helmholtz resonator within a HPEH can increase the power produced by the device.

Helmholtz resonators have been used in liquid-based medium, however compact resonators are more difficult to produce due to liquids having sound speed on the order of 1000s of meters per second, whereas ideal gases at most temperatures are on the order of 100s of meters per second (e.g. fresh water – 1481 m/s at 20^{o}C; air – 343 m/s at 20^{o}C [79]). For a HR containing a single liquid medium, a target resonance of below 1500 Hz requires either a large apparent cavity volume (e.g. liters), a long neck length (e.g. half-meter), or a narrow neck diameter (e.g. millimeters or less). The use of HRs within hydraulics has been investigated for noise control purposes. Kojima and Edge [83] presented metallic bellows HRs and "rubber bag" HR (designed like an in-line hydraulic noise suppressor) as hydraulic silencers, where the cavity of the HR contained gas, thus reducing the overall size; the HR resonances were between 300 to 500 Hz. Kela [84] presented an adjustable HR system with resonances near 25 Hz, which contained a device of nearly 1 m in length and outer diameter of 0.11 m; the smallest neck diameter was 6 mm. Earnhart and Cunefare [85] used a HR device for noise control with a syntactic foam within the cavity to increase the apparent volume of the cavity, thus reducing the actual device volume to 310 mL with a neck diameter of about 6 mm; the HR resonances were between 37 to 92 Hz, depending on the composition of the foam liner.

Outside of noise control, HRs have been used in liquids as mechanical anti-aliasing filters in hydrophones. Wang et al. [86] introduced a fiber-optic hydrophone that uses a HR with a resonance near 1200 Hz. The overall device size was only about 63.6 mL, and thus

has a narrow neck diameter of 1.6 mm. Size-wise, this device is most analogous to the HR developed for HPEH herein.

Two main challenges presented by incorporating an HR on a HPEH are targeting a low enough frequency such that the dominant frequencies are amplified and keeping the device size on par with other HPEH. The dominant frequencies within the system tested are the first and second harmonic of the pump operating frequency (225 Hz), depending on the static pressure level. HPEH devices are designed to be installed on a hydraulic system via a diagnostic-sized ports, which have outer diameters of approximately 10 to 25 mm and wall thicknesses of 3 mm or more. In addition, the overall volume of HPEH are aimed to be less than 100 mL; for instance, HPEH5-4 is nominally 55 mL. The next section introduces a model for calculating the power gain and a design of HPEH-HR devices.

3.2 Methodology

A HPEH device with a Helmholtz resonator incorporated is shown in the schematic in Figure 3.1. The HR consists of a narrow port – which connects to the hydraulic pipe – and an oil-filled cavity – which contains one edge as the interface between the piezoelectric stack and oil. The peak frequencies within the acoustic pressure of the fluid are on the order of hundreds of Hertz; therefore, the piezoelectric stack (which has a fundamental resonance on the order of tens of kHz) is excited off-resonance. The acoustic pressure amplitude, P_0, can be amplified by including a Helmholtz resonator within the HPEH housing if the resonant frequency is on the order of the dominant frequencies. While previous HPEH devices exposed the interface directly to the hydraulic system flow, the HPEH Helmholtz resonator would amplify the noise at the resonance of the device. A model of the pressure gain caused by the HR is introduced, and followed by the design of a HPEH-HR.

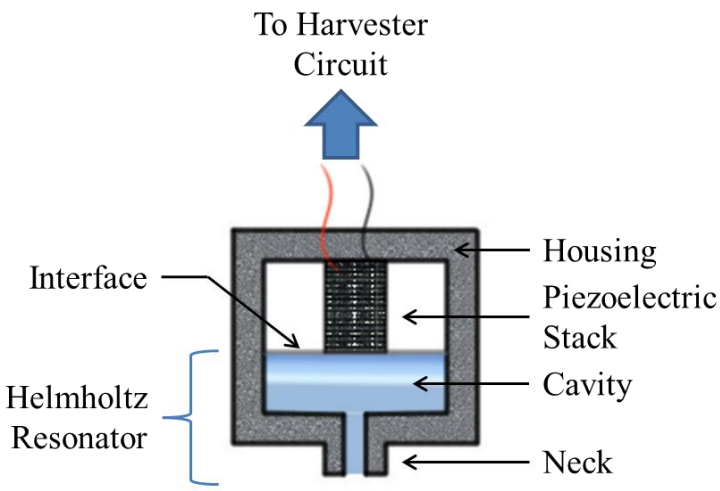

Figure 3.1: HPEH device with Helmholtz resonator

3.2.1 Model of HPEH with Helmholtz resonator

Helmholtz resonators can be modeled using lumped-element parameters because the wavelength of the acoustic disturbance is much larger than the characteristic dimensions of the resonator. The wavelength can be calculated by the speed of sound of the hydraulic fluid, c_f, which is around 1400 m/s, divided by the frequency of interest, which for hydraulic systems peak frequencies is on the order of 100s of Hz. Given that this produces wavelengths on the order of meters, whereas the dimensions of HPEH devices are on the order of centimeters, applying a lumped element model of a Helmholtz resonator is justified.

Helmholtz resonators consist of a cavity that provides compliance and a neck that connects the fluid flow pressure fluctuations (P_{pipe}) with the cavity and provides inertance and resistance. The Helmholtz resonator portion of a HPEH device modeled as a circuit is shown in Figure 3.2, with descriptions for each impedance term described below.

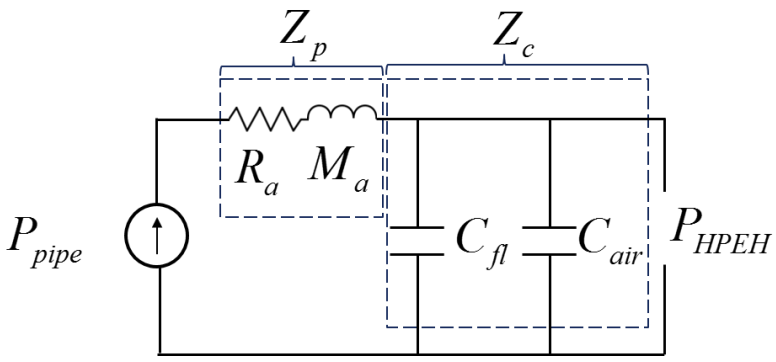

Figure 3.2: Helmholtz resonator component of HPEH modeled as a circuit with pipe pressure as the voltage source

This system is analogously modeled as a series RLC circuit or a parallel spring-mass-damper system. It includes the pressure fluctuations from the pipe containing system flow, P_{pipe}, the resulting pressure fluctuations within the cavity that are exposed to the HPEH, P_{HPEH}, the impedance from the neck inlet and radiation resistance, Z_p, and the compliance within the cavity volume, Z_c. The neck impedance consists of the acoustic resistance, R_a, and acoustic mass, M_a. The cavity compliance consists of the fluid (oil) compliance, C_{fl}, and entrained air compliance, C_{air}. The compliance can also include other factors, such as the outer housing compliance or added compliance from a different material, such as syntactic foam developed by Earnhart, Gruber and Marek as well as others [85, 87-90]. While the outer housing compliance may be an important factor in some designs, for the design presented here it is neglected; further details justifying this are discussed in Appendix A.1. The definitions and calculations of each term presented are discussed in detail after relating these terms to the potential power gain within HPEH.

The pressure gain within the resonator P_{HPEH} compared to within the pipe P_{pipe} can be modeled similar to a voltage divider, where

$$g = \frac{P_{HPEH}}{P_{pipe}} = \frac{Z_c}{Z_c + Z_p} \ . \tag{3.1}$$

The magnitude of the power gain G due to the inclusion of a Helmholtz resonator within a HPEH device is defined as

$$G = 20\log_{10}\left(\left|\frac{P_{HPEH}}{P_{pipe}}\right|\right) \tag{3.2}$$

since the HPEH power is proportional to the squared acoustic pressure amplitude P_0, and P_0 is now equivalent to P_{HPEH}, whereas previously it was equivalent to P_{pipe}. The phase difference between the pipe pressure and HPEH cavity pressure is calculated via

$$\phi = \tan^{-1}\left(\frac{\Im\{g\}}{\Re\{g\}}\right) . \tag{3.3}$$

Thus, the total power produced by HPEH-HR can be determined via

$$\Pi_{avg,l}^{total} = \sum_{n=1}^{N} \frac{\left|Z_e\right|^2 \left(\omega_n d_{33}^{eff} \kappa \gamma g_n A P_{0,n}\right)^2}{2R_l} \text{ for n} \in \omega \tag{3.4}$$

where g_n is the pressure gain ratio from an HR for a given frequency band n, γ is due to the area amplification ratio (Section 2.4.2), κ is due to the force shunt ratio (Section 2.4.3), ω is radial frequency, Z_e is the electrical impedance, R_l is the resistive load across the piezoelectric electrodes, and d_{33}^{eff} is the effective piezoelectric strain constant of the stack. Therefore, an accurate representation of HR impedances will allow HPEH-HRs to be designed and modeled.

The geometries of the HR consist of three main parameters: the cavity volume, V_{cav}, the cross sectional area of the neck, A_{neck} , and the effective neck length, $l_{n,eff}$. The cavity volume is simply defined as

$$V_{cav} = \pi\left(\frac{d_{cav}}{2}\right)^2 \left(l_{cav} + x_{spacer}\right) \approx \pi\left(\frac{d_{cav}}{2}\right)^2 l_{cav} \tag{3.5}$$

where d_{cav} is the cavity diameter, l_{cav} is the cavity height, and x_{spacer} is the change in cavity length due to the spacer displacement. The change in cavity length due to the spacer and piezoelectric stack deflection is neglected; this is because the deflection has a very minor effect on resonance and power gain, as explained in Appendix A.1. The cross sectional area of the neck is the standard definition of $A_{neck} = \pi\left(d_{neck}/2\right)^2 = \pi a^2$, where a is the neck radius. The neck length requires an end correction as it is used to determine the effective fluid mass involved in the pressure oscillations, as presented by Bolt et al. (extracted from Hansen [78]). The end corrections are defined from

$$l_N = \frac{8a}{2\pi}\left(1 - 1.25\zeta_N\right) \tag{3.6}$$

with ζ depending on the orifice termination, where the subscript indicates which termination edge. For the neck terminating into the system flow in the pipe, $\zeta_p = d_{neck}/d_{pipe}$; for the neck terminating into the HR cavity, $\zeta_c = d_{neck}/d_{cav}$. Hence, the effective neck length is defined as

$$l_{n,eff} = l_{neck} + l_p + l_c . \tag{3.7}$$

The next step is to determine the fluid properties of the oil within the system. The oil manufacturer provided the specific gravity of the oil for 15.6°C (T_{ref}) at atmospheric

pressure (0.1 MPa, P_{atm}) and the kinematic viscosity, ν, of the oil at both 40°C and 100°C [91]. The density of the oil at atmospheric pressure with changing temperature is determined via

$$\rho_{f,T} = \frac{S.G. \times \rho_{water,ref}}{\left[1 + \alpha\left(T_C - T_{ref}\right)\right]} \tag{3.8}$$

where the density of water at the referenced temperature is 999.07 kg/m^3, and T_C is the measured oil temperature in degrees Celsius, and α is the volumetric expansion coefficient. The volumetric expansion coefficient, α, of new oil can be found from online resources, such as Engineering Toolbox [92]. The kinematic viscosity of the oil at atmospheric pressure for a given temperature is

$$\nu_T = \Gamma\left(10^{\Upsilon(T_C)}\right) \tag{3.9}$$

with $\Gamma = \nu_{40C} / 10^{\Upsilon(40C)}$ and $\Upsilon = \left[-\log_{10}\left(\nu_{100C}/\nu_{40C}\right)\right]/\left[40-100\right]$. The bulk modulus of the fluid is derived from the kinematic viscosity, mean system pressure, and oil temperature. As presented by Song, et al. [93], the isothermal secant bulk modulus at atmospheric pressure for a given temperature is calculated via

$$\log_{10}\left(K_{0,T}\right) = 0.3766\left(\log_{10}\left(\nu_{T,\mathrm{cSt}}\right)\right)^{0.3307} - 0.2766 \tag{3.10}$$

where $K_{0,T}$ is in GPa and the kinematic viscosity is in centistokes. The isothermal secant bulk modulus for a given pressure is then found by

$$K_{P,T} = K_{0,T} + B_T P_{s,\mathrm{GPa}} \tag{3.11}$$

where $B_T = -0.01382 T_C + 5.851$, and the mean system pressure is in GPa. From this, as summarized by Gholizadeh et al. [94], the isothermal tangent bulk modulus can be determined using

$$K_f = \frac{K_{P,T}\left(K_{P,T} - P_{s,\mathrm{GPa}}\right)}{K_{0,T}} \tag{3.12}$$

which can then be used to estimate the density and sound speed as related by static pressure (system mean pressure). Note, when the ratio of specific heats is close to 1, then the error caused by using the isothermal bulk modulus rather than the adiabatic bulk modulus to determine the speed of sound is relatively minor, as explained in Pierce [80].

Using Taylor's series [79], as with the temperature adjustment, the density of the oil is updated with respect to pressure to be

$$\rho_f = \rho_{f,T}\left(1 + \frac{\left(P_s - P_{atm}\right)}{K_f}\right) \tag{3.13}$$

where the bulk modulus and pressure terms must be of the same unit. The speed of sound of the fluid is calculated as

$$c_f = \sqrt{\frac{K_f}{\rho_f}} \ . \tag{3.14}$$

The wavenumber for the fluid is defined as $k_f = \omega / c_f$. Despite absolute (dynamic) viscosity, μ_f, being relatively independent of pressure or density changes, kinematic viscosity is a function of density. Therefore, the kinematic viscosity is also updated to be

$$\nu_f = \frac{\mu_f}{\rho_f} = \nu_T \frac{\rho_{f,T}}{\rho_f} \ . \tag{3.15}$$

The literature on hydraulic oil bulk moduli [94] indicates that air can be present within the system in three ways: 1. a free air pocket; 2. entrained air, which are bubbles dispersed in the oil; or 3. dissolved air, which does not significantly affect the bulk modulus. As system pressure increases, the amount of dissolved air increases; however

increasing temperature impedes air from dissolving. In addition, the amount of air that can be dissolved for a given static pressure depends on the solubility. It is therefore necessary to define properties of air.

For this work, the volume of air present is defined as a fraction of the fluid volume, with the initial air fraction represented by b_0. The air fraction for a given static pressure and temperature can be derived from the ideal gas law as

$$b = b_0 \frac{P_{atm}}{P_s} \frac{T_C}{T_{ref}} \ . \tag{3.16}$$

The density of air is defined as

$$\rho_{air} = \frac{P_s}{R_{air} T_K} \tag{3.17}$$

where T_K is temperature in Kelvin and R_{air} is the specific gas constant for dry air, 287.058 J/(kg. K). The speed of sound for air is calculated from

$$c_{air} = \sqrt{\gamma_{air} P_s / \rho_{air}} \tag{3.18}$$

where γ_{air} is the ratio of specific heats for air, 1.402 [79]. Given the defined HR geometries and fluid properties, the next step is to define the acoustic compliance, mass, and resistance of the system.

The volume of the fluid is defined as $V_{fl} = V_{cav}(1-b)$ and the volume of air is $V_{air} = bV_{cav}$. Note, if a compliant foam was included in the HR cavity, then these would change to $V_{fl} = (V - V_{foam,0})(1-b) + (V_{foam,0} - V_{foam,P})$ and $V_{air} = (V - V_{foam})b$. The compliance of substance N is defined as

$$C_N = \frac{V_N}{K_N} = \frac{V_N}{\rho_N c_N^2} \tag{3.19}$$

where in this system, the substances include oil and air[79]. The effective compliance of the cavity is the sum of the substance compliances, $C_{eff} = \sum_N C_N$. Similarly, the effective density of the cavity is

$$\rho_{eff} = \sum_N \frac{V_N}{V_{cav}} \rho_N \,. \tag{3.20}$$

The cavity's effective speed of sound is defined as

$$c_{eff} = \sqrt{\frac{V_{cav}}{\rho_{eff} C_{eff}}} \tag{3.21}$$

and the overall impedance of the cavity is

$$Z_c = \frac{1}{j\omega C_{eff}} \,. \tag{3.22}$$

In essence, trapped air acts like a spring that stiffens as it is compressed, and is combined electrically in parallel. Since air is much less dense than hydraulic fluid, the inclusion of trapped air in the cavity decreases the resonant frequency which is desirable for this usage. The resonant frequency increases as the volume of trapped air shrinks and stiffens in proportion to system static pressure. The term used in this study to describe this phenomenon is resonance drift. Resonance drift due to unintentional trapped air is undesirable because it makes a resonator more difficult to precisely design for a useful resonance frequency. For instance, it can occur when an HR cavity is not purged of air prior to a hydraulic system being turned on.

The other portion of an HR is the acoustic mass and resistance due to the neck. The acoustic mass is the effective mass of the fluid within the neck over the neck cross sectional area [79]; in other words,

$$M_a = \frac{m_{neck}}{A_{neck}^2} = \frac{\rho_f A_{neck} l_{n,eff}}{A_{neck}^2} . \tag{3.23}$$

This leads to the corresponding acoustic mass impedance of

$$Z_m = j\omega M_a = \frac{j\rho_f c_f k_f l_{n,eff}}{A_{neck}} . \tag{3.24}$$

The acoustic resistance can be modeled in several different ways, depending on the characteristics of the fluid excitation, orifice geometry, and apparent viscous boundary layer. The viscous boundary layer is defined as $d_v = \sqrt{2\nu_f / \omega}$, and when the boundary layer approaches the dimensions of the neck radius, narrow tube resistance calculations are required[82]. For the HR later presented, at low static pressure levels this can occur at frequencies below 60 Hz, however the approximation presented by Kojima and Edge [83] for hydraulic fluid viscous effects works well for most cases (with exceptions discussed in Section 3.4.1). Kojima and Edge [83] reported the hydraulic oil complex coefficient representing viscous effects is

$$\begin{aligned} \xi &\approx 1 + \xi^* + \left(\xi^*\right)^2 \\ \xi^* &= \sqrt{\frac{\nu_f}{j\omega a^2}} \end{aligned} . \tag{3.25}$$

From this, the loss factor of the complex wavenumber can be calculated (as shown by Earnhart et al. [85]) via

$$\alpha_w = -\frac{\Im\{k_f \xi\}}{\Re\{k_f \xi\}} \tag{3.26}$$

from which the resistance due to viscous effects is determined (as shown by Kinsler [79]) as

$$R_w = 2\rho_f A_{neck} l_{n,eff} \omega \alpha_w . \tag{3.27}$$

If the neck radius is less than the viscous boundary layer, then the loss factor can be calculated using

$$\alpha_w = \frac{1}{k_f}\sqrt{\frac{4\omega\nu_f}{c_f^2 a^2}}, \tag{3.28}$$

which was adapted from the narrow tube attenuation coefficient presented by Pierce [80]. If the neck radius and viscous boundary layer are nearly equal, then higher order terms to Eq. (3.25) can be added to correct for the additional viscous resistance. Thus, ξ can be represented by a geometric series related to the term ξ^*, which relates the viscous boundary layer to the neck radius. Therefore, the relation for the viscous loss factor can be approximated using

$$\begin{aligned} \alpha_w &= -\frac{\mathrm{Im}\{k_f\xi\}}{\mathrm{Re}\{k_f\xi\}}, \text{ where } \xi = \frac{1}{1-\xi^*} \quad \text{for } |\xi^*| < 1 \\ \alpha_w &= \frac{1}{k_f}\sqrt{\frac{4\omega\nu_f}{c_f^2 a^2}} \qquad\qquad\qquad\quad \text{for } |\xi^*| > 1 \end{aligned}. \tag{3.29}$$

This representation provides a computationally simple method for estimating viscous losses within narrow hydraulic pipes. A more rigorous derivation can be applied to determine the viscous resistance, such as a method presented by Hansen [78] compared in Appendix A.3, however this representation accurately matched all tests performed and is deemed sufficient for this analysis and design. (Other methods are described in Ch. 6.4 in Morse and Ingard [82] and Ch. 10 in Pierce [80].)

The resistance due to the sound radiating into the fluid medium is defined as [79]

$$R_r = \frac{\rho_{eff} c_{eff} k_{eff}^2 A_{neck}^2}{2\pi}, \tag{3.30}$$

which uses the effective density of the cavity and effective speed of sound in the cavity. The overall acoustic resistance impedance is calculated via

$$R_a = \frac{R_r + R_w}{A_{neck}^2} \tag{3.31}$$

and the overall neck impedance is defined as

$$Z_p = R_a + Z_m \,. \tag{3.32}$$

Now that a model has been established, a parameter study can be performed to explore which parameters have the most impact on the power gain and resonant frequency. The natural resonant angular frequency of the undamped HR can be determined as

$$\omega_{res} = 2\pi f_{res} = \sqrt{\frac{1}{M_a C_{eff}}} \,. \tag{3.33}$$

The peak pressure gain occurs at the damped natural frequency. If $\omega_{res} \gg R_{a,avg} / \left(2M_a\right)$, then the damped natural frequency is estimated using

$$\omega_d = 2\pi f_d = \left[\sqrt{\omega_{res}^2 - \left(\frac{R_{a,avg}}{2M_a} \right)^2} \right] \,. \tag{3.34}$$

where $R_{a,avg}$ is the average acoustic resistance calculated across all frequencies (excluding zero Hz). However, this is not accurate when the resonant frequency is low (i.e. close to or less than $R_{a,avg} / \left(2M_a\right)$), such as if a large amount of air is trapped. For this reason, the natural resonant frequency, f_{res}, is used for dimensional analysis and HR design purposes, with the acknowledgement that the peak power gain occurs at a slightly lower frequency, depending on the acoustic resistance.

3.2.2 Design of HPEH with Helmholtz resonator (HPEH-HR)

The hydraulic system that the HPEH devices are tested have dominant pressure ripple at 225 Hz and 450 Hz, depending on the static pressure level and temperature of the system, as was seen in Figure 1.1. Due to the high sound speed in oil, designing a Helmholtz resonator similarly sized to HPEH devices requires either a narrow neck diameter or added compliance to the cavity. Assuming no trapped air is within the oil, the resonance frequency from Eq. (3.33) can be simplified to

$$f_{res} = \frac{1}{2\pi}\sqrt{\frac{A_{neck}c_f^2}{l_{n,eff}V_{cav}}} = \frac{1}{2\pi}\sqrt{\frac{d_{neck}^2 c_f^2}{l_{n,eff}l_{cav}d_{cav}^2}} \tag{3.35}$$

which demonstrates that the neck diameter and cavity diameter have the strongest impact. Unfortunately, all dimensions other than the neck diameter require the device size (or apparent size) to increase in order to lower the resonant frequency. Therefore, the first dimension analyzed is the neck diameter, with simulations shown in Figure 3.3. The measured points correspond to the design chosen and values measured from tests presented in the next section. As expected, the neck diameter has a strong impact on the resonant frequency; unfortunately, at resonant frequencies near and below 450 Hz, the power gain at the natural resonant frequency is near or below zero. Figure 3.3 is not showing the peak power gain, but rather the power gain when the phase passes through -90°. The peak pressure gain can be no lower than 1, i.e. 0 dB power gain, but this may occur at or near 0 Hz. As explained in the model, when the neck diameter becomes too small, the port begins to act like a narrow tube, which is impeded by the viscous boundary layer encompassing the entire cross-sectional area of the neck.

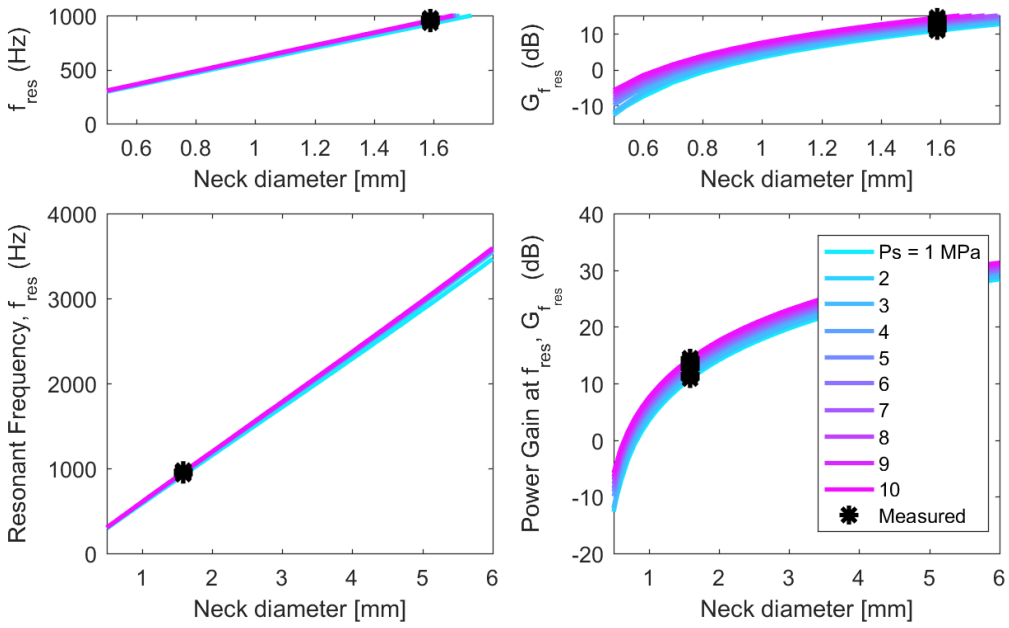

Figure 3.3: Model of resonant frequency and power gain with respect to HR neck diameter, where b_0 = 0.0003, l_{neck} = 23.75 mm, d_{cav} = 16.58 mm, and l_{cav} = 17.91 mm.

The other parameters that can be adjusted to lower the resonant frequency include the cavity diameter, cavity length, and neck length. As seen in Figure 3.4, the resonant frequency requires relatively large increases in neck length, cavity length, or cavity diameter to have any impact. For the data shown, this already includes a neck diameter of 1.59 mm (1/16”), which is considered narrow for HRs in hydraulic systems to date. While increasing these dimensions does not adversely affect the power gain (as seen with decreasing the neck diameter), it was deemed impractical when considering it needs to fit on hydraulic mobile equipment, and may have limited space.

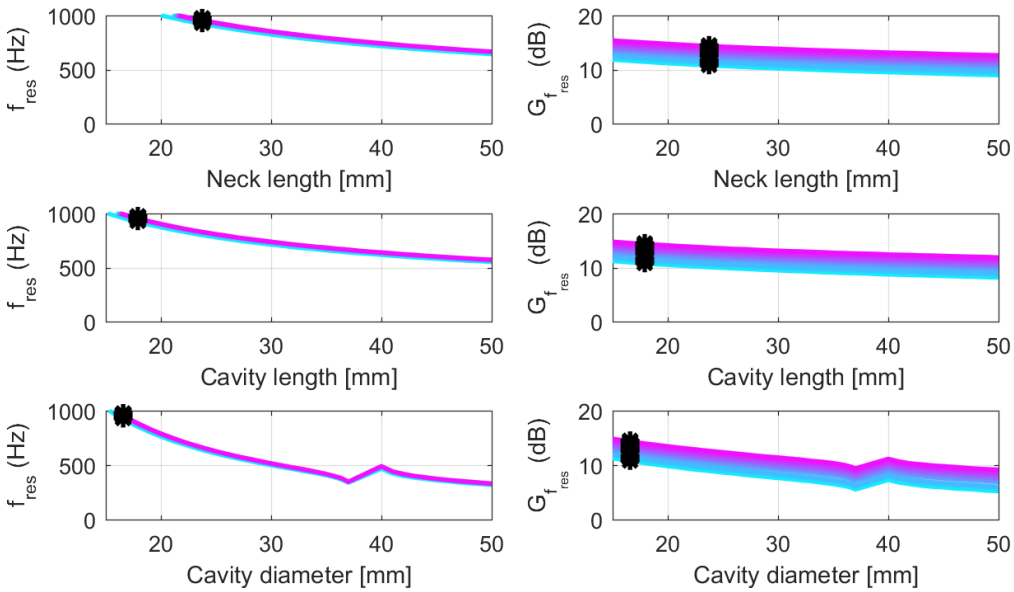

Figure 3.4: Model of resonant frequency and power gain with respect to HR neck length, cavity length, and cavity height; d_{neck} = 1.59 mm and b_0 = 0.0003 (l_{neck} = 23.75 mm, d_{cav} = 16.58 mm, and l_{cav} = 17.91 mm unless stated otherwise in graph).

Two device design dimensions are presented in Table 4 and modeled in Figure 3.5, where a) shows an HR designed to be resonant near 600 Hz and b) shows an HR designed to be resonant near 900 Hz. In the figure, the static pressure level and temperature increases from 1 MPa at 25ºC to 10 MPa at a) 60ºC and b) 42ºC . The reason for these temperature values is because they are used in later sections for model to test comparisons. The trapped air is assumed to be negligible in this model, so only temperature and static pressure affects the model.

Table 4: Design comparison for Helmholtz resonators; HPEH-HR uses "HR 900 Hz."

Dimension	**HR 600 Hz**	**HR 900 Hz**
l_{neck}	11.0 mm	23.7 mm
d_{neck}	0.67 mm	1.59 mm
l_{cav}	19.0 mm	17.9 mm
d_{cav}	15.0 mm	16.6 mm

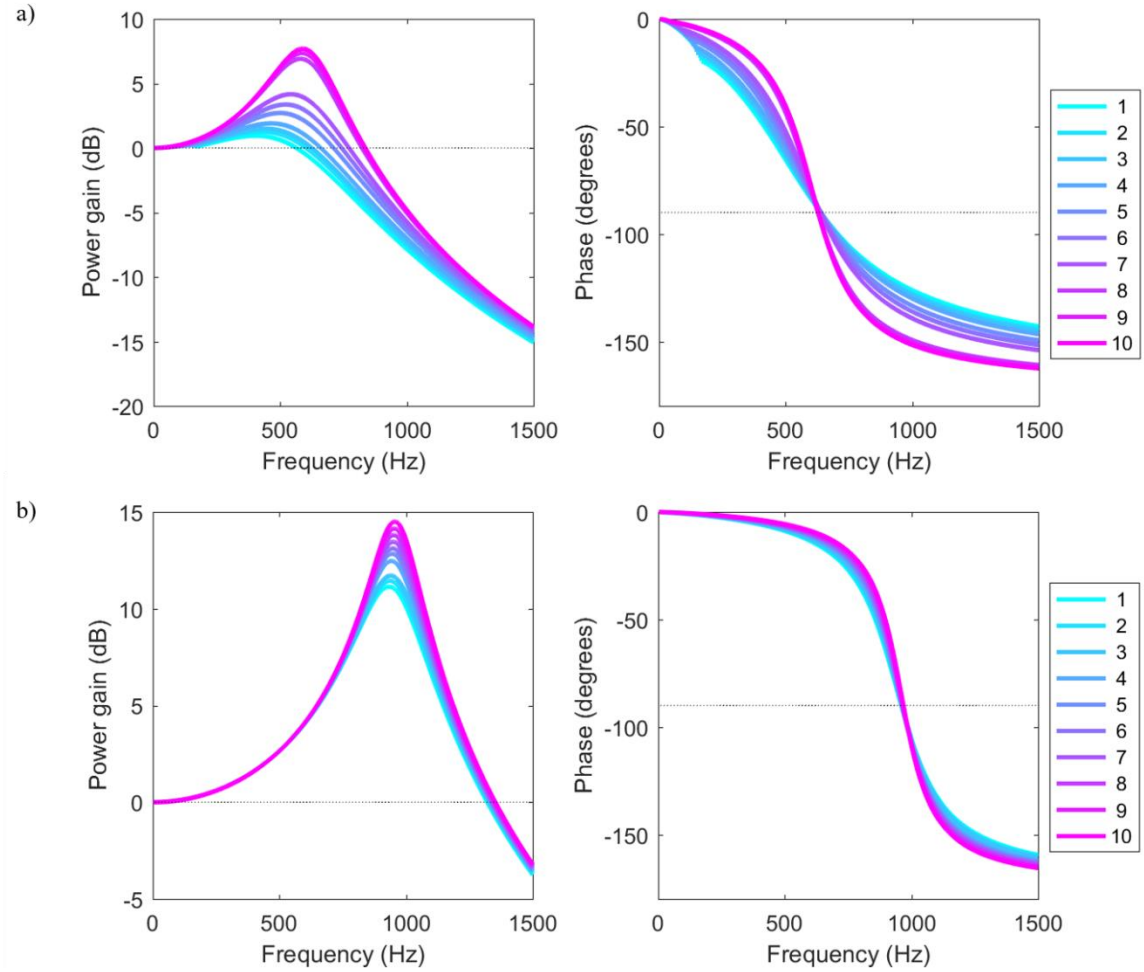

Figure 3.5: Power gain and phase for two different HR designs at static pressure levels increasing from 1 to 10 MPa (as indicated by legend), where a) is tuned near 600 Hz (temperature increasing from 25 to 60°C) and b) is tuned near 900 Hz (temperature increasing from 25 to 42°C); assumes no trapped air.

The HR designed to be resonant near 900 Hz is deemed more advantageous than the 600 Hz design, and is used with the HPEH devices; any references using HPEH-HR herein refer to the HR 900 Hz design. The HR 600 Hz design shown in Figure 3.5a contains a neck diameter of 0.67 mm and causes any power gain benefit to be quite small unless at high oil temperature and static pressure. In addition, if any air became trapped within the device, the resonance frequency would further reduce and potentially reduce the pressure within the cavity for the dominant frequencies.

Conversely, the HR 900 Hz design provides a wider bandwidth of power gain and is robust to trapped air potentially lowering the resonant frequency. The HR 900 Hz design especially amplifies the fourth pump harmonic, which for this system can sometimes reach one third the level of the second pump harmonic, which typically dominates the system at low static pressure levels. This only requires about 10 dB power gain to amplify the pressure to levels equivalent to the dominant frequency pressure levels. Additionally, as is shown in Eq. (3.4), both the squared pressure amplitude and the squared frequency are proportional to the power. Thus, an equivalent pressure level at higher pump harmonics will result in higher overall power compared to those same pressure levels at lower pump harmonics. To quantify this, a weighted pressure-frequency gain defined as

$$W = \frac{P_n f_n}{P_{450Hz}(450Hz)} \tag{3.36}$$

where P_n is the pressure within the cavity for a given frequency f_n, and P_{450Hz} is the pressure measured within the pipe at 450 Hz. If the circuit is resistive only, then the weighted pressure-frequency gain can be modified to determine the frequency for an optimal single-resistance value to

$$W_{R_{opt}} = \frac{(P_n)^2 f_n}{(P_{450\text{Hz}})^2 (450\text{Hz})} \tag{3.37}$$

which accounts for the electrical impedance as seen in Eq. (2.14). The weighting values can be changed, however for this work, 450 Hz has consistently presented the highest power potential without HR included. Also, weighted pressure uses the value measured within the system flow as the HR 900 Hz design also increases the pressure at 450 Hz, and so this provides a comparison of the power potential with and without an HR.

The HR 900 Hz design is used in combination with HPEH5-4, and provides a total device volume of 81.9 mL. The HR portion consists of about 27 mL of the HPEH-HR device. The following section discusses test results and model validation of the HPEH-HR.

3.3 Results

A Helmholtz resonator HPEH device (HPEH-HR) was designed with the damped natural frequency to be near 900 Hz. For the hydraulic system and operating parameters used, this corresponded most closely to the fourth harmonic of the pump operating pressure. This frequency contained pressure levels an order of magnitude below the dominant frequency pressure level or less, i.e. a test with 140 kPa_{rms} pressure at 450 Hz may have about 14 kPa_{rms} or less pressure at 900 Hz; however the pressure decrease at higher harmonics varies across operating parameters and systems. The Helmholtz resonator base housing attached to the upper housing of a previously discussed device, HPEH5-4, which is used for comparing the device performance. In addition to designing the HR base for the HPEH device, an additional cap (as seen in Figure 3.6a) was designed with a dynamic pressure sensor port in order to measure the amplified pressure within the Helmholtz resonator cavity. This is used for the initial model validation, followed by HPEH-HR tests at both low and high (with force shunt) static pressure tests.

3.3.1 Model validation of cavity pressure amplification

In order to validate the pressure model, a test article was manufactured with a pressure transducer port in place of a piezoelectric stack, shown in Figure 3.6, in order to measure the pressure within the cavity compared to the pressure in the pipe. The testing was performed using a 9-piston pump operating at 1500 rpm using ISO VG 46 hydraulic oil [91]. The temperature of the oil was measured within the system flow. A needle valve

downstream of the test article was used to change the system static pressure. A schematic of the test setup can be seen in Figure 3.6.

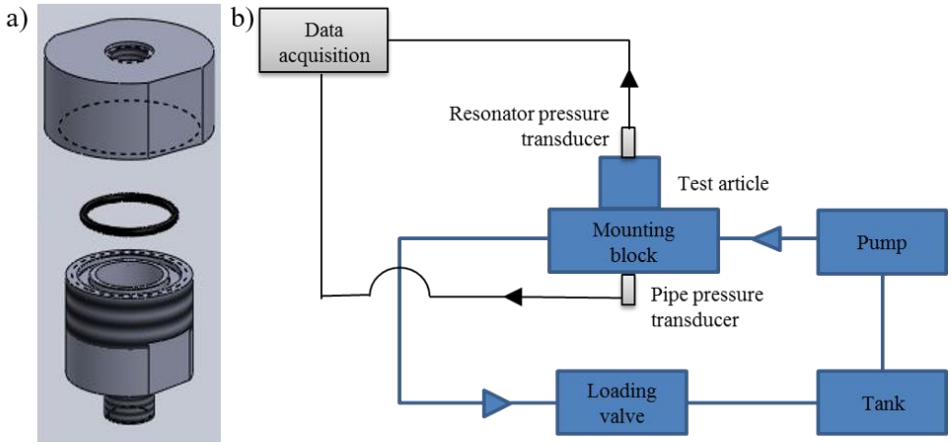

Figure 3.6: a) Test article with cap, o-ring, and housing (top to bottom) and b) testing setup schematic

The test article was filled with oil prior to assembling to minimize the air trapped within the cavity of the device. This reflects the steady-state operating condition of the device as any air trapped with the cavity would be dissolved into the oil over time. It was then tested at multiple static pressure levels, where the pressure from within the pipe and within the resonator was measured. The provided oil kinematic viscosity, ν, at atmospheric pressure is 45 cSt at 40^{o}C, with a viscosity index of 35 (meaning the kinematic viscosity at 100^{o}C corresponds to 5.7 cSt)[91] produced consistently over 10% error in power gain at resonance frequency. The new oil volumetric expansion coefficient, α, is 0.0007^{o}C^{-1} [92], however this also proved to be inaccurate when compared to the model. Modeled results poorly predicted the resonance frequency and power gain using these values.

Figure 3.7 shows the percent error between the experimental results and the model for the resonance frequency (averaged from 10 static pressure levels), and the power gain at the resonance frequency; thus, the accuracy of the model increases as the data points

approach zero for both axes. For this comparison, the resonance frequency is when the phase passes through -90° and the corresponding power gain is compared, despite this not being the peak power gain. In Figure 3.7, the model was varied with respect to oil viscosity (for four combinations, including the manufacturer-provided level; indicated by shape in legend), volumetric expansion coefficient (.0007 to .0014°C^{-1}; indicated by top graph colorbar), and air fraction volume (.0001 to .001; indicated by bottom graph colorbar).

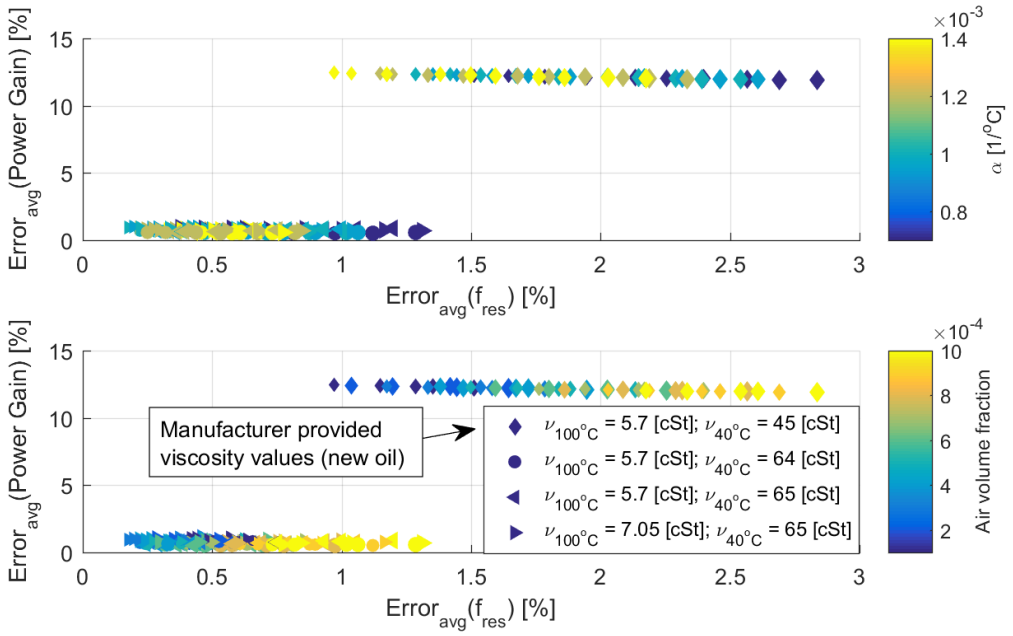

Figure 3.7: Error of modeled resonance frequency and power gain for various air fraction, kinematic viscosities and volumetric expansion coefficients.

The oil condition during experiments may be different from the provided oil properties due to the hydraulic rig oil having been used for near or over the TOST (Turbine Oil Oxidation Stability Test, ASTM D943) oxidation lifetime. Kinematic viscosity of an oil may change with temperature, pressure, or oxidation[95-97], and the oil used during testing was near or beyond its oxidation life specification[91]. The model accounts for changes due to pressure, however does not account for changes of aged oil due to

contamination or oxidation. The volumetric expansion coefficient for new oil may not be the same for the well-used oil in the test rig. In addition, the narrow neck diameter of the HR may contribute additional thermal and viscous losses beyond what is captured by the model presented. A correction was performed by using one set of static pressure experiments to compare model accuracy with respect to the kinematic viscosity and volumetric expansion coefficient. Based on experiment and model error comparisons, all simulations presented use a kinematic viscosity level of 64 cSt at 40^{o}C and 5.7 cSt at 100^{o}C, and use a volumetric expansion coefficient of 0.001^{o}C $^{-1}$, unless otherwise stated. Further justification and details regarding why these values were chosen is discussed in Appendix A.2.

The model compared to the test results matches well using the parameters discussed above. The test used to determine these parameters, which was for a filled test body, is shown in Figure 3.8. The power gain is shown in Figure 3.8a, and the phase difference is in Figure 3.8b. In addition, the Helmholtz resonator (HR) has a resonance frequency near 900 Hz, which is the intended design. The HR also increases the pressure at 450 Hz, which for the system used is typically the dominant frequency. The small shift in resonance frequency between the test at 1 MPa versus the higher static pressure levels is due to the non-negligible trapped air volume fraction of 0.0003.

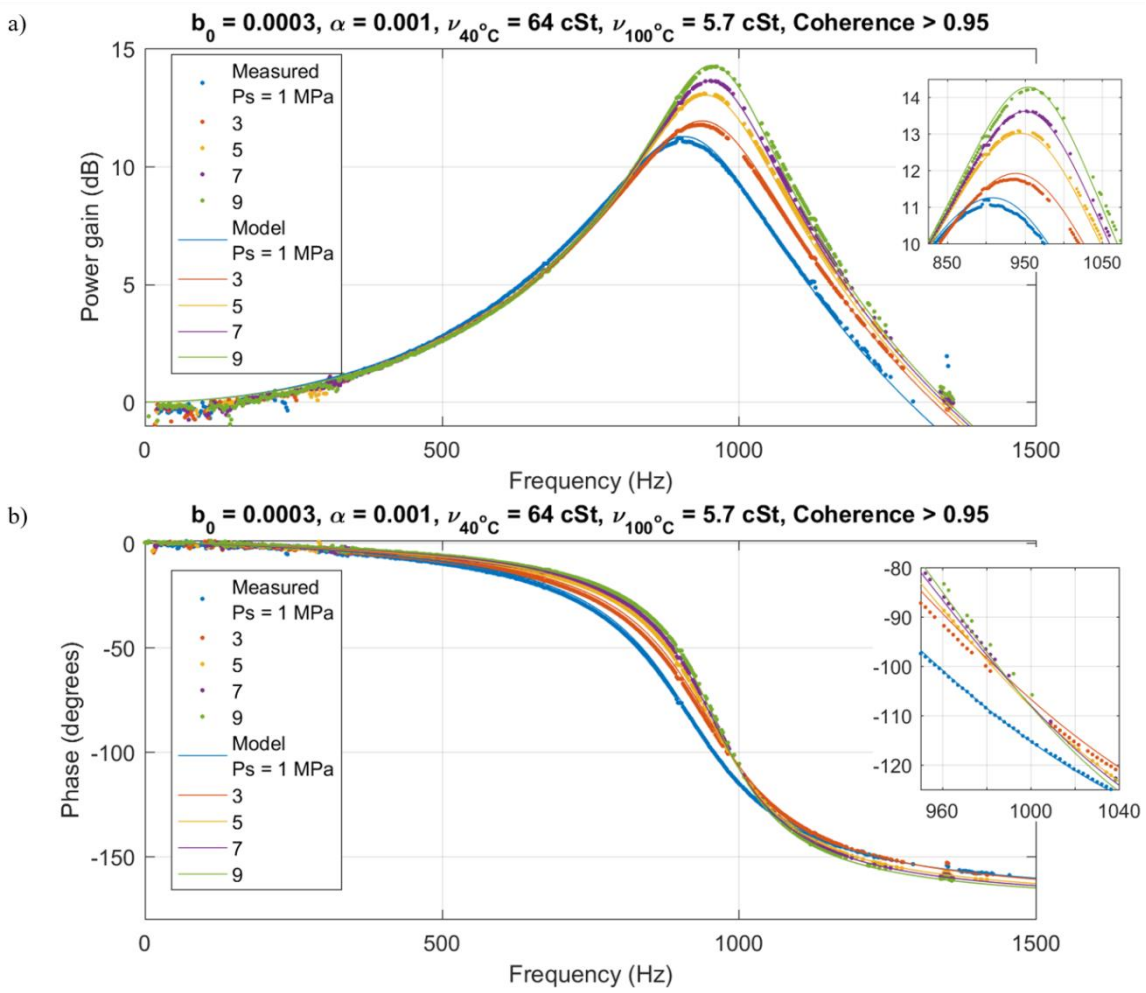

Figure 3.8: Filled test body where measured cavity is compared to pressure within pipe for multiple static pressure levels: a) power gain and b) phase difference.

The test shown above is for an HR cavity filled with oil prior to testing, however if the HR is not pre-filled with oil, the trapped air can add significant compliance to the cavity. A test where the device was not prefilled was performed and modeled to show the effect of trapped air, with results seen in Figure 3.9. The test order is with increasing pressure level. The amount of trapped air used by the model decreases with each successive test, which follows logically given that trapped air can disperse as bubbles or become dissolved within the oil [94]. In addition, the power gain predicted by the model for the lowest pressure test is higher than measured.

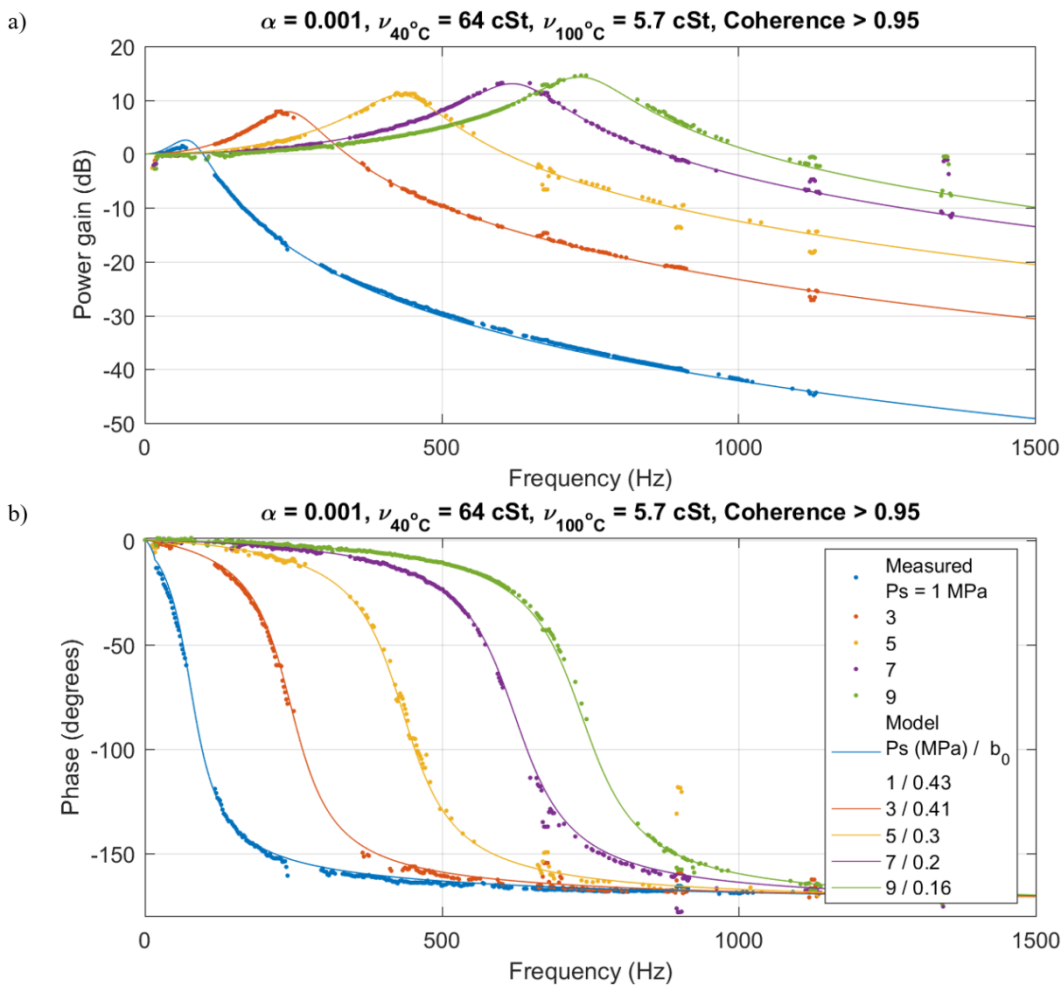

Figure 3.9: Unfilled test body where measured cavity is compared to pressure within pipe for multiple static pressure levels: a) power gain and b) phase difference. Model uses the labelled initial air fraction values, b_0, as shown, where the trapped air decreases with each successive test.

An important aspect of unfilled or only partially oil-filled resonators is the resonance drift, meaning the resonant frequency of the device shifts with changing static pressure. The modeled and measured resonance frequency for a given static pressure with respect to air fraction within the cavity volume and the corresponding power gain for that frequency is shown in Figure 3.10. For the measured points, the resonance frequency and power gain measurements at -90^o sometimes corresponded to data that was below the magnitude-squared coherence between the pipe pressure and HR cavity pressure threshold

of 0.95 (such as below 3 MPa static pressures), however the measured values are shown (rather than interpolated). As the static pressure increases, the effect of the trapped air decreases due to air compression and dissolving, and the resonant frequency rises to near the value seen for the pre-filled case (with minimal trapped air). In addition, as seen when comparing the model to the measured results, the amount of trapped air decreases as testing continues. Therefore, when dealing with unfilled HPEH-HR devices, both testing order and static pressure level affects the resonance frequency and amount of trapped air within the HR cavity, where the effect decreases with elevated static pressure levels.

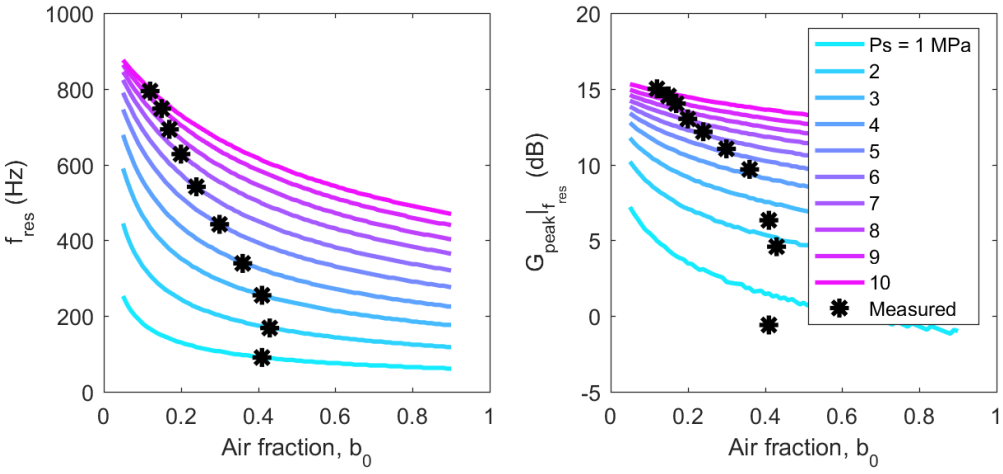

Figure 3.10: Unfilled HR resonance drift modeled for multiple cavity volume air fraction values at multiple static pressure levels with respect to resonant frequency and power gain at resonance frequency.

The mismatch between the model and experiments at low static pressure levels for unfilled-HR tests may be due to the resonance frequency being below the pump operating frequency, causing the coherence between the pipe and HR cavity to decrease (see Figure 3.11a) and the signal to noise ratio within the HR cavity to decrease (see Figure 3.11b). Due to the trapped air, the resonance frequency is lower than the pump operating frequency for static pressures below 3 MPa. The signal to noise ratio for the pressures below 3 MPa

within the cavity are significantly worse the other static pressure levels, as shown in Figure 3.11b. While the signal to noise ratio is above 20 dB, the signal is not as distinct as for static pressures above 3 MPa, and for frequencies above the pump operating frequency (225 Hz) and below the fourth harmonic (900 Hz).

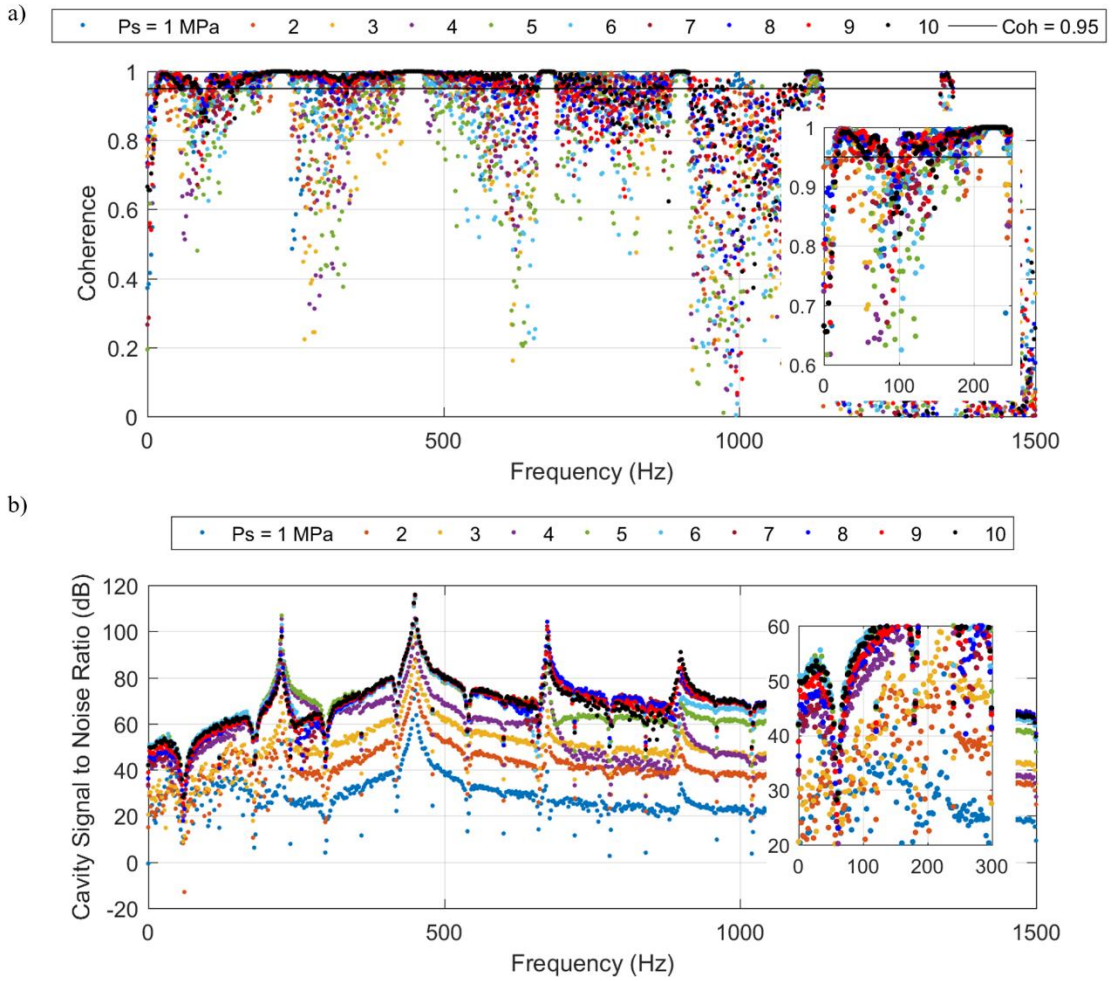

Figure 3.11: a) Coherence between the pipe and HR cavity pressures and b) signal to noise ratio within the HR cavity for tests where the resonator was not prefilled with oil. Legend at top of figures.

Prefilling the HR cavity with oil has a major impact on test results, especially at low static pressures. However, for the prototype tested, the process of pre-filling the cavity was difficult and inaccurate, meaning the amount of air trapped could not be determined

prior to measuring the HR response. Even tests where the cavity had just under 1% of the HR cavity composed of air still exhibited resonance drift, as shown in Figure 3.12. Filling the HR cavity with oil when using the cap with a pressure transducer was an easier process than when using the HPEH upper housing. It is therefore expected that trapped air will be a contributing unknown when performing and modeling HPEH-HR device experiments.

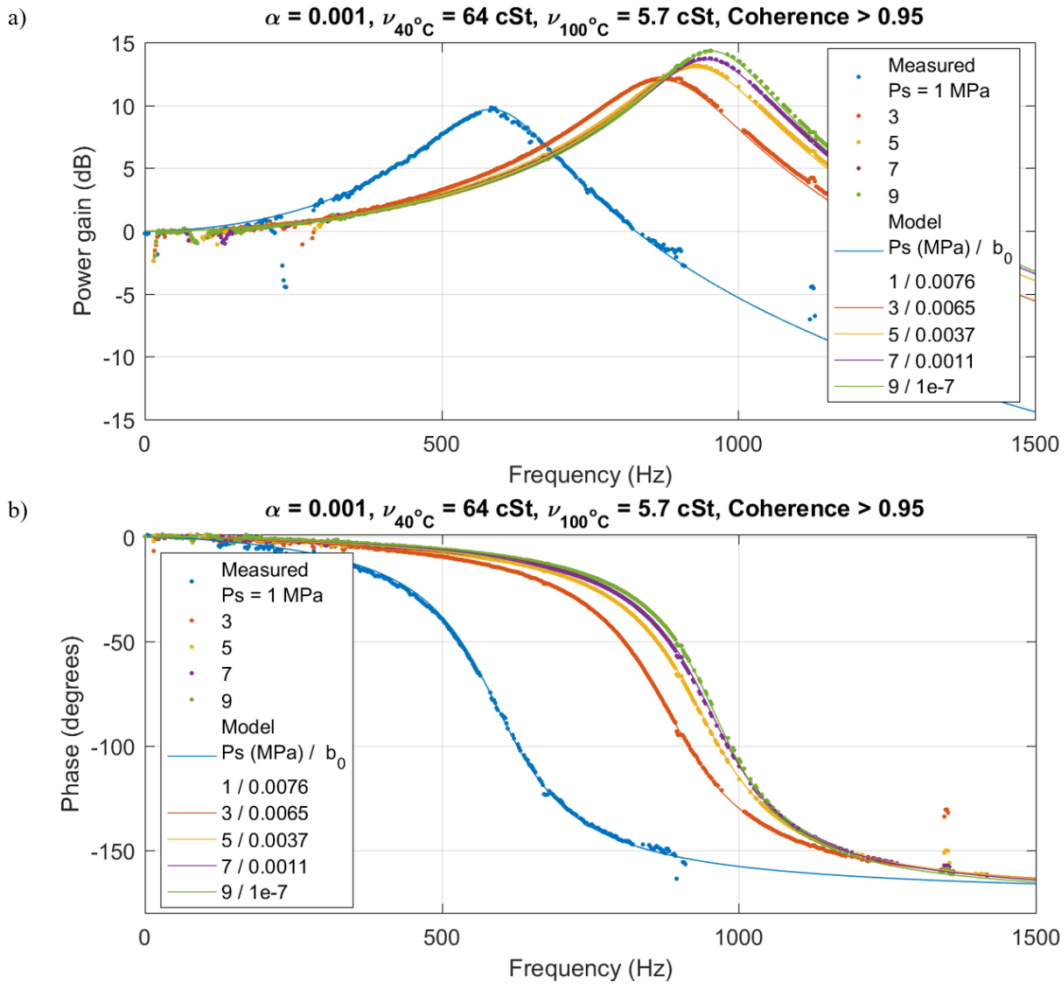

Figure 3.12: Semi-filled test body where measured cavity is compared to pressure within pipe for multiple static pressure levels: a) power gain and b) phase difference. Model uses the labelled initial air fraction values, b_0, as shown, where the trapped air decreases with each successive test.

3.3.2 HPEH-HR results at low static pressure

The HPEH-HR body consists of the HPEH5-4 upper housing and a Helmholtz resonator (HR 900 Hz) bottom housing. A HPEH5-4 test (presented later in Section 3.4.2) at the same low static pressure levels was performed to determine a reasonable force shunt ratio-area ratio $\kappa\gamma$ value, which was found to be 3.6[1]. The measured peak normalized power for HPEH5-4 tests without force shunt preload was found to be 0.155 μW/kPa^2 at 150 and 180 Ω, as previously shown in Figure 2.18. As is seen in Figure 3.13, the measured peak normalized power for the HPEH-HR device at low static pressure is 0.24 μW/kPa^2 at 150 Ω, which is an increase of 55% as compared to HPEH5-4 results. The corresponding power measurements and model are shown in Figure 3.14, with peak power of 1.94 mW at 120 and 150 Ω from 94 kPa rms-pressure amplitude (averaged across all resistive load tests at given static pressure level).

[1] The $\kappa\gamma$ for these tests is lower than previous HPEH5-4 low pressure tests because unloaded Belleville springs were within the upper housing. The HPEH5-4 upper housing has the capability of employing a force shunt, and during the low static pressure tests, the Belleville springs were still within the device. The springs were not pre-loaded, and thus a minimum static pressure level was not required, however the area ratio and force shunt product ($\kappa\gamma$) is expected to be lower than both the area ratio alone (γ) and when the device is operating at higher static pressure levels. The Belleville springs are considered to have linear stiffness; however, when testing the piezoelectric stack on an Instron load frame machine, it was found that the stiffness of the stack increased with load, thus also increasing the force shunt ratio (κ). Therefore, the value of $\kappa\gamma$ is higher at elevated static pressure levels because the stack stiffness compared to the Belleville springs is greater.

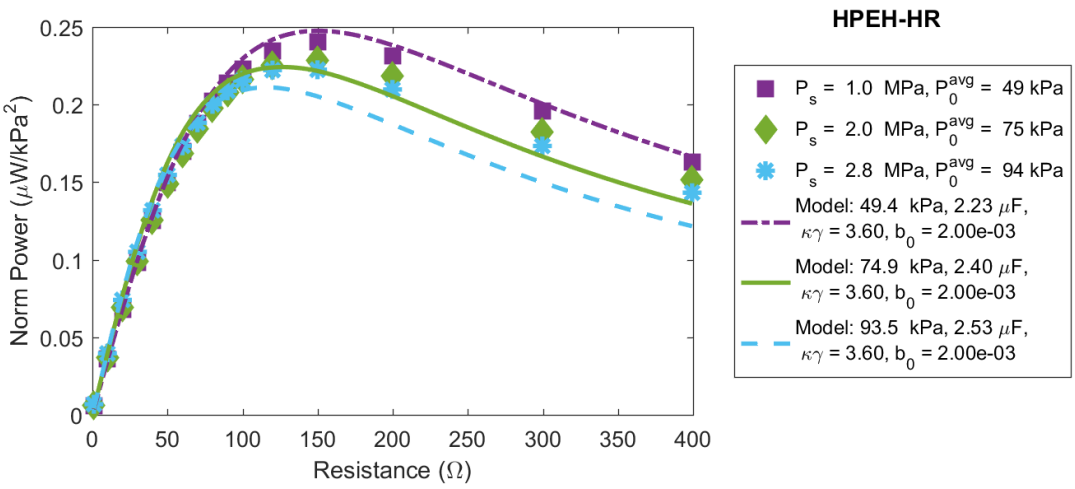

Figure 3.13: Normalized power of HPEH-HR tests at low static pressure levels.

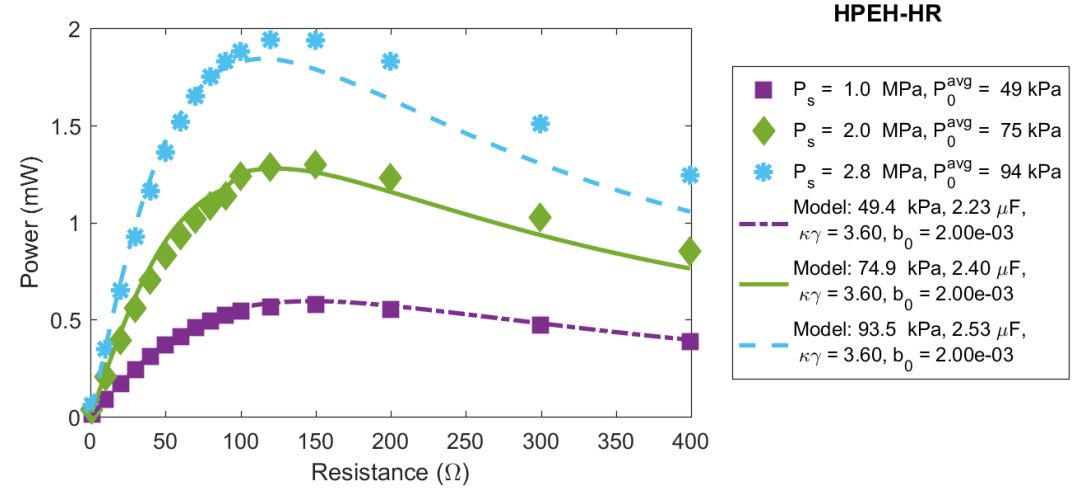

Figure 3.14: Power of HPEH-HR tests at low static pressure levels.

The optimal resistive load for a resistive-only circuit (recall $R_{l,opt} = 1/(\omega C_p)$ where ω is the radial frequency of the dominant pressure component) for a capacitance of 2.53 µF and frequency of 450 Hz is 140Ω, which is between the two peak measured power responses. This is accurate to predictions from analyzing the weighted pressure-frequency gain for resistive-only circuit, $W_{R_{opt}}$, as shown in Figure 3.15. The top set of graphs show the weighted response with respect to the pressure measured within the system flow (pipe

reference), and the bottom set show the response with respect to the modeled pressure within the HR cavity. The weighted response with respect to the cavity pressure (bottom graphs) indicate that the peak power can be obtained from 450 Hz frequency band for a resistive only circuit; if any peak in the bottom set of graphs had been above one, then that would indicate a higher power potential. The weighted response with respect to the measured pressure within the system flow (top graphs) indicate that the HR amplified power gain beyond what would be seen without an HR; if the values are below or equal to one, then it indicates that the power response at that frequency is less than or equal to the power response at 450 Hz without an HR. As is seen at 2.0 MPa and 2.8 MPa static pressure, the power potential of HPEH-HR at 900 Hz optimal resistance is greater than the response of HPEH5-4 at 450 Hz optimal resistance would be. Plus, the power potential at 450 Hz for each static pressure level was increased by the HR addition to the HPEH, as is seen by the greater than one values in the top graphs of Figure 3.15.

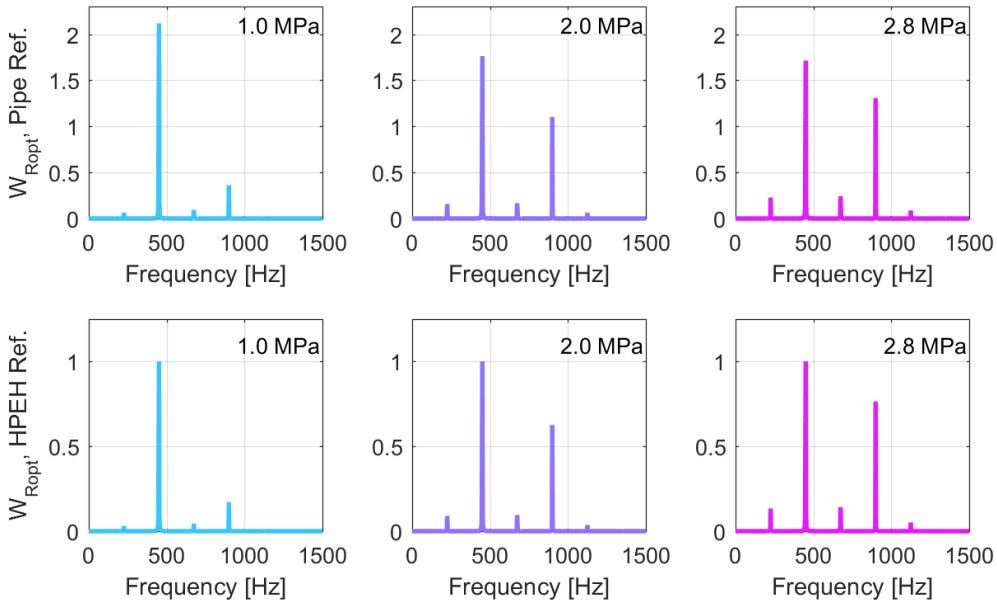

Figure 3.15: Weighted pressure-frequency gain modified for R_{opt} for HPEH-HR low static pressure tests (b_0 = 2e-3) comparing the weighted gain compared to the pressure at 450 Hz measured within the pipe (top) and within the cavity (bottom).

The HPEH-HR device at low static pressure does have resonance drift effects, as is indicated by the shift in the weighted pressure-frequency gain for resistive-only circuit in Figure 3.15. The modeled power gain for the estimated initial air fraction for each static pressure level and measured temperature level is shown in Figure 3.16. As is seen, the resonant frequency for 2.0 and 2.8 MPa tests is near 900 Hz, however the trapped air caused the 1.0 MPa test to shift toward 775 Hz; this shift also caused the power gain at 450 Hz to increase more.

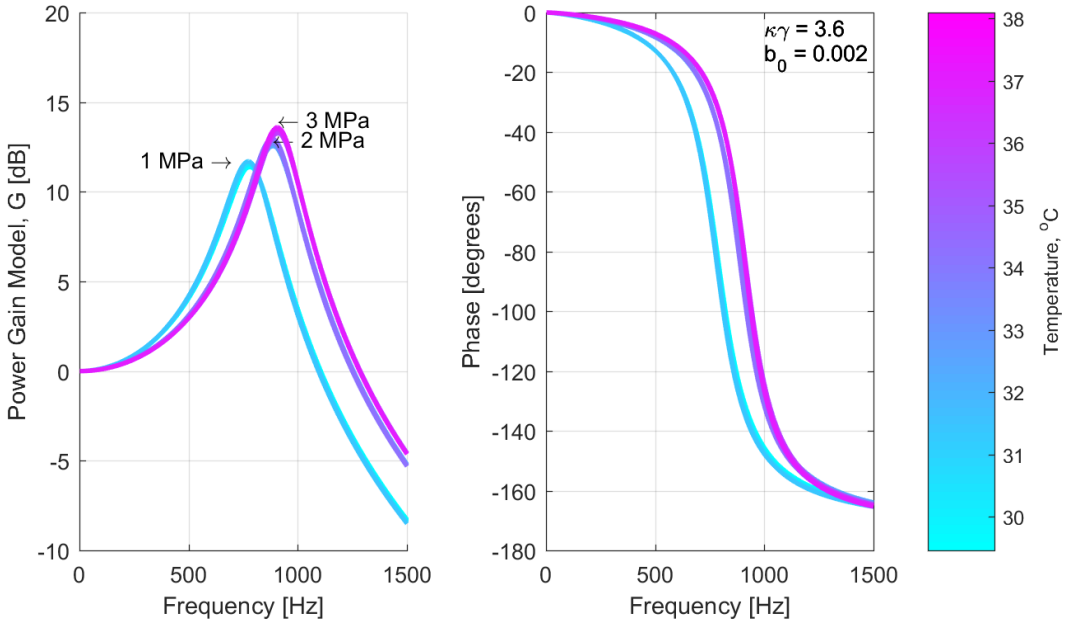

Figure 3.16: HPEH-HR low static pressure test modeled power gain and phase difference.

3.3.3 HPEH-HR results at high static pressure (with force shunt)

The HPEH-HR was tested using a force shunt at three static pressure levels above 5 MPa. First HPEH5-4 with force shunt was tested at the same static pressure levels to determine a reasonable force shunt ratio-area ratio $\kappa\gamma$ value of 4.35; the normalized power results are shown in Figure 3.17 with a peak measured value of 0.1456 μW/kPa^2. The measured and modeled normalized power for HPEH-HR with force shunt test with the same force shunt ratio-area ratio $\kappa\gamma$ value is in Figure 3.18. The HPEH-HR device was tested on a different day than the HPEH5-4 tests; in addition, the test at 7.2 MPa was measured on a different day than the tests at 5.9 and 6.6 MPa, which accounts for the air fraction change in the model. The HPEH-HR device doubled the normalized power result to 0.3133 μW/kPa^2 at 100 Ω.

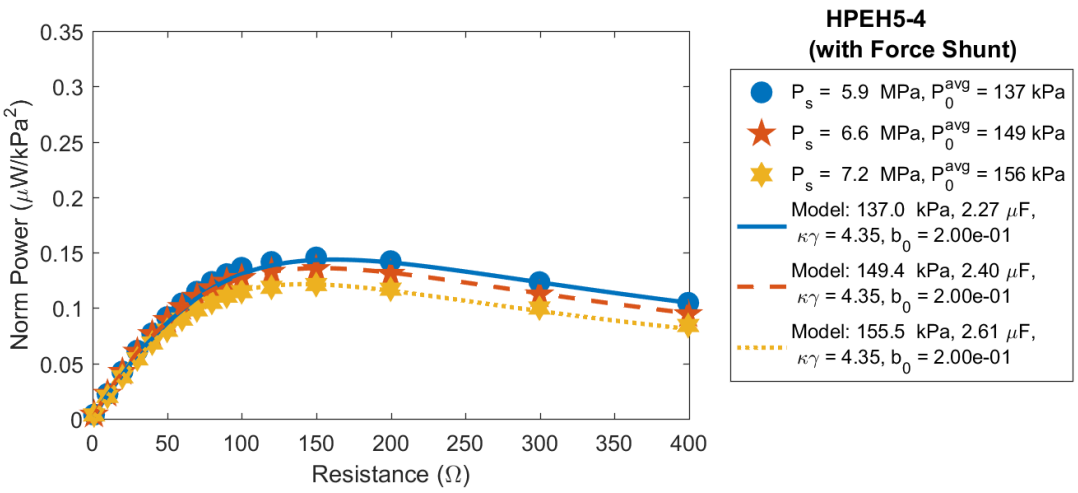

Figure 3.17: Normalized power for HPEH5-4 with force shunt for three static pressure levels.

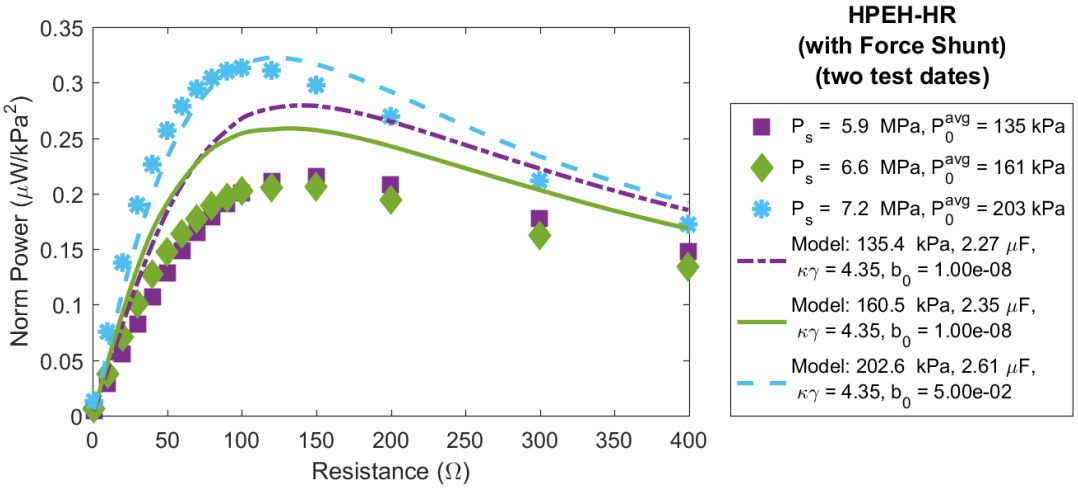

Figure 3.18: Normalized power for HPEH-HR with force shunt for three static pressure levels (from two test dates, where static pressure tests of 5.9 and 6.6 MPa were taken on a separate day than 7.2 MPa tests).

The model shown in Figure 3.18 overpredicts the measured data, however the force shunt used within HPEH5-4 and HPEH-HR was disassembled between the different test days. All HPEH5-4 tests were performed in a row; on a separate occasion, HPEH-HR tests at 5.9 and 6.6 MPa tests were performed; on a third occasion, HPEH-HR tests at 7.2 MPa was performed[2]. When assembling the force shunt, a torque wrench is used to estimate the initial force applied, however it is not precise and cause the amount of static pressure

[2] Tests were performed on separate occasions due to experimental error.

applied to the piezoelectric stack to vary. This would cause the $\kappa\gamma$ value to change. The model shown in Figure 3.19 shows a more accurate model of the normalized power results, where the $\kappa\gamma$ values have been changed to 3.90 for the 5.9 and 6.6 MPa tests, and to 4.45 for the 7.2 MPa tests.

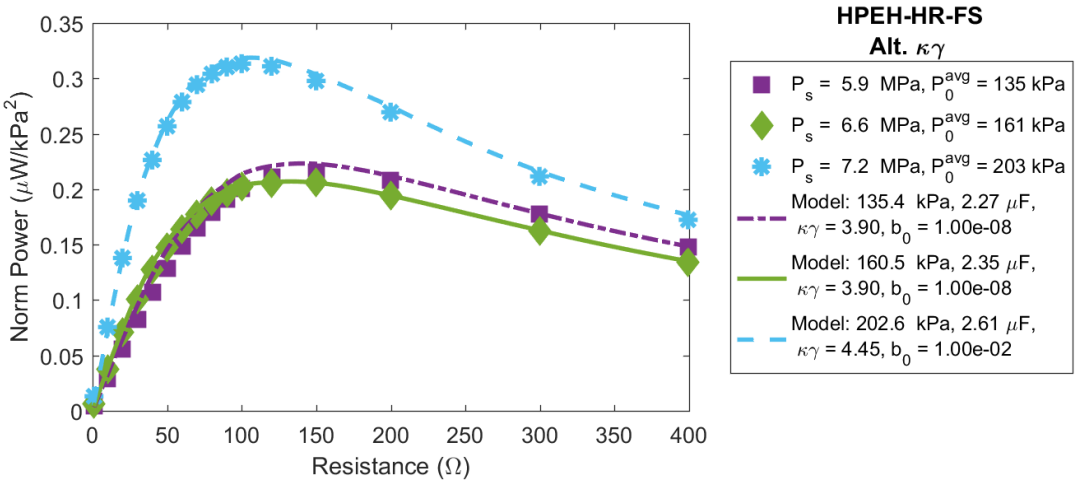

Figure 3.19: Normalized power for HPEH-HR with force shunt for three static pressure levels with force shunt-area ratio modified (from two test dates, where static pressure tests of 5.9 and 6.6 MPa were taken on a separate day than 7.2 MPa tests; all taken on a different day than HPEH5-4-FS tests).

Using the model parameters used in Figure 3.19, the weighted pressure-frequency gain for resistive-only circuit, $W_{R_{opt}}$, is modeled in Figure 3.20. For the first two static pressure levels, the dominant frequency band is 450 Hz, which provides an estimated optimal resistive load of 156 Ω and 150 Ω for the measured capacitance values. This matches with where the peak normalized power was measured, which was a resistive load of 150 Ω for both. The third static pressure level of 7.2 MPa has a dominant frequency band of both 450 Hz and 900 Hz; this corresponds to either an optimal resistive load of 135 Ω or 68 Ω, respectively. The average of the two optimal resistive loads is 102 Ω, which matches with the measured peak normalized power corresponding to 100 Ω. In addition, the normalized power raised by 30% over the other HPEH-HR measurements, showing

that pressure at 900 Hz (measured to be 15.27 kPa_{rms}) amplified by the HR combined with the pressure at 450 Hz (measured to be 140.2 kPa_{rms}) enhance the power potential of HPEH devices.

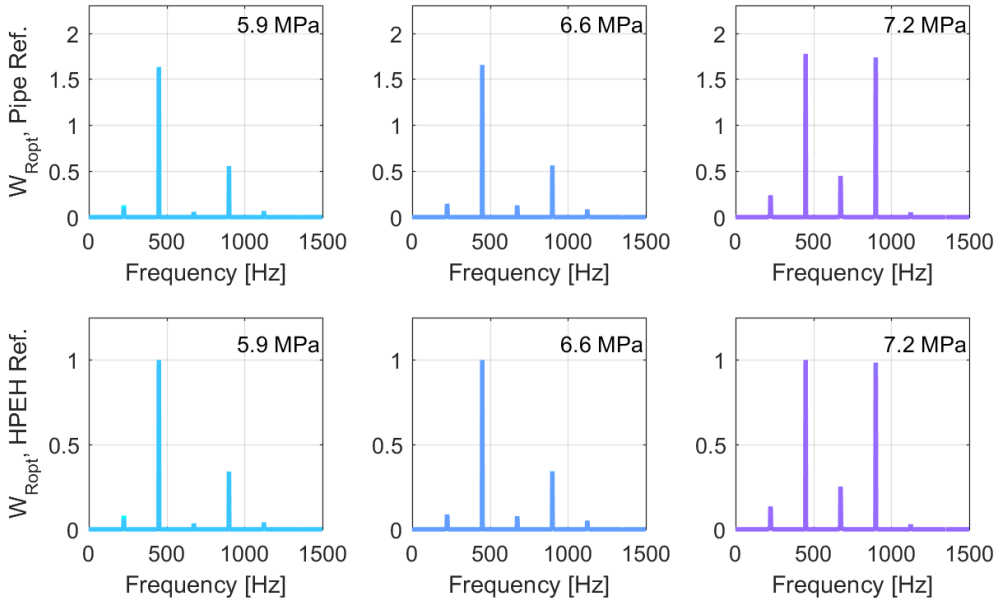

Figure 3.20: Weighted pressure-frequency gain modified for R_{opt} for HPEH-HR with force shunt (5.9 MPa, $\kappa\gamma$ = 3.9, b_0 = 1e-8; 6.6 MPa, $\kappa\gamma$ = 3.9, b_0 = 1e-8; 7.2 MPa, $\kappa\gamma$ = 4.45, b_0 = 1e-2) comparing the weighted gain compared to the pressure at 450 Hz measured within the pipe (top) and within the cavity (bottom).

One reason the HPEH-HR device amplifies the 900 Hz band more for the 7.2 MPa tests rather than the 5.9 and 6.6 MPa cases is because of increased oil temperature. The measured pressure amplitudes for 5.9, 6.6, and 7.2 MPa tests at 900 Hz are 13.6, 12.3, and 15.3 kPa_{rms}, respectively, which does not fully account for the weighted pressure-frequency gain. The HR model for the HPEH-HR with force shunt tests is shown in Figure 3.21, where the temperature of the oil is indicated by color. As the temperature of the oil increases, the power gain increases and the resonant frequency decreases. The power gains for 5.9 and 6.6 MPa at 900 Hz are 13.3 and 14.9 dB, respectively; the power gain for 7.2 MPa tests at 900 Hz is 18.1 dB.

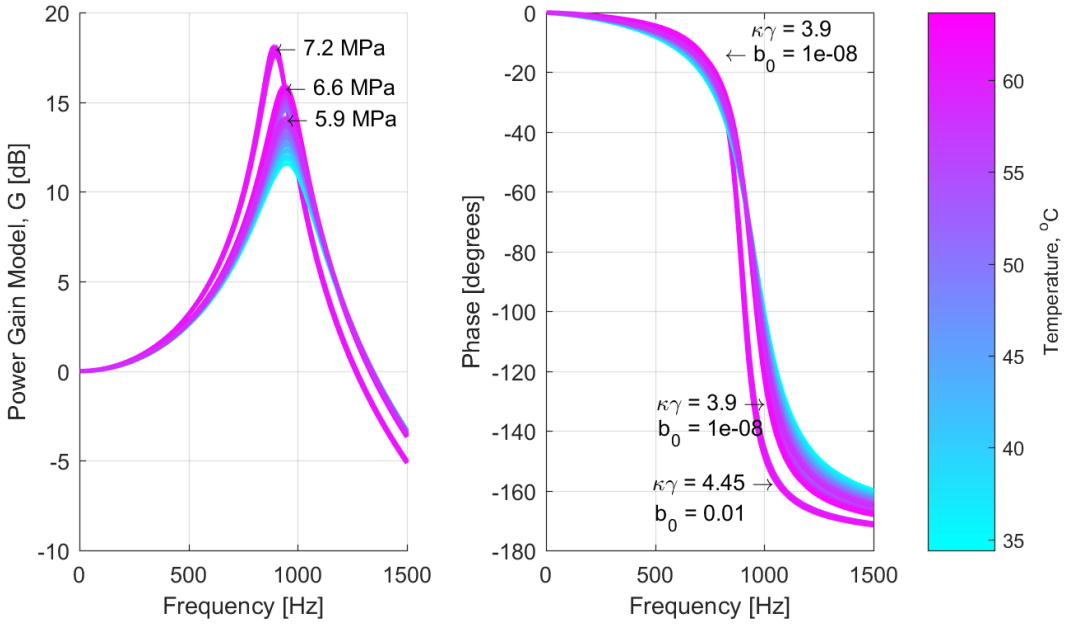

Figure 3.21: HPEH-HR high static pressure test modeled power gain and phase difference.

The measured power and modeled results for the HPEH-HR at high static pressure are shown in Figure 3.22. The peak power measured is 12.8 mW at 100 Ω from 202.6 kPa rms-pressure amplitude (averaged across all resistive load tests at given static pressure level). This is 88% higher than a HPEH5-4 test with similar dynamic pressure levels (see Figure 2.20, which has 6.8 mW at 150 Ω from 201.5 kPa rms-pressure amplitude).

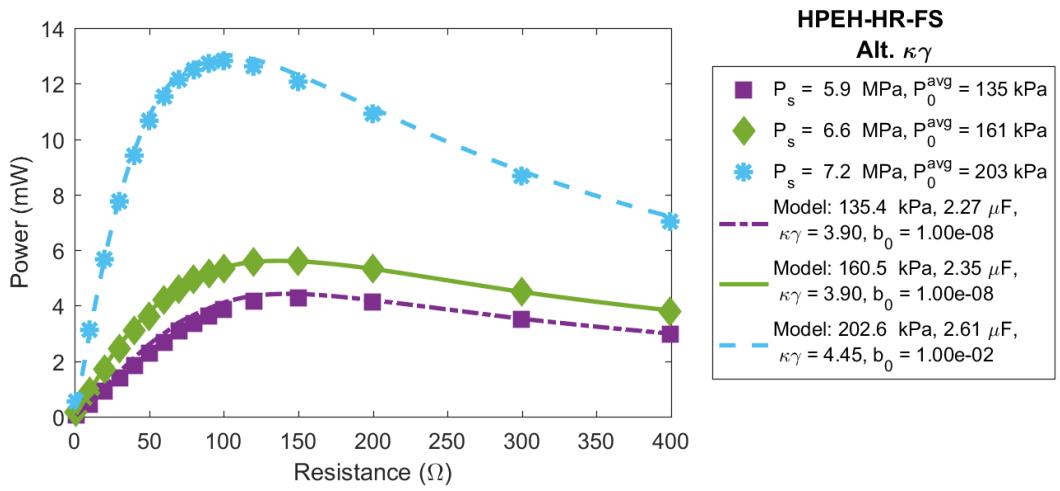

Figure 3.22: Power for HPEH-HR with force shunt for three static pressure levels (from two test dates, where static pressure tests of 5.9 and 6.6 MPa were taken on a separate day than 7.2 MPa tests).

3.4 Discussion

The HPEH-HR tests correspond well with the model presented and is able to increase HPEH efficiency, however choosing an appropriate HR design and knowing when HR characteristics may be affecting HPEH results is important. The HR resonance may be lowered by decreasing the neck size or increasing the apparent volume by adding a compliant material such as presented in hydraulic noise control research [85, 89]. Also, HPEH5-4 contains an HR design, however the resonance is tuned to well above 5000 Hz when no trapped air is present. These issues are discussed in the following subsections.

3.4.1 Design considerations

The HPEH-HR design used had a resonance frequency at over twice the dominant system frequencies, however another design with a lower resonant frequency was investigated. The HR 600 Hz design (as specified in Table 4) includes a narrower neck in order to lower the resonance frequency to near 600 Hz. The tests consisted of the same procedure described in the model validation Section 3.3.1. The measured pressure gain,

phase difference, and corresponding model are shown in Figure 3.23. While the narrow neck viscous losses rarely impeded the HPEH-HR design using HR 900 Hz, the HR 600 Hz design meets this condition as high as 168 Hz. For this body, the power gain measured at 450 Hz is 4.7 dB for the 9 MPa static pressure for trapped air fraction of 5e-4, which is greater than the 2.1 dB gain at 450 Hz from the HPEH-HR design. However, as the static pressure level decreases, the power gain decreases to the point that at 1 MPa, the measured power gain is 0 dB. In addition, an HR on a HPEH acts as a low pass filter, meaning any energy at higher frequencies within the system would be lost.

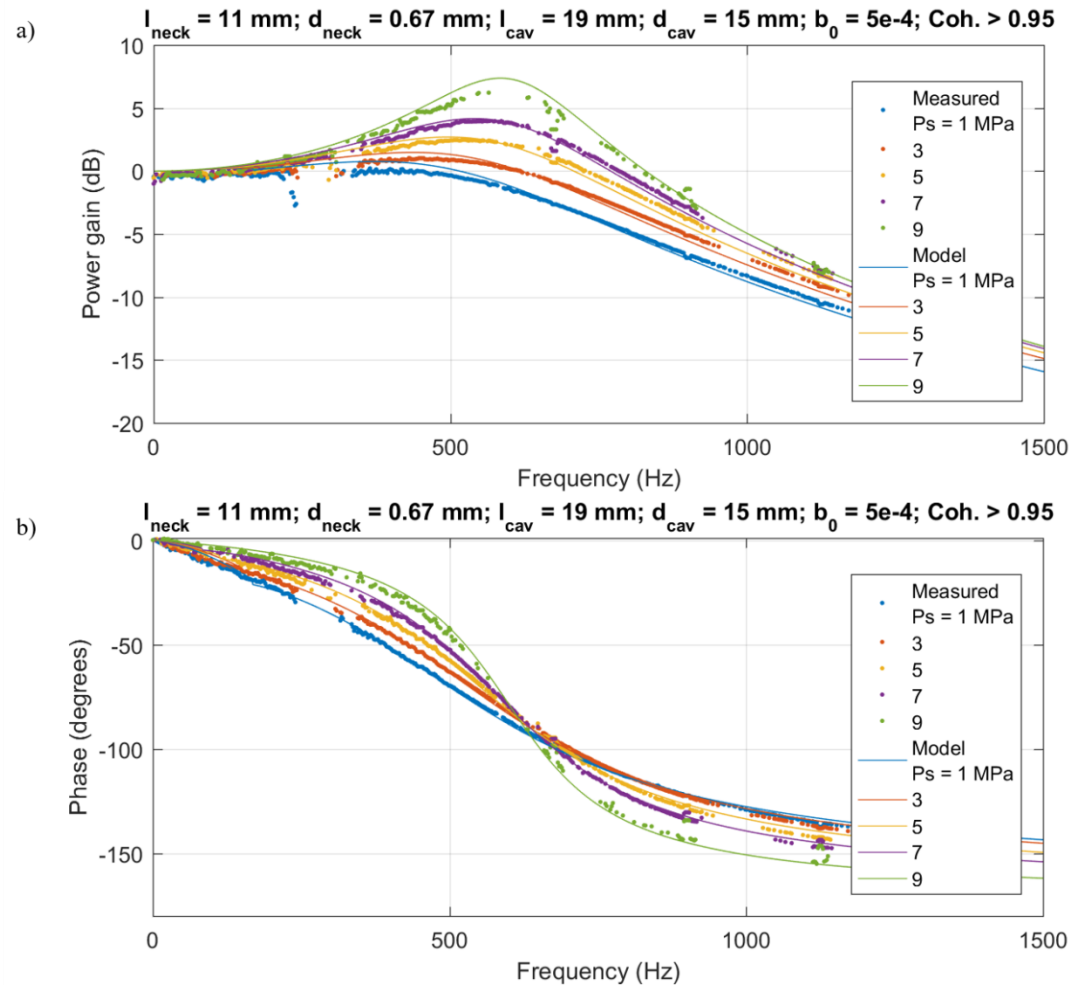

Figure 3.23: Alternative HR design with narrower neck diameter and target frequency of near 600 Hz, where viscous boundary layer causes additional damping; air fraction level of 5e-4 for all pressures in model.

Another design considered is to increase the apparent cavity volume by employing a syntactic foam, as described by Earnhart and Gruber [87, 88]. By incorporating a syntactic foam, the compliance within the cavity increases, and thus the resonant frequency will reduce. This was performed with the HR 600 Hz design using the syntactic foam GR9-625 described in [87]. The measured power gain, phase difference, and calculated model are shown in Figure 3.24. The foam dimensions are: 14.9 mm outer diameter, 10.5 mm inner diameter, and 20.3 mm height. The corresponding air fraction volume is shown within the legend for a given static pressure modeled. The foam volume was chosen as it

was expected to correspond to a resonant frequency of 450 Hz. The peak power gain measured at 450 Hz occurred at the highest static pressure measured (10 MPa, not pictured) with a value of 3.29 dB. As can be seen by the measured data, the added compliance caused the dynamic pressure within the cavity to decrease for static pressures below 8 MPa.

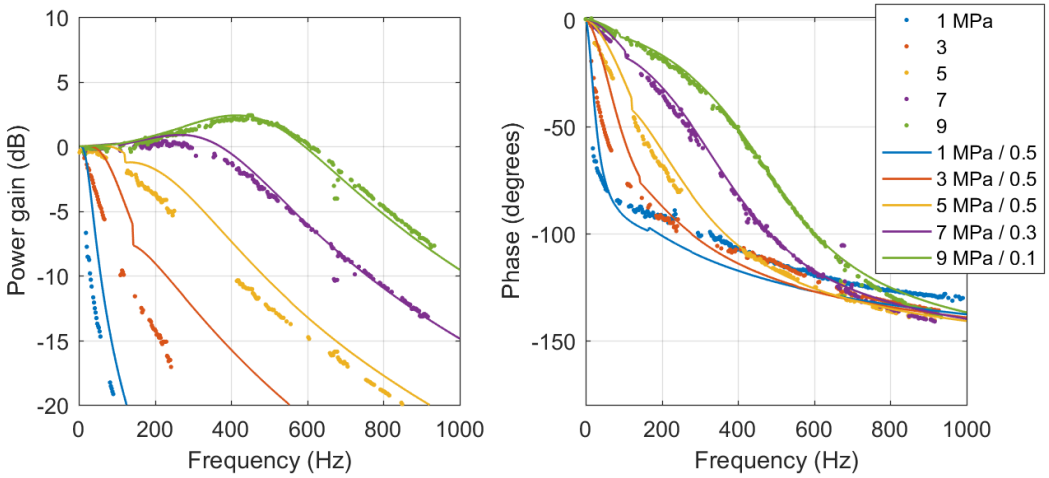

Figure 3.24: HR 600 Hz design with syntactic foam within cavity (using GR9-625 from Earnhart [87]) with initial air fraction listed in the legend for a) power gain and b) phase; foam dimensions: outer diameter – 14.9 mm, inner diameter – 10.5 mm, length – 20.3 mm.

A challenge of designing a HPEH-HR with a syntactic foam is that the foam used has different compliance at different static pressures, creating resonance drift as seen with trapped air. The benefit of syntactic foam is that change with respect to static pressure can be modeled and pre-determined for a given design. This may prove useful for future HPEH-HR designs if the device is expected to be in an environment with relatively constant static pressure levels.

3.4.2 Resonance drift due to trapped air compliance

The HPEH5-4 bottom housing is also a Helmholtz resonator, but the cavity was not prefilled during testing because the resonance (when filled with oil) is over 5000 Hz. For elevated static pressures, neglecting the HR effects despite not prefilling the cavity is

acceptable, as demonstrated in Figure 3.25. The HPEH5-4 bottom housing is modeled with an initial air fraction level of 0.99, but the resonance is still well over 1000 Hz. At lower static pressure levels, the trapped air can provide enough compliance to lower the resonant frequency to below 450 Hz. This was an unintended testing error, as at low static pressures with significant air fraction levels, the resonance can drop below the second pump harmonic.

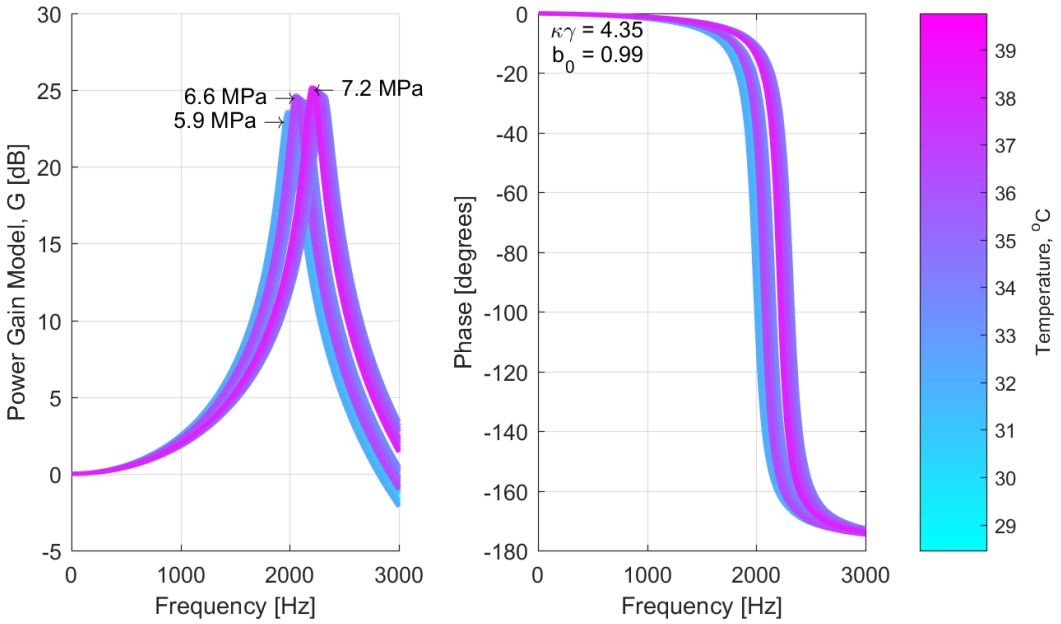

Figure 3.25: HPEH5-4 Helmholtz resonator model at elevated static pressure levels with 99% cavity volume composed of air.

To demonstrate this point, the normalized power results measured using HPEH5-4 at low static pressures are shown in Figure 3.26. In Figure 3.26a, the model uses high assumed air fraction levels and a lower force shunt-area ratio. In Figure 3.26b, the model assumes no air fraction level and a higher force shunt-area ratio. The model corresponds very well when incorporating the air fraction; however, when excluding the air fraction, the model only matches for the static pressure levels at 2.0 and 2.8 MPa.

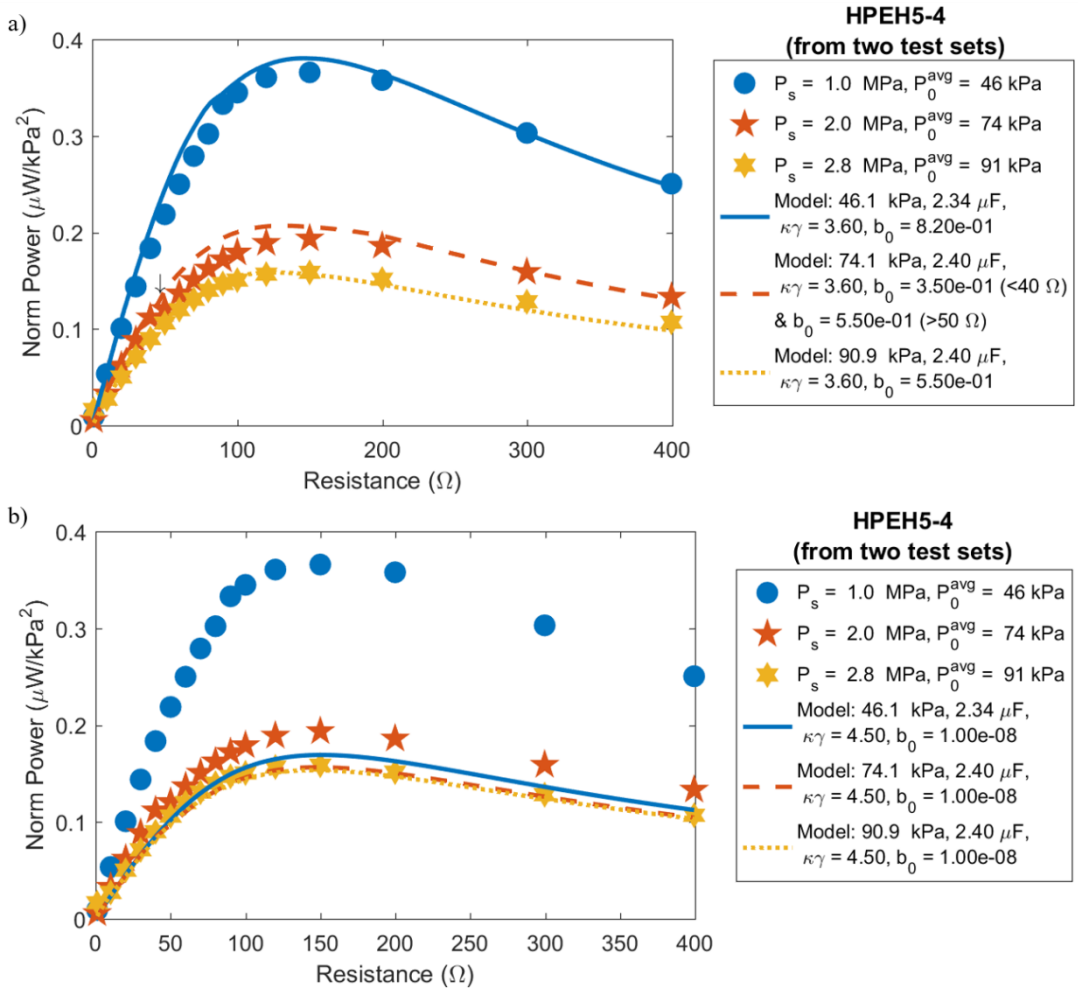

Figure 3.26: HPEH5-4 normalized power test versus modeled results at low static pressure level for a) including air fraction and b) no air fraction. Arrow indicates location of test date change in a).

At the static pressure level of 1 MPa, the air fraction level is expected to be higher as it was the first test set performed. This caused the power gain at 450 Hz to increase drastically, as shown in Figure 3.27. Also, the normalized power for 1 MPa was measured to be 0.3658 μW/kPa^2 at 150 Ω, which initially gives the impression that HPEH5-4 performs better than a HPEH device with a Helmholtz resonator. In fact, the reason HPEH5-4 reported a higher normalized pressure is due to unrecognized Helmholtz resonator effects within HPEH5-4 itself.

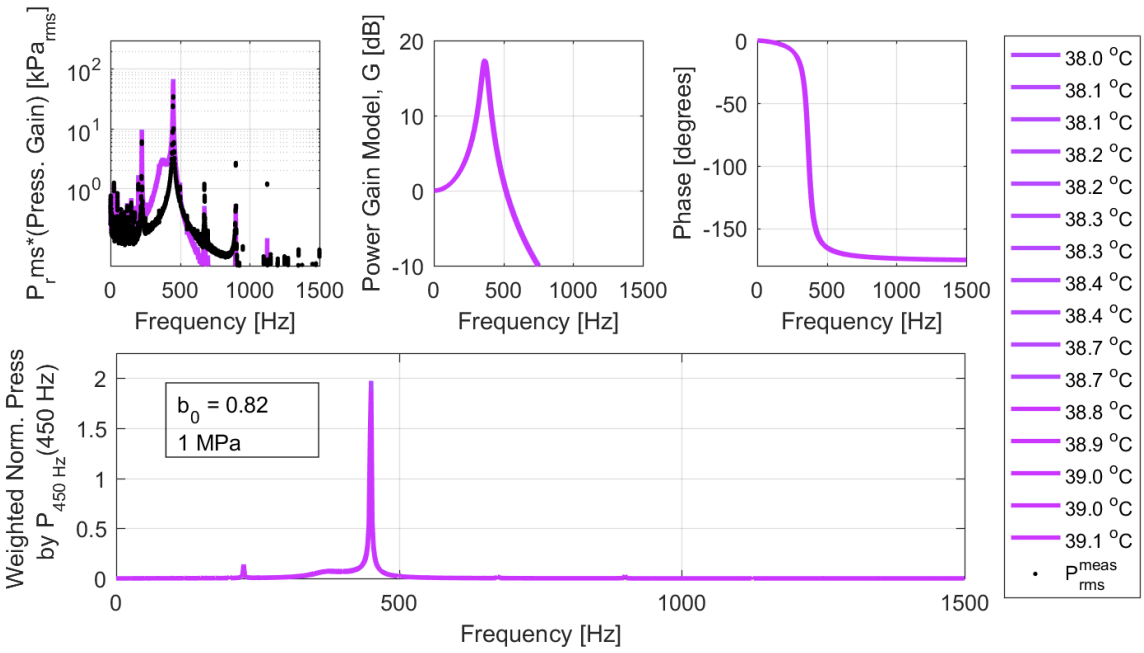

Figure 3.27: HPEH5-4 model with air fraction of 0.82 and static pressure of 1 MPa comparing the modeled cavity frequency spectrum, power gain, and weighted gain compared to the pressure at 450 Hz measured within the pipe.

The modeled HPEH5-4 bottom housing Helmholtz resonator effects are shown in Figure 3.28, where a) contains the model with initial air fraction levels, and b) contains the model without any air fraction. Note the x-axis contains different scales for these graphs. The HPEH5-4 bottom housing does not add to the power gain of the dominant frequencies when air is not trapped within the cavity, even at low static pressures. However, even for an HR designed to resonate well above dominant frequency levels, if air is trapped within the cavity, it will affect the pressure amplitudes seen by the HPEH device at low static pressure levels. Resonance drift due to unintended compliance can greatly impact the performance of HPEH devices with Helmholtz resonators.

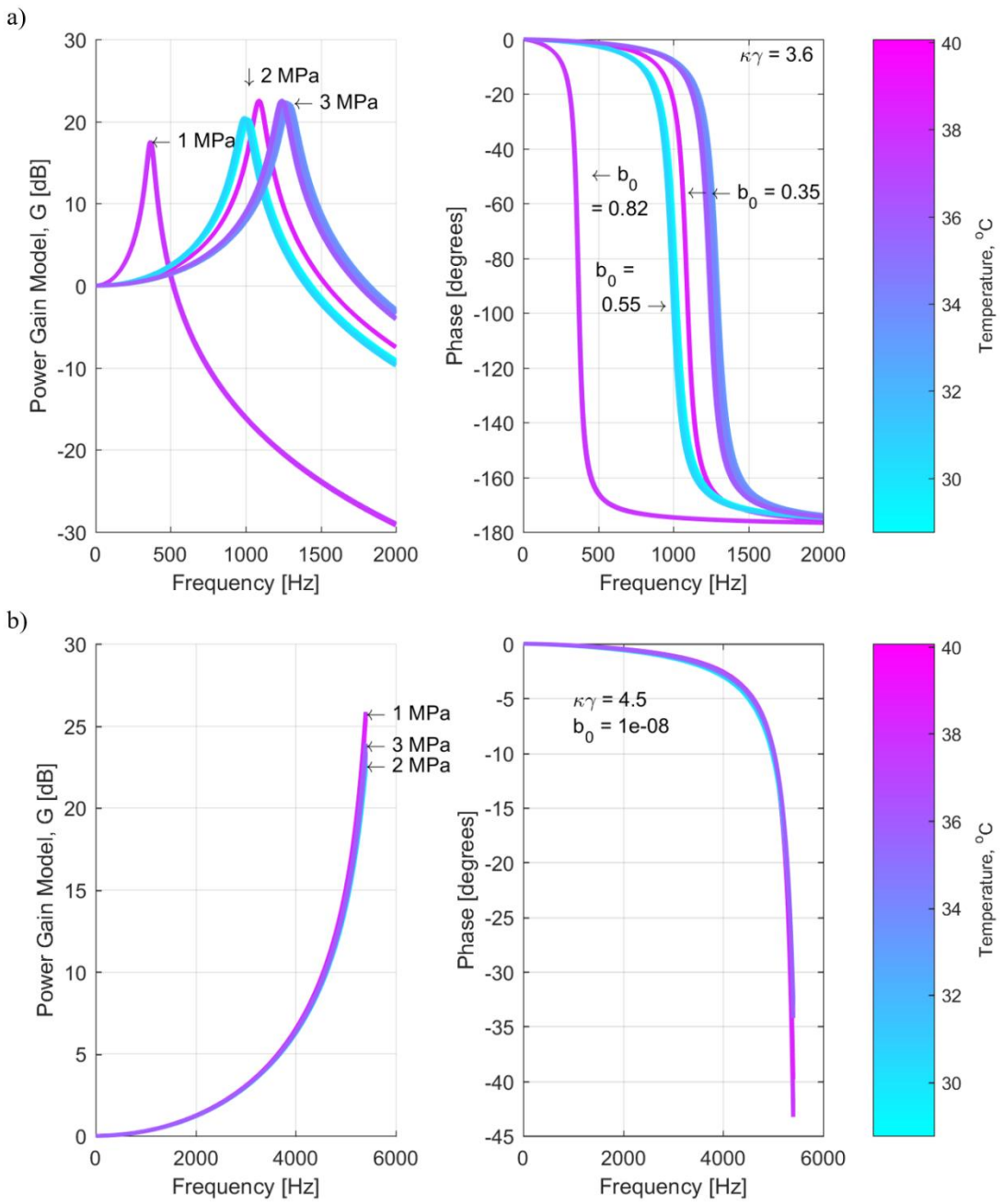

Figure 3.28: HPEH5-4 Helmholtz resonator model at low static pressure levels for a) including air fraction and b) no air fraction.

3.5 Conclusions

This chapter presents a detailed analysis of how incorporating a Helmholtz resonator (HR) in an acoustic energy harvester on hydraulic rig can be both beneficial and detrimental, depending on design and compliance contained within the cavity. Multiple

acoustic resistance models due to viscous losses within the narrow neck are explored. The HPEH-HR device provided measured an 88% power increase over similar pressure ripple measurements, and doubled the normalized power. Future work may include measuring HPEH-HR performance with a resonant electrical circuit. Syntactic foam was incorporated in a HR test body, with measured and modeled results presented, however no specific inserts were made for HPEH-HR. In addition, the foam used changed drastically with static pressure and appeared to inhibit area amplification and fluid flow into the cavity of devices tested, thus decreasing overall power performance. A more purposeful design employing syntactic foam may be pursued as future work. Also, alternative HR designs to incorporate increased apparent mass within the neck may be possible within hydraulic systems.

CHAPTER 4

MATERIAL SELECTION

While PZT piezoelectric stacks are mass produced and can immediately be implemented into hydraulic pressure energy harvester (HPEH) devices with little concern for damaging the piezoelectric material below certain stress levels, these stacks may have a lower power potential compared to piezoelectric material composition and design developments in more recent research. Research in piezoelectric materials has provided more suitable solutions for the high pressure environment found in hydraulic systems, which can reach up to 35 MPa. This chapter explores initial results of using a relaxor-PT based material that goes through a crystalline structure phase change when subjected to high stress cycles.

4.1 Piezoelectric material under high stress and energy harvesting suitability

The choice of piezoelectric material is essential to the power response, electromechanical model, and the integrity of the electromechanical conversion efficiency. The linear piezoelectric constitutive equations are typically valid for low excitation levels, excitation far from resonance, and low pre-compressive stress and electric field levels [59]. While HPEH devices operate far from material resonance, the pre-compressive stresses caused by the static pressure can be high, especially if area amplification of the interface is included in the HPEH. The high stresses may invalidate the modeling assumptions made in Chapter 2. As discussed earlier, Schäufele and Härdtl reported the transition to nonlinear depolarization behavior in soft PZT can occur from compressive stress levels as low as -20 MPa, whereas hard PZT does not experience this transition until -60 MPa [72]. A partial

or full depolarization of that material reduces the conversion efficiency of the device, as demonstrated earlier by HPEH4-1 in Figure 2.15.

It has been shown that nonlinearities can occur when these transitional stress levels are exceeded [98]. Cao and Evans [73] observed that when a piezoelectric element undergoes high compressive stress levels, the linear constitutive equations are no longer valid. Krueger [71] and Zhang et al. [76] present the change of piezoelectric parameters (such as piezoelectric strain constant and permittivity) when undergoing high stresses. If the piezoelectric element is exposed to an exceedingly high stress for a period of time, then depolarization of the piezoelectric material may occur. In addition to the potential response change, the selection of the piezoelectric material changes the HPEH conversion efficiency. While the conversion efficiency of soft PZT material is higher than that of hard PZT, the allowable stresses on the material are typically lower. It is therefore prudent to consider the piezoelectric material selected for the high stress environment of HPEH devices.

Research has shown that domain engineered relaxor ferroelectrics undergoing crystalline phase transformation have high efficiency energy conversion [99-105]. First, relaxor-PT based material research as related to phase transition points near stress and temperature conditions found within hydraulic systems is reviewed. Next, the use of these materials within HPEH devices is compared to PZT piezoelectric stack results used within HPEH devices.

4.1.1 Phase transition point with respect to temperature and stress

As presented by Gallagher, et al. [103] and later expanded upon by Dong [106], [011] cut PIN-PMN-PT materials go through a ferroelectric rhombohedral (FER) to

ferroelectric orthorhombic (FEO) phase transition. As shown in Figure 4.1 (extracted from [106]), the [011] cut PIN-PMN-PT crystal with force applied in x_2 direction has a phase transformation transition point that changes with temperature, stress (σ_{22}), and electric field (E_3). The transition exhibits steep strain and polarization jumps during the transition, and thus harvesting the energy during an FER-FEO-FER transition is much larger than obtained via a linear piezoelectric effect [102, 107]. However, in order to benefit from the high power per cycle phase transition point within an HPEH, it is necessary to know what temperature range a hydraulic system operates.

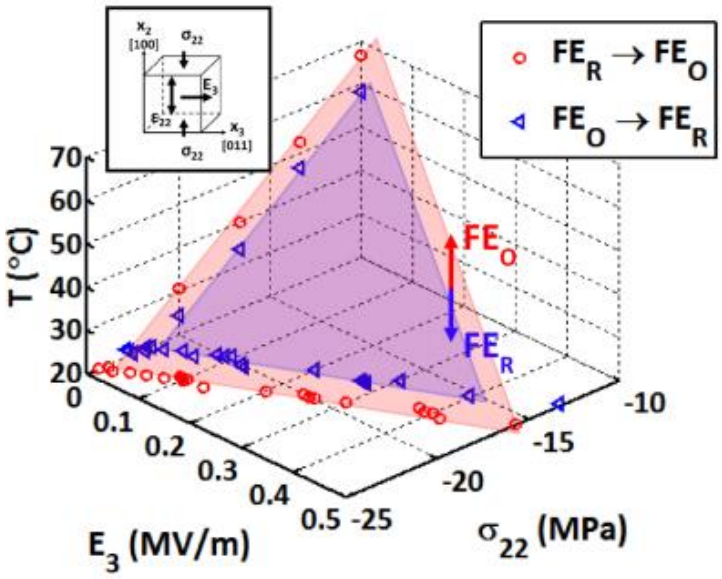

Figure 4.1: Phase transformation locations between ferroelectric orthorhombic and ferroelectric rhombohedral crystal structures, published by Dong 2015, Figure 3-7b [106].

For the initial HPEH design, it is assumed that an electric field will not be applied, however the system static pressure and fluid temperature will cause changes in the crystal stress and temperature. Safe operating temperatures of hydraulic systems depends on the oil type and viscosity, however sealing components tend to become damaged at or above 82°C [108]. Therefore, the range of temperatures of a hydraulic system are not expected to

range outside of -40°C to 82°C. Using published results from Gallagher et al. [103] for a [011] cut PIN(0.24)-PMN-PT, the FER-FEO transition points and FEO-FER transition points with respect to stress and temperature have been calculated, as shown in Figure 4.2. The approximate temperature range for tests shown in this chapter is shown in the callout figures. The specimens tested did not indicate PT% levels, however based on results, it is expected that the specimens are either 0.24PIN-0.44PMN-0.32PT or between that and 0.24PIN-0.46PMN-0.30PT. As the temperature increases, the required absolute value of the compressional stress for a transitional phase change decreases. This corresponds to a decrease in required system pressure, where the material stress is related to the system pressure via the area ratio and force shunt conditions of the HPEH device. In addition, as the temperature increases, the peak to peak dynamic stress needed for full phase transition between FER to FEO to FER decreases.

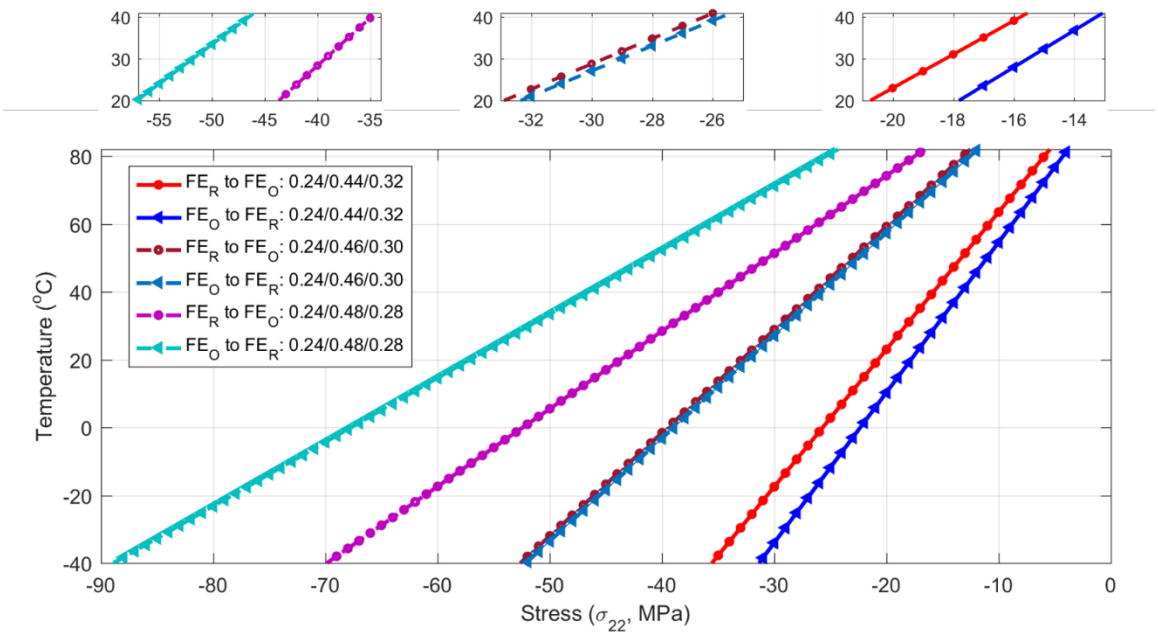

Figure 4.2: Phase transition points for [011] cut PIN24-PMN-PT based on results presented by Gallagher, et al. [103] for the expected temperature range of hydraulic systems; the temperature range of the hydraulic system used for tests presented in this chapter are shown in the callouts; based on data obtained, it is assumed that the specimens tested are either 0.24PIN-0.44PMN-0.32PT or between that and 0.24PIN-0.46PMN-0.30PT.

This phase transition also occurs in PMN-PT materials, as discussed by McLaughlin, et al. [99, 100], which is the material utilized in HPEH6-2. As before, the phase transition point is dependent on temperature, and as the temperature increases, the required system pressure for favorable stress transition decreases. Based on work by McLaughlin et al. for PMN-PT in 33-mode [100], at 40°C the compressive stress levels of about -7 to -18 MPa will be between the phase transition points; at 20°C, the phase transition starts at about -14 MPa and completing around -22 MPa. Note, this work uses the sign convention of compressive stress being negative and tensile stress being positive.

HPEH6-2 was designed specifically for low system pressures, with a designed area ratio of 14 and no force shunt. The device was tested near 1 MPa system pressure (not exceeding 1.25 MPa), which corresponds to compressive stress levels within the piezoelectric near -14 MPa. Therefore, for tests occurring at about 40°C, it is expected that

the material is near or between phase transformation points, meaning the expected power produced per cycle is higher than for tests performed at lower temperatures. This is confirmed by the test results shown in Figure 4.3. The figure shows results for resistive only circuits and resistive-inductive load circuits, with the legend indicating the order of the tests. Based on similar tests measuring oil temperature while performing the same circuit conditions, it is expected the temperature increased from room temperature (22 ^{o}C) by 0.2^{o}C or less during each sweep. After the low temperature tests, the hydraulic rig was allowed to run until it reach near 40^{o}C for the final two tests; the final temperature measured was 41^{o}C. Note, the piezoelectric material is assumed to be approximately the same temperature as the oil, as it is encased in a metal housing which was measured using an infrared thermometer to be within a few degrees of the measured oil temperature. The root-mean-square dynamic pressure for the first five tests (low temperature) measured average was 31.2 +/- 0.2 kPa, and for the last two tests (high temperature) was 25.1 +/- 0.2 kPa.

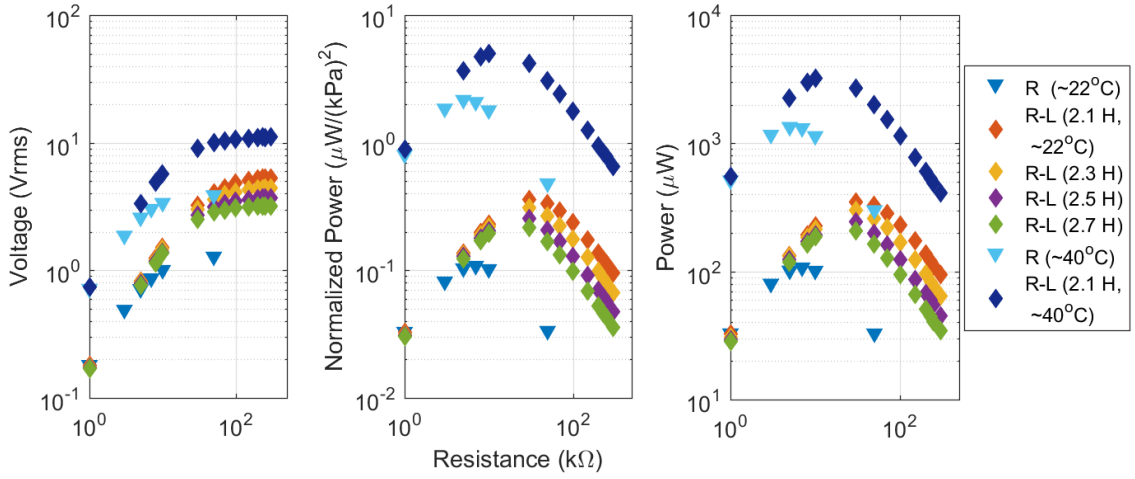

Figure 4.3: HPEH6-2 test results for P_s=1 – 1.25 MPa with resistive load only (R) and parallel resistive and inductive loads (R-L) circuits; hydraulic system was allowed to run in order to increase oil temperature for last two test; legend indicates order of tests; volume of PMN-PT 20-layer stack is 0.294 cm^3, providing peak measured volume and pressure normalized power of 17 µW/(kPa^2 cm^3).

The normalized power results for HPEH6-2 tests at 40°C performed an order of magnitude higher than the tests performed at lower temperatures, indicating the material was achieving partial phase transitions during the dynamic pressure oscillations. The peak power normalized by piezoelectric material volume and square pressure was 17 μW/(kPa^2 cm^3). In addition, the voltage levels of the HPEH device reach levels suitable for bridge rectification or other more advanced circuits, such as synchronized switch harvesting inductor circuits (SSHI) presented by Shu, et al. [109]. The design of HPEH6-2 limits the use to only hydraulic systems that are expected to have very low (~2 MPa) system pressure levels, such as fluid transport pipelines (e.g. water). These results indicate utilizing a relaxor-PT based material within an HPEH is conducive to high power per cycle. In addition, they show that the temperature of the fluid does affect the material response despite not being in direct contact with the fluid.

4.1.2 Comparing HPEH containing relaxor-PT piezoelectric materials versus PZT materials

As discussed in Section 2.2, one method to compare the material power performance of a HPEH device is by comparing the power performance at the optimal resistance load. For a resistive load only circuit, the power can be normalized by the volume of material if the optimal load resistance is used via

$$\frac{\Pi_{avg,l}\Big|_{R_l=R_l^{opt}}}{V_{stack}\left(\kappa\gamma P_{rms}\right)^2}=\frac{\omega\left(d_{33}^{i}\right)^2}{\varepsilon_{33}^{\sigma}} \tag{4.1}$$

where V_{stack} is the volume of piezoelectric material, κ is the force shunt ratio, and γ is the area ratio. This comparison between previous HPEH devices discussed in Chapter 2 and tests performed within this chapter is summarized in Figure 4.4, including tests using [011]

cut PIN-PMN-PT single crystal elements (shaker tests and HPEH7 results presented later) and the PMN-PT layered single crystal stack in HPEH6. To clearly distinguish the different materials in the results shown, note that the resistive loads used for the single crystal material tests are above 10^3 Ω, whereas the resistive loads for the soft PZT stack tests are below 10^3 Ω. In addition, Figure 4.5 compares the power performance of a given volume of piezoelectric material per applied force.

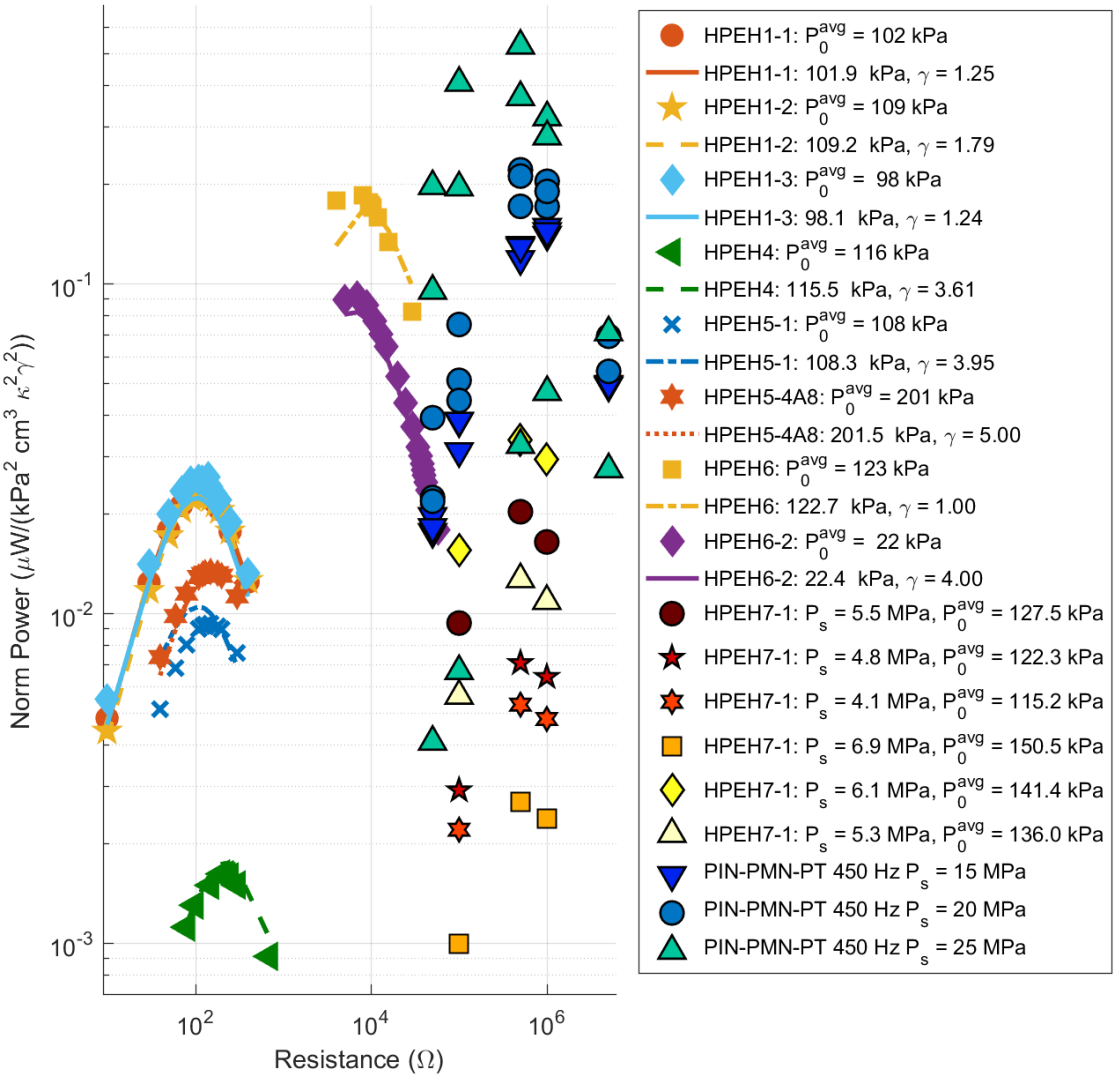

Figure 4.4: HPEH device performance normalized by volume and squared force, for resistive load circuit only. HPEH7-1 force input calculated using measured dynamic pressure amplitude, A_{stack} = 16 mm^2, γ = 11.4, and κ = 88.5%; order of HPEH7-1 tests. Tests labelled "PIN-PMN-PT" were performed using a shaker, where the dynamic and static force was measured directly and the pressure was calculated using the area of the single crystal.

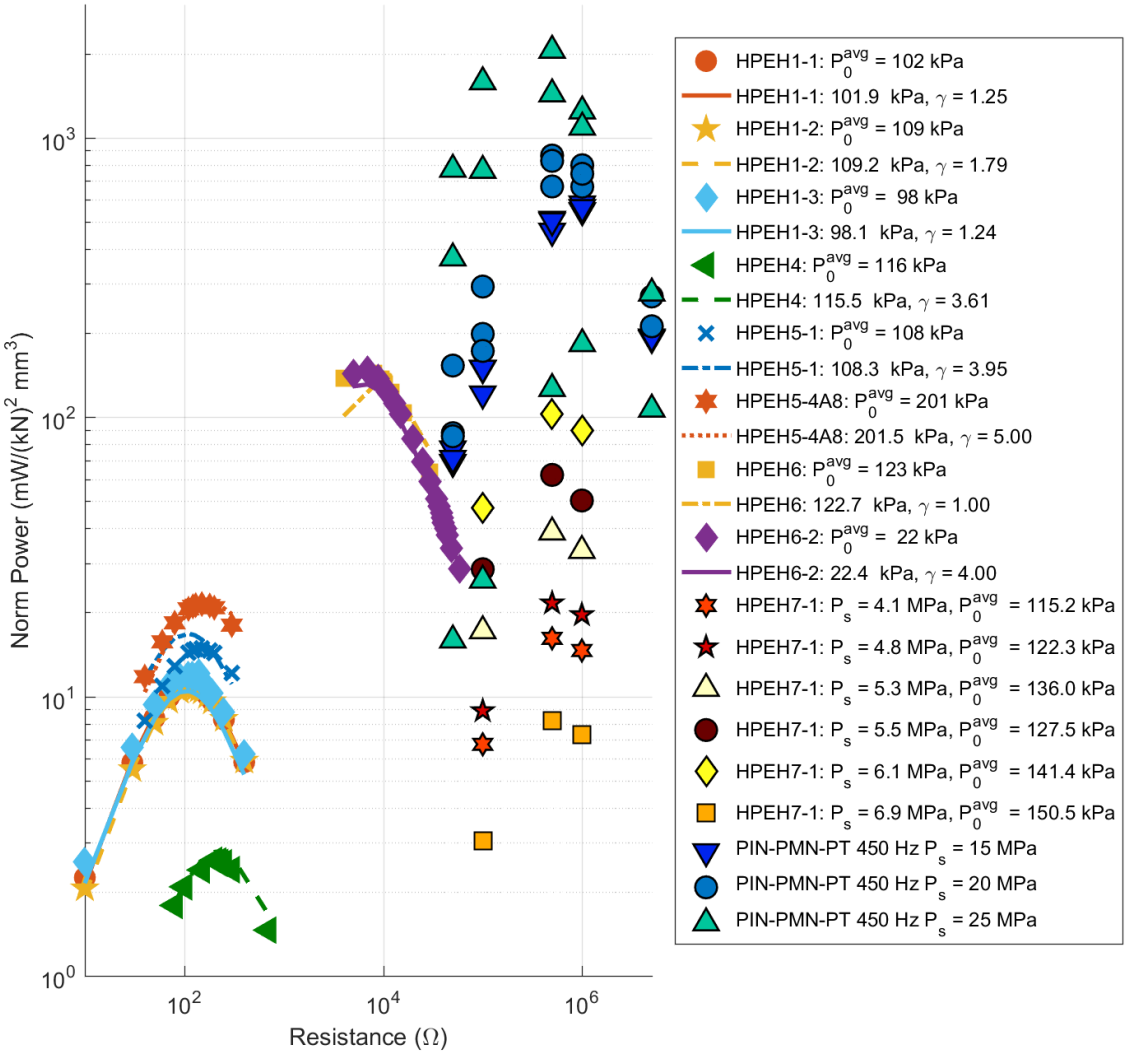

Figure 4.5: HPEH device performance normalized by volume and squared force, for resistive load circuit only. HPEH7-1 force input calculated using measured dynamic pressure amplitude, A_{stack} = 16 mm^2, γ = 11.4, and κ = 88.5%; order of HPEH7-1 tests. Tests labelled "PIN-PMN-PT" were performed using a shaker, where the dynamic and static force was measured directly.

The conditions of the PIN-PMN-PT test results are detailed in later sections, however there are a few material comparisons that can be made immediately. One is that HPEH6 and HPEH7 devices both contain relaxor-PT based materials: HPEH6 contains a PMN-PT layered single crystal stack; HPEH7 contains a PIN-PMN-PT single crystal element that contained a crack along one edge extending from the edge to about an eighth

of the length. The piezoelectric, dielectric, and compliant properties for these materials has been shown to be dependent on stress and temperature [100, 104]. Therefore, the results from piezoelectric materials with relatively constant permittivity and piezoelectric coupling properties, such as HPEH1 devices, normalize to a single curve, whereas devices and tests with the PMN-PT or PIN-PMN-PT materials, such as HPEH6, HPEH7, and the shaker tests, vary significantly.

Despite this variance, the test results normalized using Eq. (4.1) for undamaged single crystal elements had an order of magnitude higher performance in a majority of the test results; some of these tests are shown in Figure 4.4, indicated by the final three legend entries. The few test results equal to or below the other devices for the PIN-PMN-PT results were either damaged specimens (small crack) or at high stress levels (beyond -25 MPa). The high stress levels (beyond -25 MPa) are expected to remain only in the ferroelectric orthorhombic (FEO) phase, which have been shown to have much lower piezoelectric constant properties than when going through the phase transformation or if within the ferroelectric rhombohedral (FER) phase [102, 104].

The normalized power density performance of the material, shown in Figure 4.5, shows that most of the relaxor-PT based ferroelectric materials (HPEH6, HPEH7, and PIN-PMN-PT shaker results) have a higher or comparable response than the PZT based materials, including the HPEH7 results where the specimen had been damaged. These results are consistent with other research efforts which have shown higher performance of relaxor-PT based ferroelectric materials as compared to PZT materials [110, 111]. The PIN-PMN-PT shaker test and HPEH7 test methodology and results are further detailed in the remainder of this chapter.

4.2 Methodology

As first shown by Dong et al. [102, 107], a [011] cut PIN-PMN-PT single crystal produces high power levels per cycle when the oscillations force the specimen through an FER-FEO-FER phase transformation loop, as the mechanical work converted into electrical energy is much higher than the wasted mechanical work. As demonstrated earlier in Figure 4.1 and Figure 4.2, a mean stress near the transition area (e.g. -19 MPa at 20^{o}C) must be achieved, and the oscillation force must allow the specimen to oscillate between the two transition points (e.g. ±3.5 MPa). The circuit used by Dong, et al., remained as open circuit while applying the stress and then switched to connect to a bridge rectifier with an electrical resistive load for the phase transformation in order to increase the mechanical work converted to electrical work. The specimen was placed within an X-spring (to allow for motion amplification in the transverse direction of the loading), with the force and strain measured using a load cell and strain gauge. The specimen was tested at frequencies from 1 Hz to 100 Hz, with resistive loads kept below the optimal resistive load $R_l^{opt} = 1/(\omega C_p)$.

Both the work by Dong et al. and the preliminary results shown by HPEH6-2 indicate that designing a HPEH device for relaxor-PT based materials with the pressure ripple inducing a phase transformation will extract power levels an order of magnitude higher than other devices. A [011] cut PIN(0.24)-PMN-PT single crystal with the dimensions of 12 mm x 4 mm x 4 mm was chosen for demonstrating this concept. Two testing phases were performed: 1) specimen testing using a shaker to simulate the HPEH device for controlled frequency levels, however neglecting temperature effects on material;

and 2) testing on the hydraulic system using a HPEH device specifically designed to induce phase transformation energy harvesting. The following section is organized by discussing the shaker test setup design and then the HPEH designed for phase transformation energy harvesting.

4.2.1 Testing using shaker setup

A test frame shown in Figure 4.6 and test set-up shown in Figure 4.7 were designed to simulate both 1) a hydraulic system and 2) the HPEH design, however be actuated using a shaker (LDS V408 shaker with PA 500L power amplifier). The design consists of the single crystal test specimen, four Belleville springs (two parallel in series with two other springs in series), a 10-32 bolt and lock nut for applying and maintaining a preload, an outer frame to contain components and a post secured to a table in the center. The steel post was designed to be relatively rigid compared to the single crystal. The outer frame was considered rigid, however it is free to move with the shaker as it is not connected to the post or table other than static loads between the single crystal and bolt. A stinger connected to the frame near the single crystal is used to apply the dynamic forces. The static force was measured using a Flexiforce HT201 sensor placed between the single crystal and post. The dynamic force was measured using a PCB impedance sensor (Model 288D01) placed between the frame and the single crystal. The strain of the single crystal was measured using an Omega strain gauge (KPH-3-120-C1-11L1M2R) using an NI 9237 data acquisition system, which has a 50 kSamples/second capability. The electrical impedance load applied to the test specimen was a resistive-only circuit using two decade-resistance boxes to create a voltage divider.

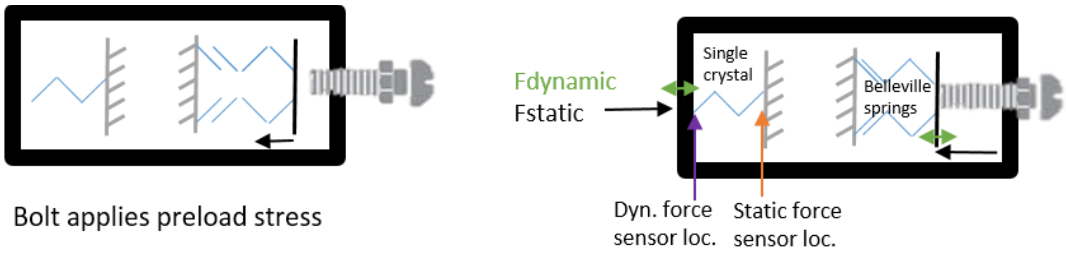

Figure 4.6: Test frame schematic used for controlled shaker testing (top view).

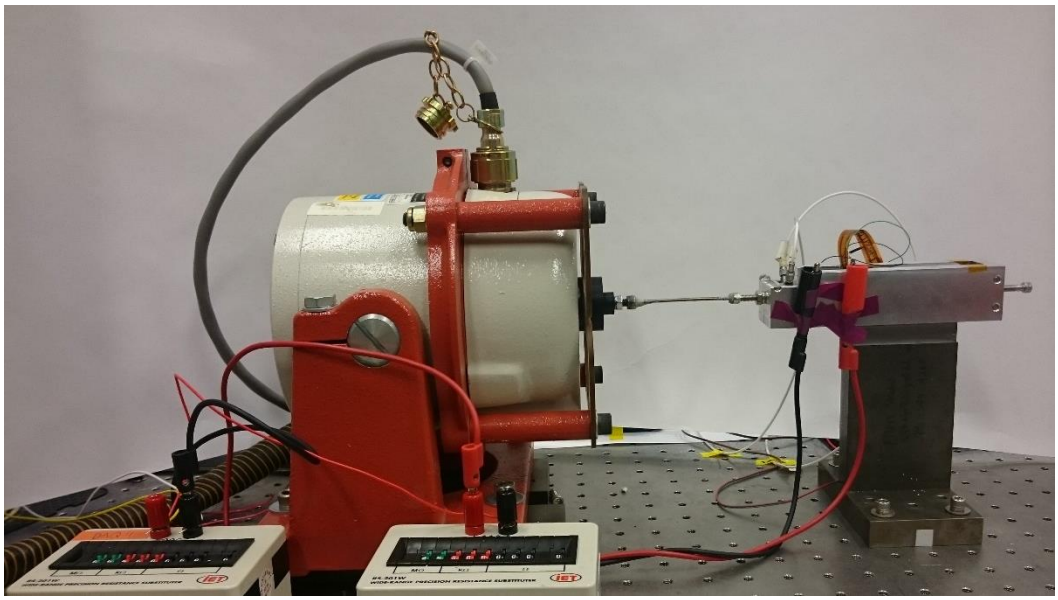

Figure 4.7: Side view of shaker test assembly, including test frame, shaker, and two decade resistance boxes used for voltage multiplier and loading of single crystal.

The top view of the test frame (schematically shown previously) can be seen in Figure 4.8. In order to properly setup the test frame, the following procedure was used. First, all of the left hand side components internal to the test frame (test specimen, static force sensor, dynamic force sensor, post) were placed within the test frame. Next the Belleville springs were placed within the internal frame and the static load was applied by tightening the 10-32 bolt and lock nut. Since the center post is fixed, as the bolt is tightened and the springs are compressed, the frame must move towards the right (away from the

shaker) and compresses the single crystal. This creates a static force (preload) applied to both the single crystal and Belleville springs. Second, the stinger is attached to both the shaker and outer test frame. This process is monitored with the static force sensor to note any changes to the static force applied to the single crystal. This means the shaker can apply the force oscillations to the test frame, thus simulating the pressure ripple found within hydraulic systems.

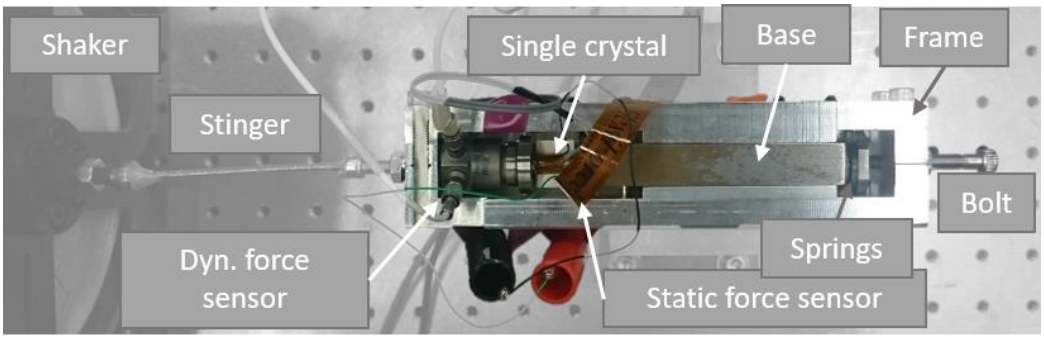

Figure 4.8: Top view of test frame used in shaker test; see Figure 4.6 for schematic view.

4.2.2 HPEH7-1 design for PIN-PMN-PT single crystal

The HPEH designed for testing phase transformations of a [011] cut PIN-PMN-PT single crystal on a hydraulic rig is termed HPEH7-1. The design is an adaptation of the force shunt concept introduced in Section 2.4.3. A schematic of this concept is shown in Figure 4.9. The main difference between the force shunt concept and the design for phase transformations is that a static preload is applied to both the single crystal and Belleville springs, rather than only the latter.

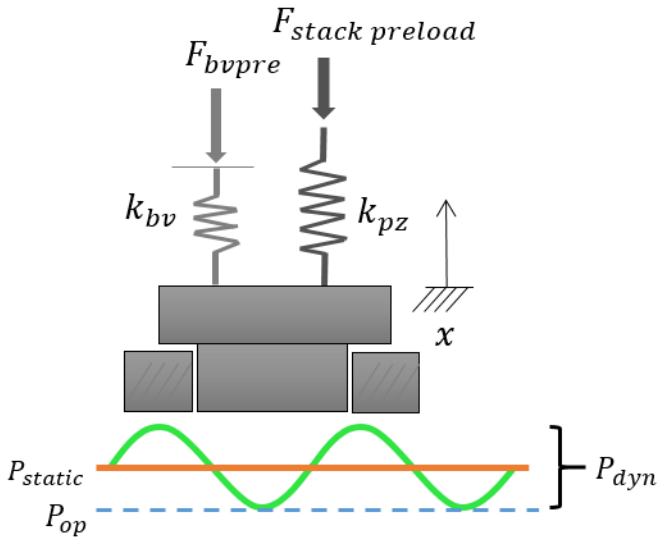

Figure 4.9: Schematic of HPEH7-1 loading; similar to force shunt concept in Section 2.4.3, however includes loading of single crystal.

HPEH7-1 design is based on the force shunt concept, area amplification, and pre-loading the piezoelectric element, with the designed body parts shown in Figure 4.10. Since it is necessary to have a high oscillating force to induce phase transformations, the dynamic pressure within the hydraulic system most likely requires amplification. This can be achieved by using a large area ratio. However, this large area ratio also increases the stress in the piezoelectric, which may place the mean stress beyond the phase transition area. Thus a force shunt using Belleville washers is used to apply a preload and counteract the hydraulic rig system pressure. The final adjustment is to ensure the single crystal is near the phase transition area for the given hydraulic system pressure and force shunt preload, which is set by applying a preload to the keyed spacer, shown in Figure 4.10, and thus the single crystal.

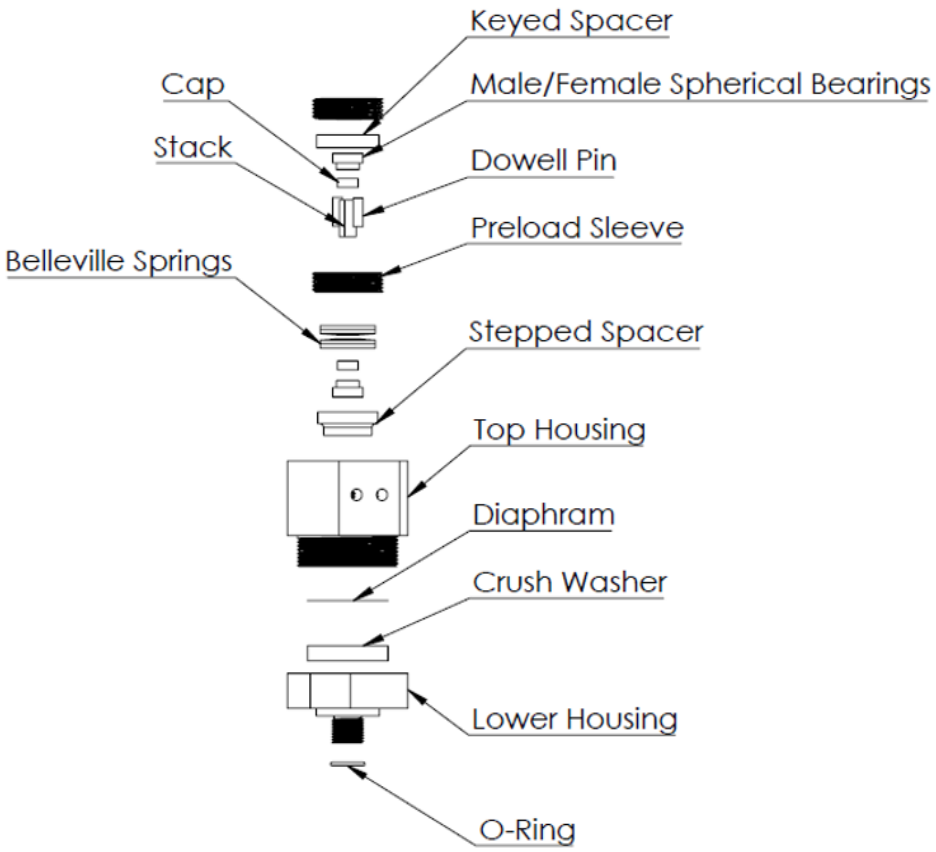

Figure 4.10: HPEH7-1 design components.

The equation of motion for HPEH7-1 design is conceptually the same as the force shunt design, however it now includes the additional single crystal preload

$$\begin{aligned}&\left[m_{spacer}\ddot{x}+\left(k_{bv}+k_{pz}\right)x\right]H(x)=\\&\left(P_0+P_s\right)A^{eff}-F_{bvpre}-F_{SCpre}+R_x\left[1-H(x)\right]\end{aligned} \tag{4.2}$$

where F_{SCpre} represents the force applied to the single crystal. Also, the calculation for the operating pressure changes to

$$F_{bvpre}+F_{SCpre}=\left(P_s-0.5P_{dyn}\right)A_{spacer}=P_{op}A_{spacer} \tag{4.3}$$

where the force applied to the single crystal is determined via the desired static stress level required to be near the phase transformation transition point for the given hydraulic system

temperature. As before, the area ratio is still $\gamma = A_{spacer} / A_{piezo}$, however because the PIN-PMN-PT single crystal is a [011] cut specimen, the cross-sectional area of the piezo refers to area where the pressure is applied (in this case 4 mm x 4 mm), which differs from the electrode area (in this case 4 mm x 12 mm). The force shunt ratio initially is for the linear regime of the single crystal, and thus remains as $\kappa = k_{pz} / \left(k_{bv} + k_{pz} \right)$; this value is used for the initial preload calculations. When the single crystal goes through the phase transformation, the force shunt ratio changes to

$$\kappa(x) = \frac{U_{piezoelectric}}{U_{total}} = \frac{k_{pz}(x)}{k_{bv} + k_{pz}(x)} \tag{4.4}$$

where the piezoelectric stiffness is a function of the compressive displacement of the single crystal, as one of the observed effects of phase transformation is a large change in strain [99, 101, 105].

For a given operating pressure, the dynamic pressure must be either estimated or measured prior to determining the appropriate area ratio to use, as the dynamic pressure must be amplified from the 100s of kPa range to around 5 MPa, depending on the force shunt ratio and single crystal composition. The area ratio and initial force shunt ratio (neglecting stiffness changes during phase transformation) designed for HPEH7-1 are summarized in Table 5.

Table 5: HPEH7-1 area amplification ratio and force shunt ratio.

	Stepped Spacer	**Single Crystal**	**Area Amplification**
Area (m^2)	182.4e-06	16e-06	11.4
	Belleville Springs	**Single Crystal**	**Force Shunt**
Stiffness (N/m)	1.44e+06	1.11e+07	88%

4.3 Results and discussion

Two [011] cut PIN-PMN-PT specimen were tested using a shaker and one was tested on the hydraulic rig. The shaker tests were performed at 450 Hz and are assumed to be at relatively constant room temperature. Each specimen had a different mean stress loading order during the shaker test. The specimen tested on the hydraulic rig was assumed to have the same temperature as the oil; this specimen was observed to have a small crack, and thus one-to-one comparisons between the test results cannot be made. The results of these two test set-ups are discussed herein.

4.3.1 Shaker tests

Using the test structure set-up discussed in Section 4.2.1, two specimens were tested at varying static pressures and resistive loads, as shown in Figure 4.11. Within Figure 4.11, the shape indicates which specimen (of two), and the color indicates the power normalized by the squared force and volume (which is the same comparison made between all devices previously in Figure 4.5). As the material properties may be dependent on the loading cycle order, the testing order has been included. Three nominal mean compressive stress levels were tested, -15 MPa, -20 MPa, and -25 MPa, as it was expected beyond -25 MPa would be past the phase transition point based on initial specimen testing and literature review. The stress levels were calculated using the force measured and the 4 mm x 4 mm cross sectional area of the test specimen. For 450 Hz, the optimal resistance load is expected to be between 1.1 and 2.45 MΩ for capacitance levels between 144 pF and 310 pF, which covers the range of measured capacitance levels while at mean pressure. Therefore, the resistive loads tested ranged from 50 kΩ to 5 MΩ. In addition to measuring results at resistive loads higher than the predicted optimal resistive load, the dynamic force level was

varied at each mean stress level. This was controlled via current input to the shaker, but the corresponding peak-to-peak stress levels (calculated using 4 mm x 4 mm cross sectional area) ranged from -0.95 MPa to -6.4 MPa.

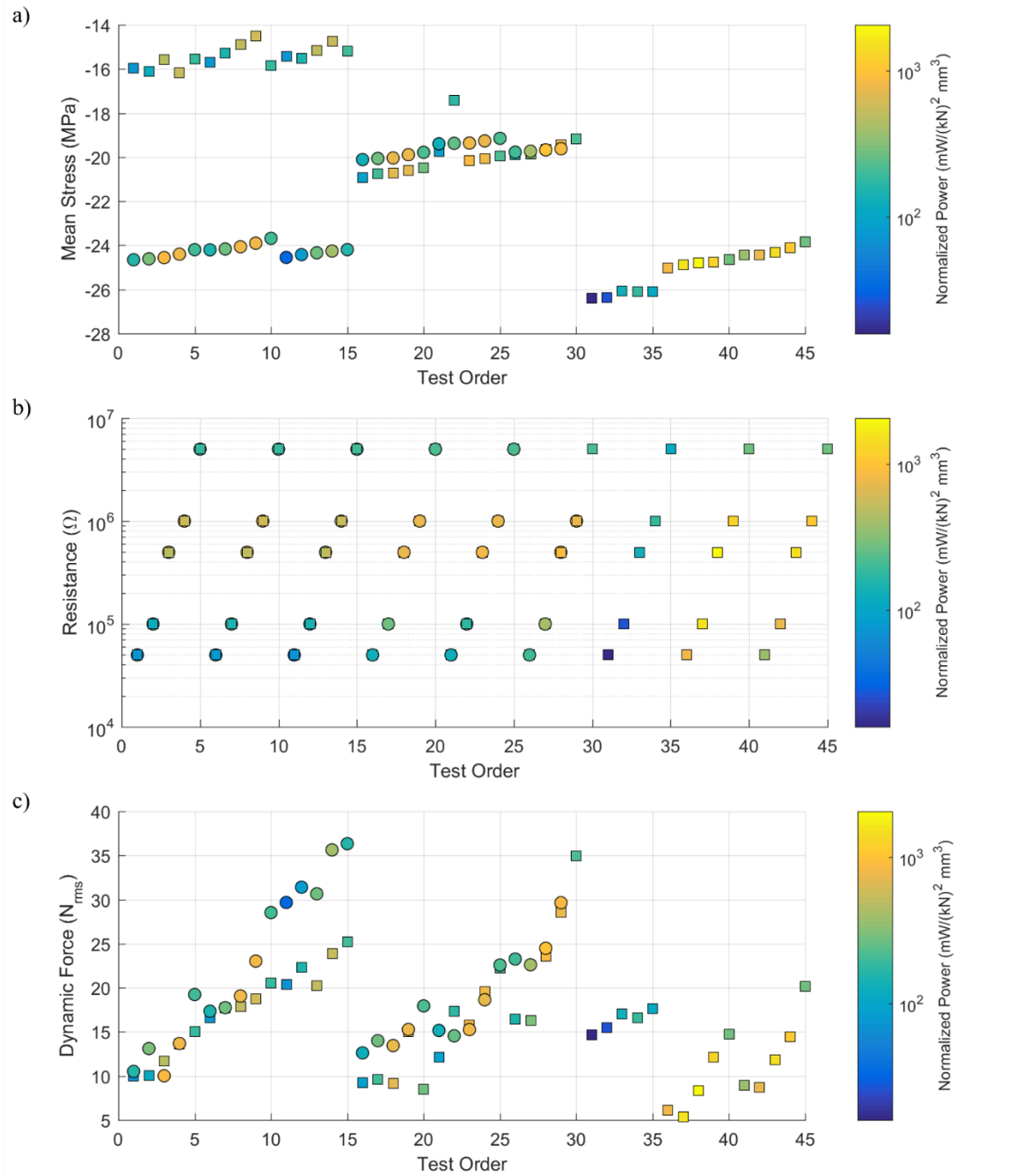

Figure 4.11: Shaker test order for two specimens (indicated by shape) compared to power normalized by squared dynamic force and volume of single crystal (indicated by color) with respect to a) mean stress, b) resistive load, and c) root-mean-square dynamic force.

The lowest and highest normalized power occurred at the nominal mean stress level of -25 MPa; however, the highest average power response occurred at the nominal mean stress level of -20 MPa. These results are due to the mean stress levels and dynamic loads applied, and can be seen in Figure 4.12 and Figure 4.13.

The peak power response for both specimens corresponded with nominal mean stress levels of -20 MPa, resistive loads of 1 MΩ (which is near the optimal resistance), and dynamic force levels of about 29 N_{rms} (which corresponds to about 5.1 MPa peak-to-peak stress oscillations). These results can be seen in Figure 4.12, where the peak values are 141 mW and 116 mW for the specimen indicated by the circle and square, respectively. These results correspond to test order 29 in Figure 4.11 for both specimens, which is the highest dynamic force applied at that mean stress level and resistive load. As discussed in Chapter 2, typically higher dynamic force will lead to higher power response assuming resistive loads are the same; however since this material goes through partial phase transformation, this normalization method is not constant when mean stress levels change. For instance, a test with a higher dynamic force for the resistive load of 1 MΩ was test 14 at nominally -25 MPa mean stress level (as indicated by circles in Figure 4.11), however this was only the third highest power level for that resistive load in Figure 4.12. In order to explain why this point is of interest, the effects of the phase transformation points and the piezoelectric material properties of FER versus FEO regions on the normalized power results must first be discussed.

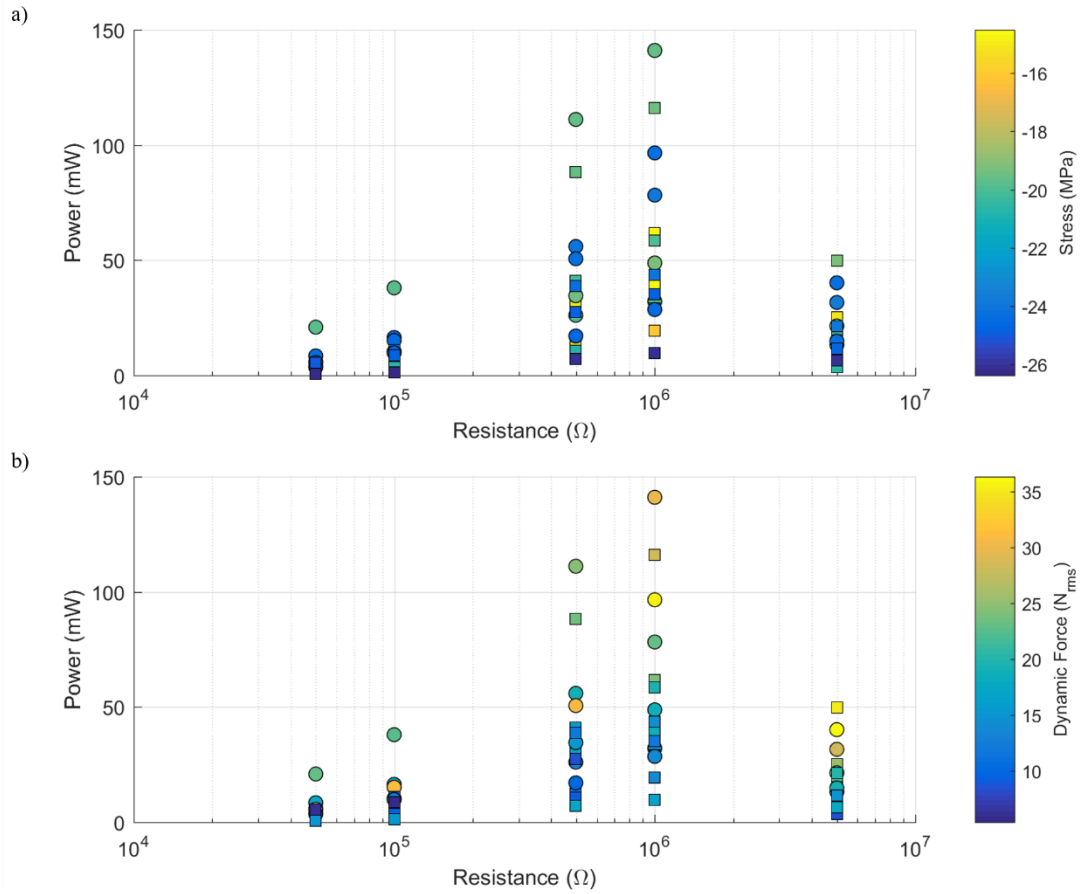

Figure 4.12: Power with respect to resistive load; color indicates measured a) mean stress level or b) root-mean-square dynamic force level; shape of point indicates different single crystal specimen.

In Figure 4.13, the power normalized by squared dynamic force and volume of piezoelectric material is shown with respect to resistive load, specimen as indicated by shape, and mean stress (Figure 4.13a) or root-mean-square dynamic force (Figure 4.13b) as indicated by color. Both the highest and lowest normalized power resistive load sweeps occurred at nominally -25 MPa mean stress level, and the next highest occurred at nominally -20 MPa. For a clearer demonstration of the normalized power versus resistive sweeps for a given stress range, see Figure 4.15. This indicates that that phase transformation occurs between -20 MPa and -25 MPa for the specimens tested at room temperature and corresponds well with predictions from the literature (recall Figure 4.1 and Figure 4.2). The piezoelectric constant for the FER region (expected between the phase

transformation transition point and 0 MPa) is higher in absolute value than for the FEO region (expected at compressive stresses beyond the phase transformation transition point). It is therefore expected that the lowest normalized power responses occur when the material is in the FEO region, the next highest is in the FER region, and the highest is when the material partially or fully transitions between the two regions. If the stress oscillations extend from the phase transformation transition point into either the FER or FEO region, it is expected that tending toward the FER region would have higher response than toward the FEO region.

The normalized power results do follow this pattern, as seen in Figure 4.13: the lowest normalized power response occurs when the specimen is at -26 MPa mean stress level, which is above the expected phase transition point for the specimen, and therefore in the FEO region. This is also seen via the increased strain level; additional results showing stress, strain, and electric field for a given test are shown in Appendix B. The next group are at nominally -15 MPa, which is expected to remain in the FER region, followed by -20 to -25 MPa mean stress levels, which are expected to have undergone partial phase transformations.

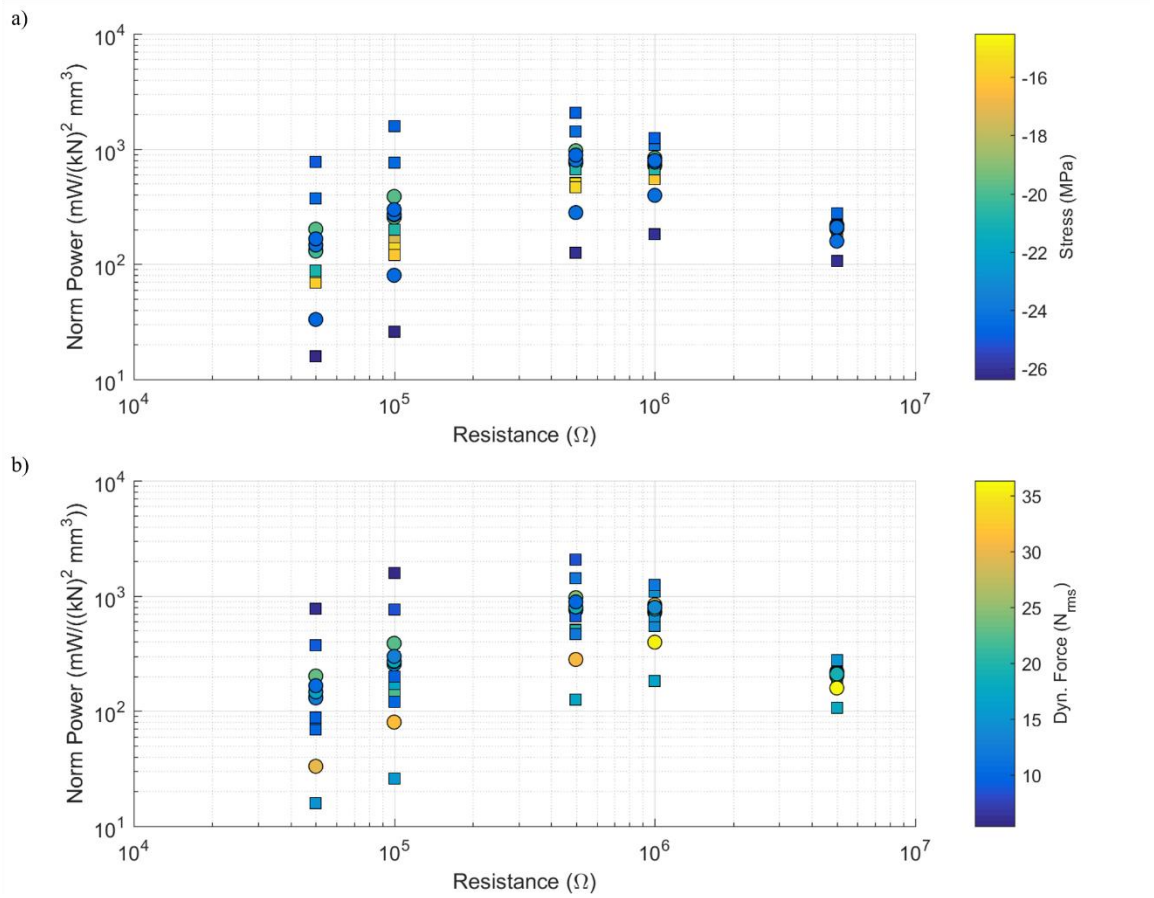

Figure 4.13: Power normalized by squared dynamic force and volume of single crystal with respect to resistive load; color indicates measured a) mean stress level or b) root-mean-square dynamic force level; shape indicates different single crystal specimen.

The two sweeps with the highest normalized power (tests 36 to 44, with mean stress levels of -25 MPa and dynamic force levels of 15 N_{rms} or less) occurred after the specimen stress level had reduced to -16 MPa prior to the tests being recorded, and therefore were near the FER to FEO transition point. It is also expected that the specimen did not fully transform to FEO, which would have caused the transition point to change to a lower absolute mean stress level for the FEO-FER transition point (recall Figure 4.2). Since these two sweeps had relatively low dynamic stress levels (thus not deviating into the purely FER or FEO state), and the mean stress began in a region near the transition point, the normalized power results are deceptively high. If the dynamic stress levels had been higher

while at this mean stress level, then the normalized power results would have decreased due to transitioning into the lower power FEO region. As mentioned earlier, the tests with the highest dynamic force occurred at the mean stress level of -25 MPa, and show this phenomenon via tests 11 thru 15 for the specimen indicated by circles. In Figure 4.13, these tests correspond to the second lowest normalized power sweep, and in Figure 4.12 to the third highest power sweep. This demonstrates the importance of tuning the specimen to a proper stress region for phase transformation in order to benefit from the high power performance potential.

If a full phase transformation was achieved, in other words stress oscillations from about -17 MPa to -26 MPa (requiring about 51 N_{rms} dynamic force for a mean stress of 21.5 MPa), then it is expected that the results would be optimal for the normalized power response. In a hydraulic system, this may be difficult to achieve due to the varying mean stress levels, dynamic pressure oscillations and temperatures; but as seen, partial phase transformation does produce higher power responses than purely FER (or FEO) phase region results. Contrary to the two highest normalized power results, after ensuring the specimen is close to the phase transformation transition point, it is best for the stress oscillations to be near the FER region rather than the FEO region, i.e. lower pressure or pre-load on the piezoelectric element. This allows the energy harvester to benefit from the more favorable FER electromechanical properties rather than be disadvantaged by the FEO properties.

The highest normalized power occurs at 500 kΩ or 1 MΩ, depending on the stress range (as in, combined effect of mean stress level and dynamic force). This is shown in both Figure 4.14, which provides the respective dynamic force and mean stress level for

each test, and Figure 4.15, which allows easy comparison of each resistive load sweep for a given mean stress range. The trend of the normalized power with respect to resistive load at low stress levels shown in Figure 4.15a is relatively constant. As the mean stress level increases (Figure 4.15b), the power per squared dynamic force begins to deviate from a single curve, and the optimal resistive load begins to shift from 1 MΩ to 500 kΩ. At the highest stress levels tested (Figure 4.15c), the power per square dynamic force is no longer a single curve, and the only sweeps where 1 MΩ corresponds to the peak performance is for the two tests that are expected to mainly lie in the FEO region. This variance in power per square force is also an indication of partial phase transformation, as otherwise the response would fall to a single normalized curve as seen in Figure 4.15a.

While it may appear that the phase transformation is causing the optimal resistive load to shift, this conclusion cannot be confirmed from a single resistive sweep shown due to the increasing dynamic force with each resistive load (see Figure 4.11b and c); however it is confirmed when comparing alternative sweeps. The shaker used for testing was controlled via the current provided to the shaker, and not by the dynamic force applied. The change of resistive load alters the effective stiffness of the specimen, and thus the interaction between the shaker dynamic force and the specimen changed. Because it has been established that normalized power results may decrease with increasing dynamic force, the shift in optimal resistive load may be affected by the test setup.

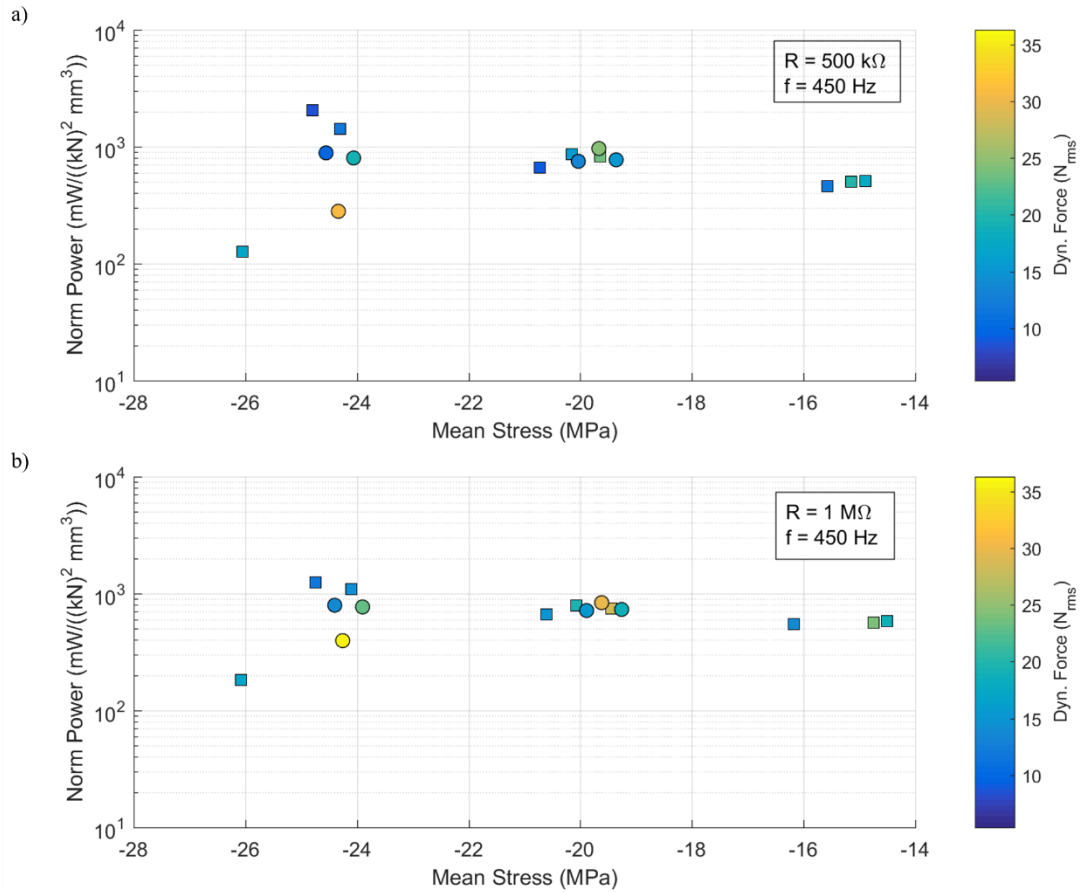

Figure 4.14: Power normalized by squared dynamic force and volume of single crystal with respect to mean stress at a) 500 kΩ and b) 1 MΩ; color indicated dynamic force; shape indicates different single crystal specimen.

Each sweep with partial phase transformation appears to have an optimal resistive load closer to 500 kΩ rather than 1 MΩ, as clearly seen in Figure 4.15. In addition, each respective sweep had a higher dynamic force applied during the 1 MΩ case than the 500 kΩ case. In order to determine whether this is simply due to the increased dynamic force causing a deceptively high normalized power value, or due to the phase transformation causing the peak response to change, situations where the dynamic force applied to the 500 kΩ load was larger than or similar in value to the 1 MΩ load for a similar mean stress level were found. Four cases were compared, and in each case, the normalized power response was higher for the 500 kΩ load; these case studies are summarized in Table 6.

Table 6: Comparing normalized power responses when the dynamic force is higher for the 500 kΩ resistive load than the 1 MΩ resistive load.

	500 kΩ			1 MΩ			Norm. Power	
Specimen	**Test**	**Dyn. F. (N_{rms})**	**Mean σ (MPa)**	**Test**	**Dyn. F. (N_{rms})**	**Mean σ (MPa)**	**(μW/N^2) 500 kΩ**	**(μW/N^2) 1 MΩ**
1 (□)	28	23.6	-19.6	24	19.6	-20.1	158.8	153.2
1 (□)	43	11.9	-24.3	39	12.1	-24.7	275.4	239.3
3 (o)	28	24.5	-19.7	24	18.6	-19.2	185.5	140.4
3 (o)	8	19.1	-24.1	4	13.7	-24.4	153.9	152.6

As seen in the test results shown in Figure 4.14, Figure 4.15 and Table 6, when the ferroelectric material undergoes phase transformation, the optimal resistive load decreases. This also matches well theoretically. The dielectric coefficient is related to the electric displacement and electric field. As published by Gallagher, et al. [103], when a [011] cut PIN-PMN-PT single crystal undergoes phase transformation with constant preload and applied electric field, the slope of the electric field versus electric displacement increases, indicating that the dielectric coefficient increases. This indicates that the capacitance also increases, as these terms are proportionally related (Eq. (2.4)), and thus the optimal resistive load, $R_l \approx 1/(\omega C_p)$, decreases.

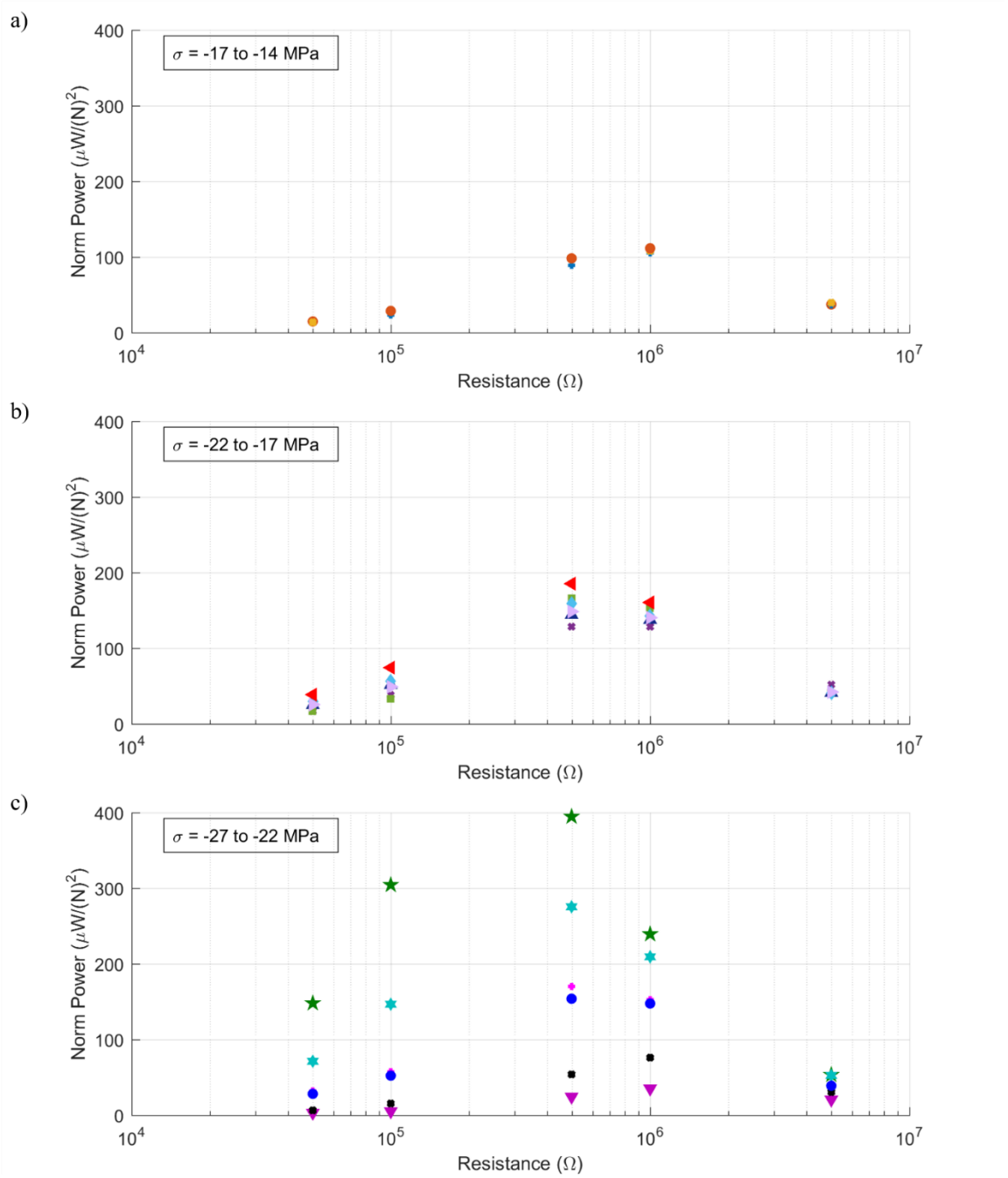

Figure 4.15: Power normalized by squared force versus resistance, for a) 15 MPa, b) 20 MPa, and c) 25 MPa stress levels.

As mentioned in the literature review, one aspect of phase transformation in relaxor-PT based ferroelectrics is a large change in strain [99-101, 105]. Piezoelectric strain is easier to measure within a HPEH device than the exact forces applied to the housed piezoelectric material. Therefore, knowing where the peak power responses may occur

with respect to the measured strain can be helpful for tuning the initial pre-strain due to the pre-force applied to the single crystal within an HPEH device, as discussed in Section 4.2.2. The power normalized by squared dynamic force and piezoelectric volume compared to mean strain and resistive load is shown in Figure 4.16. The power normalized by squared dynamic force with respect to the mean strain is shown in Figure 4.17; the bars on each point indicate the range of the strain during the 450 Hz excitation, the color indicates the resistive load, and the shape corresponds to the dynamic force level for a given resistive sweep. The peak normalized power response occurred near 500 kΩ and -2500 με, and the trends of both specimens tested tended toward this maximum. It should be recalled that the material properties change with temperature [103, 104, 106], and therefore HPEH tests beyond room temperature may differ from the trends shown by the shaker tests.

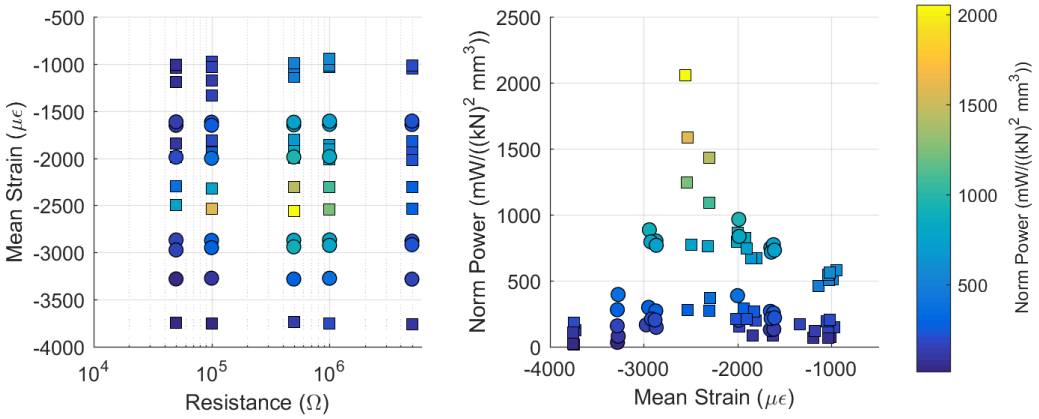

Figure 4.16: Power normalized by squared dynamic force and volume of single crystal with respect to resistive load and mean strain.

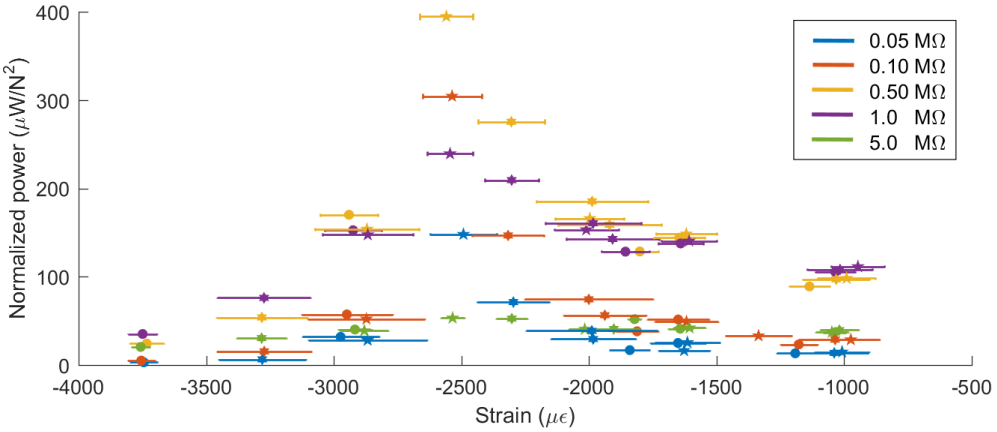

Figure 4.17: Power normalized by dynamic force versus strain; strain indicated by x-axis; bars on points indicates strain range and shape of point indicate dynamic force level; color indicates resistive load; excitation at 450 Hz.

The dynamic shaker tests provided a more controllable environment to simulate a HPEH device using a [011] cut PIN-PMN-PT material, although these tests neglect temperature effects. Four key points are determined to be important when considering this material for hydraulic energy harvesting. First, the highest normalized power regions are within the phase transformation (PT) region, the next highest is the FER region (less compressive stress than PT region), and the lowest normalized power occurs in the FEO region (more compressive stress than PT region). Second, the normalized power for a low dynamic force test may be deceptively high: the normalized power may decrease with higher dynamic forces if those forces are not within the phase transformation region. Third, while within a phase transformation region, the optimal resistive load may decrease in comparison to the value calculated for the FER or FEO region. And fourth, the measured strain level can be used to predict phase transformation transition points, which can be useful for when the forces are difficult to measure. For the specimens to be used in HPEH7-1, the phase transformation appears to occur between -3000 and -2000 με at room temperature with the optimal resistive load to be near 500 kΩ for 450 Hz harmonic

excitation. In addition, the root-mean-square stress oscillations for full phase transformation are about 3200 kPa, which corresponds to about 51 N_{rms} dynamic force about a mean stress of -21.5 MPa. Other tests at 5 Hz and 100 Hz were performed on these specimen, however are not included in this discussion for brevity and because during the 100 Hz tests, small cracks formed in the specimens. The undamaged tests performed at 5 Hz are compared to work by Dong, et al. [102] next.

4.3.2 Shaker test results compared to other published works

The purpose of this chapter is to analyze ferroelectrics that undergo phase transformation and consider their feasibility for energy harvesting, specifically for hydraulic pressure energy harvesting. Dong, et al. [102, 106, 107], previously analyzed [011] cut PIN-PMN-PT single crystals for energy harvesting under ideal phase transformation, meaning it underwent full phase transformation rather than partial. The comparison between work presented herein and work by Dong, et al., is summarized in Table 7 for a 5 Hz excitation level. The specimens used in this work and by Dong, et al., have the volume of 4 mm x 4 mm x 12 mm, poled in the [011] direction, force applied on the 4 mm x 4 mm surface ([011] direction), and electric field in the [011] direction. Because the energy efficiency decreased when approaching resistive loads for optimal power response, Dong did not perform resistive load sweeps beyond the linear range. Since the goal of energy harvesting for hydraulic systems is to optimize the power, these values are included in the table and figures from work herein. It is clear from Table 7 that the idealized phase transformation cycle performance measured by Dong, et al., was higher than the performance per cycle measured herein.

Table 7: Comparison of shaker test results and work published by Dong [106]. †Assumes 3.5 MPa peak to peak stress oscillation (19.8 N_{rms}) and mean stress range from discussion in section, however not explicitly stated.

	This work	***This work***	***Dong (table 5-2, section 5.3)*** *[106]*
Resistance (MΩ)	49.8	10	10
Frequency (Hz)	5	5	5
W_{elec} (J m^{-3} $cycle^{-1}$)	1667	578	1389.22
Power (mW)	1.6	0.55	1.33
Norm. Power (μW/N^2)	1.3	0.44	3.39†
Volt (Vrms)	286	72	114
Mean Stress (MPa)	-13.9	-14.1	-22.25†

The idealized test results of power per volume and work per volume per cycle presented by Dong, et al., (Figure 5-11 in reference [106] or Figure 12 in reference [102]) is reproduced in Figure 4.18. The corresponding results for the shaker tests presented in Section 4.3.1 are provided in Figure 4.19. Note that from the work presented by Dong, et al., the results end at 10^{10} Ω Hz^2 with the power per volume being slightly above 10^5 Wm^{-3} for the idealized cycled conditions; this corresponds to the beginning of the results in Figure 4.19a, with the peak response being on par with those presented by Dong, et al. For the energy per volume per cycle results, the final results shown are at 7×10^7 Ω Hz with the values being 1.35×10^3 and 1.83×10^3 Jm^{-3} $cycle^{-1}$, which is a higher performance level than measurements shown in Figure 4.19. As a direct comparison, the peak performance at 5×10^7 Ω Hz in Figure 4.19 is 440 Jm^{-3} $cycle^{-1}$, which is below the corresponding performance levels of 998.70 and 1389.22 Jm^{-3} $cycle^{-1}$ published by Dong, et al.

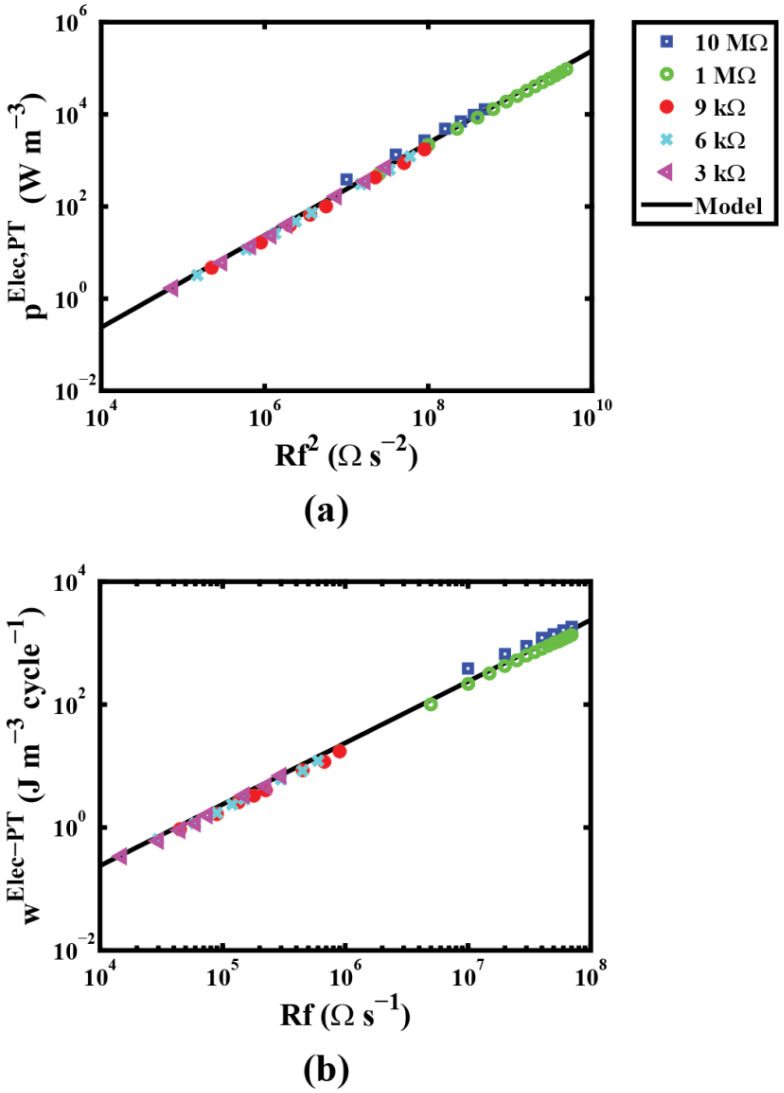

Figure 4.18: Power per volume and work per volume per cycle for full phase transition "idealized" test results, frequency ranging from 1 Hz to 100 Hz; x-axis represents the product of the load resistance and excitation frequency; from Dong [106] Figure 5-11 or Dong et al. [102] Figure 12.

The decrease in performance as compared to the idealized phase transformation cycles is not unexpected as the experiments performed by Dong, et al. were strain controlled to ensure the full phase transformation occurred, whereas the experiments presented here used a variety of static and dynamic force levels, as is seen in hydraulic systems. The peak power per volume and energy per volume per cycle performance for

450 Hz is shown when the resistive load reached 1 MΩ, however as discussed previously, this is also due to the high dynamic force levels during those tests.

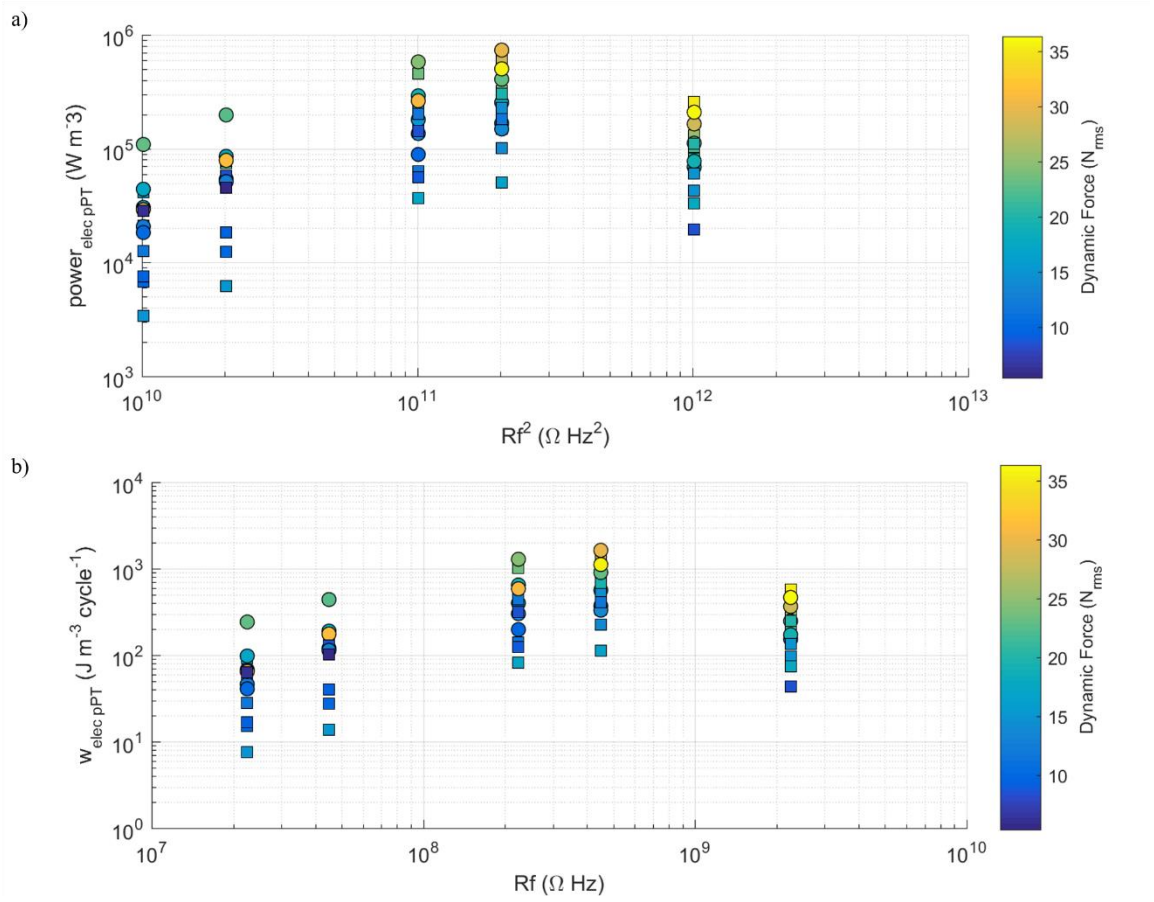

Figure 4.19: Power per volume and work per volume per cycle from shaker test results including power optimized resistive load; tested at 450 Hz; shape indicates specimen tested; color indicates level of dynamic force; three mean stress levels tested - nominally -15 MPa, -20 MPa, and -25 MPa.

While the peak performance for constant temperature is easy to predict for a given dominant frequency, the power response has an order of magnitude performance range depending on the stress range and excitation levels. The performance levels in general are still considered to be high, however ensuring that a HPEH device is tuned properly to undergo partial phase transformation may be challenging to implement outside of an experimental setting.

4.3.3 HPEH7-1 test

HPEH7-1 was assembled and tested based on results from the shaker tests, however the specimen used had a small crack that had formed during shaker tests at 100 Hz (not presented). The assembly of HPEH7-1 (seen in Figure 4.10) contained four Belleville springs (two parallel springs in series with two springs in series) with a 2.82 N-m (25 lbf-in) torque applied to the preload sleeve to apply F_{bvpre}. Next, the single crystal was preloaded via the top cap, where the measured strain level reached 1.5 mε. This corresponds to about 12.5 MPa initial stress based on stiffness measurements prior to shaker tests, however the specimen used within HPEH7-1 had formed a small crack after shaker tests and prior to HPEH tests. The measured capacitance prior to the preload was 300 pF, and after the preload was 152 pF.

HPEH7-1 was tested at three resistive load levels for each system static pressure level: 100 kΩ, 500 kΩ, and 1 MΩ. Each sweep was performed at six different static pressure levels, in order: 5.5 MPa (800 psi), 4.8 MPa (700 psi), 4.1 MPa (600 psi), 6.9 MPa (1000 psi), 6.0 MPa (870 psi), and 5.3 MPa (770 psi). The first static pressure level was determined by measuring the strain level on the single crystal and then recording a range of static pressure levels around this point; the first strain level for the first static pressure level was measured as -2570 με. In addition, the lowest static pressure level tested corresponded to the initial strain due to the pre-load; this corresponded to -1530 με. The oil temperature was recorded for each test, with the temperature increasing from 33.5°C for test one to 41.6°C for test 18.

The root-mean-square dynamic pressure ranged from 115 kPa_{rms} to 152 kPa_{rms}, which corresponds to 18.6 N_{rms} to 24.6 N_{rms} assuming the full spacer area and determined

force shunt ratio from Table 5 apply. As seen from test and model comparisons in Chapter 2, it is likely that these values overestimate the actual force applied to the single crystal. The approximate mean stress (neglecting initial stresses from the preload) and dynamic forces applied to the [011] cut PIN-PMN-PT specimen in HPEH7-1 are shown in Table 8, with the caveat that these values likely overestimate the stress and forces applied to the single crystal.

Table 8: Approximate mean stress from static pressure (does not include initial stress from single crystal preload) and dynamic force values applied to [011] cut PIN-PMN-PT single crystal within HPEH7-1 during tests. Calculated via designed area ratio, spacer area, and force shunt ratio provide in Table 5. Pre-strain during assembly (prior to turning on hydraulic rig) was about 1.5 mε, which corresponds to about 12.5 MPa initial stress for the specimen prior to shaker tests.

Test Order:	1 to 3	4 to 6	7 to 9	10 to 12	13 to 15	16 to 18
Approx. Mean Stress from P_s (MPa):	-13.9	-7.0	0.0	-27.8	-19.5	-11.8
Resistive Load (kΩ)	**Approx. Dynamic Force (N_{rms})**					
100	20.6	19.7	18.6	24.1	22.8	22.0
500	20.6	19.7	18.6	24.2	22.8	21.9
1000	20.6	19.8	18.6	24.6	22.8	21.9

While comparisons between the shaker test and HPEH7-1 forces are difficult to make, comparisons between the resistive loads and strains are more readily available. In addition, HPEH7-1 power per squared dynamic pressure is a good indication of HPEH performance, even though it does not accurately depict material performance. Due to the specimen being damaged, it is expected that these results are minimum performance indicators, i.e. without damage, better performance is expected.

Normalized power results versus strain, resistive load, static pressure, and temperature are shown in Figure 4.20. Since, the range of dynamic forces is relatively small (see Table 8), it is expected that higher normalized power results are not due to an abnormally low forcing level, as discussed in Section 4.3.1. The normalized power peak

response occurred at 500 kΩ for each resistive load sweep, which is consistent from the shaker test results. As can be seen, partial phase transformation occurred between the strain values of above -4000 με and below -1500 με, as the normalized power for a given resistive load changes with system pressure, and thus mean stress.

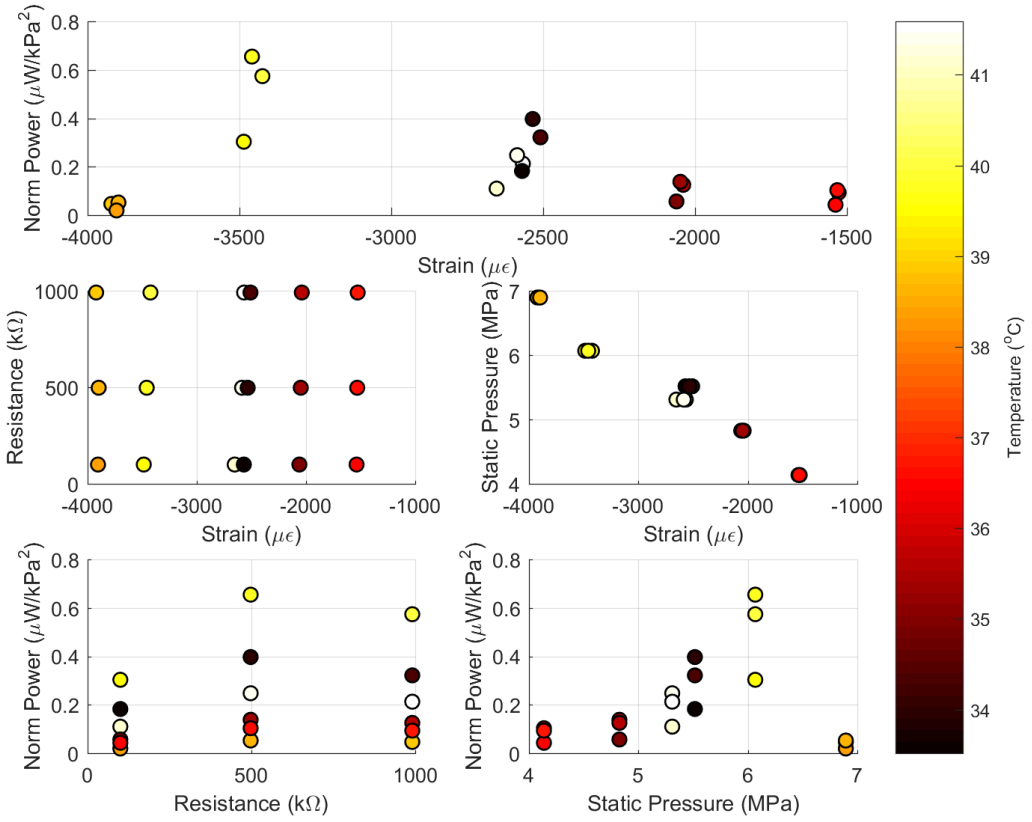

Figure 4.20: Results from HPEH7-1 tests comparing power normalized by (measured hydraulic) squared dynamic pressure, strain, resistive load, and hydraulic system pressure. Color indicates measured oil temperature, where the temperature of the oil gradually increased during testing.

The power and normalized power (with respect to force and volume of piezoelectric material) are shown in Figure 4.21 and Figure 4.22. The horizontal axis represents the measured mean micro-strain, where the bars indicate the strain range during excitation. The order of the legend is according to test order, and color indicates temperature. The

lines connecting points indicate a resistive load sweep for a given static pressure level. The peak performance of 13.1 mW (130.9 mW $kN^{-2}mm^{-3}$; 0.65 μW/kPa^2) occurred at -3460 με and 500 kΩ, which occurred at 6 MPa static pressure, 39.8°C, and had 141 kPa root-mean-square pressure. As seen by the strain range bars, the peak performance also corresponded to large jumps in strain, despite the dynamic pressure magnitude being similar to the other tests shown. This is at a higher strain level than expected, however it has been shown in the literature that the strain response of ferroelectric materials changes with temperature [99-101, 103, 106]. It can also be seen that the normalized response near -2500 με changes, most likely due to the oil temperature change affecting the material response.

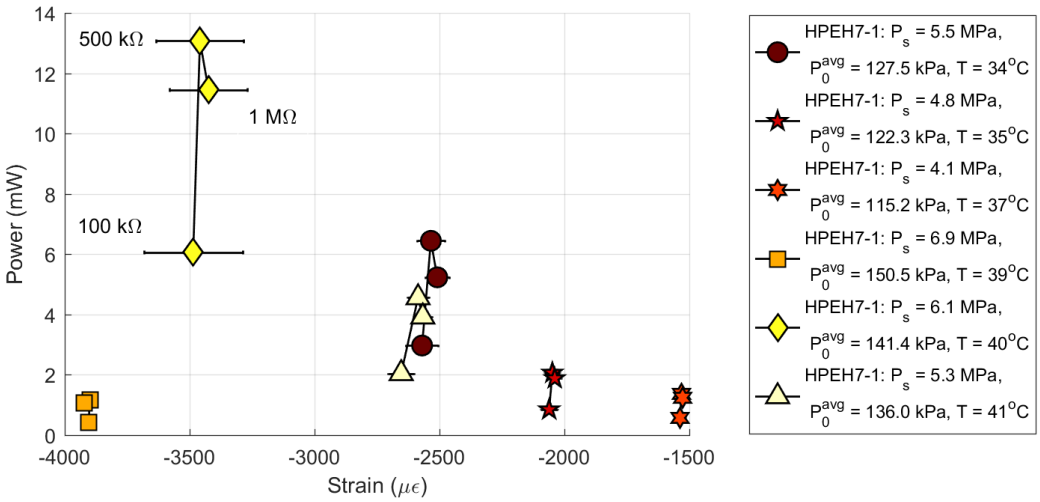

Figure 4.21: Power with respect to strain for HPEH7-1 test results, where the errorbars indicate the standard deviation of the strain cycle. Order of legend is order of tests; color is indicative of temperature; level of resistive loads is indicated for one sweep, where unlisted sweeps followed the same pattern.

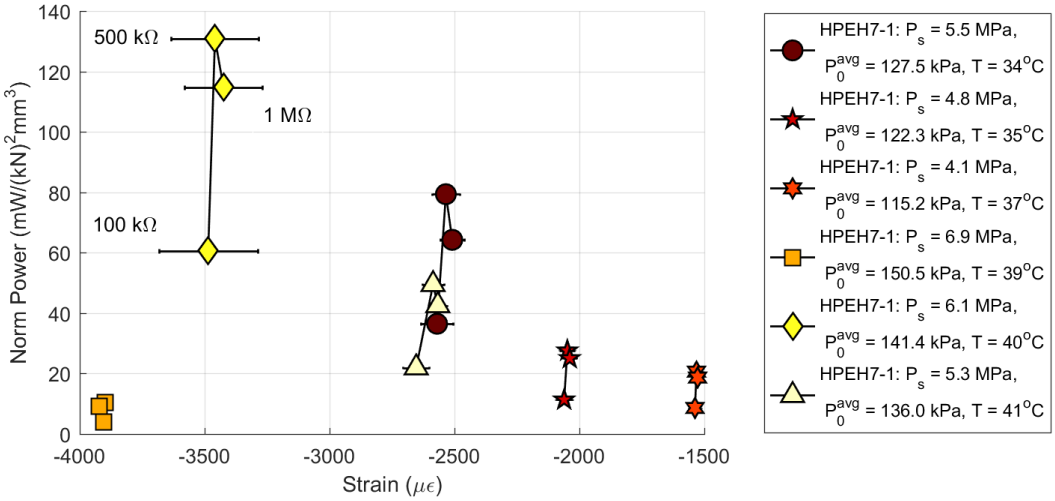

Figure 4.22: Power normalized by squared dynamic force and piezoelectric volume with respect to strain for HPEH7-1, where the errorbars indicate the standard deviation of the strain cycle. Order of legend is order of tests; color is indicative of temperature; level of resistive loads is indicated for one sweep, where unlisted sweeps followed the same pattern.

As shown in Chapter 2, the key indication of an HPEH performance is the power response normalized by the squared dynamic pressure and volume of piezoelectric material. This comparison for HPEH7-1 to all other HPEH devices when tested with resistive load only is made in Figure 4.23. HPEH7-1 contained a [011] cut PIN-PMN-PT single crystal that had minor damages, and was designed to include a force shunt and area amplification in order to induce conditions for phase transformation. When undergoing phase transformation, HPEH7-1 was the highest performing device, and nearly an order of magnitude above devices that do not contain a relaxor-PT based ferroelectric. When not under phase transformation, the device still performed on par or above other HPEH devices.

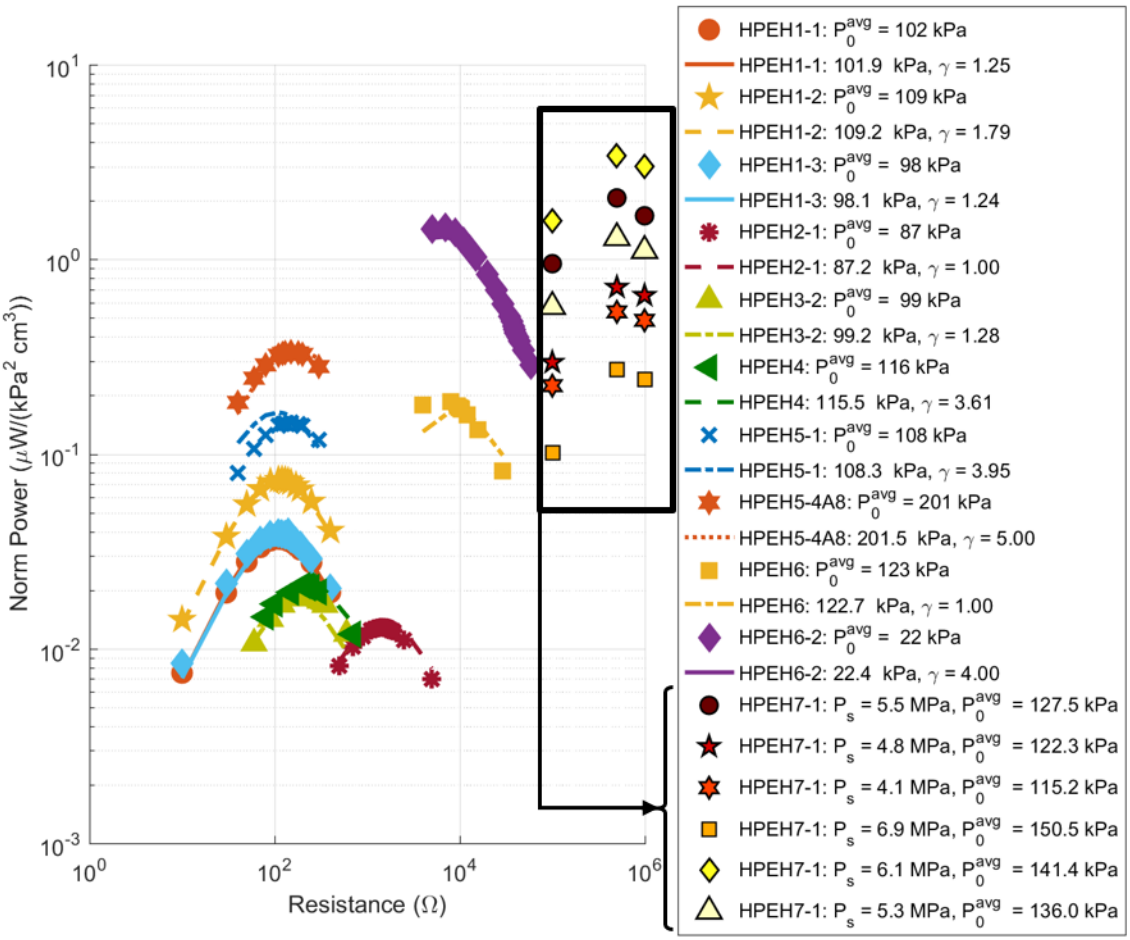

Figure 4.23: HPEH7-1 power normalized by squared dynamic pressure and single crystal volume compared to all other HPEH prototypes (normalized by volume of piezoelectric material and squared dynamic pressure).

4.4 Conclusions

Research in materials has shown that ferroelectrics undergoing phase transformation have great potential for energy harvesting applications. In addition, methods for comparing a materials' performance within an HPEH device were elucidated, including phase transformation transition point changes due to increasing oil temperature. Two types of tests were performed in order to test [011] cut PIN(0.24)-PMN-PT single crystal specimens within HPEH devices: 1) shaker tests, which allowed applied forces to be measured, and 2) a HPEH device specifically designed to induce phase transformation within the single crystal while coupled to the hydraulic pressure ripple.

In addition to presenting results from tests on this material at higher frequency and resistive loads than previously published, this work provides an initial design and results of phase transformation energy harvesting induced from a naturally occurring ambient energy source found within hydraulic systems. The two ferroelectric materials presented (labelled HPEH6 and HPEH7) both have the highest normalized power performance (accounting for area ratio, dynamic pressure, and piezoelectric material volume) when undergoing partial phase transformation. In addition, HPEH7-1 had the highest power per volume and squared dynamic pressure despite having a small crack form prior to testing.

While the phase transformation allows for orders of magnitude higher power performance, there are a number of drawbacks. First, the material response changes drastically when within a phase transformation zone versus linear region. This may cause issues for power conditioning or predictions of power performance. This is a challenge that will need to be addressed prior to implementing outside of a laboratory environment, as hydraulic systems do not typically operate at a constant static pressure and or constant temperature. Second, this material is brittle and easy to damage. While a damaged specimen still performed well, this aspect may be an issue with respect to the longevity of an energy harvesting device implementing a single crystal. If the specimen cannot last longer than current batteries on the market, implementing energy harvesters with phase transformation may be a waste of resources. Fatigue life and crack formations must be considered prior to implementing outside of a laboratory environment. Assuming these issues can be addressed, the domain engineered ferroelectric materials are highly recommended for energy harvesting due to their high power performance, and were the highest performing materials tested for this work.

CHAPTER 5

POWER CONDITIONING

Hydraulic pressure energy harvester (HPEH) devices convert acoustic power to electric power by exciting piezoelectric stacks off-resonance, which produces a low-voltage, low-frequency alternating current power response. It is necessary to determine an efficient power conditioning method to make this energy harvesting solution viable for powering sensors or recharging batteries. Power conditioning can refer to changing the voltage level (i.e. raising or lowering voltage, depending on device) or rectifying the alternating current (AC) to direct current (DC), or often a combination of both. To illustrate, if a component requires approximately 2.4V DC input voltage level (analogous to two series AA batteries), then AC must be converted to DC and the level of the voltage needs to be adjusted to match the component requirement. This chapter introduces a modified voltage multiplier circuit and model to solve this problem inherent in energy harvesters using piezoelectric stacks excited off-resonance.

Portions of this chapter have been published and presented at SPIE Active and Passive Smart Structures and Integrated Systems 2016 [112].

5.1 Power conditioning of low-voltage, low-frequency energy harvesters

Piezoelectric energy harvesting and power conditioning has been widely studied for typical high voltage scenarios (10s of volts), however limited research has been done for low-voltage (less than 1V) piezoelectric stack energy harvesters [3, 113, 114]. Off-resonance piezoelectric stack energy harvesting produces AC voltages typically less than 1 V, which is exhibited in hydraulic pressure energy harvesters [11, 58]. In order to charge

a storage component, initial power conditioning of such devices requires both boosting the voltage level in addition to rectification, both of which have been studied for electromagnetic energy harvesting and piezoelectric cantilevers aimed for MEMS devices.

Two methods that have been used for power conditioning of low-frequency low-voltage level energy harvesters include (1) using a transformer plus an AC-DC rectification component, such as a diode bridge, or (2) using a voltage multiplier [115]. A voltage multiplier simultaneously raises the voltage level and rectifies the current, which can reduce the overall energy circuitry complexity [115], and is beneficial when high voltage transformer winding is inconvenient [116].

Concerning method (1), Garbuio, et al. performed low threshold rectification of a piezoelectric energy harvester beam by using a Synchronized Switch Harvesting on Inductor with Magnetic Rectifier (SSHI-MR), which is similar to a series SSHI technique except that the inductive element is replaced with a transformer [117]. Conversely, Ching, et al., demonstrated the use of a voltage multiplier employing Schottky diodes with an electromagnetic generator [118]. James, et al. employed a low-frequency (50-300 Hz) magnetic coil generator to compare the power efficiencies and size of power conditioning circuits using a transformer and diode bridge versus a voltage multiplier. James, et al. reported that the voltage multiplier circuit provided the more space and weight efficient solution, while the power performance was comparable [115].

Torah, et al. [119] and Saha, et al. [120] developed an electromagnetic generator intended for office air conditioning units, which have resonant peaks between 40 and 50 Hz. One paper focused on a complete “autonomous wireless condition monitoring sensor system,” which used a voltage multiplier circuit and a microcontroller subsystem to enable

cold-start power conditioning [119]. The other effort used a circuit analogous to a voltage multiplier, however employed active switches and comparators instead of diodes [120].

Cheng, et al. used an active voltage doubling AC-DC converter for use with low-voltage, low frequency energy harvesting components; they used active components (comparator and MOSFET) which require a very low supply voltage, meaning the quiescent power consumption of the active components of 560 nW is comparable to the dissipated power within a Schottky diode, estimated around 600 nW [121, 122]. It is noted that the external power supply for the active elements can be eliminated via a later stage; in the same research group, this concept was shown with an energy harvester power conditioning method with active elements that eliminated standby power by shutting down when the input voltage amplitude was too low [123].

The present work is intended for energy harvesting devices that employ piezoelectric stacks producing low-voltage levels, such as seen in hydraulic pressure energy harvesters. As discussed in the previous chapters, HPEH devices are excited by the acoustic pressure within hydraulic systems, which is typically concentrated in the 100s of Hz range depending on operating conditions. During the course of this project, HPEH prototypes demonstrated the ability to power a thermocouple and wirelessly transmit the readings using a commercially available power conditioning circuit (Cymbet CBC-EVAL-09) intended for electromagnetic generators and MEMS devices, details of which were presented in [124], which uses a bridge rectifier and low-voltage charge pump; however the input force was an order of magnitude higher than will be demonstrated here. As previously demonstrated by Figure 1.3, water and sewage pipes have lower acoustic pressure levels than high-pressure fluid power systems, such as excavators, which

necessitates the analysis and refinement of power conditioning methods specifically for HPEH devices.

The following focuses on implementing a voltage multiplier to rectify the low-voltage AC output from a piezoelectric stack excited at low frequencies relative to its fundamental resonance frequency, schematically shown in Figure 5.1. Voltage multipliers were chosen for their passive nature, ability to simultaneously rectify the current and raise the voltage level, and because they typically have lower forward voltage requirements than diode bridges. Since piezoelectric stacks excited at low frequencies are conducive to RL shunting, as shown earlier [58], an inductor can be placed in parallel with the piezoelectric stack to counteract the reactance of the piezoelectric stack capacitance, shown in Figure 5.1b. In the remaining portion of the chapter, first this system is simulated numerically in SPICE environment, and then modeled and analyzed using the method of harmonic balance. In an experimental setting, an electrodynamic shaker is used to excite the piezoelectric stack and power conditioning circuit, with the results compared to the model.

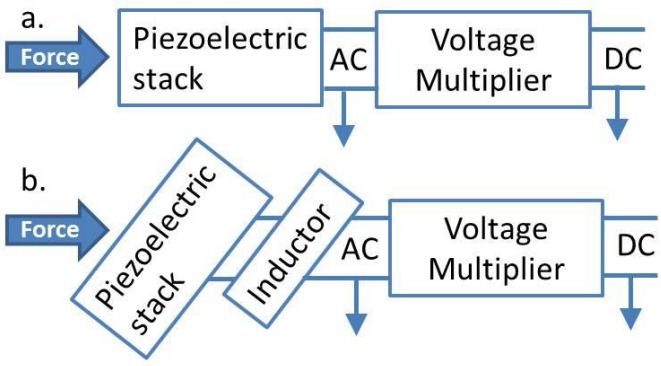

Figure 5.1: Piezoelectric stack AC-power rectified using a voltage rectifier with: (a) no inductive component and, (b) matched impedance inductive load.

5.2 Methodology

A piezoelectric stack excited off-resonance can be represented using a current source in parallel with its internal capacitance, as seen in Figure 5.2. The current source is the product of the piezoelectric strain constant for the stack, d_{33}^{eff}, and the time derivative of the force excitation, $\dot{F}$; the capacitive term is the total capacitance of the stack, C_p. The voltage multiplier implemented in this study is a voltage quadrupler with four Schottky diodes. Schottky barrier diodes may be modeled using the Shockley diode expression,

$$i_D = I_s\left[\exp\left(\frac{v_D}{nV_T}\right)-1\right], \tag{5.1}$$

where I_s is the reverse current, v_D is the voltage at the *p*-*n* junction, $V_T = k_b T_K/q$ is the thermal voltage, estimated as 26 mV at room temperature, and n is the quality or ideality factor, which ranges between 1 and 2 depending on the diode. Although the experimentally measured characteristics have been found to be more complex, especially with low voltage levels, [125], this model will be used for its simplicity with the acknowledgment that as the circuit load changes, the corresponding ideality parameters may change. The model also assumes the ideality factor and saturation current is the same for each diode, noting that the value used may not correspond directly to a single diode, but rather the group.

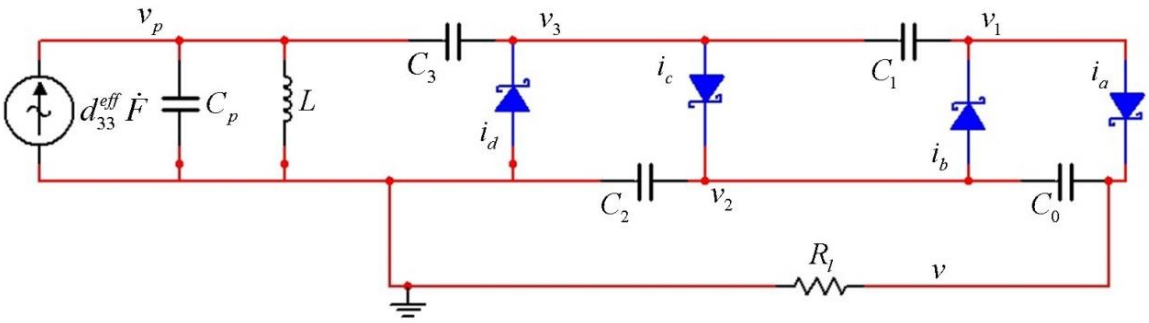

Figure 5.2: Power conditioning circuit schematic for piezoelectric stack with parallel inductive load, voltage multiplier, and a resistive load.

The circuit represented in Figure 5.2 can be represented by

$$\begin{bmatrix} -C_p - C_3 & C_3 & 0 & 0 & 0 \\ C_3 & -C_3 - C_1 & C_1 & 0 & 0 \\ 0 & C_1 & -C_1 & 0 & 0 \\ 0 & 0 & 0 & -C_2 - C_0 & C_0 \\ 0 & 0 & 0 & C_0 & -C_0 \end{bmatrix} \begin{bmatrix} \dot{v}_p \\ \dot{v}_3 \\ \dot{v}_1 \\ \dot{v}_2 \\ \dot{v} \end{bmatrix} + \begin{bmatrix} B_p \\ B_3 \\ B_1 \\ B_2 \\ B_0 \end{bmatrix} = \begin{bmatrix} 0 \\ 0 \\ 0 \\ 0 \\ 0 \end{bmatrix} \tag{5.2}$$

with the vector B terms defined as

$$\begin{aligned} B_p &= d_{33}^{eff}\dot{F} - i_L \\ B_k &= I_s \begin{vmatrix} \exp(-v_k/nV_T) & \exp(v_k/nV_T) \\ \exp(-v_{k-1}/nV_T) & \exp(v_{k+1}/nV_T) \end{vmatrix}, \text{ for } k = 1 \ldots N-1 \\ B_N = B_3 &= I_s \begin{vmatrix} \exp(-v_3/nV_T) & \exp(v_3/nV_T) \\ \exp(-v_2/nV_T) & 1 \end{vmatrix} \\ B_0 &= I_s \begin{vmatrix} \exp(-v/nV_T) & 1 \\ 1 & \exp(-v_1/nV_T) \end{vmatrix} - \frac{v}{R_l} \end{aligned} \tag{5.3}$$

where i_L is the current across the inductive load. This expression can be expanded or reduced depending on the number of voltage doublers in use. Also note that the voltage and B terms with subscripts p, 3, and 1 are related to AC-voltage responses, while the terms with subscripts 2 and 0 are related to DC-voltage responses.

Equation (5.2) may be rearranged to a format conducive to state-space representation,

$$\begin{bmatrix} \dot{\mathbf{v}}_{\mathbf{A}} \\ \dot{\mathbf{v}}_{\mathbf{D}} \end{bmatrix} = \begin{bmatrix} \mathbf{A} & \mathbf{0} \\ \mathbf{0} & \mathbf{D} \end{bmatrix} \begin{bmatrix} \mathbf{B}_{\mathbf{A}} \\ \mathbf{B}_{\mathbf{D}} \end{bmatrix}$$

$$\dot{\mathbf{v}}_{\mathbf{A}} = \begin{bmatrix} \dot{v}_p \\ \dot{v}_3 \\ \dot{v}_1 \end{bmatrix},\ \mathbf{A} = \begin{bmatrix} C_p^{-1} & C_p^{-1} & C_p^{-1} \\ C_p^{-1} & C_p^{-1}+C_3^{-1} & C_p^{-1}+C_3^{-1} \\ C_p^{-1} & C_p^{-1}+C_3^{-1} & C_p^{-1}+C_3^{-1}+C_1^{-1} \end{bmatrix},\ \mathbf{B}_{\mathbf{A}} = \begin{bmatrix} B_p \\ B_3 \\ B_1 \end{bmatrix}, \tag{5.4}$$

$$\dot{\mathbf{v}}_{\mathbf{D}} = \begin{bmatrix} \dot{v}_2 \\ \dot{v}_0 \end{bmatrix},\ \mathbf{D} = \begin{bmatrix} C_2^{-1} & C_2^{-1} \\ C_2^{-1} & C_2^{-1}+C_0^{-1} \end{bmatrix},\ \mathbf{B}_{\mathbf{D}} = \begin{bmatrix} B_2 \\ B_0 \end{bmatrix}$$

where **A** and **D** are related to the AC-voltage and DC-voltage responses, respectively. To facilitate numerical simulations, the nondimensional state space is defined as

$$\mathbf{u}' = \mathbf{f}(\tau, \mathbf{u}), \tag{5.5}$$

where **u** is the nondimensional state vector and $()'$ is the derivative with respect to nondimensional time, τ. This leads to the system state representation using characteristic time T_c and voltage V_c scales, with the variables defined as follows:

$$\begin{aligned} &i_L = u_1,\ \ \frac{\partial i_L}{\partial t} = u_1{}' = \frac{v_p - R_{int} i_L}{L} \\ &v_p = u_2 V_c,\ \dot{v}_p = u_2{}' V_c / T_c \\ &v_1 = u_3 V_c,\ \dot{v}_1 = u_3{}' V_c / T_c \\ &v_2 = u_4 V_c,\ \dot{v}_2 = u_4{}' V_c / T_c \\ &v_3 = u_5 V_c,\ \dot{v}_3 = u_5{}' V_c / T_c \\ &v = u_6 V_c,\ \dot{v} = u_6{}' V_c / T_c \end{aligned} \quad . \tag{5.6}$$

and the Jacobian matrix of the system is

$$J_{ij} = \frac{\partial f_i}{\partial u_j}. \tag{5.7}$$

Further details regarding the implementation of the method of harmonic balance, including the code modified for simulation, can be found in [126].

For harmonic excitation, the impedance of an inductive load and a parallel RC circuit can be represented as

$$\begin{aligned} Z_s &= R_{in} + j\omega L \\ Z_e &= \left(j\omega C_p + \frac{1}{R_{in} + j\omega L} \right)^{-1}, \end{aligned} \tag{5.8}$$

where ω is the angular frequency, L is the inductive load, and R_{int} is the series parasitic resistance of the inductor. In order to counteract the reactance caused by the piezoelectric capacitance, the power-optimized shunt inductance is predicted to be

$$L = \frac{1}{\omega^2 C_p} \left(\frac{1 \pm \sqrt{1 - \left(2\omega C_p R_{in} \right)^2}}{2} \right), \tag{5.9}$$

which is the optimal inductance for an RL shunt with high resistive load.

5.3 Results

To verify the model simulations, a soft-PZT piezoelectric stack was excited with a shaker at an excitation frequency of 450 Hz with measured root-mean-square (RMS) force input of 2.0 N_{rms}. Schottky diodes (1N5817) were used, which have a maximum instantaneous forward voltage between 0.32 to 0.75 volts, depending on the current [127]. A smoothing capacitor of 2200 μF was used to reduce the ripple of the DC response, in combination with three the other capacitors. The circuit board and test setup can be seen in

Figure 5.3, and the measured value for each respective component is listed in Table 9. Two circuits were tested: (1) circuit A used the same size capacitors as the smoothing capacitor, and (2) circuit B, which was formulated to minimize capacitor size while maintaining low ripple level (less than 0.1%) as suggested by Brugler [116].

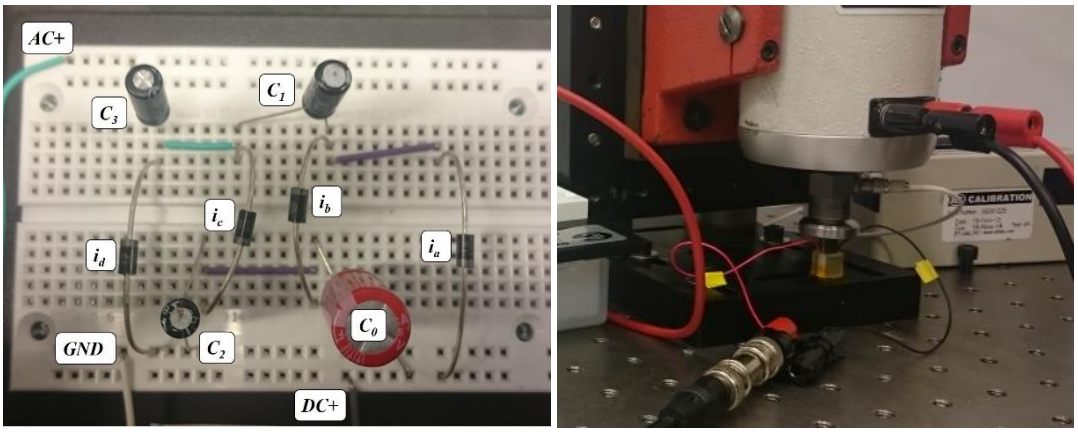

Figure 5.3: (left) Voltage multiplier (circuit B) bread-board and (right) piezoelectric stack excited via shaker, connected to harvesting circuit.

Table 9: Measured parameters of tested system.

Parameter	Circuit A	Circuit B
Piezoelectric strain constant, d_{33}^{eff}	141.9 nC/N	141.9 nC/N
Piezoelectric capacitance, C_p	1.93 µF	1.93 µF
VM capacitor, C_0	2330 µF	2330 µF
VM capacitor, C_1	2300 µF	9.5 µF
VM capacitor, C_2	2320 µF	9.7 µF
VM capacitor, C_3	2320 µF	24 µF
RMS force, F	2.0 N_{rms}	2.0 N_{rms}
Excitation frequency, f	450 Hz	450 Hz

In addition to the voltage multiplier (VM) model described previously, multiple circuits were simulated using National Instrument's Multisim transient analysis, which is

a SPICE-based simulator, including bridge rectifier circuits. It was determined that this circuit schematic would be a reliable test for demonstrating the concept, verifying the harmonic balance VM model, and showing better performance than a bridge rectifier for this system, since the AC input is very low. Figure 5.4 shows the comparison between tested results and simulation. The simulation under-predicts the observed response by approximately 22%.

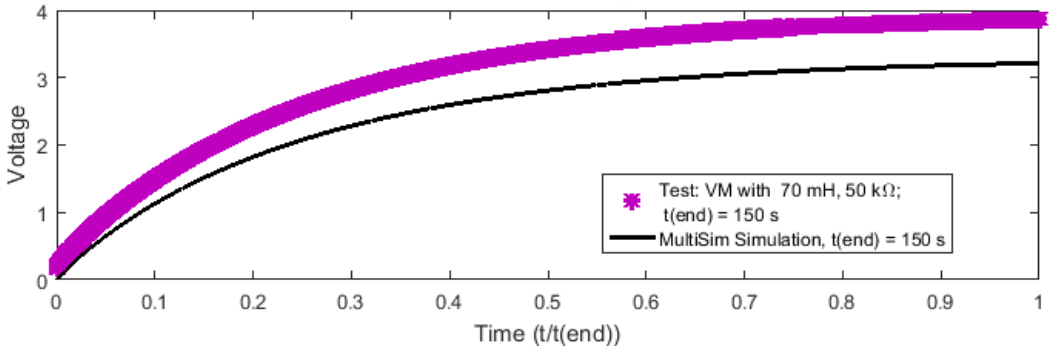

Figure 5.4: NI MultiSim circuit A model compared to circuit A test results using equivalent parameters.

Both inductive load sweeps and resistive load sweeps were performed. The VM inductive load sweep held the resistive load at 50 kΩ, and the VM resistive load sweep held the inductive load at 66 mH. For the tested system, the inductance load for minimizing circuit reactance was predicted to be near 66 mH. It should be noted that determining the optimal inductive load may require an iterative process because it is dependent on the inductive series parasitic resistance, which may be difficult to determine prior to knowing the general range of the optimal inductance.

The time response results for the inductive load of 66 mH and the highest resistance load tested (100 kΩ) is shown in Figure 5.5, indicating steady state was reached. Note, each capacitor was discharged prior to testing, however the system did not begin recording until a force excitation trigger value of 2 Nrms was obtained; this is why the results shown

for t(0) = 0 s start at voltage levels above zero. Circuit B reached steady-state faster than circuit A and will be used for the VM harmonic balance method (HBM) model analysis. Otherwise, the circuits tested had similar performance results for a given inductive and resistive load pairing, with deviation of the results being less than 5% of the average.

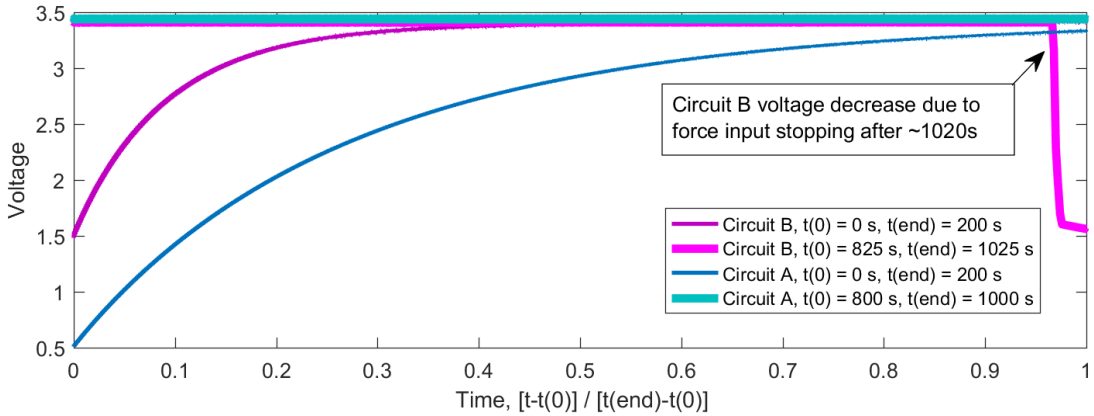

Figure 5.5: Time response of test results reaching steady state for R = 100 kΩ, L = 66 mH and excitation frequency at 450 Hz for the two circuits tested. Time normalized by total time displayed, 200 seconds.

The HBM for the given system was used with the diode ideality factor set to n = 1.7, the saturation current set to 10^{-13} A, the measured inductive loads with corresponding measured internal resistive loads, and all previously defined parameters. The validity of this assumption is discussed in Section 5.4. The voltage and power results for the VM HBM with inductance are shown in Figure 5.6 as the solid lines, and the test results are shown as colored points. The percent error between the VM HBM and tested power results is shown in Figure 5.7. The minimum error between the power model and test results was 0.6%, however the average error was 528% (with a standard deviation of over 1000 points, and maximum error of 5298%). A summary of the peak power results is summarized in Table 10. The average error level is greatly decreased in the next section, which assumes the saturation current and ideality factor change as a function of the inductive load.

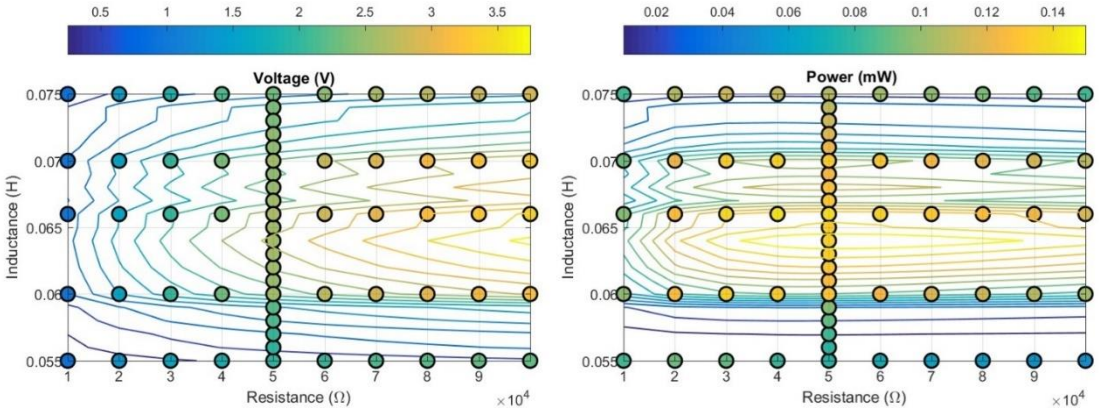

Figure 5.6: Voltage level and power level for 2 N_{rms} excitation force at 450 Hz (points) compared to modeled results (lines), which uses saturation current $I_s = 10^{-13}$ and ideality factor $n = 1.7$.

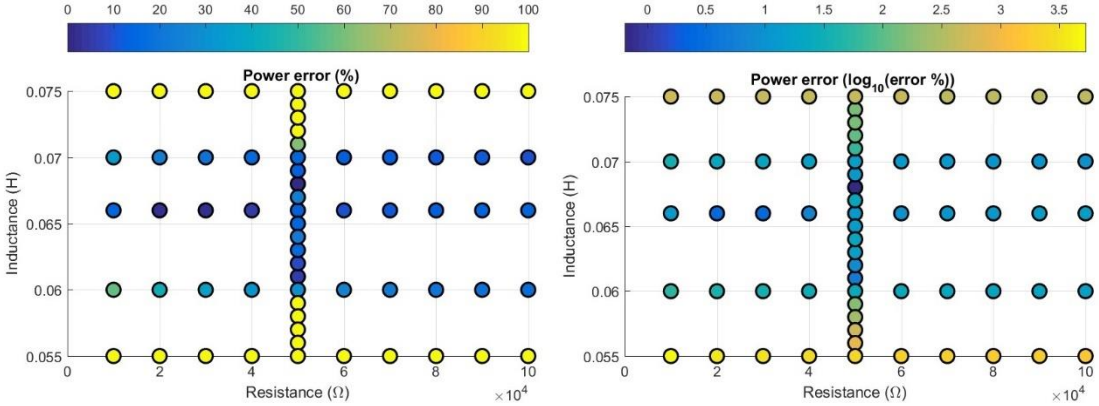

Figure 5.7: Power error in percentage (lefthand graph; colorbar capped to 100%) and the percent error on a base-10 logarithmic scale (righthand graph; $\log_{10}$(error %)) for the modeled case where saturation current $I_s = 10^{-13}$ and ideality factor $n = 1.7$.

Table 10: Comparing measured and modeled results (for Circuit B, f = 450 Hz, F = 2 Nrms, n = 1.7, Is = 10-13).

Description	Power (µW)	Voltage (V)	L (mH)	R (kΩ)
RLC Max. Modeled	238	0.59 (rms)	64	1.478
VM Max. Measured	141.6	2.4	66	40
VM Corr. Simulated	136	2.3	66	40

The peak average power that can be expected from this energy harvester is deemed limited to the peak RLC average power for the given excitation level, which was modeled to be 238 µW. The maximum measured power from the VM circuit was 141.6 µW, with a corresponding voltage level of 2.4 V_{DC}; this corresponds to an efficiency of 59%, where

efficiency is defined as the percent ratio of the DC-power over the maximum AC-power. The model error increases as the tested inductance value deviated from the inductive shunt that minimize the reactance, as predicted by Eq. (5.9). While the voltage and power levels of the model predictions are not accurately depicted when assuming a constant ideality factor and saturation current for each diode, the resistive and inductive loads for the peak power points corresponded to the measured peak power points, which is useful for estimating optimal loads.

5.4 Discussion

The modified VM HBM with inductance modeled results in the previous section assumes a single ideality factor and saturation current for all four diodes in the circuit. However, the voltages across each diode vary, and for loading cases where the resistive load is low or the inductive load is not matched, the voltage levels are predicted to reach as low as 0.3 V. The modeled voltage level for each voltage node defined by Figure 5.2 is shown in Figure 5.8. As explained in section 5.2, the low voltage levels may cause the ideality factor and saturation current needed to model a diode to vary. The following section will investigate how the model can be improved by accounting for effects on the combined diode parameters due to some diode voltage levels being lower than others, depending on the shunt loading and location in the cascade.

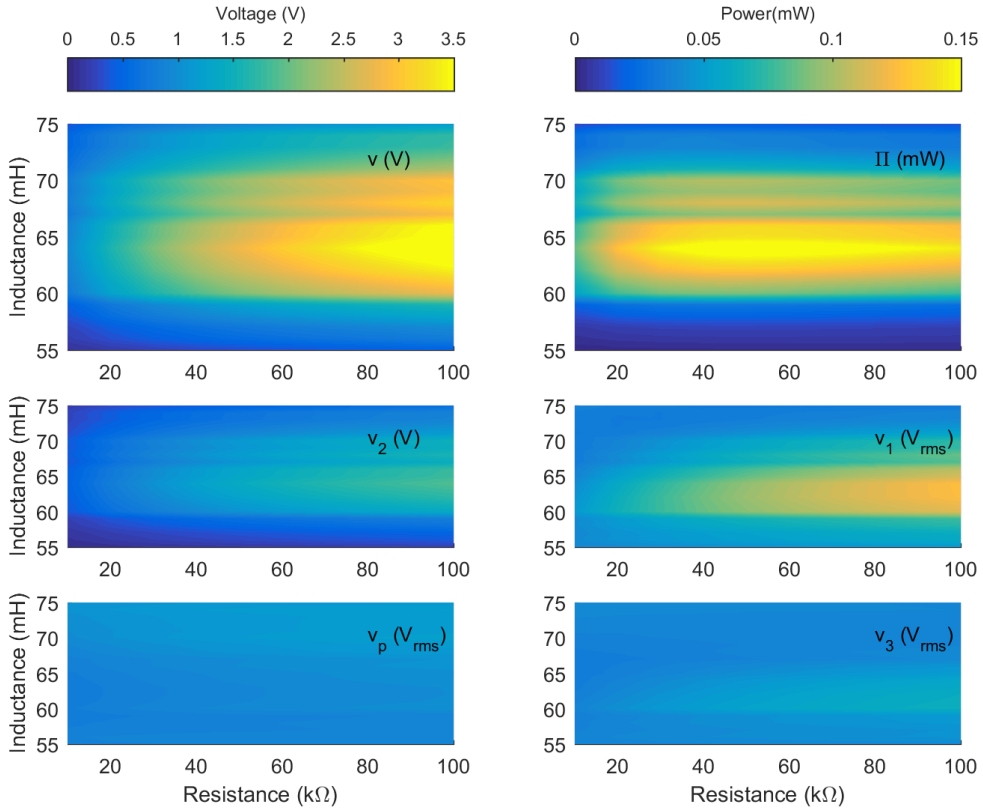

Figure 5.8: Modeled voltage level for each node for Circuit B and corresponding power level.

To further investigate the change in the group ideality factor n and group saturation current I_s from Eq. (5.3), the model is compared to the test results with either the ideality factor varying between 1 and 2, shown in Figure 5.9, or the saturation exponent z varying between -9 and -13 with the saturation current equaling 10^z, shown in Figure 5.10, while the other variable stays constant (either $I_s = 10^{-13}$ or $n = 1.7$, respectively). The results indicate that the group diode parameters change with the voltage levels and the piezoelectric reactive components.

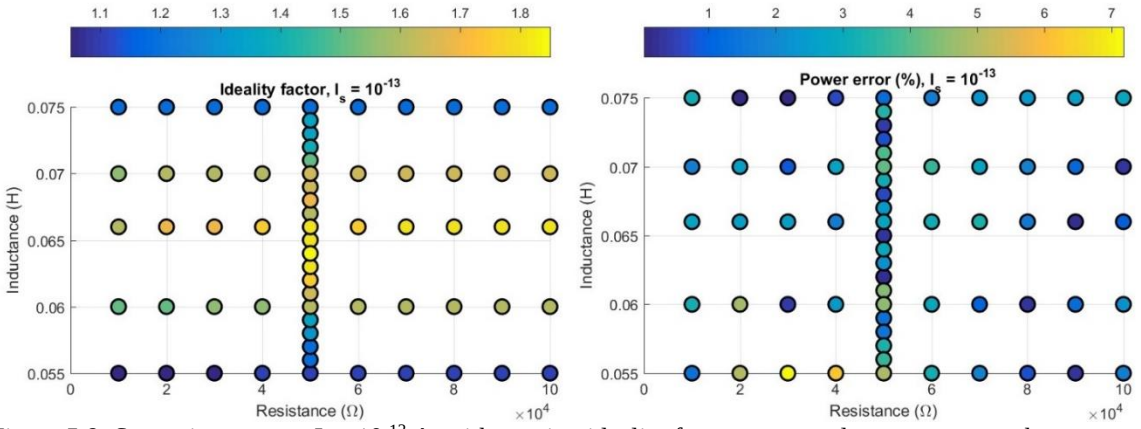

Figure 5.9: Saturation current $I_s = 10^{-13}$ A, with varying ideality factor compared to percent error between test result power levels and modeled power levels.

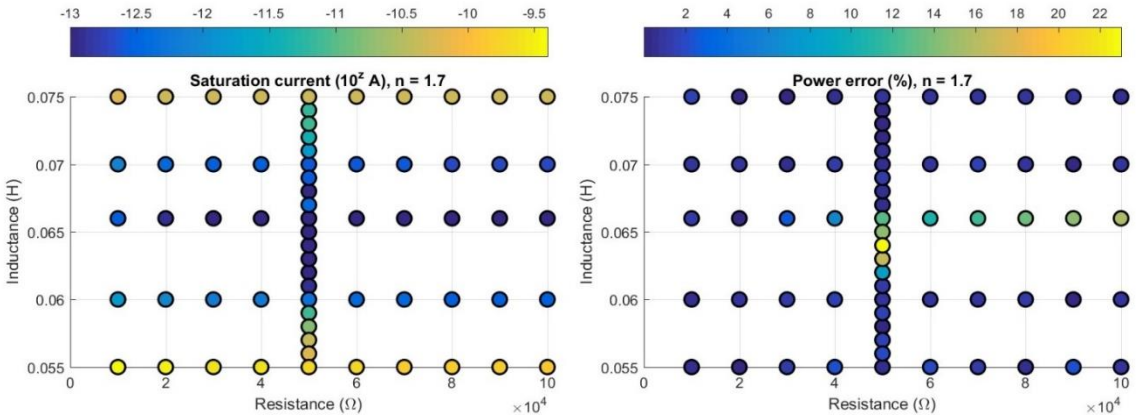

Figure 5.10: Ideality factor $n = 1.7$, with varying saturation current compared to percent error between test result power levels and modeled power levels; the saturation current colorbar scale shows the power z of the saturation current 10^z.

To provide a more accurate VM with inductance HBM model that accounts for the change in group diode parameters, both the ideality factor and saturation current were simultaneously varied and the group diode values that corresponded to the least power error were plotted with respect to changing inductance. A quadratic fit with respect to the inductive load sweep was used to estimate the ideality factor and the saturation current. Figure 5.11 shows the HBM model power results and error that uses the ideality factor as a function of inductance and saturation current as a function of inductance.

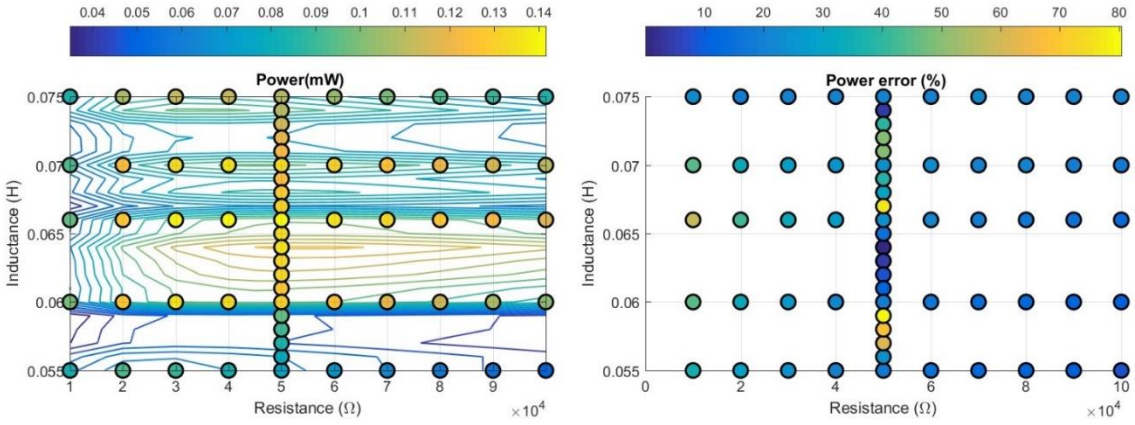

Figure 5.11: Test results compared to VM HBM model where saturation current and ideality factor values change as a function of inductance: $n = (-4.6e3)L^2 + (6.1e2)L - 18.3;$
$I_s = 10^z;\ z = (1.4e4)L^2 - (1.8e3)L + 45.$

The HBM model predicts the VM with inductance response with less overall error, with average error of 25% (standard deviation of 16 points, minimum error of 0.06%, maximum error of 80%). Higher error occurs in three general cases. The first case occurs when the modeled inductive load is far from the inductive load predicted to minimize circuit reactance, which causes a lower initial voltage level. The second case occurs when the resistive load is relatively small, thus also causing a lower expected initial voltage level. The third case is an inductive load near the predicted peak, however if the capacitance of the piezoelectric stack varies from the value used in the model, the predicted matching inductive load also varies. This would change the overall voltage level for a given inductive value. For each case, the model under predicts the voltage level. The squared voltage level is proportional to the power, and thus the underpredicted voltage causes higher error in the average power predicted. For the first two cases, underpredicting voltage response is expected to be inconsequential as one goal is to determine the resistive and inductive loads which produce the maximum power, and these locations are not near local maxima. These

errors may be due in part to the Shockley diode model used; implementing a more rigorous model that focuses on diode characteristics near the forward voltage lower limits may improve the HBM model accuracy. The third case is likely due to the piezoelectric capacitance varying, which would require a more rigorous model of the piezoelectric material or incorporating the capacitance measurements for each test; currently the model assumes the capacitance of the piezoelectric material is constant. The model does show trends for a piezoelectric stack with constant capacitance, and from this the resistive and inductive loads can be obtained for the maximum predicted power.

With the added ideality factor and saturation current fitted functions to predict the group diode parameters, the HBM model is able to predict power performance with similar accuracy as the SPICE-based time domain transient analysis, but with less overall computational time. By way of example, for the computer used for these analyses, the SPICE model for one loading case took 44 seconds; the HBM model described here with ideality factor and saturation current quadratic functions for all inductive and resistance loads shown, which totals 231 loading cases, only took 16 seconds.

5.5 Conclusions

This chapter investigated a power conditioning circuit for low voltage piezoelectric stack energy harvesters. A piezoelectric stack in parallel with a matched inductive load is used in combination with a voltage multiplier circuit to both increase the voltage level and rectify the current. The peak measured power for a 450 Hz, 2 N_{rms} excitation level was 142 µW with 2.4 V_{DC}, which corresponded to 59% efficiency. A voltage multiplier with parallel inductance harmonic balance method was analyzed and compared to the test results. Non-ideal diode behavior is accounted for using Shockley model. Model simulations compared

with experimental results with acceptable accuracy, and computational speed of VM HBM model was over 600 times faster than using a SPICE-based simulation. Future work to improve power conversion efficiency could include implementing active circuit components, such as a comparator and a MOSFET.

CHAPTER 6

CONCLUSIONS

Hydraulic systems contain low power sensors (e.g. pressure, temperature, health monitoring, etc.) are currently powered via wires or chemical-based batteries. This work presents and develops an energy harvester which converts pump-byproduct acoustic pressure into electricity to actualize self-sustaining hydraulic sensors. The hydraulic pressure energy harvester (HPEH) demonstrates piezoelectric stacks excited off-resonance can convert milliwatt level power from acoustic pressure within hydraulic systems.

HPEH development and research combines, implements, and builds from research in multiple subjects. Starting with hydraulics and noise control research, it identifies an unused energy source, and from recent wireless sensor developments within hydraulics, it motivates an energy harvesting solution. Building from research in energy harvesting and piezoelectric materials, the base for the electromechanical energy harvester and circuitry was developed. Research in tribology, hydraulic oil characterization, and noise control solutions contributed to the acoustic pressure amplification design, and thus increased power, applied to HPEH devices. Research in domain engineered ferroelectric materials contributed to the increased pressure ripple to electricity power transduction of HPEH devices. And research in electromagnetic energy harvesting power conditioning contributed to the low-voltage, high capacitance power conditioning solution developed for HPEH devices. A summary of the contributions of this work are as follows:

- Presents a hydraulic pressure energy harvester design and an electromechanical model, where optimal resistive-only and optimal parallel resistive-inductive load

circuits are derived (Section 2.2). Includes discussion of resistive-inductive load shunt efficiency and broadband nature. Model validation performed with HPEH prototypes tested on hydraulic rig (Section 2.3-2.4), including design developments to increase HPEH efficiency via area amplification (Section 2.4.2) and to increase hydraulic system static pressure range of use via force shunt ratio (Section 2.4.3). (Chapter 2)

- Designs, models, and implements narrow-port small-volume Helmholtz resonator (HR) on HPEH device. Derives and validates a narrow-port HR pressure gain model within hydraulic systems, including added compliance situations, both from incidental trapped air and intentionally incorporated syntactic foam (Sections 3.2.1, 3.3.1, 3.4.1, and 3.4.2). Discusses hydraulic oil HR design limitations caused by viscous layer effects and resonance drift (Section 3.4.1). Designs a HPEH device with small-volume HR and validates that its inclusion can increase power transduced by HPEH (Sections 3.2.2, 3.3.2, and 3.3.3). (Chapter 3 and Appendix A)
- Designs and implements a crystalline phase-transitioning acoustic pressure energy harvester, including presenting experimental results using hydraulic pump byproduct as energy source. Presents experimental results of PIN-PMN-PT material undergoing partial phase transition at an excitation frequency of 450 Hz (Section 4.3.1). Designs a HPEH for phase-transition energy harvesting on hydraulic system (Section 4.2.2). Validates that phase-transition can be induced via hydraulic pressure ripple and increases power transduced by HPEH (Section 4.3.3). (Chapter 4 and Appendix B)

- Develops, models, and implements an electromechanical power conditioning circuit intended for high-capacitive, low-voltage applications. The circuit both increases voltage level and rectifies current of piezoelectric stacks excited off-resonance. Circuit consists of a voltage multiplier with inductor, and is modeled with the electromechanical system via a computationally efficient harmonic balance modeling solution (Section 5.2). Model validated using a piezoelectric stack connected to a voltage multiplier with inductor circuit and excited via electrodynamic shaker (Section 5.3-5.4). (Chapter 5)

This work presents the development of an initial hydraulic pressure ripple energy harvesting design which implements a piezoelectric stack or single crystal within a housing that connects to a hydraulic port, such as for diagnostic sensors. Future work to consider is as follows:

- Implementing piezoelectric material within the layers of a hydraulic hose.
- Developing a combination of piezoelectret foam (see Anton et al. [128] as an example) with syntactic foam used in hydraulic suppressors (e.g. [87-90]) to provide an energy harvesting and noise control solution.
- Improving power conditioning through implementing active circuit components within the voltage multiplier with inductive load circuit.
- Improving the durability of phase transitioning material (or layers of material) or implementing a more conservative design of HPEHs using this material.
- Performing a hydraulic system work load study to determine best operating pressures if implementing a force shunt design; alternatively, designing a multi-

step spacer to account for changing system pressures while still converting pressure ripple and protecting the piezoelectric material.

APPENDIX A: HELMHOLTZ RESONATOR

A.1 Compliance of Helmholtz resonator housing

The outer housing of the Helmholtz resonator is made from 17-4 PH stainless steel, with the inner diameter of nominally 16.6 mm and outer diameter of 38.1 mm. The effective bulk modulus of the fluid within the cavity changed from 1.60 GPa to 1.56 GPa, which causes calculated resonant frequency to decrease by less than 15 Hz. The bulk modulus of the outer housing can be calculated via

$$K_{housing} = \left[\frac{2}{E_h} \left(\frac{r_o^2 + r_i^2}{r_o^2 - r_i^2} + \upsilon_h \right) \right]^{-1} \tag{7.1}$$

where E_h is the Young's modulus of the housing, υ_h is Poisson's ratio, and the subscripts on r stand for outer and inner radii [87]. The effective fluid compliance is thus

$$C_{fluid,eff} = V_{fluid} \left(\frac{1}{\rho_{fluid} c_{fluid}^2} + \frac{1}{K_{housing}} \right). \tag{7.2}$$

This change is not considered significant, because changing the neck diameter by 0.03 mm causes the resonant frequency to increase by slightly more than 15 Hz. This is demonstrated in Figure A.1. Since the tolerance for measuring the neck diameter had a greater effect than the outer housing on the resonant frequency, this parameter was neglected in the model presented. If the bulk modulus of shell approached the bulk modulus of the fluid, such as by decreasing the housing thickness, then this calculation may need to be included.

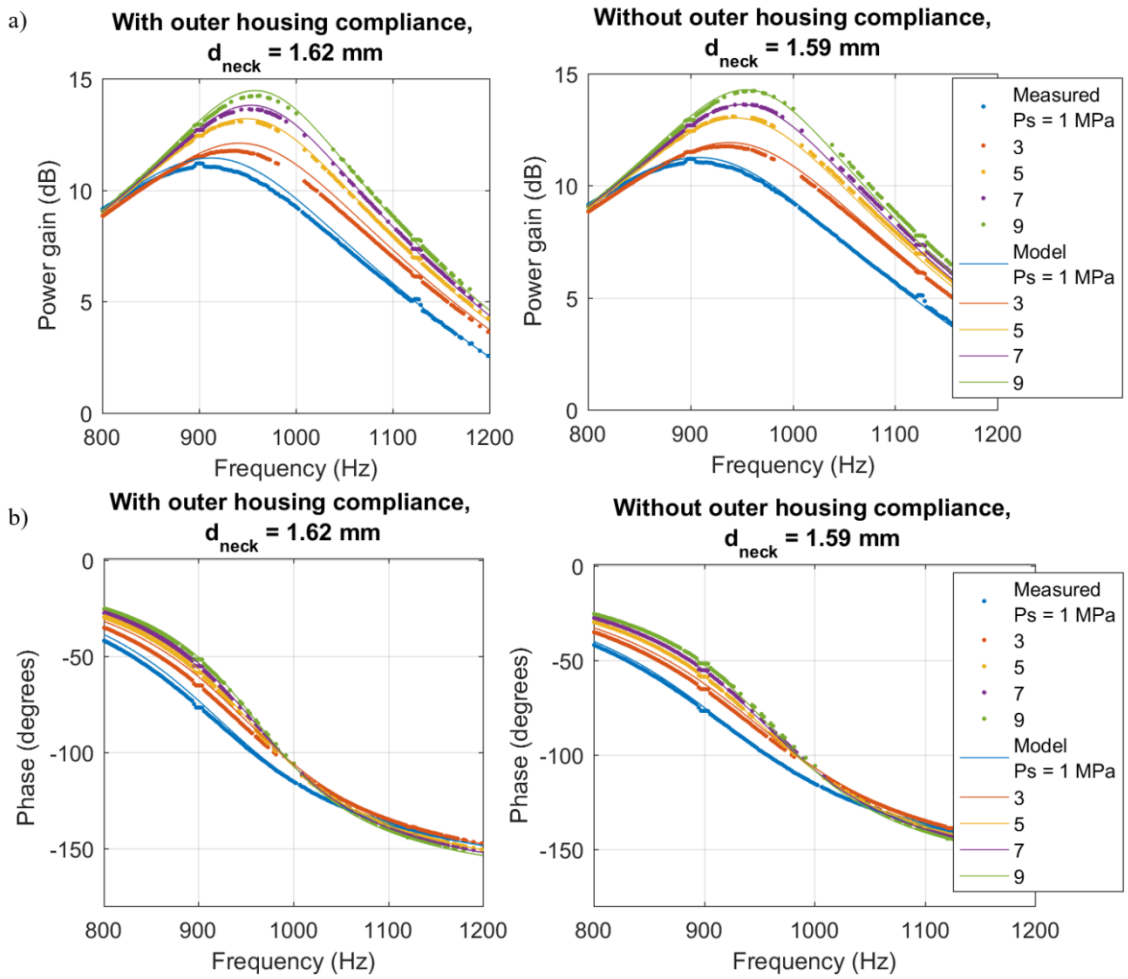

Figure A.1: Resonant frequency change due to neck diameter and housing compliance with respect to a) power gain and b) phase.

The stiffness of the piezoelectric stack used within the HPEH-HR device was measured to have a nominal stiffness of 11,860 kN/m; the spacer area was 182.4 mm^2. This indicates that length of cavity changes by less than 0.54 mm from 35 MPa system pressure, and only by 0.0031 mm from 200 kPa pressure amplitude. The resonance change caused by this is deemed minor, as demonstrated in Figure A.2, which compares the resonance and power gain change due to cavity length versus neck diameter. The power gain response is negligible for cavity length changes, and while there is a slight change in resonance

frequency, other factors (such as air compliance, neck diameter, viscosity of fluid) have a greater impact than this parameter.

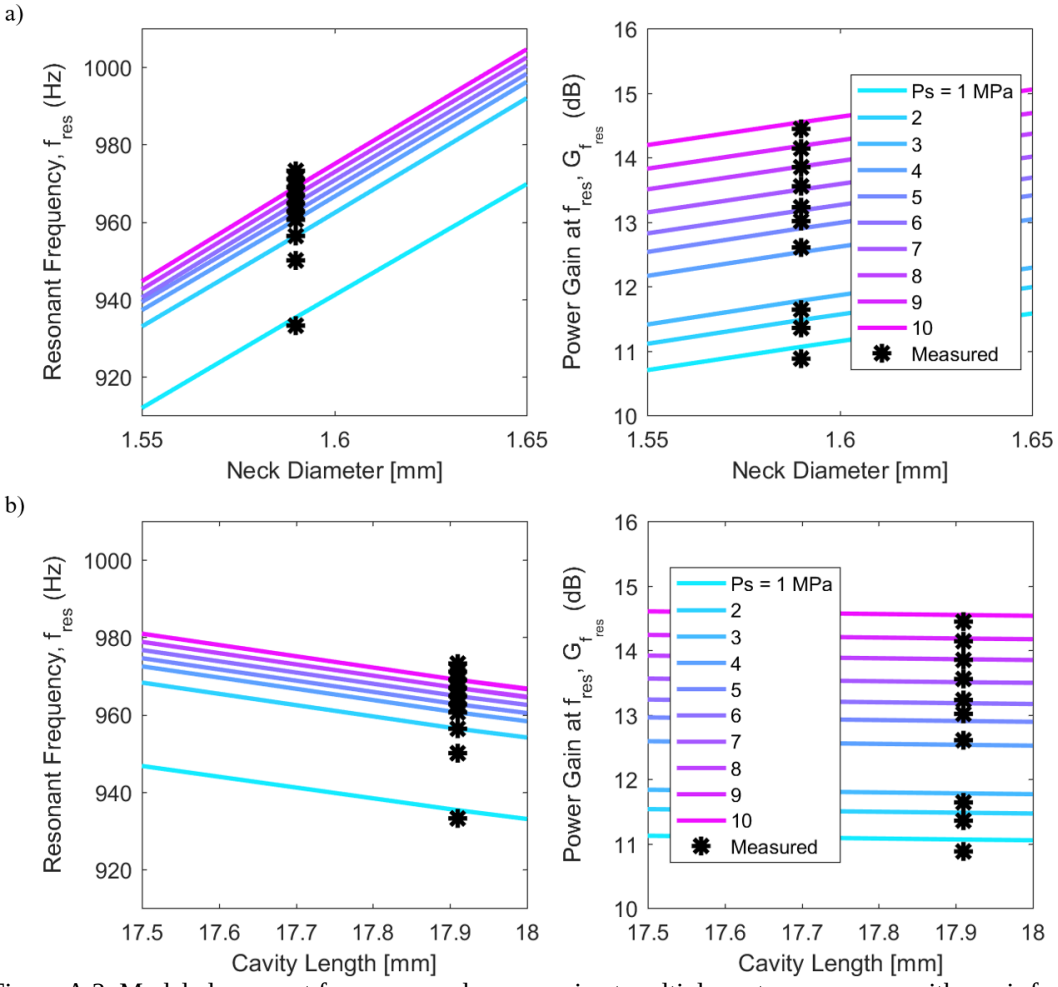

Figure A.2: Modeled resonant frequency and power gain at multiple system pressures with an air fraction of 0.0003 for a) neck diameter and b) cavity length.

A.2 Viscosity and volumetric expansion coefficient

Initial model results using the provided kinematic viscosity and typical volumetric coefficient of expansion of new oil had consistently over 10% error levels in power gain at resonance frequency; however, due to the hydraulic rig oil having been used for near or over the TOST oxidation lifetime (Turbine Oil Oxidation Stability Test, ASTM D943), the oil condition during experiments are expected to be different from the provided oil

properties. The viscosity and volumetric expansion coefficient of the hydraulic oil used in experiments were not measured using separate tests, but instead deduced from comparing Helmholtz resonator model and experimental results. The oil had been used frequently for four years prior to testing, so is likely different from manufacturer provided and referenced values (manufacturer provided: $\nu_{40°C}$ = 45 cSt, $\nu_{100°C}$ = 5.7 cSt at atmospheric pressure; typical oil volumetric expansion coefficient: α = 0.0007 1/°C at atmospheric pressure)[91, 92]. A test at ten static pressure levels using the Helmholtz resonator and cap with a pressure transducer port was used to analyze the average error of the model with different kinematic viscosity, volumetric expansion coefficient, and cavity volume air fraction values. It was found that $\nu_{40°C}$ = 64 cSt, $\nu_{100°C}$ = 5.7 cSt, α = 0.001 1/°C at atmospheric pressure worked well for the pre-filled test body experiments. A kinematic viscosity level of 64 cSt is an ISO 68 viscosity grade (rather than specified ISO 46 viscosity grade), however all viscosity values corresponding to ISO 46 cause high power gain error and frequency gain error. These values were then applied to all other modeling of the HR test body and HPEH experiments, with error values significantly reduced. If future measurements of the kinematic viscosity and volumetric expansion coefficient prove to match the manufacturer provided values, then the following numerical correction is either due additional thermoviscous losses not captured by the model, likely due to the narrow neck diameter, or due to the error caused by using the isothermal tangent bulk modulus rather than the adiabatic bulk modulus.

It should be noted that ISO Viscosity Grade 46 has a minimum kinematic viscosity value of 41.4 cSt and maximum of 50.6 cSt at 40°C[96]. Also, while not required, at 100°C, it typically has a minimum value of 6.22 cSt and maximum of 7.05 cSt[96]. The

manufacturer provided level was 45 cSt at 40℃ and 5.7 cSt at 100℃, with an average oxidation life of 1500 hours [91]. Oxidation can cause multiple lubrication issues, including increasing the oil viscosity[95]; the oil used in these tests likely was near or beyond its TOST oxidation life specification.

The volumetric expansion coefficient of unused oil is reported at $0.0007℃^{-1}$, however this also provided higher error levels. Levels up to $0.0014℃^{-1}$ were compared between the experiment and model.

The exact testing and filtering history of the oil within the rig is unknown by the author, however it was used frequently for 4 years prior to these tests, and was used for testing new syntactic foam materials (for noise suppression). The oil was never tested to ensure the kinematic viscosity levels corresponded to manufacturer values during the testing process, nor was the volumetric expansion coefficient tested to see if it matched the unused oil parameter.

As seen in Figure A.3, the manufacturer provided viscosity levels produced a power gain error of over 10% at the resonant frequency for all air volume fraction and volumetric expansion coefficient values. While the kinematic viscosity at 100℃ (which also corresponds to the viscosity index) had little effect on model accuracy, increasing kinematic viscosity at 40℃ from 45 cSt to 65 cSt caused the power gain error to decrease from over 10% to less than 1%. The air fraction can decrease the resonant frequency error, however has little effect on the power gain at resonance error. The volumetric expansion coefficient also affects both the resonant frequency error and power gain at resonant frequency error. At the unused value of $0.0007℃^{-1}$, the frequency error was greater than

the 0.001°C^{-1} and 0.0012°C^{-1} levels, as seen in the Figure A.3 callout. Greater than 0.0012°C^{-1} caused the frequency error to increase.

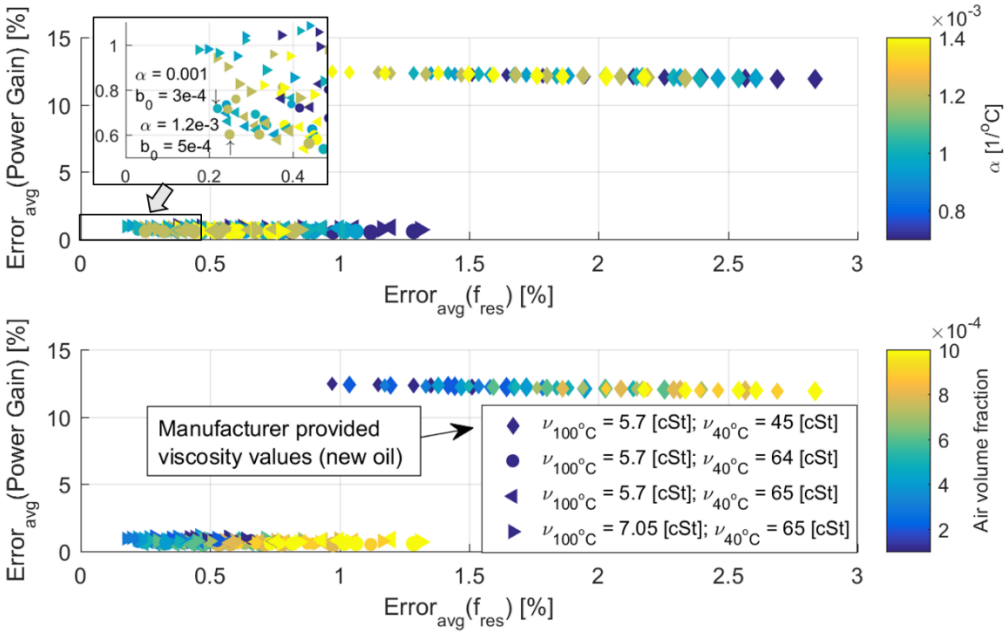

Figure A.3: Resonant frequency and power gain error with respect to volumetric expansion coefficient and air fraction volume for four kinematic viscosity combinations. Same data as Figure 3.7, except including callout.

The error change due to varying kinematic viscosity levels and multiple air fraction levels is shown in Figure A.4 for the two most accurate volumetric expansion coefficient levels tested of a) 0.001°C^{-1} and b) 0.0012°C^{-1}. Both graphs follow a similar trend, with the resonant frequency error and power gain error decreasing until around 65 cSt, at which point the error levels begin to increase with increasing kinematic viscosity. In addition, at a certain air fraction level, the error line follows the same slope for both increasing and decreasing error levels (as kinematic viscosity increases). This is shown by the circle data points. When the air fraction goes below or above this level (shown by downward triangle and upward triangle, respectively), when the error begins to increase with increasing

kinematic viscosity, the paths for each value switch. This is more clearly seen in the close-up version of this data, shown in Figure A.5 and Figure A.6.

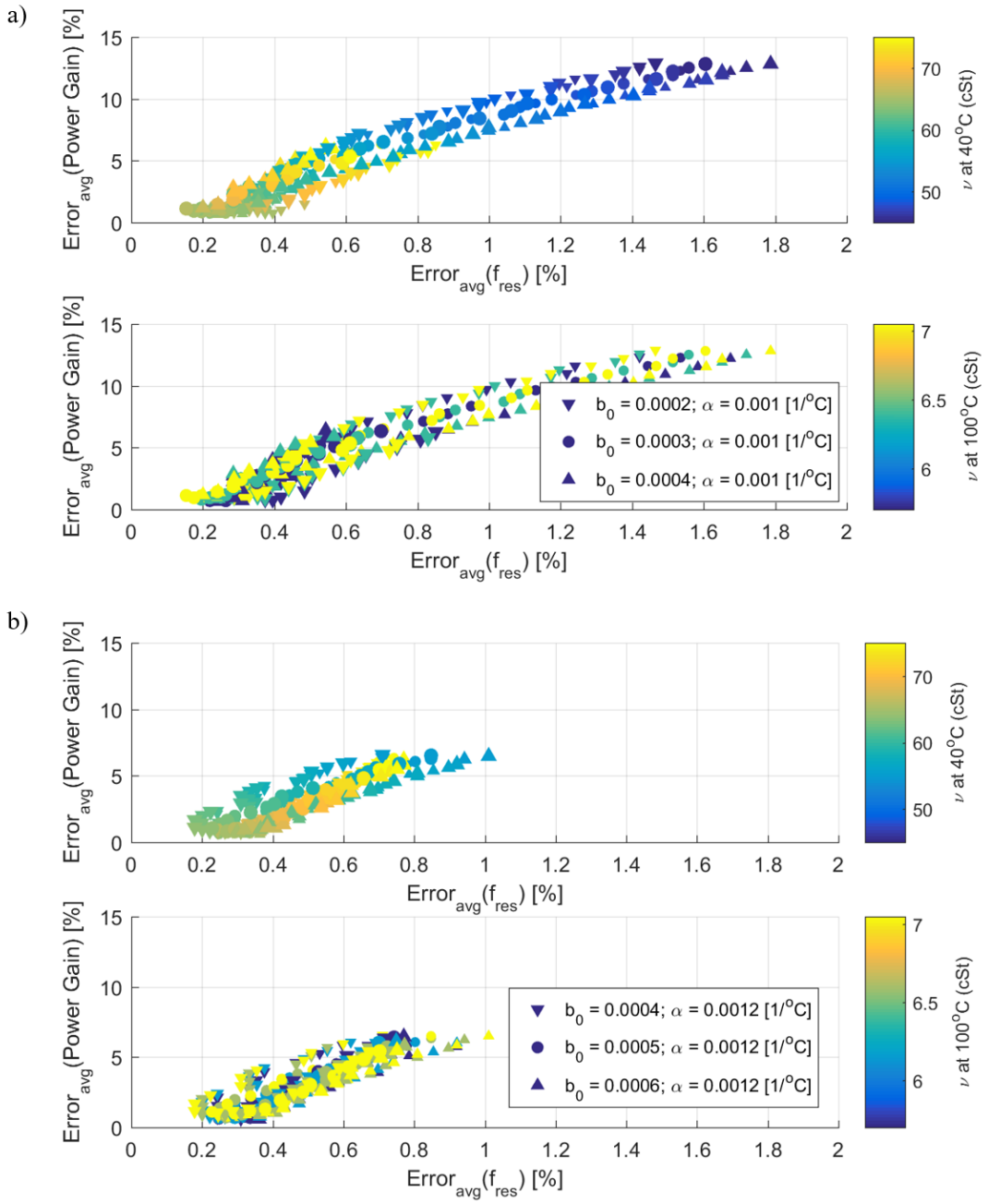

Figure A.4: Resonant frequency and power gain error with respect to kinematic viscosity for multiple air fraction volumes and a) volumetric expansion coefficient of 0.001°C^{-1} and b) 0.0012°C^{-1}.

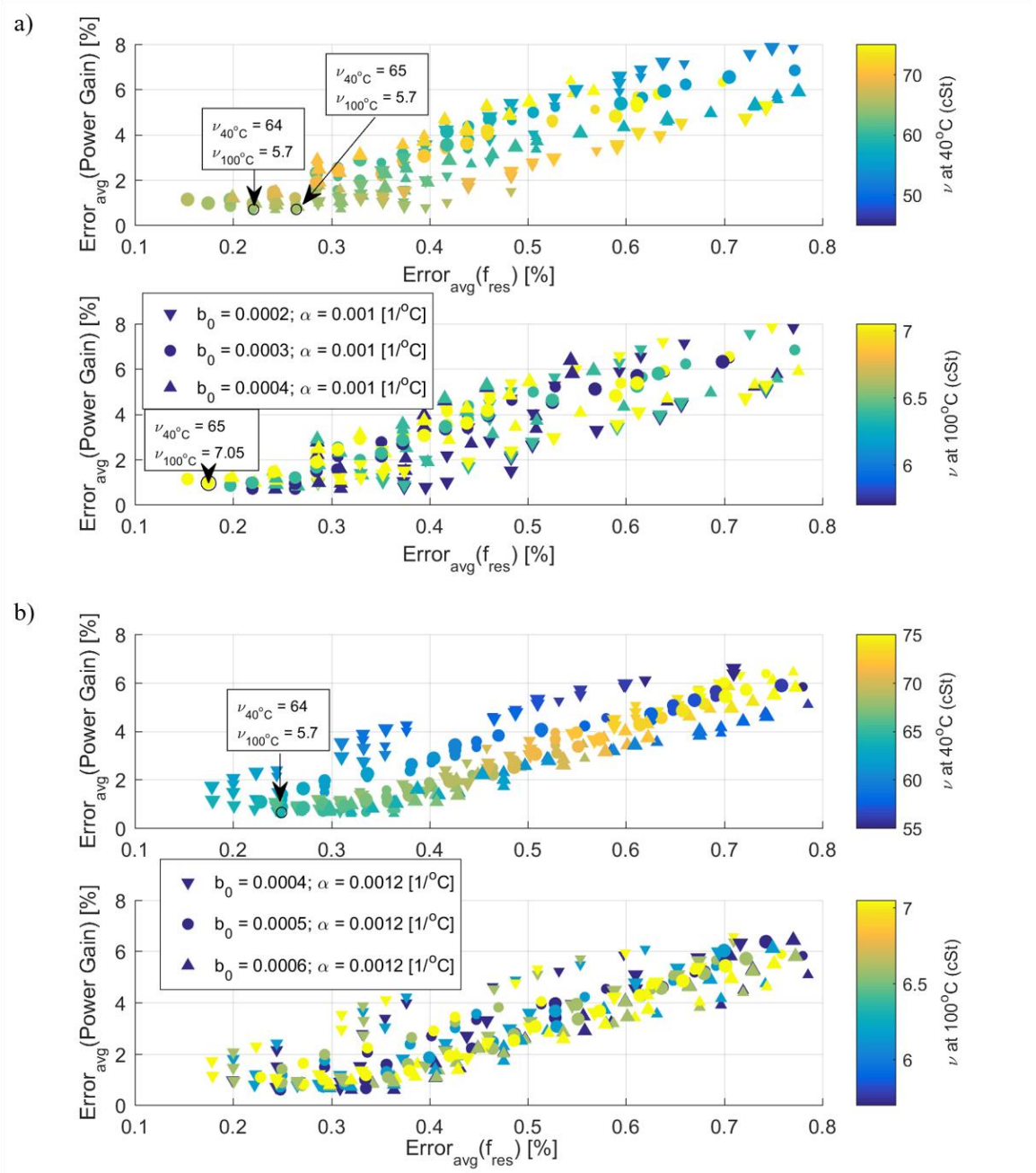

Figure A.5: Close view of resonant frequency and power gain error with respect to kinematic viscosity for multiple air fraction volumes and a) volumetric expansion coefficient of 0.001°C^{-1} and b) 0.0012°C^{-1}. (Note colorbar scale is different for figure b).

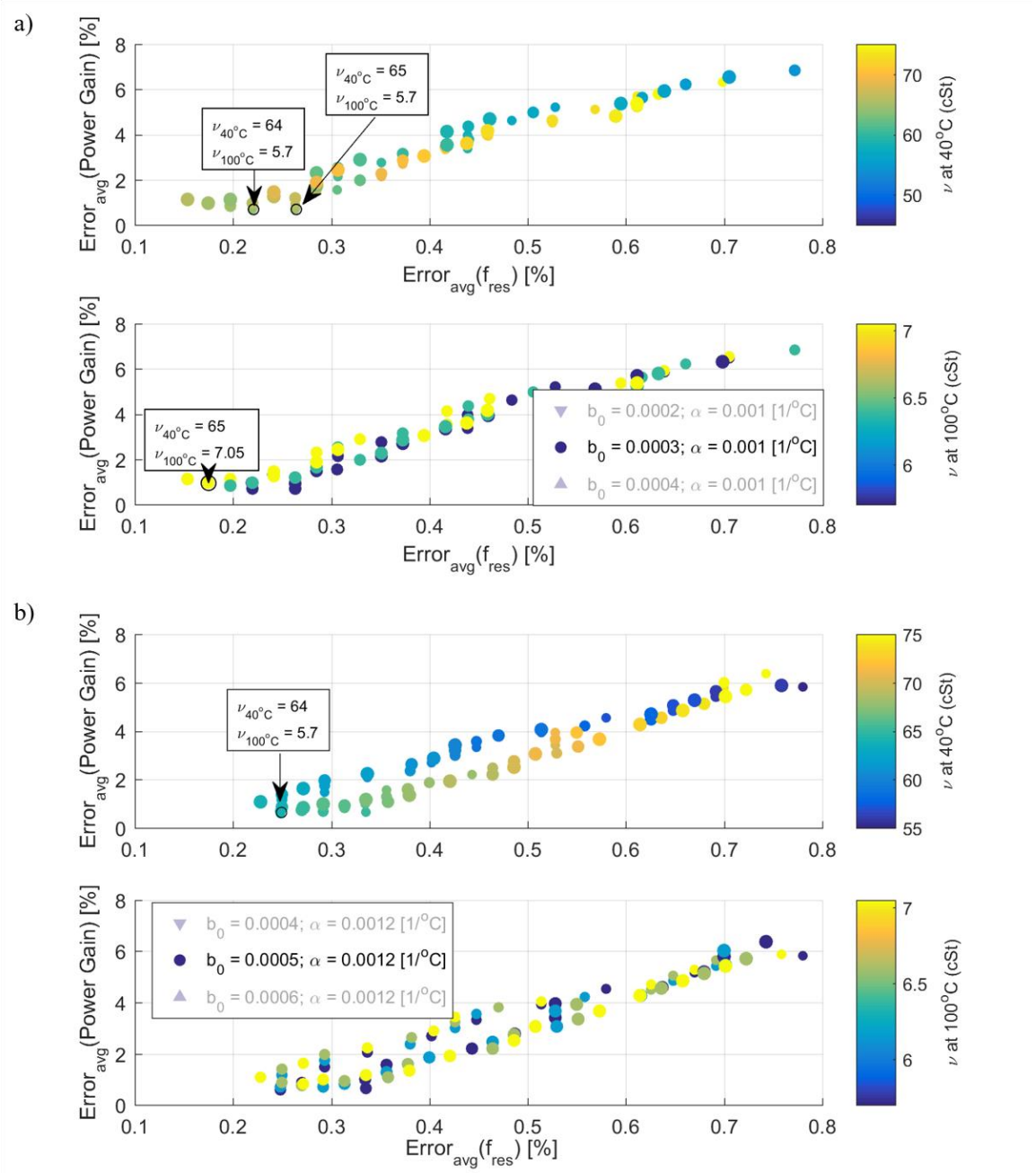

Figure A.6: Close view of resonant frequency and power gain error with respect to kinematic viscosity for a) volumetric expansion coefficient of 0.001°C^{-1} and air fraction of 0.0003 and b) 0.0012°C^{-1} and air fraction of 0.0005. (Note colorbar scale is different for figure b).

The data compared to the model provides a few values with very low error, with slight trade-offs between the resonant frequency error and the power gain at the resonant frequency error. This is observed with both the volumetric expansion coefficient and the

kinematic viscosity. As mentioned, at a certain kinematic viscosity level at 40°C, the error began to increase with increasing viscosity. The kinematic viscosity level at 100°C was a minor trade-off between power gain level error and resonant frequency error. The kinematic viscosity level of 64 cSt at 40°C and 5.7 cSt at 100°C were chosen because it provided the lowest power gain error and less than 0.3% resonant frequency error between the experiment and modeled results. The volumetric expansion coefficient had less resonant frequency error for the $0.001°C^{-1}$ case than the $0.0012°C^{-1}$ case for all air fraction and kinematic viscosity levels tested, and was therefore chosen as the model parameter.

Additionally, the changes to the bulk modulus and speed of sound properties due to the viscosity and volumetric expansion coefficient adjustments are relatively minor. The isothermal bulk modulus and fluid density are used to calculate the speed of sound, and is calculated from the fluid viscosity. The changes caused a less than 1.89% change in sound speed, less than 3.52% change in bulk modulus, and less than 0.83% change in density. As stated by Pierce [80], the discrepancy between the speed of sound calculated using the adiabatic bulk modulus versus the isothermal bulk modulus can be determined via

$$\frac{K_S - K_T}{K_S} = \frac{\gamma_s - 1}{\gamma_s} \tag{7.3}$$

where γ_s is the specific heat ratio for the fluid, K_S is the adiabatic bulk modulus, and K_T is the isothermal bulk modulus. The adiabatic bulk modulus for the oil used was not determined, but Gholizadeh et al. [94] provide tangent bulk modulus values for a typical hydraulic oil (20°C, 50 MPa) for both adiabatic, 2.41 GPa, and isothermal, 2.15 GPa, cases. From their stated values, the discrepancy is calculated to be 10.8%, which is a greater potential error than seen by the changes to viscosity and volumetric expansion coefficient herein.

Futhermore, the changes to the speed of sound due to 0.0003 air volume fraction cause a 2.8% sound speed change at 1 MPa, which is on par with the changes caused by the kinematic viscosity and volumetric expansion coefficient changes. The significance of tuning the volumetric expansion coefficient of new oil to the used oil within the tests primarily causes the resonant frequency to be more accurately predicted. The significance of tuning the kinematic viscosity manufacturer provided values to tests primarily manifests itself in the modeled viscous boundary layer, which affects both the amplitude of the pressure gain and the damped natural frequency.

A.3 Acoustic resistance predicted by using specific heat ratio, as discussed by Hansen [78]

Determining an accurate representation of the viscous boundary layer and acoustic resistance, R_a, value within the neck is an important feature for predicting Helmholtz resonator (HR) designs within hydraulic systems. Due to the high sound speed within fluids, the design of a reasonably sized HR device typically requires either creative methods to add compliance within the cavity or a narrow neck diameter (less than 2 mm). When a narrow neck diameter is pursued, the viscous boundary layer may hamper the pressure gain within the HR cavity.

A derivation of the acoustic resistance found within pipes is derived by Hansen [78] to be (adjusted for the HR presented here)

$$R_a = \frac{\rho_f c_f}{A_{neck}}\left[\frac{k_f d_v l_{n,eff}\left(2\pi a\right)}{2A_{neck}}\left[1+\left(\gamma_s-1\right)\sqrt{\frac{5}{3\gamma_s}}\right]+0.288k_f d_v \log_{10}\left[\frac{4A_{neck}}{\pi\varsigma^2}\right]+\frac{Ak_f^2}{2\pi}+M\right] \tag{7.4}$$

where γ_s is the ratio of specific heats, $d_v = \sqrt{2\nu_f/\omega}$ is the viscous boundary layer , ς is related to half the system pipe thickness or viscous boundary layer, and M is the mean flow Mach number. All other variables are defined in Section 3.2.1.

The first set of terms relates to the loss along the length of the neck due to viscous boundary layer effects, and is relevant to this system due to the narrow neck diameter. The second set of terms relate to viscous losses at the neck entry. The term *h* is either the neck edge radius or the viscous boundary layer, whichever is larger. The third set of terms is simply the radiation loss, as seen by R_r from Eq. (3.30). The final term is the mean flow Mach number, and is only valid in this equation if it is less than 0.2, and otherwise set to zero. It is calculated from Morse and Ingard [82] Eq. 11.3.37 first term. For the hydraulic system and HR tested, this term was typically set to zero, as it did not meet the condition to be included.

The difficulty with implementing this set of equations is due to the specific heat ratio, γ_s, for hydraulic oil can be difficult to determine, and neglecting this term by setting it equal to one insufficiently predicts the acoustic resistance. Hodges (pg. 59, Table 7.2 [129]) provides typical specific heat ratios for mineral oils at three temperatures – 10, 60, and 120°C – and two pressures – atmospheric and 70 MPa. The values range from 1.13 (for 120°C at 70 MPa) to 1.75 (for 10°C at atmospheric pressure). In addition, the specific heat ratio calculated from bulk moduli presented in [94] is 1.1079, which is from oil at 20°C and 50 MPa. This indicates that the specific heat ratio varies with both pressure and temperature, however the documentation of these trends is not clearly defined in the literature.

To compare the acoustic resistance model presented by Hansen [78] to the model presented in Chapter 3 (see Eqs. (3.27), (3.29)-(3.31)), three cases are compared. The first case in Figure A.7 is the HR body used with the HPEH device, where the cavity was pre-filled with oil (as seen in Figure 3.8); this is presented in Figure A.7. Three specific heat values are compared a) 1.00, b) 1.1079, and c) 1.15, with d) containing the Chapter 3 model. Setting the specific heat ratio to one causes error in both phase an power gain; the higher static pressure levels matched to the specific heat level provided in [94]; the low pressure levels match better with the 1.15 specific heat value; overall, the model presented in Chapter 3 provides the best match to the data for all static pressures.

The second case in Figure A.8 is also the HR body used with the HPEH device, however it was unfilled and thus contains a larger air fraction (as seen in Figure 3.9). All specific heat values work reasonably well, however the power gain and phase match at low static pressure levels for Figure A.8d (Chapter 3 model) matches best.

The third case in Figure A.9 is a different HR body which contains a narrower neck diameter of 0.67 mm (as seen in Figure 3.23). The specific heat ratios compared are a) 1.00, b) 1.15, and c) 1.175, which was the highest found value referenced for hydraulic oil; all values overpredict the power gain. When narrow neck diameters are used within hydraulic systems, the model presented in Chapter 3 has the lowest overall error between test and modelled results. Given that the model presented in Chapter 3 provides the lowest overall error and is simple to implement, it is used for HPEH-HR analyses.

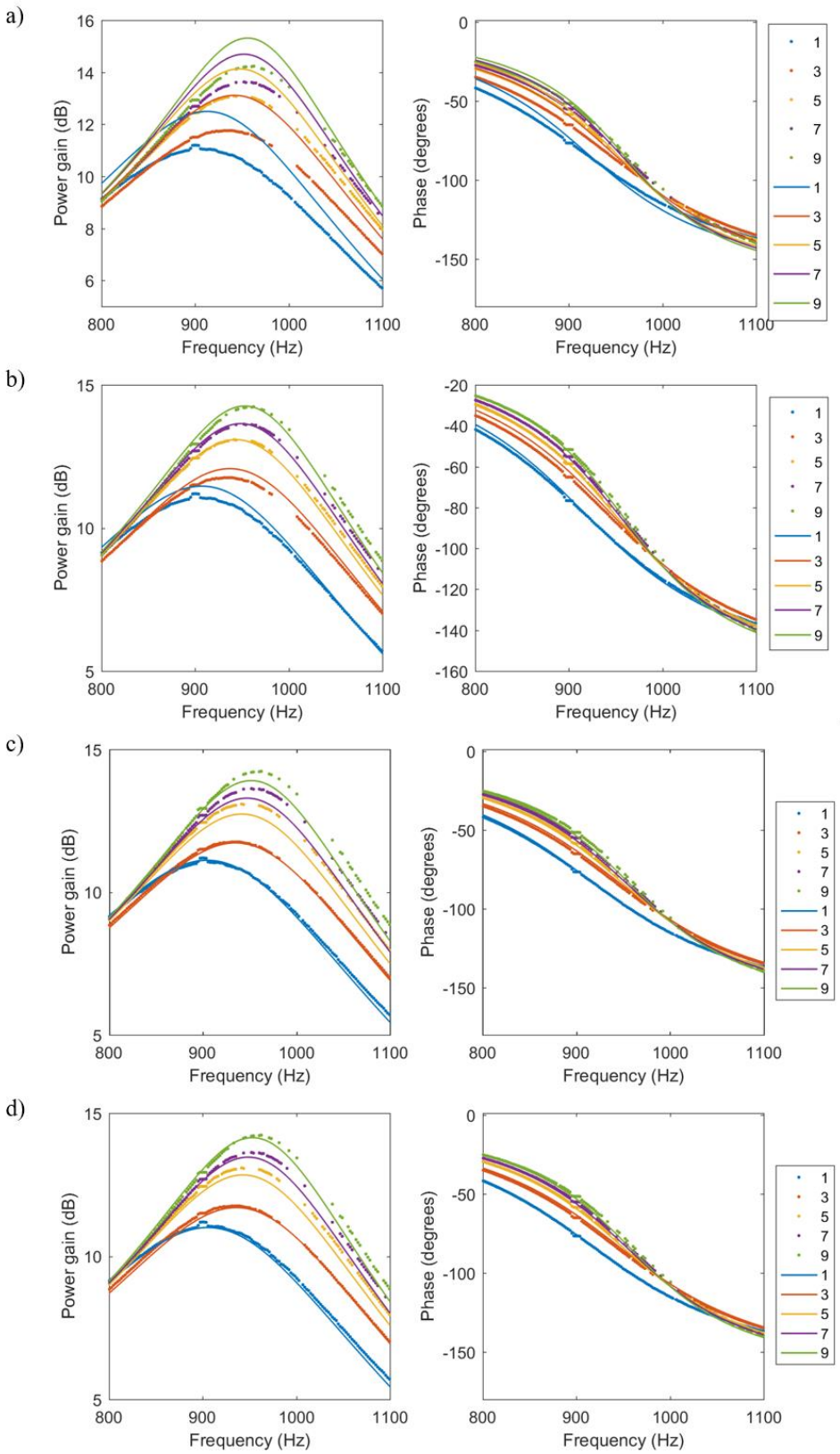

Figure A.7: Hansen acoustic resistance model for specific heat ratio of a) 1.00, b) 1.1079, c) 1.15, and d) contains the model presented in Chapter 3.

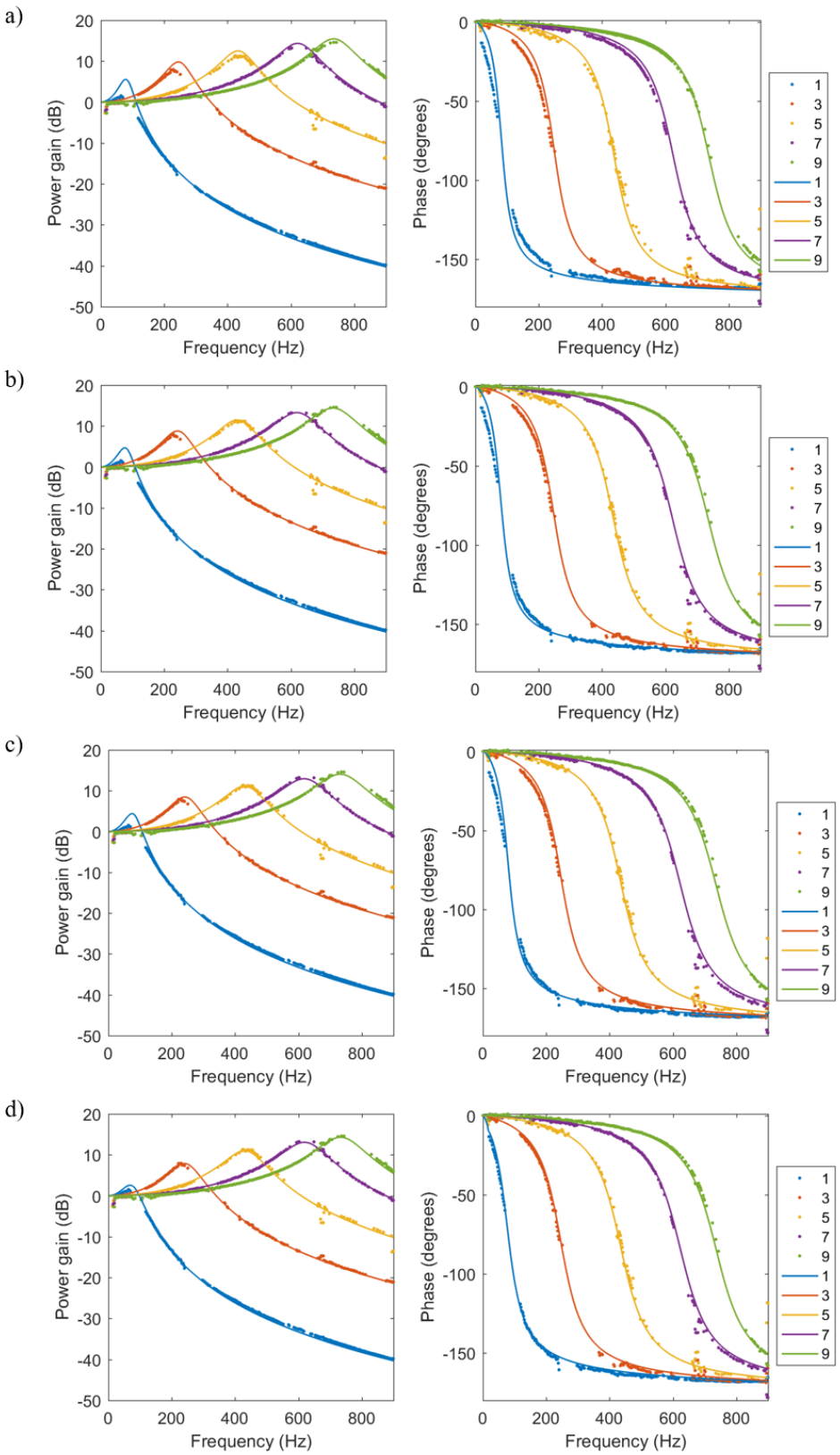

Figure A.8: Hansen acoustic resistance model for specific heat ratio of a) 1.00, b) 1.1079, c) 1.15, and d) contains the model presented in Chapter 3.

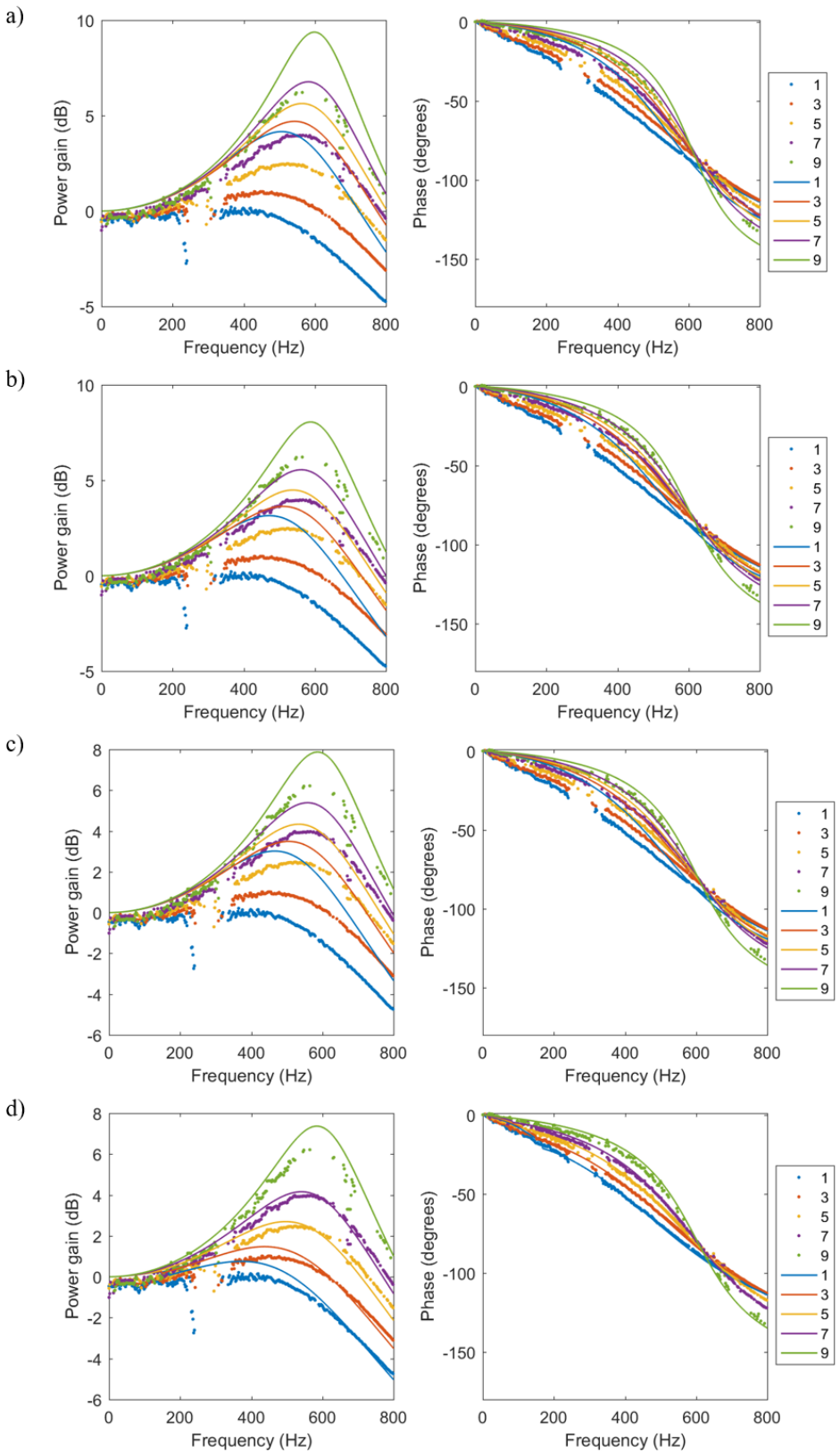

Figure A.9: Hansen acoustic resistance model for specific heat ratio of a) 1.00, b) 1.15, c) 1.175, and d) contains the model presented in Chapter 3.

APPENDIX B: PIN-PMN-PT TEST RESULTS

B.1 Shaker test results

The following are measured test results from PIN-PMN-PT single crystal excited at 450 Hz for multiple resistive loads. The measured forces, strain, voltage, and test conditions are provided in legends and captions.

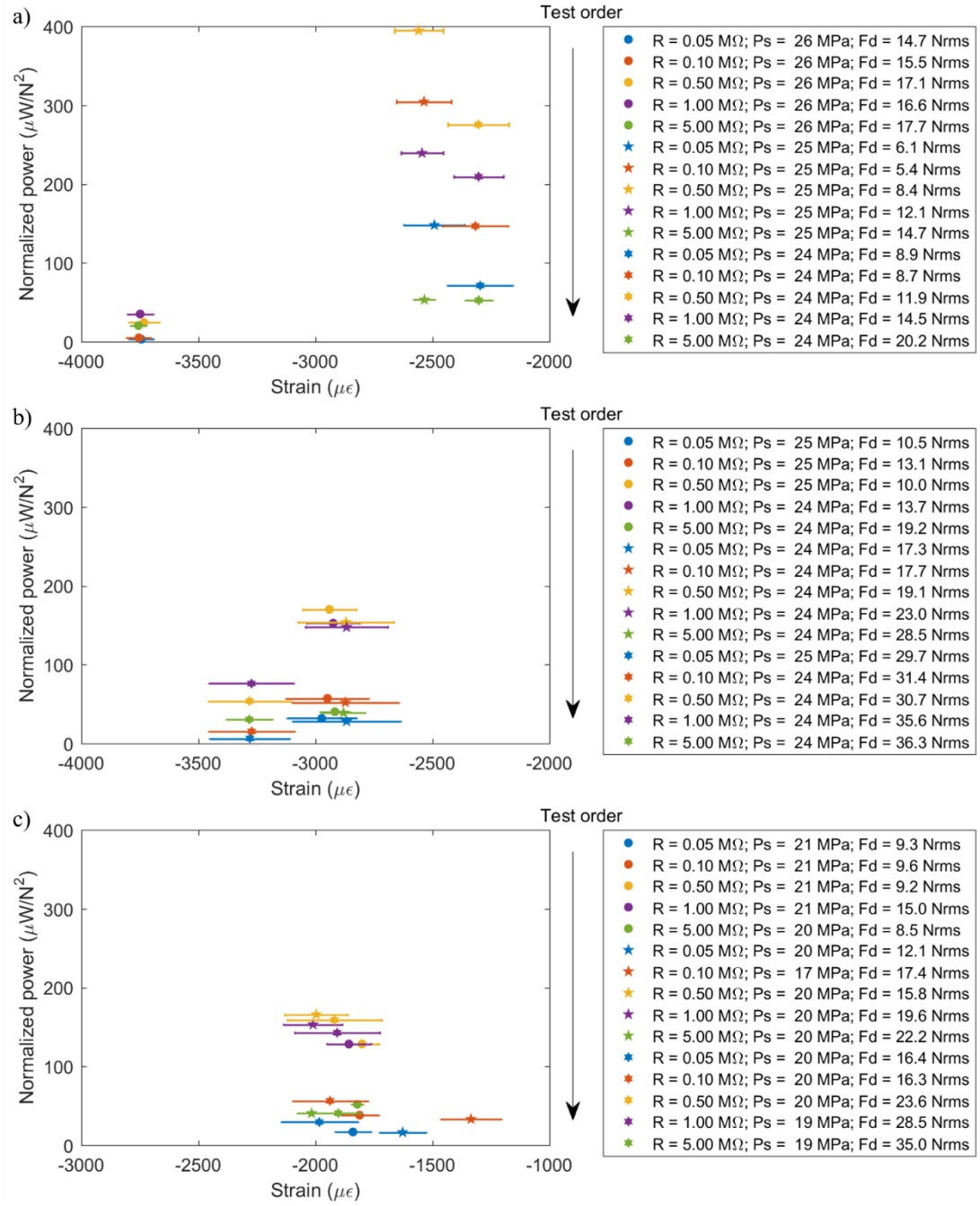

Figure B.10: Power normalized by dynamic force versus strain; strain indicated by x-axis; bars on points indicates strain range and shape of point indicate dynamic force level; color indicates resistive load; excitation at 450 Hz. Two specimen tests results, where a) is specimen SC1 at nominally 25 MPa, b) SC3 at 25 MPa, and c) SC1 at 20 MPa.

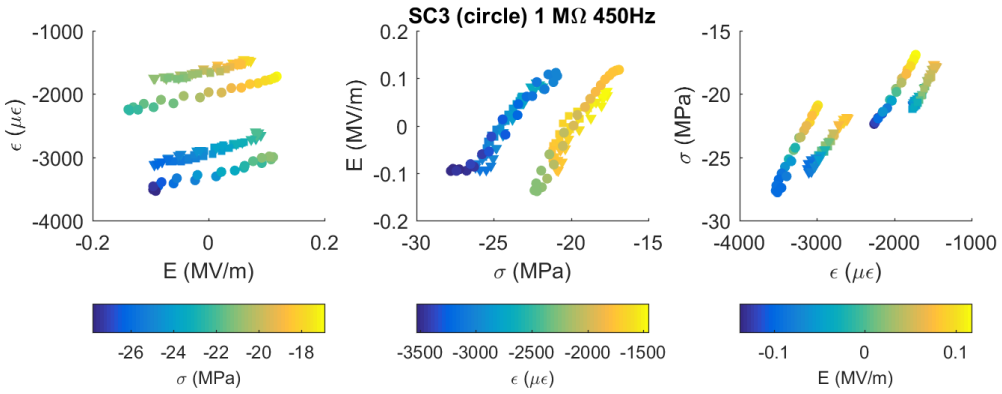

Figure B.11: Strain, stress, and electric field for 1 MΩ shaker tests, Specimen 3, indicated by a circle in Section 4.3.1.

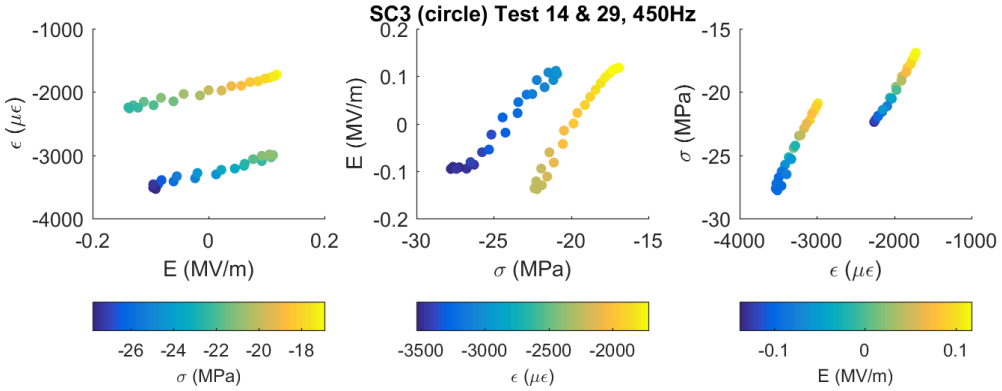

Figure B.12: Strain, stress, and electric field for shaker test 14 and 29, Specimen 3, indicated by a circle in Section 4.3.1. Tests both included high dynamic force levels and produced high power levels, however altered on being more toward FER (mean -20 MPa) or FEO (mean -25 MPa) regions.

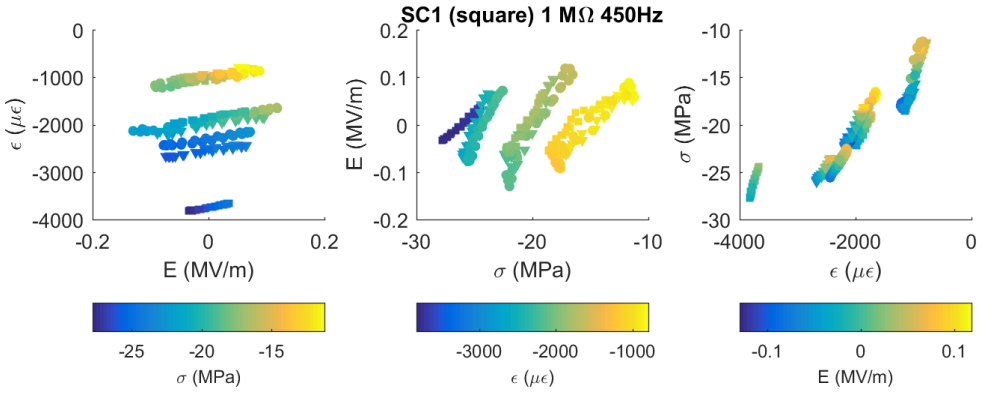

Figure B.13: Strain, stress, and electric field for 1 MΩ shaker tests, Specimen 1, indicated by a square in Section 4.3.1.

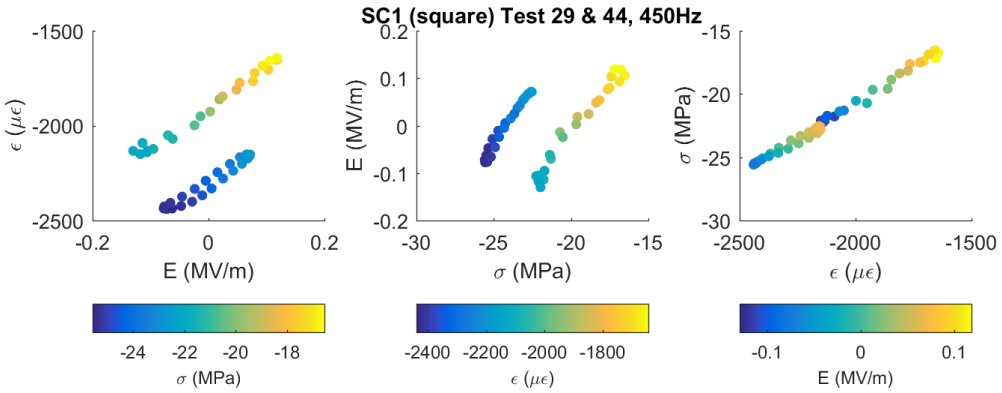

Figure B.14: Strain, stress, and electric field for shaker test 29 and 44, Specimen 1, indicated by a square in Section 4.3.1. Tests both produced high normalized power levels, however altered on being more toward FER (mean -20 MPa) or FEO (mean -25 MPa) regions.

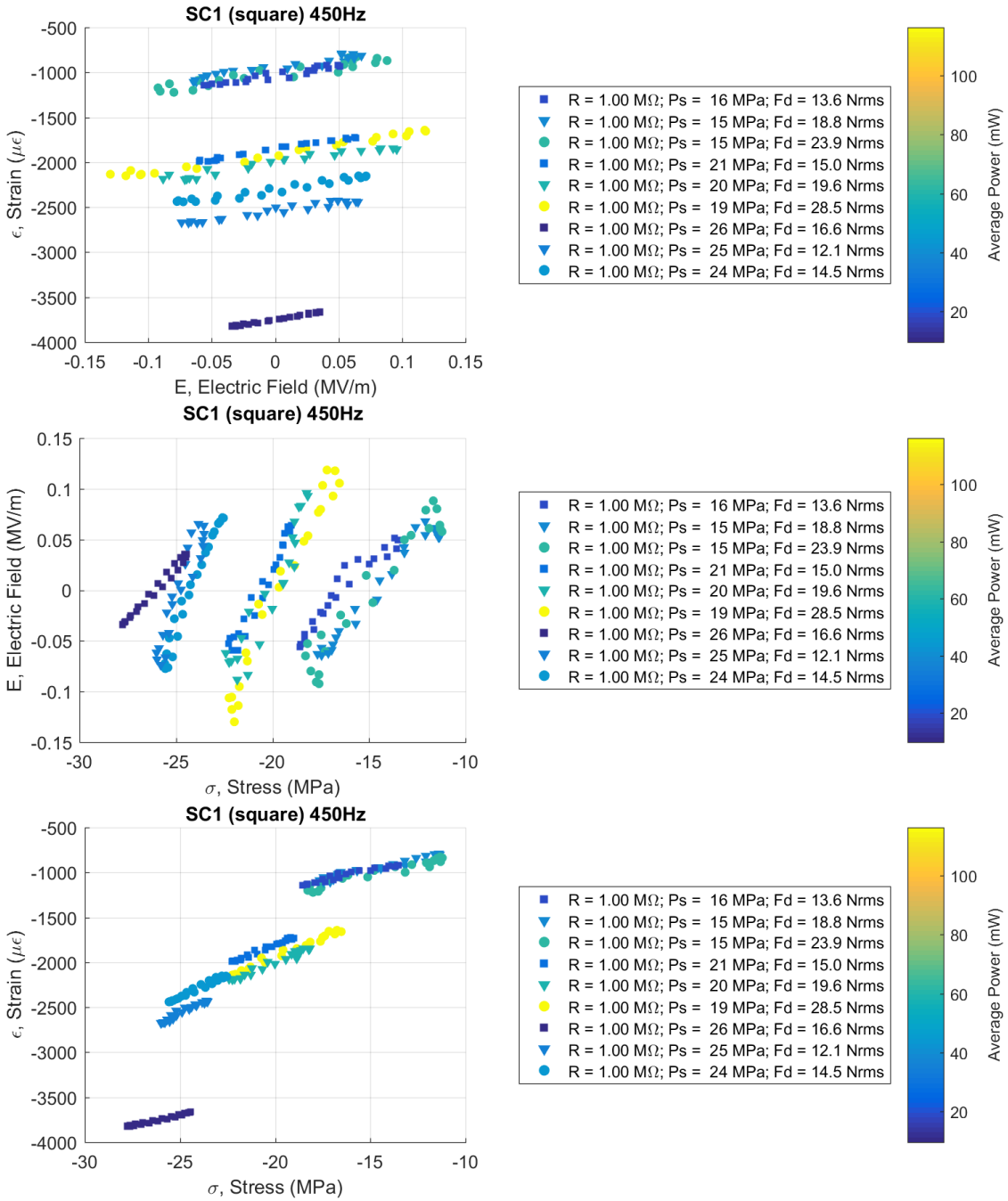

Figure B.15: Stress, strain, and electric field versus average power response for all 1 MΩ tests performed on specimen 1 at 450 Hz.

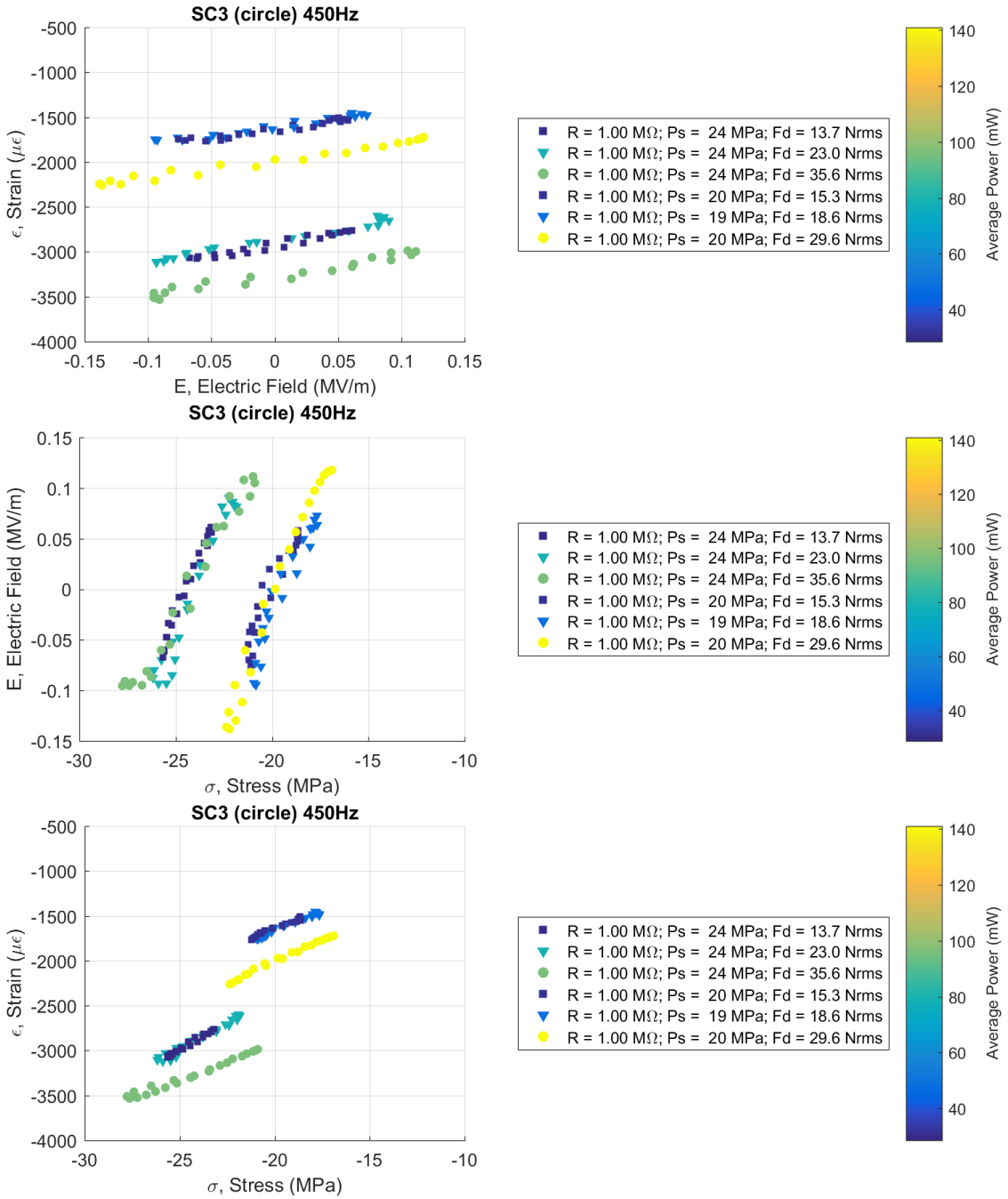

Figure B.16: Stress, strain, and electric field versus average power response for all 1 MΩ tests performed on specimen 3 at 450 Hz.

The following figures are provided to show how resistive loads change the stress vs. strain vs. electric field at each mean stress level tested.

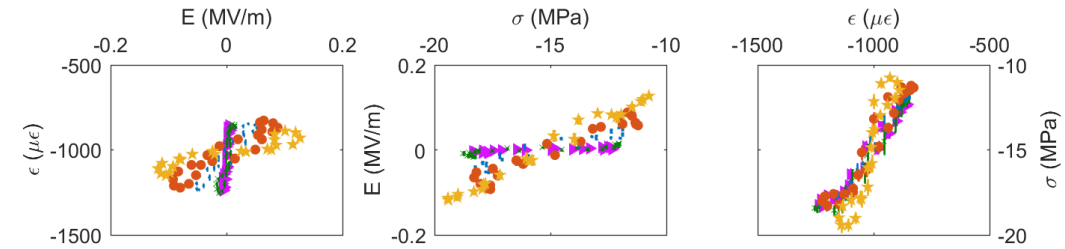
E (MV/m)
σ (MPa)
ϵ ($\mu\epsilon$)
ϵ ($\mu\epsilon$)
E (MV/m)
σ (MPa)

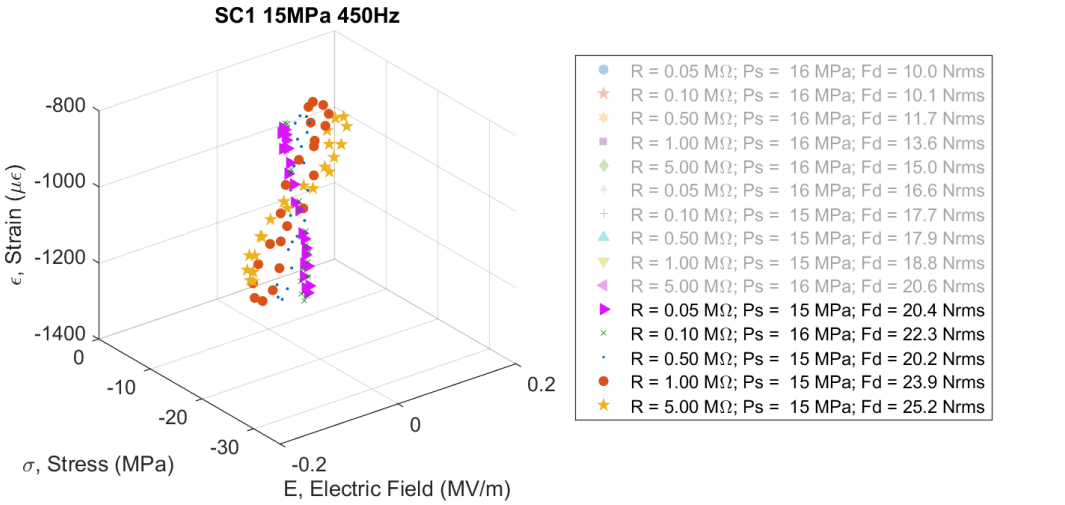
SC1 15MPa 450Hz
ϵ, Strain ($\mu\epsilon$)
σ, Stress (MPa)
E, Electric Field (MV/m)
R = 0.05 MΩ; Ps = 16 MPa; Fd = 10.0 Nrms
R = 0.10 MΩ; Ps = 16 MPa; Fd = 10.1 Nrms
R = 0.50 MΩ; Ps = 16 MPa; Fd = 11.7 Nrms
R = 1.00 MΩ; Ps = 16 MPa; Fd = 13.6 Nrms
R = 5.00 MΩ; Ps = 16 MPa; Fd = 15.0 Nrms
R = 0.05 MΩ; Ps = 16 MPa; Fd = 16.6 Nrms
R = 0.10 MΩ; Ps = 15 MPa; Fd = 17.7 Nrms
R = 0.50 MΩ; Ps = 15 MPa; Fd = 17.9 Nrms
R = 1.00 MΩ; Ps = 15 MPa; Fd = 18.8 Nrms
R = 5.00 MΩ; Ps = 16 MPa; Fd = 20.6 Nrms
R = 0.05 MΩ; Ps = 15 MPa; Fd = 20.4 Nrms
R = 0.10 MΩ; Ps = 16 MPa; Fd = 22.3 Nrms
R = 0.50 MΩ; Ps = 15 MPa; Fd = 20.2 Nrms
R = 1.00 MΩ; Ps = 15 MPa; Fd = 23.9 Nrms
R = 5.00 MΩ; Ps = 15 MPa; Fd = 25.2 Nrms

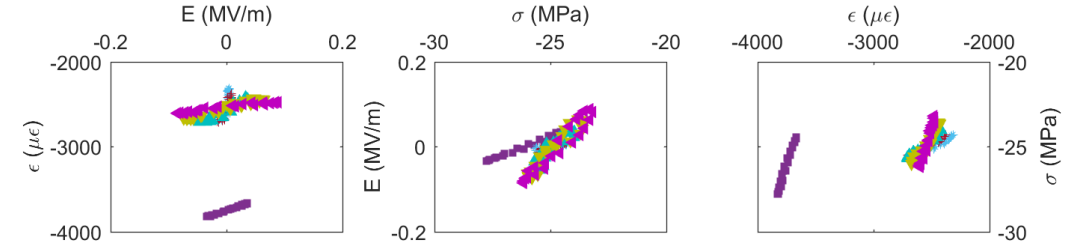
E (MV/m)
σ (MPa)
ϵ ($\mu\epsilon$)
ϵ ($\mu\epsilon$)
E (MV/m)
σ (MPa)

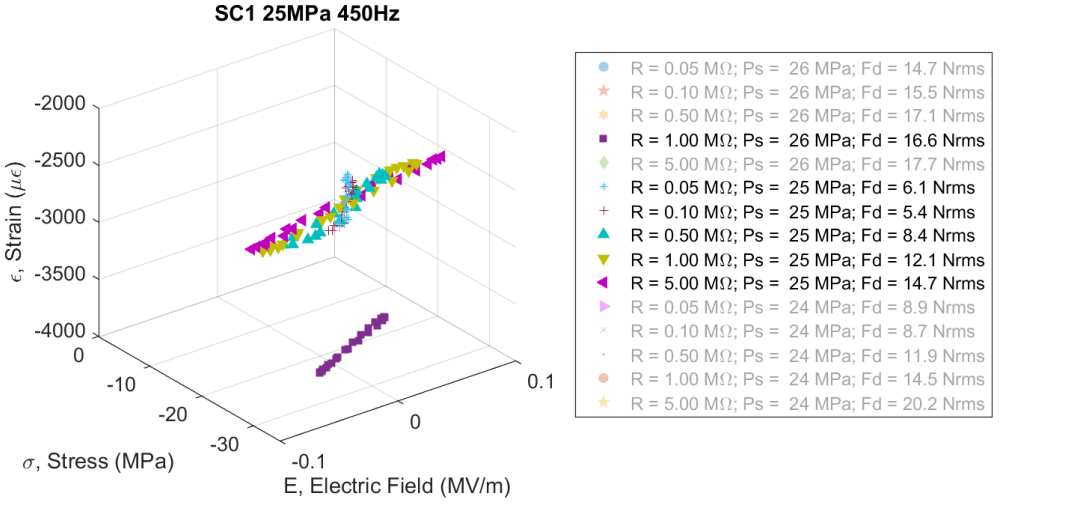
SC1 25MPa 450Hz
ϵ, Strain ($\mu\epsilon$)
σ, Stress (MPa)
E, Electric Field (MV/m)
R = 0.05 MΩ; Ps = 26 MPa; Fd = 14.7 Nrms
R = 0.10 MΩ; Ps = 26 MPa; Fd = 15.5 Nrms
R = 0.50 MΩ; Ps = 26 MPa; Fd = 17.1 Nrms
R = 1.00 MΩ; Ps = 26 MPa; Fd = 16.6 Nrms
R = 5.00 MΩ; Ps = 26 MPa; Fd = 17.7 Nrms
R = 0.05 MΩ; Ps = 25 MPa; Fd = 6.1 Nrms
R = 0.10 MΩ; Ps = 25 MPa; Fd = 5.4 Nrms
R = 0.50 MΩ; Ps = 25 MPa; Fd = 8.4 Nrms
R = 1.00 MΩ; Ps = 25 MPa; Fd = 12.1 Nrms
R = 5.00 MΩ; Ps = 25 MPa; Fd = 14.7 Nrms
R = 0.05 MΩ; Ps = 24 MPa; Fd = 8.9 Nrms
R = 0.10 MΩ; Ps = 24 MPa; Fd = 8.7 Nrms
R = 0.50 MΩ; Ps = 24 MPa; Fd = 11.9 Nrms
R = 1.00 MΩ; Ps = 24 MPa; Fd = 14.5 Nrms
R = 5.00 MΩ; Ps = 24 MPa; Fd = 20.2 Nrms

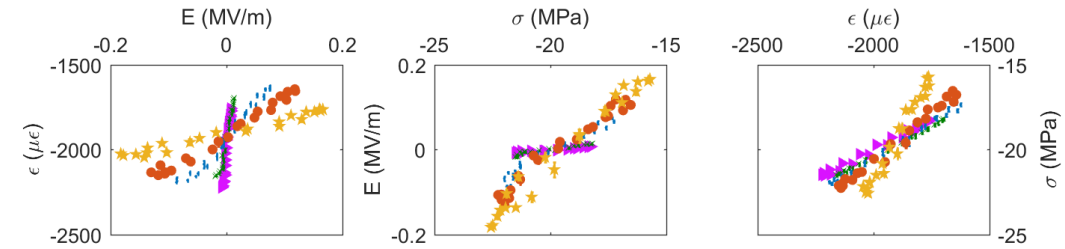
E (MV/m)
σ (MPa)
ϵ ($\mu\epsilon$)
ϵ ($\mu\epsilon$)
E (MV/m)
σ (MPa)

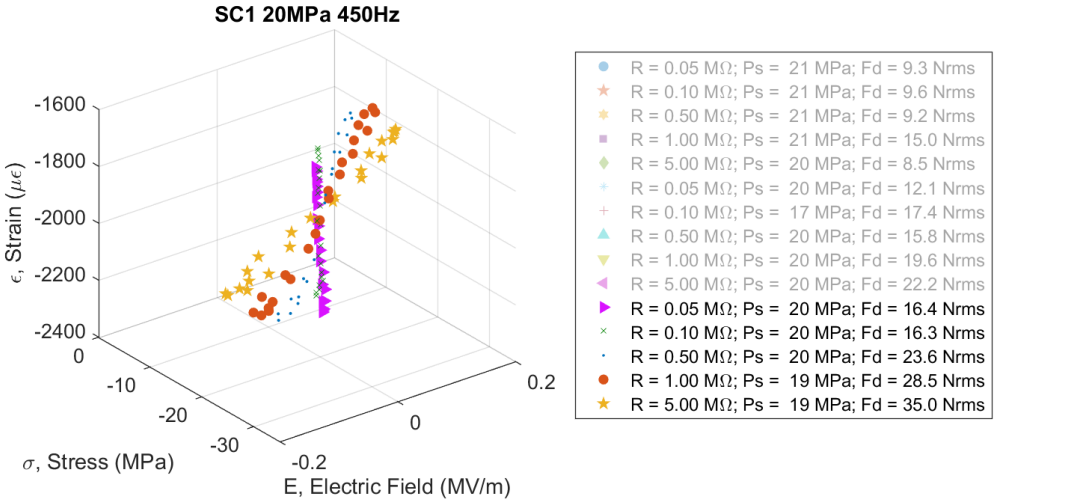
SC1 20MPa 450Hz
ϵ, Strain ($\mu\epsilon$)
σ, Stress (MPa)
E, Electric Field (MV/m)
R = 0.05 MΩ; Ps = 21 MPa; Fd = 9.3 Nrms
R = 0.10 MΩ; Ps = 21 MPa; Fd = 9.6 Nrms
R = 0.50 MΩ; Ps = 21 MPa; Fd = 9.2 Nrms
R = 1.00 MΩ; Ps = 21 MPa; Fd = 15.0 Nrms
R = 5.00 MΩ; Ps = 20 MPa; Fd = 8.5 Nrms
R = 0.05 MΩ; Ps = 20 MPa; Fd = 12.1 Nrms
R = 0.10 MΩ; Ps = 17 MPa; Fd = 17.4 Nrms
R = 0.50 MΩ; Ps = 20 MPa; Fd = 15.8 Nrms
R = 1.00 MΩ; Ps = 20 MPa; Fd = 19.6 Nrms
R = 5.00 MΩ; Ps = 20 MPa; Fd = 22.2 Nrms
R = 0.05 MΩ; Ps = 20 MPa; Fd = 16.4 Nrms
R = 0.10 MΩ; Ps = 20 MPa; Fd = 16.3 Nrms
R = 0.50 MΩ; Ps = 20 MPa; Fd = 23.6 Nrms
R = 1.00 MΩ; Ps = 19 MPa; Fd = 28.5 Nrms
R = 5.00 MΩ; Ps = 19 MPa; Fd = 35.0 Nrms

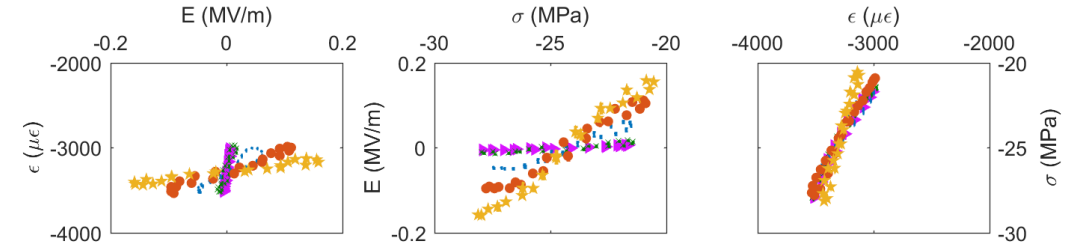
E (MV/m)
σ (MPa)
ϵ ($\mu\epsilon$)
ϵ ($\mu\epsilon$)
E (MV/m)
σ (MPa)

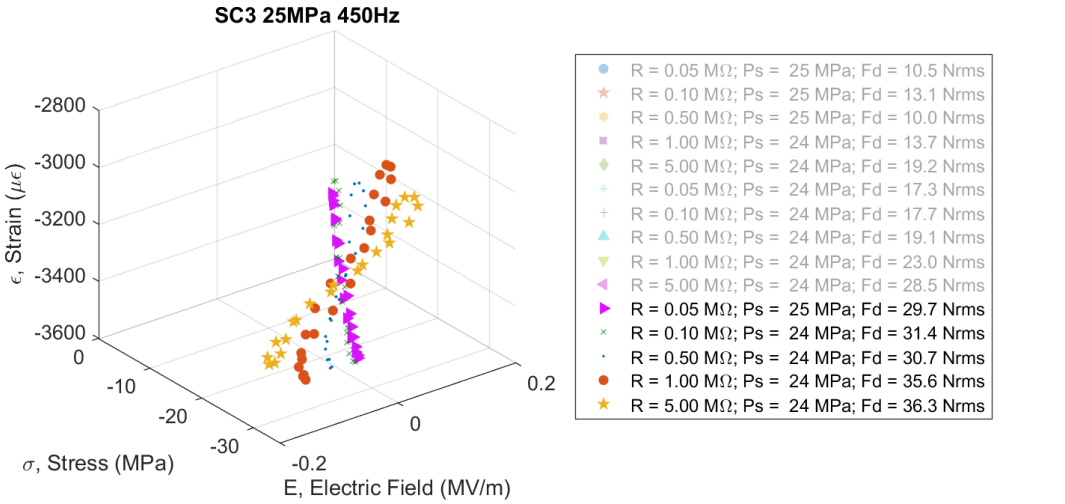
SC3 25MPa 450Hz
ϵ, Strain ($\mu\epsilon$)
σ, Stress (MPa)
E, Electric Field (MV/m)
R = 0.05 MΩ; Ps = 25 MPa; Fd = 10.5 Nrms
R = 0.10 MΩ; Ps = 25 MPa; Fd = 13.1 Nrms
R = 0.50 MΩ; Ps = 25 MPa; Fd = 10.0 Nrms
R = 1.00 MΩ; Ps = 24 MPa; Fd = 13.7 Nrms
R = 5.00 MΩ; Ps = 24 MPa; Fd = 19.2 Nrms
R = 0.05 MΩ; Ps = 24 MPa; Fd = 17.3 Nrms
R = 0.10 MΩ; Ps = 24 MPa; Fd = 17.7 Nrms
R = 0.50 MΩ; Ps = 24 MPa; Fd = 19.1 Nrms
R = 1.00 MΩ; Ps = 24 MPa; Fd = 23.0 Nrms
R = 5.00 MΩ; Ps = 24 MPa; Fd = 28.5 Nrms
R = 0.05 MΩ; Ps = 25 MPa; Fd = 29.7 Nrms
R = 0.10 MΩ; Ps = 24 MPa; Fd = 31.4 Nrms
R = 0.50 MΩ; Ps = 24 MPa; Fd = 30.7 Nrms
R = 1.00 MΩ; Ps = 24 MPa; Fd = 35.6 Nrms
R = 5.00 MΩ; Ps = 24 MPa; Fd = 36.3 Nrms

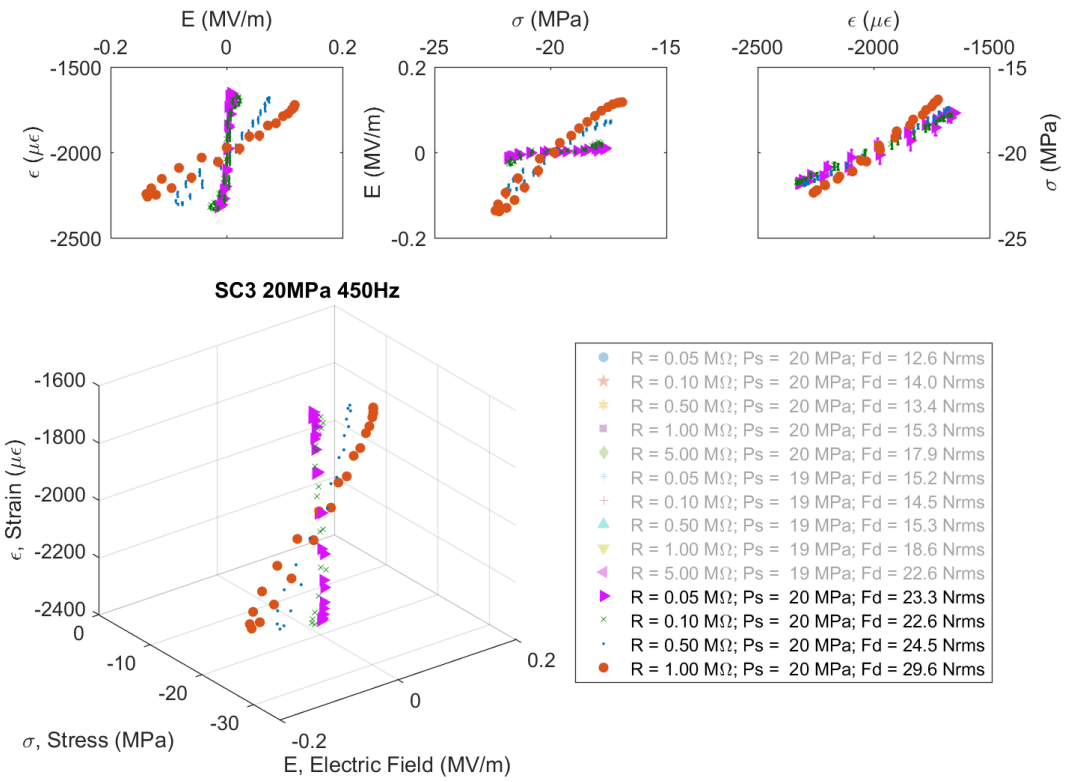

B.2 HPEH7-1 Tests

The following are pictures of HPEH7-1 during testing, provided such that the design of the device is clearer.

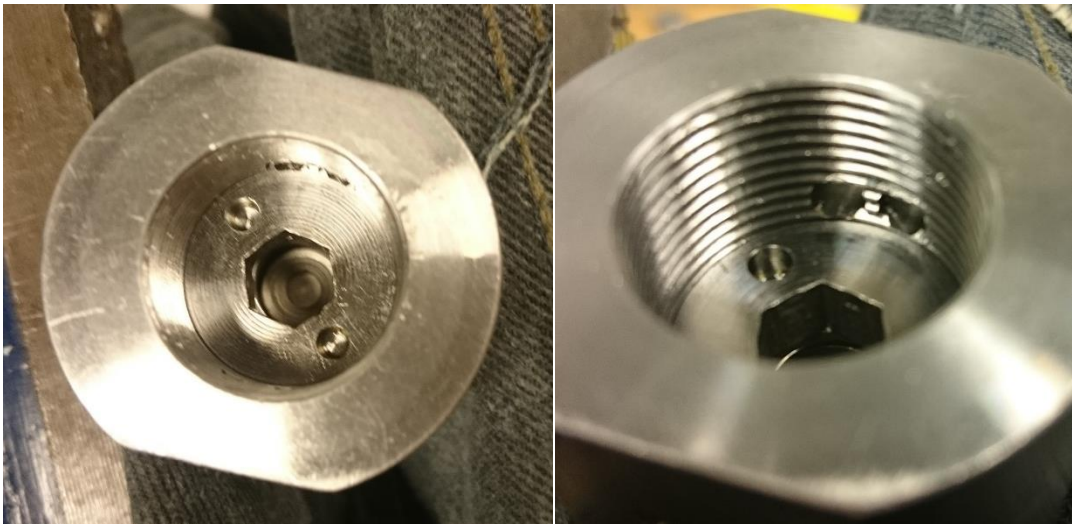

Figure B.17: Internal view of HPEH7-1 during assembly after torque is applied to preload sleeve. One female spherical bearing is in place within device. Note that preload sleeve is below ports intended for strain gauge and electrode wires.

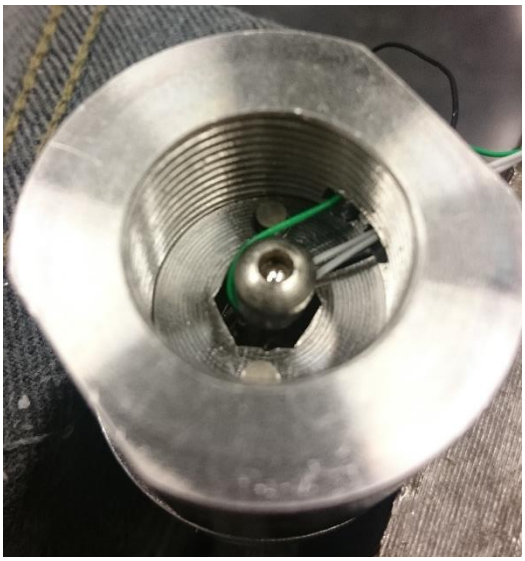

Figure B.18: Internal view of HPEH7-1 during assembly, with single crystal in place, dowel pins in place, male spherical bearing on single crystal, and wires from electrodes and strain gauge wired through ports.

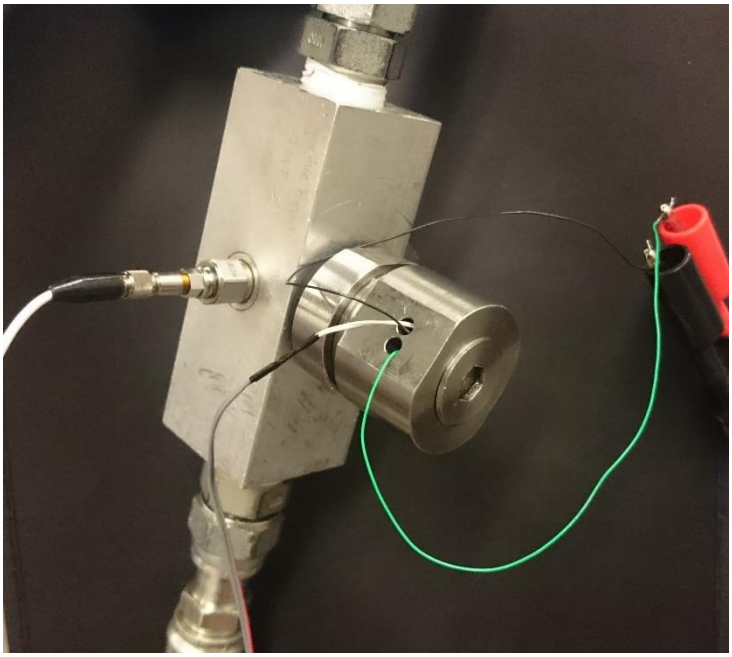

Figure B.19: HPEH7-1 fully assembled and attached to hydraulic rig. Dynamic pressure sensor is also shown.

REFERENCES

[1] P. Piezotronics. *Pressure Transducers - Sensors for Test & Measurement*. [cited 2016; Available from: http://www.pcb.com/testmeasurement/pressure#.

[2] S. Priya, *Advances in energy harvesting using low profile piezoelectric transducers.* Journal of Electroceramics, 2007. **19**(1): p. 167-184.

[3] N. Elvin and A. Erturk, *Advances in energy harvesting methods*. 2013: Springer.

[4] A. Erturk and D.J. Inman, *Piezoelectric energy harvesting*, ed. D.J. Inman. 2011, Chichester: Wiley.

[5] S.A. Smith and D.H. Capesius. *Intrinsic hydraulic hose condition monitoring for prevention of catastrophic failure* in *ASME 2011 Conference on Smart Materials, Adaptive Structures and Intelligent Systems*. 2011. Scottsdale, AZ: ASME.

[6] *MEAS M5600 Wireless Pressure Transducer*. 2016, TE Connectivity Sensors.

[7] *SensoNode Blue sensor instruction sheet*. 2016, Parker Hannifin Corp.

[8] H.D. Akaydin, N. Elvin, and Y. Andreopoulos, *Wake of a cylinder: a paradigm for energy harvesting with piezoelectric materials.* Experiments in Fluids, 2010. **49**(1): p. 291-304.

[9] J.J. Allen and A.J. Smits, *Energy harvesting eel.* Journal of Fluids and Structures, 2001. **15**(3-4): p. 629-640.

[10] S. Keddis and N. Schwesinger. *Power source for wireless sensors in pipes* in *Proc. SPIE 9799, Active and Passive Smart Structures and Integrated Systems* 2016. Las Vegas, NV.

[11] K.A. Cunefare, et al., *Energy harvesting from hydraulic pressure fluctuations.* Smart Materials and Structures, 2013. **22**(2): p. 025036.

[12] M. Deterre, E. Lefeuvre, and E. Dufour-Gergam, *An active piezoelectric energy extraction method for pressure energy harvesting.* Smart Materials and Structures, 2012. **21**(8): p. 85004-85012.

[13] K.A. Cunefare, E.A. Skow, and A. Erturk. *Transduction as energy conversion; harvesting of acoustic energy in hydraulic systems*. 2013. Montreal, Canada: ASA.

[14] W. Durfee and Z. Sun, *Fluid Power System Dynamics*. 2009, Center for compact and efficient fluid power.

[15] *Fluid Power Handbook & Directory*. 2014-2015; Available from: hydraulicspneumatics.com.

[16] E. Skow, K. Cunefare, and A. Erturk. *Design and Modeling of Hydraulic Pressure Energy Harvesters for Low Dynamic Pressure Environments* in *ASME 2014 International Mechanical Engineering Congress and Exposition*. 2014: American Society of Mechanical Engineers.

[17] J. Curie and P. Curie, *Development by pressure of polar electricity in hemihedral crystals with inclined faces.* Bull. soc. min. de France, 1880. **3**: p. 90.

[18] S.P. Beeby, M.J. Tudor, and N.M. White, *Energy harvesting vibration sources for microsystems applications.* Measurement Science & Technology, 2006. **17**(12): p. R175-R195.

[19] C.C. Federspiel and J. Chen, *Air-powered sensor*. Proceedings of the Ieee Sensors 2003, Vols 1 and 2, 2003: p. 22-25.
[20] S. Priya, et al., *Piezoelectric windmill: A novel solution to remote sensing*. Japanese Journal of Applied Physics Part 2-Letters & Express Letters, 2005. **44**(1-7): p. L104-L107.
[21] R. Myers, et al., *Small scale windmill.* Applied Physics Letters, 2007. **90**(5).
[22] F.J. Xu, et al., *Design of a miniature wind turbine for powering wireless sensors.* Sensors and Smart Structures Technologies for Civil, Mechanical, and Aerospace Systems 2010, 2010. **7647**.
[23] S. Pobering, S. Ebermeyer, and N. Schwesinger. *Generation of electrical energy using short piezoelectric cantilevers in flowing media* in *Active and Passive Smart Structures and Integrated Systems 2009, 9 March 2009*. 2009. USA: SPIE - The International Society for Optical Engineering.
[24] C. De Marqui, A. Erturk, and D.J. Inman, *Piezoaeroelastic Modeling and Analysis of a Generator Wing with Continuous and Segmented Electrodes.* Journal of Intelligent Material Systems and Structures, 2010. **21**(10): p. 983-993.
[25] C. De Marqui, et al., *Modeling and Analysis of Piezoelectric Energy Harvesting From Aeroelastic Vibrations Using the Doublet-Lattice Method.* Journal of Vibration and Acoustics-Transactions of the Asme, 2011. **133**(1).
[26] M. Bryant, E. Wolff, and E. Garcia, *Parametric Design Study of an Aeroelastic Flutter Energy Harvester.* Active and Passive Smart Structures and Integrated Systems 2011, 2011. **7977**.
[27] M. Bryant, A. Fang, and E. Garcia, *Self-powered smart blade: Helicopter blade energy harvesting.* Active and Passive Smart Structures and Integrated Systems 2010, Pts 1 and 2, 2010. **7643**.
[28] A. Erturk, et al., *On the energy harvesting potential of piezoaeroelastic systems.* Applied Physics Letters, 2010. **96**(18).
[29] V.C. Sousa, et al., *Enhanced aeroelastic energy harvesting by exploiting combined nonlinearities: theory and experiment.* Smart Materials & Structures, 2011. **20**(9).
[30] Z.L. Peng and Q. Zhu, *Energy harvesting through flow-induced oscillations of a foil.* Physics of Fluids, 2009. **21**(12).
[31] D. St Clair, et al., *A scalable concept for micropower generation using flow-induced self-excited oscillations.* Applied Physics Letters, 2010. **96**(14).
[32] N.G. Elvin and A.A. Elvin, *The Flutter Response of a Piezoelectrically Damped Cantilever Pipe.* Journal of Intelligent Material Systems and Structures, 2009. **20**(16): p. 2017-2026.
[33] L.S. Tang, M.P. Paidoussis, and J. Jiang, *Cantilevered flexible plates in axial flow: Energy transfer and the concept of flutter-mill.* Journal of Sound and Vibration, 2009. **326**(1-2): p. 263-276.
[34] J.A. Dunnmon, et al., *Power extraction from aeroelastic limit cycle oscillations.* Journal of Fluids and Structures, 2011. **27**(8): p. 1182-1198.
[35] S.D. Kwon, *A T-shaped piezoelectric cantilever for fluid energy harvesting.* Applied Physics Letters, 2010. **97**(16).
[36] A. Giacomello and M. Porfiri, *Underwater energy harvesting from a heavy flag hosting ionic polymer metal composites.* Journal of Applied Physics, 2011. **109**(8).

[37] S.B. Horowitz, et al., *A MEMS acoustic energy harvester*. Journal of Micromechanics and Microengineering, 2006. **16**(9): p. S174-S181.
[38] H.J. Jung and S.W. Lee, *The experimental validation of a new energy harvesting system based on the wake galloping phenomenon.* Smart Materials & Structures, 2011. **20**(5).
[39] D.B. Zhu, et al., *A Novel Miniature Wind Generator for Wireless Sensing Applications.* 2010 Ieee Sensors, 2010: p. 1415-1418.
[40] D.A. Wang and N.Z. Liu, *A shear mode piezoelectric energy harvester based on a pressurized water flow*. Sensors and Actuators a-Physical, 2011. **167**(2): p. 449-458.
[41] S. Zhao and A. Erturk, *Deterministic and band-limited stochastic energy harvesting from uniaxial excitation of a multilayer piezoelectric stack.* Sensors and Actuators A, 2014. **214**: p. 58-65.
[42] R. Taylor, et al., *Technology Development for Electromechanical Acoustic Liners*, in *Active 04*. 2004: Williamsburg, VA. p. paper a04_093.
[43] F. Liu, et al., *Acoustic energy harvesting using an electromechanical Helmholtz resonator*. Journal of the Acoustical Society of America, 2008. **123**(4): p. 1983-1990.
[44] A. Phipps, et al., *Demonstration of a wireless, self-powered, electroacoustic liner system.* Journal of the Acoustical Society of America, 2009. **125**(2): p. 873-881.
[45] T. Matsuda, et al., *Lead-zirconate-titanate acoustic energy harvester equipped with sound-collecting helmholtz resonator.* IEICE Transactions on Electronics, 2013. **E96-C**(5): p. 722-725.
[46] H.Y. Lee and B. Choi, *A multilayer PVDF composite cantilever in the Helmholtz resonator for energy harvesting from sound pressure*. Smart Materials and Structures, 2013. **22**(11).
[47] W.-C. Wang, et al., *Acoustic energy harvesting by piezoelectric curved beams in the cavity of a sonic crystal.* Smart Materials & Structures, 2010. **19**(4).
[48] L.-Y. Wu, L.-W. Chen, and C.-M. Liu, *Experimental investigation of the acoustic pressure in cavity of a two-dimensional sonic crystal.* Physica B-Condensed Matter, 2009. **404**(12-13): p. 1766-1770.
[49] L.-Y. Wu, L.-W. Chen, and C.-M. Liu, *Acoustic energy harvesting using resonant cavity of a sonic crystal.* Applied Physics Letters, 2009. **95**(1).
[50] M. Lallart, et al., *Nonlinear optimization of acoustic energy harvesting using piezoelectric devices.* Journal of the Acoustical Society of America, 2010. **128**(5): p. 2739-2748.
[51] S.H. Kim, et al., *An electromagnetic energy scavenger from direct airflow*. Journal of Micromechanics and Microengineering, 2009. **19**(9).
[52] J.W. Stevens. *Design and test of a thermoelectric ground-source heat Engine* in *Asme International Mechanical Engineering Congress and Exposition*. 2007. Seattle. WA: ASME.
[53] M. Nouh, O. Aldraihem, and A. Baz. *Analysis and optimization of thermoacoustic-piezoelectric energy harvesters: An electrical circuit analogy approach* in *Active and Passive Smart Structures and Integrated Systems 2013, March 10, 2013 - March 14, 2013*. 2013. San Diego, CA, United states: SPIE.

[54] J. Smoker, et al., *Energy harvesting from a standing wave thermoacoustic-piezoelectric resonator.* Journal of Applied Physics, 2012. **111**(10).
[55] R. Hernandez, S. Jung, and K.I. Matveev, *Acoustic energy harvesting from vortex-induced tonal sound in a baffled pipe.* Proceedings of the Institution of Mechanical Engineers Part C-Journal of Mechanical Engineering Science, 2011. **225**(C8): p. 1847-1850.
[56] R. Montheard, et al., *Powering a Commercial Datalogger by Energy Harvesting from Generated Aeroacoustic Noise.* Journal of Physics: Conference Series, 2014. **557**(1): p. 012025.
[57] F.U. Khan and M.U. Khattak, *Contributed Review: Recent developments in acoustic energy harvesting for autonomous wireless sensor nodes applications.* Review of Scientific Instruments, 2016. **87**(2): p. 021501.
[58] E.A. Skow, K.A. Cunefare, and A. Erturk, *Power performance improvements for high pressure ripple energy harvesting.* Smart Mater. Struct., 2014. **23**(10): p. 104011.
[59] IEEE, *IEEE Standard on Piezoelectricity*. 1988, The Institute of Electrical and Electronics Engineers, Inc: New York.
[60] N.W. Hagood and A. von Flotow, *Damping of structural vibrations with piezoelectric materials and passive electrical networks.* Journal of Sound and Vibration, 1991. **146**(2): p. 243-268.
[61] A.J. Fleming, S. Behrens, and S.O.R. Moheimani, *Synthetic impedance for implementation of piezoelectric shunt-damping circuits.* Electronics Letters, 2000. **36**(18): p. 1525-1526.
[62] J.M. Renno, M.F. Daqaq, and D.J. Inman, *On the optimal energy harvesting from a vibration source.* Journal of Sound and Vibration, 2009. **320**(1–2): p. 386-405.
[63] A. Erturk and D.J. Inman, *An experimentally validated bimorph cantilever model for piezoelectric energy harvesting from base excitations.* Smart Materials and Structures, 2009. **18**(2): p. 025009.
[64] N.E. DuToit and B.L. Wardle, *Experimental verification of models for microfabricated piezoelectric vibration energy harvesters.* AIAA journal, 2007. **45**(5): p. 1126-1137.
[65] A. Erturk, J. Hoffmann, and D. Inman, *A piezomagnetoelastic structure for broadband vibration energy harvesting.* Applied Physics Letters, 2009. **94**(25): p. 254102.
[66] S.C. Stanton, C.C. McGehee, and B.P. Mann, *Reversible hysteresis for broadband magnetopiezoelastic energy harvesting.* Applied Physics Letters, 2009. **95**(17): p. 174103.
[67] PiezoSystemsInc., *Low voltage piezoelectric stacks.* 2011. **Catalog #8**(2011): p. 56-57.
[68] PICeramic. *PI Material Data*. 2012; Available from: https://www.piceramic.com/en/piezo-technology/piezoelectric-materials/.
[69] PiezomechanikGmbH. *Low voltage co-fired multilayer stacks, rings and chips for actuation*. 2012; -- Piezomechanik_Multilayer_Katalog_E_2011.05.11_WEB600:[Available from: http://www.piezomechanik.com/products/.

[70] NEC/TOKIN. *Piezoelectric Ceramics*. 2013 Oct. 11, 2013; 9470PIEVOL05E1309H1:[Available from: https://www.nec-tokin.com/english/product/pdf_dl/piezoelectricceramics.pdf.
[71] H.H.A. Krueger, *Stress Sensitivity of Piezoelectric Ceramics: Part 1. Sensitivity to Compressive Stress Parallel to the Polar Axis.* The Journal of the Acoustical Society of America, 1967. **42**(3): p. 636-645.
[72] A.B. Schaufele and K.H. Hardtl, *Ferroelastic properties of lead zirconate titanate ceramics.* Journal of the American Ceramic Society, 1996. **79**(10): p. 2637-2640.
[73] H.C. Cao and A.G. Evans, *NONLINEAR DEFORMATION OF FERROELECTRIC CERAMICS.* Journal of the American Ceramic Society, 1993. **76**(4): p. 890-896.
[74] D.Y. Zhou, M. Kamlah, and D. Munz, *Effects of uniaxial prestress on the ferroelectric hysteretic response of soft PZT.* Journal of the European Ceramic Society, 2005. **25**(4): p. 425-432.
[75] Q.M. Zhang and J. Zhao, *Electromechanical properties of lead zirconate titanate piezoceramics under the influence of mechanical stresses.* Ultrasonics, Ferroelectrics and Frequency Control, IEEE Transactions on, 1999. **46**(6): p. 1518-1526.
[76] Q.M. Zhang, et al., *Change of the weak-field properties of Pb(ZrTi)O-3 piezoceramics with compressive uniaxial stresses and its links to the effect of dopants on the stability of the polarizations in the materials.* Journal of Materials Research, 1997. **12**(1): p. 226-234.
[77] J. Park and D.L. Palumbo, *A new approach to identify optimal properties of shunting elements for maximum damping of structural vibration using piezoelectric patches.* 2004.
[78] C. Hansen, *Noise control from concept to application*. 2005, New York, NY: Taylor & Francis. 419.
[79] L. Kinsler, et al., *Fundamentals of Acoustics. 2000.* World scientific Washington.
[80] A.D. Pierce, *Acoustics: an introduction to its physical principles and applications*. Vol. 20. 1981: McGraw-Hill New York.
[81] J.W.S.B. Rayleigh, *The theory of sound*. Vol. 2. 1896: Macmillan.
[82] P.M. Morse and K.U. Ingard, *Theoretical acoustics*. 1968: Princeton university press.
[83] E. Kojima and K. Edge. *Experimental determination of hydraulic silencer transfer matrices and assessment of the method for use as a standard test procedure* in *Innovations in Fluid Power: 7th Bath International Fluid Power Workshop.* 1994: University of Bath.
[84] L. Kela, *Resonant frequency of an adjustable Helmholtz resonator in a hydraulic system.* Archive of Applied Mechanics, 2009. **79**(12): p. 1115-1125.
[85] N.E. Earnhart and K.A. Cunefare, *Compact Helmholtz resonators for hydraulic systems.* International Journal of Fluid Power, 2012. **13**(1): p. 41-50.
[86] Z. Wang, et al., *Fiber-optic hydrophone using a cylindrical Helmholtz resonator as a mechanical anti-aliasing filter.* Optics letters, 2008. **33**(1): p. 37-39.
[87] N.E. Earnhart, *Modeling and validation of a syntactic foam lining for noise control devices for fluid power systems*. 2012, Georgia Institute of Technology.
[88] E.R. Gruber, *High-Pressure Compliant Syntactic Foam For Hydraulic Noise Control*. 2016, Georgia Institute of Technology.

[89] E. Gruber and K. Cunefare. *Material Modeling of High-Pressure Compliant Syntactic Foams* in *ASME/BATH 2015 Symposium on Fluid Power and Motion Control*. 2015: American Society of Mechanical Engineers.
[90] K.A. Marek, *The modeling and use of syntactic foams for passive control of fluid-borne noise*. 2014, Georgia Institute of Technology.
[91] M. LUBRICANTS. *Product Information: True-Flo Anti Wear Hydraulic Oils*. [cited 2016; Available from: http://xtremeoil.com/wp-content/uploads/2015/01/PDS-Xtreme-AW-Hydraulic-Oil.pdf.
[92] E. Toolbox. *Volumetric or Cubical Expansion Coefficients of Liquids*. [cited 2017; Available from: http://www.engineeringtoolbox.com/cubical-expansion-coefficients-d_1262.html.
[93] H. Song, E. Klaus, and J. Duda, *Prediction of bulk moduli for mineral oil based lubricants, polymer solutions, and several classes of synthetic fluids.* Journal of tribology, 1991. **113**: p. 675.
[94] H. Gholizadeh, R. Burton, and G. Schoenau, *Fluid bulk modulus: a literature survey.* International Journal of Fluid Power, 2011. **12**(3): p. 5-15.
[95] D. Wooton. *Oxidation - the lubricant's nemesis*. Practicing Oil Analysis May 2007; Available from: http://www.machinerylubrication.com/Read/1028/oxidation-lubricant.
[96] H.P. Bloch, *Practical lubrication for industrial facilities*. 2009: The Fairmont Press, Inc.
[97] D. Troyer. *Understanding Absolute and Kinematic Viscosity*. [cited 2017 March 6, 2017]; Available from: http://www.machinerylubrication.com/Read/294/absolute-kinematic-viscosity.
[98] D.A. Hall, *Review nonlinearity in piezoelectric ceramics.* Journal of Materials Science, 2001. **36**(19): p. 4575-4601.
[99] E.A. McLaughlin, T. Liu, and C.S. Lynch, *Relaxor ferroelectric PMN-32% PT crystals under stress and electric field loading: I-32 mode measurements.* Acta Materialia, 2004. **52**(13): p. 3849-3857.
[100] E.A. McLaughlin, T. Liu, and C.S. Lynch, *Relaxor ferroelectric PMN-32% PT crystals under stress, electric field and temperature loading: II-33-mode measurements.* Acta Materialia, 2005. **53**(14): p. 4001-4008.
[101] T. Liu and C.S. Lynch, *Domain Engineered Relaxor Ferroelectric Single Crystals.* Continuum Mechanics and Thermodynamics, 2006. **18**(1): p. 119-135.
[102] W.D. Dong, et al., *Energy harvesting using the FER–FEO phase transformation in [011] cut single crystal PIN-PMN-PT.* Journal of Intelligent Material Systems and Structures, 2014.
[103] J.A. Gallagher, J. Tian, and C.S. Lynch, *Composition dependence of field induced phase transformations in [0 1 1]C PIN–PMN–PT relaxor ferroelectric single crystals with d322 piezoelectric mode.* Acta Materialia, 2014. **81**: p. 512-523.
[104] J.A. Gallagher, J. Tian, and C.S. Lynch, *Effects of composition and temperature on the large field behavior of [011]C relaxor ferroelectric single crystals.* Applied Physics Letters, 2014. **105**(5): p. 052909.
[105] J.A. Gallagher and C.S. Lynch, *Combining experiments and modeling to characterize field driven phase transformations in relaxor ferroelectric single crystals.* Acta Materialia, 2015. **89**: p. 41-49.

[106] W. Dong, *Characterization, Modeling, and Energy Harvesting of Phase Transformations in Ferroelectric Materials*. 2015, UCLA.
[107] W.D. Dong, et al., *Giant electro-mechanical energy conversion in [011] cut ferroelectric single crystals.* Applied Physics Letters, 2012. **100**(4): p. -.
[108] B. Casey. *Hydraulic Equipment Reliability: Beyond Contamination Control*. 2005 [cited 2016; Available from: http://www.machinerylubrication.com/Read/772/hydraulic-equipment-reliability.
[109] Y.C. Shu, I.C. Lien, and W.J. Wu, *An improved analysis of the SSHI interface in piezoelectric energy harvesting.* Smart Materials and Structures, 2007. **16**(6): p. 2253.
[110] S. Zhang, et al., *Advantages and challenges of relaxor-PbTiO3 ferroelectric crystals for electroacoustic transducers – A review.* Progress in Materials Science, 2015. **68**: p. 1-66.
[111] S. Zhang and F. Li, *High performance ferroelectric relaxor-PbTiO3 single crystals: Status and perspective.* Journal of Applied Physics, 2012. **111**(3): p. 031301.
[112] E. Skow, et al. *Power conditioning for low-voltage piezoelectric stack energy harvesters*. 2016.
[113] N. Kong, et al., *Resistive impedance matching circuit for piezoelectric energy harvesting.* Journal of Intelligent Material Systems and Structures, 2010. **21**(13): p. 1293-1302.
[114] G.K. Ottman, et al., *Adaptive piezoelectric energy harvesting circuit for wireless remote power supply.* IEEE Trans. Power Electron., 2002. **17**(5): p. 669-676.
[115] E. James, et al., *An investigation of self-powered systems for condition monitoring applications.* Sensors and Actuators A: Physical, 2004. **110**(1): p. 171-176.
[116] J. Brugler, *Theoretical performance of voltage multiplier circuits.* Solid-State Circuits, IEEE Journal of, 1971. **6**(3): p. 132-135.
[117] L. Garbuio, et al., *Mechanical energy harvester with ultralow threshold rectification based on SSHI nonlinear technique.* Industrial Electronics, IEEE Transactions on, 2009. **56**(4): p. 1048-1056.
[118] N.N. Ching, et al., *A laser-micromachined multi-modal resonating power transducer for wireless sensing systems.* Sensors and Actuators A: Physical, 2002. **97**: p. 685-690.
[119] R. Torah, et al., *Self-powered autonomous wireless sensor node using vibration energy harvesting.* Measurement Science and Technology, 2008. **19**(12): p. 125202.
[120] C. Saha, et al., *Step-up converter for electromagnetic vibration energy scavenger.* DTIP of MEMS & MEOMS, 2007.
[121] S. Cheng, et al., *A bridge voltage doubler AC/DC converter for low-voltage energy harvesting applications.* Proceedings of PowerMEMS, 2009: p. 25-28.
[122] S. Cheng, et al., *An active voltage doubling AC/DC converter for low-voltage energy harvesting applications.* Power Electronics, IEEE Transactions on, 2011. **26**(8): p. 2258-2265.
[123] Y. Rao and D.P. Arnold, *An input-powered vibrational energy harvesting interface circuit with zero standby power.* Power Electronics, IEEE Transactions on, 2011. **26**(12): p. 3524-3533.

[124] E.A. Skow, et al. *Pressure Ripple Energy Harvester Enabling Autonomous Sensing* in *International Fluid Power Expo*. 2014. Las Vegas, NV.
[125] J. Ranuarez, F.G.a. Sánchez, and A. Ortiz-Conde, *Procedure for determining diode parameters at very low forward voltage.* Solid-State Electronics, 1999. **43**(12): p. 2129-2133.
[126] S. Leadenham, *Advanced Concepts in Nonlinear Piezoelectric Energy Harvesting: Intentionally Designed, Inherently Present, and Circuit Nonlinearities*, in *Mechanical Engineering*. 2015, Georgia Institute of Technology.
[127] O. Semiconductor, *1N5817/D*. 2006, Semiconductor Components Industries, LLC, 2006: http://www.onsemi.com/pub_link/Collateral/1N5817-D.PDF.
[128] S. Anton, K. Farinholt, and A. Erturk, *Piezoelectret foam–based vibration energy harvesting.* Journal of Intelligent Material Systems and Structures, 2014. **25**(14): p. 1681-1692.
[129] P. Hodges, *Hydraulic fluids*. 1996: Butterworth-Heinemann.